Doctoral Thesis

# Complex Baseband Modeling and Digital Predistortion for Wideband RF Power Amplifiers

Peter Singerl

---

Faculty of Electrical and Information Engineering
Graz University of Technology, Austria


First Advisor:
Prof. Dr. Gernot Kubin, Graz University of Technology, Austria
Second Advisor:
Prof. Dr. Hermann Eul, Leibniz Universität Hannover, Germany

Graz, December 2006

## Zusammenfassung

Moderne Modulationsverfahren, die in mobilen Kommunikationssystemen (UMTS) der dritten Generation eingesetzt werden, erzeugen eine stark schwankende Einhüllende des Sendesignals. Diese Eigenschaft bewirkt eine Störung, die durch das nichtlineare Verhalten des HF Verstärkers (HF PA) hervorgerufen wird. Wir schlagen verschiedene Modellstrukturen für solche Verstärker vor, die entweder auf Memory Polynome oder auf die Approximationen von Frequenzbereichs Volterra Kernen beruhen, wodurch sich die Anzahl an freien Parametern um $80\%$ gegenüber dem Volterra Reihen Ansatz verringern lässt. Da diese Modelle Gedächtnis aufweisen, sind wir in der Lage die nichtlinearen Störungen von HF PAs mit ausreichender Genauigkeit (z.B. $-30$ dB rel. Modellierungsfehler) auch für Breitbandsignale ( 4-Träger WCDMA Signal mit $B = 20$ MHz) zu modellieren. Ausserdem schlagen wir ein Verfahren zur Konstruktion von RF PA Modellen basierend auf frequenzabhängigen AM/AM und AM/PM Konvertierungen vor. Für die Kompensation der Nichtlinearitäten analysieren und simulieren wir verschiedene digitale Vorverzerrer bezüglich Komplexität und Linearisierungsleistung. Vorverzerrer basierend auf Memory Polynomen (7ter Ordnung), können eine vergleichbare Linearisierungsleistung wie Volterra Vorverzerrer erreichen, benötigen jedoch eine wesentlich geringere Anzahl an Parametern ($11$ statt $42$). Schließlich schlagen wir eine neue Vorverzerrer Struktur vor, bei der die Kosten für die ADCs im Rückwärtspfad auf Grund der niedrigen Abtastrate bei der Systemidentifikation deutlich reduziert werden können.

## Abstract

Modern modulation methods as used in 3rd generation mobile communications (UMTS) generate strongly fluctuating transmission signal envelopes with high peak-to-average power ratios. These properties result in significant distortion due to the nonlinear behavior of the radio-frequency power amplifier (RF PA). We propose different nonlinear model structures for such amplifiers, based on memory polynomials and frequency-domain Volterra kernel expansion, where we can reduce the number of free parameters by $80\%$ compared to traditional Volterra series approaches. Because these nonlinear models incorporate memory, we are able to model the nonlinear distortion of RF PAs with sufficient accuracy (e.g., $-30$ dB relative modeling error ), including the wideband case (bandwidth $B = 20$ MHz as needed for four-carrier WCDMA). Furthermore, we propose a method to construct RF PA models from frequency-dependent AM/AM and AM/PM conversions. For the compensation of the nonlinearities, we analyze and simulate different digital predistorter structures in terms of complexity and linearization performance. As a result, memory-polynomial predistorters (7th order) can achieve a linearization performance comparable to the full Volterra predistorter, while the number of parameters is reduced from $42$ to $11$. Finally we propose a new predistortion scheme with low-rate system identification and Volterra kernel interpolation which allows a drastic cost reduction for the feedback ADC.

## Acknowledgment

Several people made this thesis possible. First of all, I would like to thank Dr. Franz Dielacher, who made this work possible. Furthermore, I am grateful to Professor Gernot Kubin, whose support throughout my research has led to this thesis and who has shaped my understanding of nonlinear systems and signal processing. I would like to thank Professor Hermann Eul for being my second advisor for this thesis.

Many thanks to my family for their continuous support and encouragement and to all of my friends for the great time we had in Graz and Villach. Furthermore, I would like to thank everybody from the SPSC Lab and especially the people from the CD Lab for Nonlinear Signal Processing for the numerous interesting and fruitful discussions and the fun we had. A special thanks goes to Olof Tornblad and Gordon Ma for providing the physical RF PA models. Furthermore, I would like to thank Birgit Vogel for the careful proof-reading of this thesis.

Finally, special thanks goes to Infineon Technologies Austria AG and the Christian Doppler Forschungsgesellschaft for the funding of this research project.

Graz, December 2006 Peter Singerl

# Contents

# List of Figures

# List of Tables

# Chapter 1

# Introduction

In the past years the rising number of subscribers in mobile communication networks led to the development of new 3rd -generation standards like UMTS (Universal Mobile Telecommunications Standard). In particular the demand for higher data rates, e.g., for multimedia applications, and for fast internet access have been considered here. In addition both the modulation scheme and the multiple user access method were designed for a higher spectral efficiency compared with former mobile communications standards like GSM (Global System for Communication).

Modern modulation formats such as OFDM (Orthogonal Frequency Division Multiplexing) or WCDMA (Wideband Code Division Multiple Access) possess strong fluctuations in their signal envelopes with high peak-to-average power ratios (PAPR $> 10$ dB) [48, 50, 32]. For this reason, highly linear transmitters are needed to avoid an unacceptably high nonlinear distortion of the transmission signal. To obtain a sufficient output power level to cover the range within a mobile communication cell, RF power amplifiers (RF PA) with RF output powers of $P \geq 100$ W are needed. As these devices are one of the most cost intensive components within a basestation, it is of fundamental importance to operate the RF PA near the $1$ dB compression point to obtain the highest possible efficiency [50, 32].

The main problem is the nonlinear behavior of the RF PA in combination with the mentioned high PAPR of the transmission signal envelope if we drive the RF PA deep into compression ( efficiency is approximately inversely proportional to linearity) [50, 32]. This leads to intermodulation distortion and spectral regrowth of the transmission signal. If we made no attempt to linearize the RF PA, we would generally obtain an unacceptably high bit-error rate on the receiver side and a violation of the spectral transmission masks which are specified by the regulatory bodies.

To overcome these problems we basically have two options. The first one is to back-off the RF PA which leads to bad efficiencies [32, 15, 16] or we can develop proper RF PA concepts including linearization. The most widespread concept for today's RF PAs is Class-AB with feedforward linearization [32, 15, 16]. Unfortunately, this concept is cost-intensive because all blocks for the linearization (power splitter, delay-lines, auxilary-amplifier) have to be implemented in the high frequency domain. Another difficulty is the demand for adaptive control of the linearization scheme to be able to react to the slightly time-varying behavior of the RF PA (temperature, aging,...). The basic concept of a feedforward linearization is depicted in the block diagram of Fig. 1.1. The RF input signal $x(t)$ is fed to the RF PA, which generates the distorted output signal given by

$$y_{PA}(t) = G_1 x(t - \tau_1) + d(t), \tag{1.1}$$

where $G_1$ denotes the gain of the RF PA and $\tau_1$ the latency of the RF PA. The output signal of the RF PA in (1.1) is composed of the amplified input signal and the distortion $d(t)$, which is caused by the inherent nonlinearity of the RF PA. If we subtract the delayed input signal $y_1(t) = x(t - \tau_1)$ from a portion of the RF PA output signal in (1.1), we obtain a weighted error signal given by

$$e(t) = \gamma_1 G_1 x(t - \tau_1) + \gamma_1 d(t) - x(t - \tau_1), \tag{1.2}$$

where the constant factor $\gamma_1$ describes the attenuation of the directional-coupler. If $\gamma_1 = 1/G_1$, the error signal is purely determined by the weighted distortion of the RF PA given by

$$e(t) = \gamma_1 d(t). \tag{1.3}$$

Because the power of the error signal in (1.3) is in general much lower than the power of the amplified RF PA input signal, we can use a linear low-power auxiliary PA to generate

$$\begin{aligned} y_2(t) &= G_2 e(t - \tau_2) \\ &= G_2 \gamma_1 d(t - \tau_2), \end{aligned} \tag{1.4}$$

which is used to cancel out the nonlinear distortion of the RF PA. The final output signal is given by

$$z(t) = G_1 x(t - \tau_1 - \tau_2) + d(t - \tau_2) - \gamma_2 G_2 \gamma_1 d(t - \tau_2), \tag{1.5}$$

where $\tau_2$ denotes the latency of the low-power auxiliary PA. If the gain of the auxiliary PA $G_2 = 1/(\gamma_1 \gamma_2)$, the output signal of the RF PA is given by

$$z(t) = G_1 x(t - \tau_1 - \tau_2). \tag{1.6}$$

Thus the output signal of the feed-forward linearization concept in Fig. 1.1 is an amplified and time-delayed replica of the input signal with the nonlinear distortion from the main RF PA removed.

## 1.1 Introduction to Digital Predistortion

As nowadays digital signal processors (DSPs) are very fast and powerful, the purely analog state-of-the-art linearization methods such as feedforward [32, 15, 16, 50] are replaced more and more by digital predistortion concepts. By using digital predistortion we can increase the overall efficiency (RF output power at the antenna over the whole DC-power which is needed to operate a basestation) from approximately $10$ % for feedforward linearization concepts to approximately $20$ %, because no auxiliary amplifier is needed anymore [50].

A digital predistorter is a functional block (it incorporates the inverse of the RF PA) implemented in the digital baseband domain which precedes the RF PA in order to linearize the whole transmitter chain. Therefore, we can advantageously employ advanced digital signal

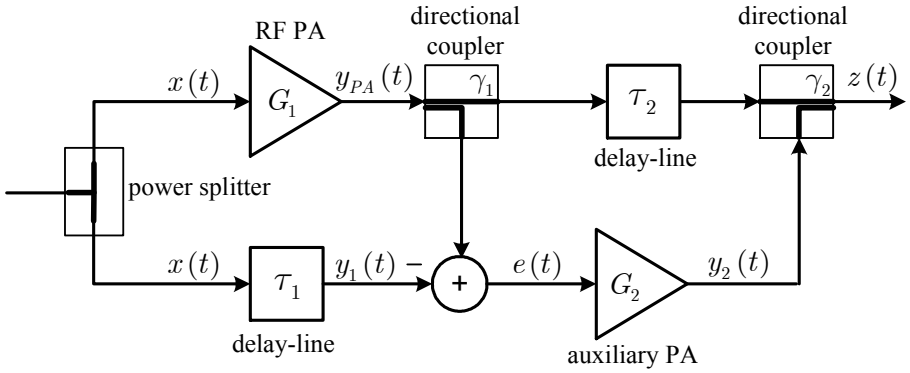


**Figure 1.1:** Blockdiagram of a feedforward linearization concept.

processing methods for nonlinear system identification, parameter adaptation and predistortion without the difficulties which arise in an analog feedforward linearization concept.

Figure 1.2 shows a block diagram of a wireless basestation transmitter with digital predistortion in a direct up-conversion architecture [39]. The complex baseband signal (I,Q) from the baseband unit is fed to a peak-to-average power ratio (PAPR) reduction block [38], where the PAPR can be reduced from approximately $10$ dB to approximately $6$ dB. This allows us to increase the average input power of the multi-carrier PA (MC PA) without increasing the nonlinear distortion (higher efficiency) [32]. The complex baseband signal after PAPR reduction is pre-distorted by the digital predistorter-core (DPD-core) and up-converted to the desired RF carrier frequency. The multi-carrier RF PA (MC PA) is in general designed to cope with input signal bandwidths of approximately $20$ MHz, to transmit up to four WCDMA-carriers simultaneously. Because the behavior of the RF PA is in general not known in advance and the behavior is also slightly time-varying (aging, temperature-drifts,...), we need a feedback path (frequency down-converter in Fig. 1.2) from the output of the RF PA back to the digital predistortion processor (DPD-processor) to adjust the predistorter parameters accordingly.

The most critical part of a digital predistorter is the right choice of the predistorter architecture, which must be able to perform at least an approximate inverse (most nonlinear systems do not possess an exact inverse [40, 12, 56]) of the RF PA. At this time, most of the commercial digital predistorters used in basestation transmitters are based on static nonlinear systems which compensate the AM/AM-conversion and AM/PM-conversion [32, 8, 51] of an RF PA with simple look-up table techniques [13, 32, 17, 43, 41, 14].

The basic concept of such a predistorter is shown in Fig. 1.3. The complex baseband input signal $\tilde{x}$ from the PAPR reduction block (see Fig. 1.2 and Fig. 1.3) will be multiplied with the complex correction term $F(|\tilde{x}|)$ (based on the inverse AM/AM- and AM/PM-conversion) from a look-up table. The predistorted output signal $\tilde{y}[k] = \tilde{x}[k]F(|\tilde{x}[k]|)$ will be frequency up-converted to the desired carrier frequency and amplified with the complex gain $G(|\tilde{y}|)$ (based on the AM/AM- and AM/PM-conversion) of the MC PA in Fig. 1.2.

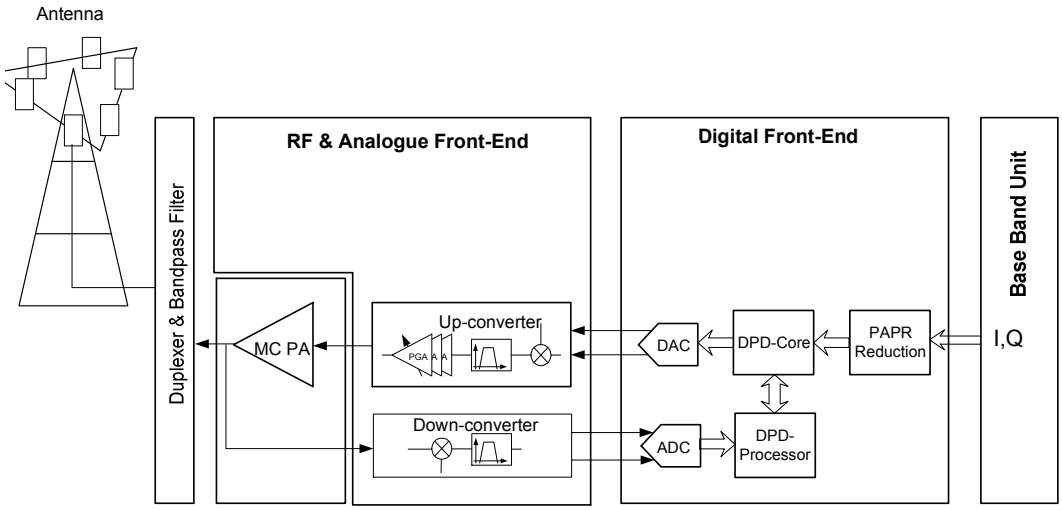


**Figure 1.2:** Blockdiagram of a wireless basestation transmitter including peak-to-average power ratio reduction (PAPR) to increase the average power (higher efficiency) and digital predistortion for the linearization of the multi-carrier RF PA (MC PA). The digital predistorter core (DPD-core) incorporates the approximate inverse of the MC PA in order to linearize the transmitter chain. Because the behavior of the MC PA is slightly time-variant, a feedback path (down-converter) is necessary to adjust the DPD parameters accordingly.

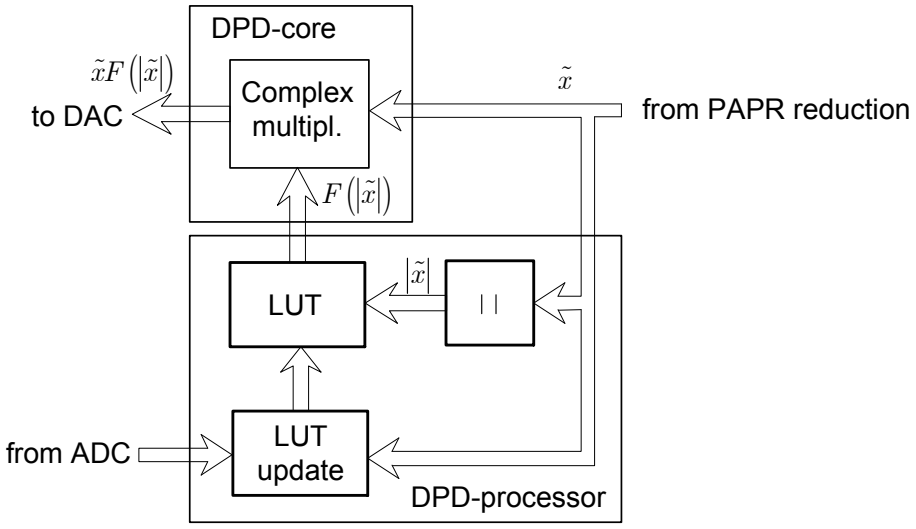


**Figure 1.3:** Blockdiagram of a particular digital predistorter-core (complex multiplier) and a digital predistortion-processor (look-up table (LUT) and LUT update) from Fig. 1.2 to linearize the MC PA in Fig. 1.2. The DPD is only suitable for narrowband applications because this system is purely based on the inverse AM/AM- and AM/PM-conversion (static nonlinearities).

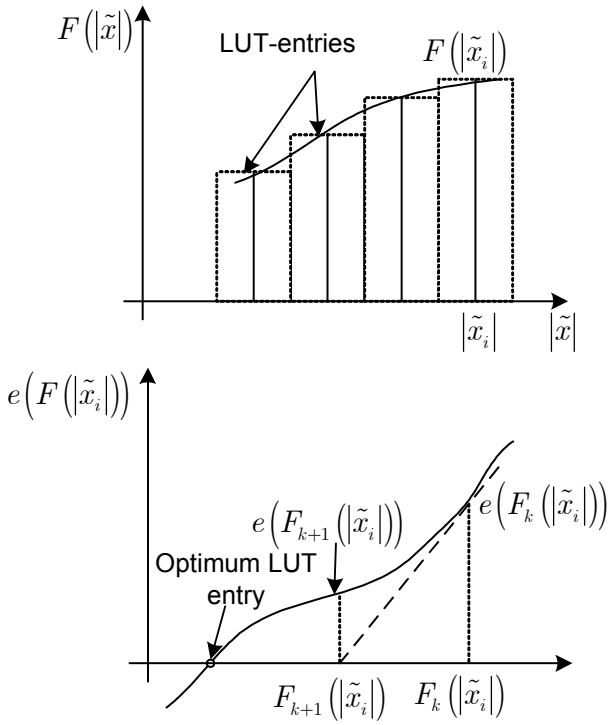


**Figure 1.4:** Newton algorithm to update the look-up table (LUT) entries. The magnitude of the complex input signal $|\tilde{x}|$ will be quantized to index a finite number of complex LUT entries $F(|\tilde{x}|)$ (for a convenient representation the values in the figures are assumed to be real valued). This values are are multiplied with the complex baseband input signal $\tilde{x}[n]$ in order to linearize the RF PA in Fig. 1.2. Once we have calculated one output sample we can compare it with the corresponding input sample to recalculate a better LUT entry.

Therefore, the PA output signal in the equivalent discrete-time baseband domain is given by

$$z[k] = \tilde{x}[k]F(|\tilde{x}[k]|)G(|\tilde{x}[k]|\,|F(|\tilde{x}[k]|)|), \tag{1.7}$$

which is in the ideal case an amplified replica of the input signal $K\tilde{x}[k]$, where $K$ is a real constant (gain). The look-up table will be indexed by the magnitude of the complex input signal $|\tilde{x}|$, because the gain $G(|\tilde{y}|)$ ( and also the AM/AM-conversion and the AM/PM-conversion) of the MC PA are static nonlinear functions which are solely dependent on the input signal magnitude. The optimum look-up table entries $F(|\tilde{x}|)$ are calculated from the input signal samples $\tilde{x}[k]$ and the down-converted and digitized MC PA output signal samples in the DSP-processor. Once we have calculated one output signal sample in (1.7), we can compare the scaled output signal sample $(1/K)$ with the corresponding input signal sample. If the LUT entry $F_k(|\tilde{x}_i|)$ is not the optimum value, the corresponding error $e(F_k(|\tilde{x}_i|) \neq 0$ (see Fig. 1.4). If we use the present LUT entry and the corresponding error at time $k$, we can calculate (e.g. with a Newton algorithm) a new LUT entry for the given $|\tilde{x}_i|$ for the time-instant $k+1$, which leads hopefully to a smaller error (see convergence

conditions in [13]). It is important to note that the LUT entries are updated in an arbitrary sequence which depends on the appearance of the different input signal magnitudes.

Unfortunately, the digital predistorter in Fig. 1.3 is only suitable for narrowband amplifiers (as will be explained further below in Chap. 2). If we consider wideband input signals such as four-carrier WCDMA, and/or high power RF transistors, the RF PA can no longer be described sufficiently accurately with the AM/AM-conversion and AM/PM-conversion [36, 51]. This is due to the memory effects of the RF PA which are introduced by matching networks, biasing networks and the self heating of the RF power transistors [11, 36, 69, 70]. For such applications, the RF PA behaves as a dynamic nonlinear system whose output signal at a certain time-instant may depend on the whole history of the input signal.

This fact makes the task of digital predistortion much more difficult, because in this case we cannot perform a linearization by using a simple multiplicative correction of the input signal as shown in Fig. 1.3 to achieve the required linearization performance. Although most commercial products still use feed-forward linearization or digital predistortion based on look-up table techniques, the growing demand for cheaper linearization concepts which can handle more than one carrier has lead to the development of more sophisticated predistortion concepts.

Several researchers have shown that Volterra series [56, 52, 40] can be used to describe RF PAs with memory and their (approximate) inverse [75]. Unfortunately, the number of free parameters increases immensely with the order of the nonlinearity and the memory length [40]. This leads in general to an unacceptably high computational complexity for the hardware which is available today. For this reason, several special structures which are based on a simplification of full Volterra series descriptions were developed in the past. These are for example Wiener-models (cascade connection of a linear filter and a static nonlinear function), Hammerstein-models (cascade-connection of a static nonlinear function and a linear filter) and models which are composed of a nonlinear function embedded between two linear filters (L-N-L) [5, 6, 4, 19, 30]. Although these models incorporate memory, the linearization performance is quite limited if the input signal bandwidth is as large as, e.g., in the case of a four carrier WCDMA excitation. Another problem is that most of these models are nonlinear in their parameters (higher-order Volterra kernels are products of lower-order kernels as e.g. $h_m(k_1, \ldots, k_m) = h(k_1) \cdots h(k_m)$), which makes the parameter estimation much more difficult. Other models such as parallel Wiener or memory-polynomials are more promising to obtain the required linearization performance for wideband applications [36, 51, 33, 21].

In all these nonlinear models, the number of free parameters are in general significantly reduced compared to the full Volterra model, while the linearization performance is still comparable to full Volterra models.

For the estimation of the predistorter parameters, basically two different procedures are known from the literature. The first one is used to identify the behavior of the RF PA and to calculate the approximate inverse e.g. $p$th-order inverse [56, 54, 40], and the second one is used to identify the inverse of the RF PA directly [22, 20, 21].

The first procedure leads to complicated predistortion structures (especially for higher orders) which are composed of higher order nonlinear operators and the inverse of the linear operator which describes the behavior of the RF PA. Another difficulty is the estimation

of the individual Volterra operators from input/output measurements because of their non orthogonal property [56].

The latter, called indirect learning architecture (direct estimation of the inverse) is easier to handle especially if the predistorter is linear in its parameters. In this case the optimum postdistorter can be found by minimizing a certain cost-function with standard linear optimization algorithms (LMS, RLS,...) [26, 40]. Once the optimum post-inverse is found, the postdistorter is used as a predistorter with the assumption that the post-inverse is a good approximation for the pre-inverse of the RF PA. This assumption is valid (experimentally verified) as long as the cost-function of the

if the resulting cost-function become sufficiently small during the postdistorter training process.

## 1.2 Scope of the Work

The aim of this work is to use digital signal processing and mixed signal methods to linearize an RF PA (whole transmitter) for wireless basestation transmitters in order to increase the efficiency and to reduce the nonlinear distortion. The predistorter should be applicable for modern modulation formats such as WCDMA or OFDM with bandwidths up to $20$ MHz (four WCDMA carriers). For such large input signal bandwidths, the RF PA can no longer be described by two static nonlinearities (AM/AM-conversion and AM/PM-conversion) as in the case of small input signal bandwidths and/or low-power RF amplifiers. Therefore the predistortion structures become more complex, which increases the hardware requirements in general. For this reason, the focus should not only be the achievement of a good linearization performance, but also the hardware complexity should be considered as a key-issue in this work. Digital Predistorters act as an approximate inverse of the RF PA in its equivalent baseband representation [49, 8]. To develop efficient predistortion structures, it is of fundamental importance to understand the RF PA behavior in the complex baseband domain. For this reason a considerable part of this work refers to nonlinear complex baseband modeling. Such nonlinear models can not only be used to develop digital predistorters, these models can also be used in system-level simulations, e.g., to test the spectral emission masks, or to predict the error vector magnitudes (EVM) which is defined as the square-root of the ratio of the mean error vector power to the mean reference power expressed in percent. [50, 42].

To test the predistorter performance in terms of adjacent channel power ratio (ACPR) [3, 50], we apply the different predistorter algorithms implemented in a MATLAB® environment to an Infineon $2.2$ GHz, $90$ W, Class-AB RF power amplifier [28]. This amplifier is implemented in the physical RF simulation tool Microwave Office®, which allows a realistic simulation of RF components in the frequency (harmonic balance mode [37]) or the time domain.

## 1.3 Outline of the Thesis and Main Contributions

In this thesis we focus on modeling nonlinear passband systems in the equivalent complex baseband domain and the digital predistortion of RF power amplifiers for wideband appli-

cations. The term ”wideband” refers to input signal bandwidths where the memory effects of the RF PAs are no longer negligible (e.g., four-carrier WCDMA) if we want to obtain a sufficient modeling accuracy or linearization performance. In the following, we give a chapter by chapter overview for the thesis and for the main contributions which often have led to publications and/or patent applications during this work.

**Introduction:** In chapter 1 we give an introduction to digital predistorters and a problem statement.

**Baseband Modeling of Nonlinear Passband Systems:** In chapter 2 we address the problem of complex baseband modeling of real valued nonlinear passband systems such as RF PAs. We show the difficulties which arise if we apply the well known quasi-memoryless models (AM/AM-conversion and AM/PM-conversion) to describe an RF PA baseband system under wideband excitation (four carrier WCDMA). To overcome the limitations of these quasi-memoryless models we replace them by complex baseband Volterra series models which improve the modeling accuracy considerably. Furthermore, we show the relationship between Volterra series models and quasi-memoryless models and extend the concept of the AM/AM-conversion and AM/PM-conversion to make these nonlinear functions frequency dependent. The extended functions can be used to construct memory-polynomial models (Volterra series models where the off-diagonal entries are zero) from simple multi-tone measurements.

- Peter Singerl and Gernot Kubin, Constructing Memory-Polynomial Models from Frequency-dependent AM/AM and AM/PM Measurements, submitted to IEEE International Symposium on Circuits and Systems (ISCAS), New Orleans (USA), May 2007 [67].
- Peter Singerl, Gernot Kubin, Constructing Memory-Polynomial Models from Frequency-dependent AM/AM and AM/PM Measurements, pending patent application, Germany and United States, 19.04.2006 [65].

**Frequency-Domain Volterra Kernel Expansion:** In chapter 3 we transform the time-domain complex Volterra series models from chapter 2 to the frequency domain. If the frequency-domain Volterra kernels are quite smooth over the input signal bandwidth, it could be useful to expand these kernels with multi-variate orthogonal functions to reduce the number of free parameters. If we transform the new frequency-domain representation back to the time-domain, we obtain a model which is composed of a bank of linear filters and a multi-variate polynomial function. Because this model is still linear in the parameters, we can estimate them with linear optimization algorithms as, e.g., least squares.

- Peter Singerl and Gernot Kubin, Chebyshev Approximation of Baseband Volterra Series for Wideband RF Power Amplifiers, IEEE International Symposium on Circuits and Systems, Kobe (Japan), May 2005, vol. 3, pp. 2655-2658 [66].

- Peter Singerl, A New Approach for Efficient Modeling of Nonlinear Passband Systems for Communication Applications, International Workshop on Nonlinear Circuits and Signal Processing, Honolulu (USA), March 2005, pp. 379-382 [58].
- Peter Singerl and Gernot Kubin, Frequency-Domain Volterra Series Expansion for Efficient Modeling of Wideband RF Power Amplifiers, to be submitted to IEEE Transactions on Circuits and Systems.
- Peter Singerl, Gernot Kubin, Efficient Approximation of Baseband Volterra Series for Wideband RF Power Amplifiers, pending patent application, Germany and United States, 9.05.2006 [68].

**Volterra Kernel Interpolation for System Modeling and Predistortion Purposes:** In chapter 4 we use the fact that nonlinear systems can be identified on a sampling-rate which only fulfills the Nyquist theorem regarding the input signal bandwidth. Based on this knowledge, we show how such low-rate models can be upsampled by simple multi-dimensional zero-padding, to obtain high-rate models which are needed for system modeling and digital predistortion as well. This technique requires almost no additional computational complexity.

- Peter Singerl and Heinz Koeppl, Volterra Kernel Interpolation for System Modeling and Predistortion Purposes, IEEE International Symposium on Signals, Circuits and Systems, Iasi (Romania), July 2005, pp. 251-254 [63].
- Peter Singerl, Heinz Koeppl, Volterra Kernel Interpolation of Nonlinear Systems, pending patent application, Germany and United States, 22.04.2005 [64].

**Digital Baseband Predistortion for RF Power Amplifiers:** In chapter 5 we address the problem of digital predistortion for RF power amplifiers. The digital predistortion is implemented by a functional block (approximate inverse of the RF PA) which precedes the RF PA in order to linearize them (whole transmitter). We develop different predistorter architectures based on Volterra series models, apply them to a 2.2-Ghz 90-W Class-AB RF PA and compare their complexities and linearization performances. Furthermore, we develop a simple predistorter architecture where a low-rate system identification and upsampling as shown in chapter 4 can be applied.

- Peter Singerl and Heinz Koeppl, A Low-Rate Identification Method for Digital Predistorters Based on Volterra Kernel Interpolation, IEEE Midwest Symposium on Circuits and Systems, Cincinnati (USA), August 2005, pp. 1533-1536 [62].
- Peter Singerl, Aditya Agrawal, Aditya Garg, Neelabh, Gernot Kubin and Hermann Eul, Complex Baseband Predistorters for Nonlinear Wideband RF Power Amplifiers, IEEE Midwest Symposium on Circuits and Systems, San Juan (USA), August 2006, [60].
- Heinz Koeppl and Peter Singerl, An Efficient Scheme for Nonlinear Modeling and Predistortion in Mixed Signal Systems, to appear in IEEE Trans. Circuits Syst., December 2006 [34].

- Peter Singerl and Heinz Koeppl, A Low-Rate Identification Method for Digital Predistorters Based on Volterra Kernel Interpolation, invited for submission to the Springer Journal, Analog Integrated Circuits and Signal Processing.
- Peter Singerl, Digital Predistorter Based on Frequency-Domain Volterra Kernel Approximation, pending patent application, Germany and United States, 22.05.2005, [59].
- Peter Singerl, Heinz Koeppl, An Efficient Scheme for Nonlinear Modeling and Predistortion in Mixed Signal Systems, pending patent application, Germany and United States, 02.05.2006, [61].

**Concluding Remarks:** In chapter 6 we summarize and conclude the work and discuss further research objectives.

**Hilbert Transform of Complex Modulated Passband Signals:** In appendix A we derive the Hilbert transform of amplitude and phase modulated passband signals, which is needed for the development of a closed-form representation of quasi-memoryless passband systems in Chap. 2.

**Optimum Parameter Calculation of Multi-Variate Orthogonal Polynomials:** In appendix B we derive the optimum parameter calculation for multi-variate orthogonal polynomials which are needed in Chap. 3.

**Professional Awards:**

- IEEE Student paper award for ”A Low-Rate Identification Method for Digital Predistorters Based on Volterra Kernel Interpolation”, IEEE Midwest Symposium on Circuits and Systems, Cincinnati (USA), August 2005.
- Student paper award for ”A New Approach for Efficient Modeling of Nonlinear Passband Systems for Communication Applications”, from Research Institute of Signal Processing Japan, International Workshop on Nonlinear Circuits and Signal Processing, Honolulu (USA), March 2005.

Furthermore, the author contributed to publications which are outside the scope of this thesis, which are

- Peter Singerl and Christian Vogel, An Analysis of a Low Complexity Received Signal Strength Indicator for Wireless Applications, Austrochip 2004, Proceedings of the Austrochip 2004, Villach (Austria), October 2004, pp. 57-60.
- Peter Singerl and Christian Vogel, A Fast and Accurate Automatic Gain Control for a Wireless Local Area Network Receiver, Global Mobile Congress (GMC 2005), Chongqing (China), October 2005, pp. 379-382.
- Wolfgang Horn and Peter Singerl, Thermally Optimized Demagnetization of Inductive Loads, European Solid-State Circuits Conference, Leuven (Belgium), September 2004, pp. 21-23.

# Chapter 2

# Baseband Modeling of Nonlinear Passband Systems

This chapter deals with the problem of modeling nonlinear passband systems by the means of quasi-memoryless models and Volterra series based models in the complex baseband domain. The resulting baseband models can be employed, e.g., in system-level simulations, to predict the generated distortion (intermodulation and spectral regrowth), without considering a frequency up-conversion unit which shifts the baseband signal to the RF carrier frequency. Since with these baseband models, we only relate the complex input and output envelopes, the computational complexity to calculate the output signal of the nonlinear model can be significantly reduced.

In Sec. 2.1 we introduce complex nonlinear baseband modeling and review existing literature. In Sec. 2.2 we transform a static nonlinear system which is composed of two polynomial functions acting on two orthogonal carriers and a linear passband filter to the baseband domain. Depending on whether the resulting parameters are real or complex, we either obtain a so called memoryless or a quasi-memoryless nonlinear model. In Sec. 2.3 we replace the passband nonlinearity from Sec. 2.2 by a real Volterra series. The resulting complex baseband Volterra series model is able to represent memory effects which are of fundamental importance for wideband applications. In Sec. 2.4 we consider the relationship between a quasi-memoryless baseband model and a complex Volterra series model. We extend the concept of the AM/AM and AM/PM-conversion for the case of a Volterra model in Sec. 2.5, and use the frequency-dependent AM/AM and AM/PM surfaces to identify the complex linear filters of a memory-polynomial model.

## 2.1 Introduction

Nonlinear baseband behavior models relate the complex input and output envelopes directly in the complex baseband domain [8, 7, 10]. In general, these baseband models can be applied to narrow and wideband applications as long as the carrier frequency is much larger than the bandwidth of the complex-modulated passband input signal. If the input signal is narrowband, real nonlinear passband system behaves statically, which means that the complex output envelope of the passband system depends purely on the current magnitude of the complex input envelope.

Such a nonlinear passband system can be modeled by two static nonlinear functions which act on two orthogonal carriers to affect both, the magnitude and the phase of the

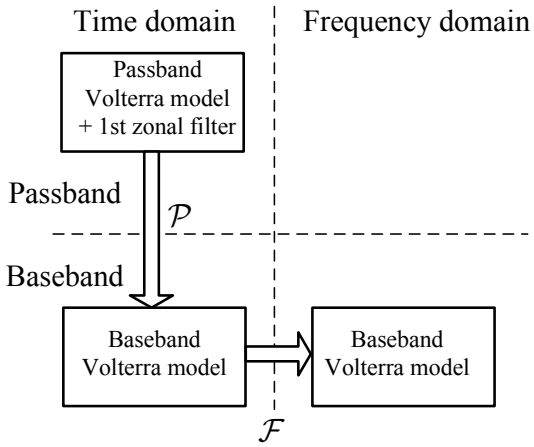


**Figure 2.1:** The cascade of a nonlinear passband system and a linear filter can be transformed to an equivalent baseband model, which relates the complex input and output envelopes of the nonlinear passband system. The frequency-domain representation of the complex baseband model is used to derive a narrowband model.

output signal (cf. Fig. 2.3). This nonlinear passband model is well known and discussed in several publications [8, 7, 51, 32, 15, 16]. It is remarkable that although this kind of a nonlinear passband model incorporates memory which is introduced by a Hilbert transformer to shift the carrier phase by 90°, the equivalent baseband model does not do so (cf. Fig. 2.7). From a system point of view, the baseband model results in a purely static nonlinear model. For this reason the complex baseband model is called quasi-memoryless. If we do not introduce a Hilbert transformer in the real passband model we are not able to change the phase of the output signal. In this case the parameters of the equivalent baseband model become real. Such a nonlinear baseband model is called memoryless. The concept of a quasi-memoryless nonlinear model is very popular in the RF literature e.g. for modeling RF power amplifiers [8, 32, 15, 16, 53, 31], because this model can be characterized through two static nonlinear functions called AM/AM-conversion (amplitude to amplitude conversion) and AM/PM-conversion (amplitude to phase conversion) [32, 15, 16, 36].

The so far considered quasi-memoryless baseband model is only sufficient for narrowband applications, because only in this case, the frequency-domain Volterra kernels can be approximated by complex constants (will be considered in more detail in Sec. 2.4). If we employ modern modulation schemes such as OFDM (orthogonal frequency division multiplexing) or WCDMA (wideband code division multiple access) [32, 27], the modeling of a real passband system such as an RF power amplifier (PA) with a quasi-memoryless system generally leads to poor modeling results [36, 75]. The reason for the large modeling error can be found in the frequency dependency of the nonlinear passband system which can be physically explained by the electrical and thermo-electrical memory effects [70, 69, 11].

These nonlinear memory effects generate additional spectral components which are in general not symmetric around the carrier frequency [11]. Unfortunately we can not ex-

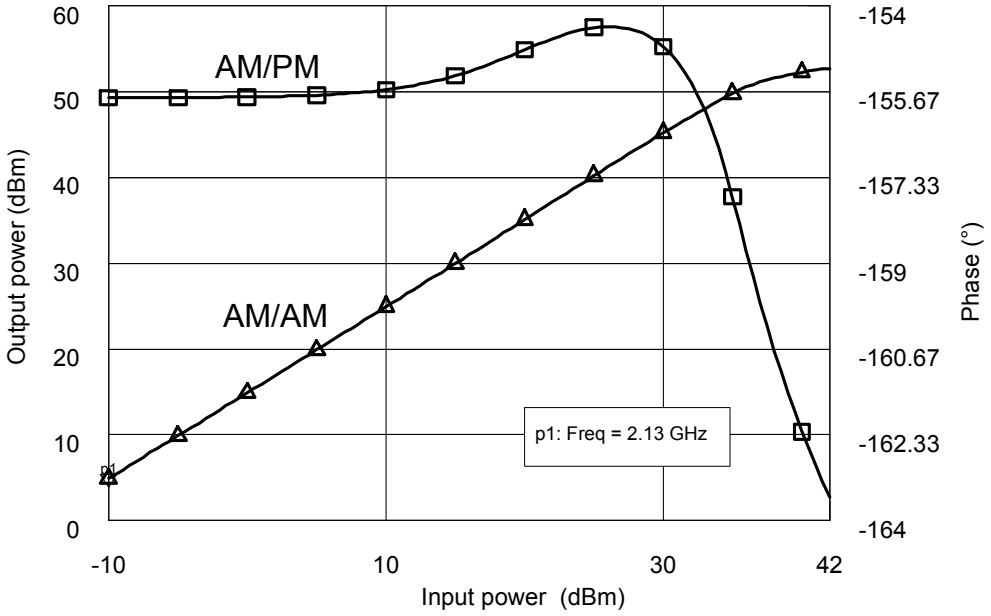


**Figure 2.2:** AM/AM- and AM/PM-conversion of a $2.2$-GHz, $90$-W Class AB RF power amplifier, excited with a single-tone with a frequency of $2.13$ GHz and a swept power of $-10$ dBm up to $42$ dBm. Both curves are evaluated for the fundamental output signal at $2.13$ GHz.

plain these spectral asymmetries neither with a memoryless nor with a quasi-memoryless baseband model as shown in [74].

To overcome this problem we employ a more general real passband Volterra model, and transform this model to the baseband domain. This process is depicted in Fig.2.1, where $\mathcal{P}$ denotes the transform of a cascade of a real passband Volterra model and a 1st-zonal [8, 10] filter, which only passes the frequency components centered around the angular carrier frequency $\omega_c$, to an equivalent baseband model. This procedure has been first proposed in [7] for modeling a nonlinear satellite link. For developing a narrowband model, we need a frequency-domain representation of the complex baseband Volterra model, which is obtained by applying the Fourier transform $\mathcal{F}$ to the output signal of the complex baseband Volterra model (see Fig, 2.1).

A general treatise on real Volterra series in the continuous and discrete-time domain can be found in [56, 52, 40].

## 2.2 Memoryless and Quasi-Memoryless Baseband Modeling

If we excite a nonlinear passband system, e.g., an RF PA, with a single tone $x(t) = a\cos(\omega_c t + \phi_0)$, where $a$ is the magnitude, $\omega_c$ is the angular carrier frequency (in the future

simply called carrier frequency) and $\phi_0$ is the phase, the output signal is composed of harmonics at the multiples of the carrier frequency $\pm k\omega_c$ for $k = 0, 1, \ldots, L$, where $L$ denotes the highest polynomial order of the nonlinearity in the real passband system. If we vary the input signal magnitude $a$, both the amplitude and the phase of the fundamental output signal at $\pm\omega_c$ vary with the input signal magnitude $a$ in a nonlinear way. These nonlinear functions are called AM/AM-conversion (amplitude modulation to amplitude modulation) and AM/PM-conversion (amplitude modulation to phase modulation) [8, 32, 15, 16, 53, 31]. Figure 2.2 shows the AM/AM-conversion and AM/PM-conversion for a 2.2-GHz, 90-W, Class AB RF PA excited with a 2.13-GHz single tone. The curves are generated with a physical RF simulator (Microwave Office ®) in harmonic balance mode [37].

Figure 2.3 depicts a real passband model whose input-output behavior can be characterized by an AM/AM and AM/PM conversion as depicted in Fig. 2.2. In order to model the amplitude dependent phase behavior, we employ two different polynomial functions acting on two orthogonal carriers [7, 8, 32, 15, 16, 53, 31]. The resulting distorted signals are filtered with a 1st-zonal filter (passband filter centered at $\pm\omega_c$) to pass only the spectral components of interest near the carrier frequency $\pm\omega_c$ [8, 10]. Therefore the real nonlinear passband system can be modeled by a tandem connection of a nonlinear system described by the operator **G** and a dynamic linear system decribed by the operator **F** as illustrated in Fig. 2.3. The real passband signal $x(t) = a(t)\cos(\omega_c t + \phi_0(t))$ is fed to the nonlinear system described by the nonlinear system operator **G** to obtain the output signal

$$\begin{aligned} u(t) &= \mathrm{G}[x(t)] \\ &= \sum_{n=1}^{2} u_n(t), \end{aligned} \tag{2.1}$$

where

$$u_1(t) = \sum_{l=1}^{L} b_l x^l(t), \quad u_2(t) = \sum_{l=1}^{L} c_l x_s^l(t), \tag{2.2}$$

are the output signals of the static nonlinearities in Fig. 2.3. The signal $x_s(t) = \mathcal{H}\{x(t)\} = a(t)\sin(\omega_c t + \phi_0(t))$ (cf. Appendix A) denotes the Hilbert transform [45, 46, 29] of the complex modulated passband input signal $x(t)$. The output signal $u(t)$ of the nonlinear operator **G** is filtered by a linear 1st-zonal filter described by the linear operator **F**, to obtain the overall output signal of the nonlinear passband systems in Fig. 2.3 and Fig. 2.4 by

$$\begin{aligned} y(t) &= (\mathbf{F} \circ \mathbf{G})\,[\,x(t)] \\ &= \mathbf{H}\,[\,x(t)] \\ &= \sum_{n=1}^{2} \mathbf{F}\,[\,u_n(t)]\,, \end{aligned} \tag{2.3}$$

which incorporates only the spectral components located around the carrier frequency $\omega_c$. $\mathbf{H} = \mathbf{F} \circ \mathbf{G}$ describes the cascade of the nonlinear passband system (e.g. RF PA) and the 1st-zonal filter in Fig. 2.4 in an operator notation. To describe the input-output behavior

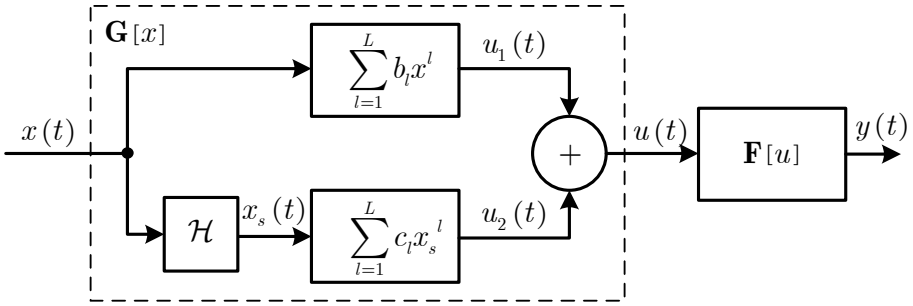


**Figure 2.3:** Nonlinear passband model which can be characterized by the AM/AM- and the AM/PM-conversion. The Hilbert transformer $\mathcal{H}$ shifts the carrier of the input signal at $90^\circ$ to affect the phase of the output signal. The output signal $u(t)$ is fed to a 1st-zonal filter $\mathbf{F}[u]$ (bandpass filter) to pass only the spectral components of interest near the carrier frequency.

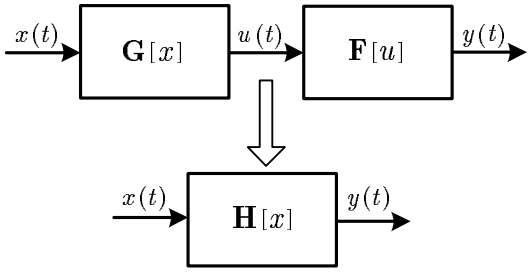


**Figure 2.4:** Cascade of the nonlinear passband system **G** and a linear 1st-zonal filter **F** to pass only the spectral components of interest around the carrier frequency $\pm\omega_c$. $\mathbf{H} = \mathbf{F} \circ \mathbf{G}$ denotes the cascade of the nonlinear system and the linear filter in operator notation.

of the passband model in Fig. 2.3 and Fig. 2.4 in the baseband domain, we rewrite the real passband input signals

$$\begin{aligned} x(t) &= \mathrm{Re}\left\{\tilde{x}(t)\exp(j\omega_c t)\right\} \\ &= \frac{1}{2}\Big(\tilde{x}(t)\exp(j\omega_c t) + \tilde{x}^*(t)\exp(-j\omega_c t)\Big) \end{aligned} \tag{2.4}$$

and

$$\begin{aligned} x_s(t) &= \mathrm{Im}\left\{\tilde{x}(t)\exp(j\omega_c t)\right\} \\ &= \frac{1}{2j}\Big(\tilde{x}(t)\exp(j\omega_c t) - \tilde{x}^*(t)\exp(-j\omega_c t)\Big) \end{aligned} \tag{2.5}$$

in an exponential form, where $\tilde{x}(t) = a(t)\exp(j\phi_0(t))$ describes the complex baseband input signal. Therefore the output signal $u_1(t)$ of the static nonlinear system in Fig. 2.3 is

given with (2.2) and (2.4) by [8, 72]

$$\begin{aligned} u_1(t) &= \sum_{l=1}^{L} \frac{b_l}{2^l} \Big( \tilde{x}(t) \exp(j\omega_c t) + \tilde{x}^*(t) \exp(-j\omega_c t) \Big)^l \\ &= \sum_{l=1}^{L} \frac{b_l}{2^l} \sum_{k=0}^{l} \binom{l}{k} \left[\tilde{x}(t)\right]^{l-k} \left[\tilde{x}^*(t)\right]^k \exp(j\omega_c t(l-2k)) \\ &= \sum_{l=1}^{L} u_{1_l}(t), \end{aligned} \tag{2.6}$$

where

$$u_{1_l}(t) = \frac{b_l}{2^l} \sum_{k=0}^{l} \binom{l}{k} \left[\tilde{x}(t)\right]^{l-k} \left[\tilde{x}^*(t)\right]^k \exp(j\omega_c t(l-2k)). \tag{2.7}$$

The output signal $u_2(t)$ of the static nonlinear system in Fig. 2.3 is given with (2.2) and (2.5) by

$$\begin{aligned} u_2(t) &= \sum_{l=1}^{L} \frac{c_l}{(j2)^l} \Big( \tilde{x}(t) \exp(j\omega_c t) - \tilde{x}^*(t) \exp(-j\omega_c t) \Big)^l \\ &= \sum_{l=1}^{L} \frac{c_l}{(j2)^l} \sum_{k=0}^{l} \binom{l}{k} (-1)^k \left[\tilde{x}(t)\right]^{l-k} \left[\tilde{x}^*(t)\right]^k \exp(j\omega_c t(l-2k)) \\ &= \sum_{l=1}^{L} u_{2_l}(t), \end{aligned} \tag{2.8}$$

where

$$u_{2_l}(t) = \frac{c_l}{(j2)^l} \sum_{k=0}^{l} \binom{l}{k} (-1)^k \left[\tilde{x}(t)\right]^{l-k} \left[\tilde{x}^*(t)\right]^k \exp(j\omega_c t(l-2k)). \tag{2.9}$$

Figure 2.5 depicts the different contributions from (2.7) and (2.9) in the frequency-domain for $L = 3$ qualitatively, where $U_{1_l}(\omega) = \mathcal{F}\{u_{1_l}(t)\}$ and $U_{2_l}(\omega) = \mathcal{F}\{u_{2_l}(t)\}$ denotes the Fourier transforms [45, 46, 48] of the corresponding time-domain signals $u_{1_l}(t)$ and $u_{2_l}(t)$ in (2.7) and (2.9).

Because of the bandpass behavior of the input signals $x(t)$ and $x_s(t)$, each even order nonlinearity $l \in \mathbb{N}_e$ in (2.6) and (2.8) generates spectral components around the even multiples of the carrier frequency $2k\,\omega_c$ for $k = 0, 1, \ldots, l/2$ , and each odd order nonlinearity $l \in \mathbb{N}_o$ generates spectral components around the odd multiples of the carrier frequency $(2k+1)\,\omega_c$ for $k = 0, 1, \ldots, (l-1)/2$.

The shapes of the spectra in Fig. 2.5 illustrate the fact that the products of the time-domain signals in (2.6) and (2.8) result in a convolution [45, 46, 48] of the corresponding frequency-domain signals. If $\omega_c \geq B(2L-1)$, where $2B$ is the bandwidth of the bandpass

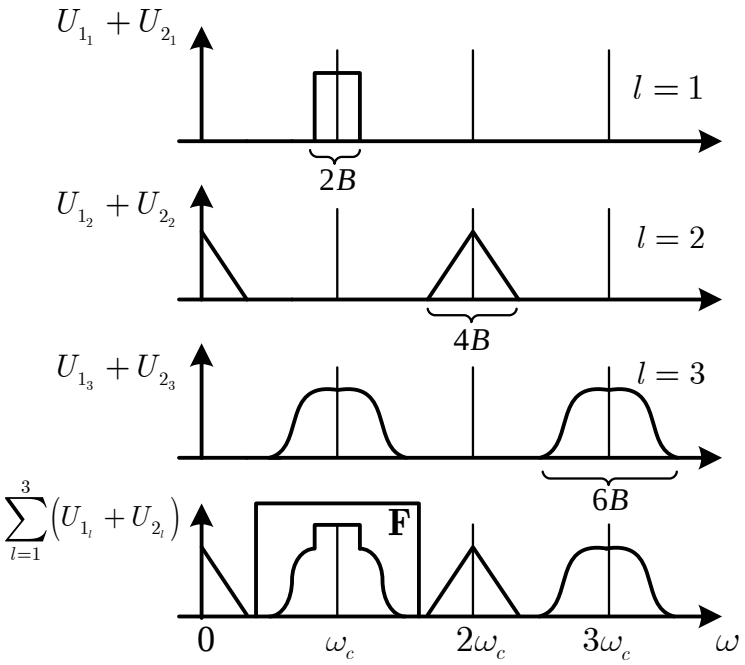


**Figure 2.5:** Output signal spectra of the quasi-memoryless system in Fig. 2.3, with contributions from the different orders of the nonlinearity up to $L = 3$.

signal $x(t)$, the individual spectra caused by the different orders of the passband nonlinearity remain separate (cf. Fig. 2.5). Therefore, the ideal frequency-domain filtering process in Fig. 2.5 is accomplished in the time domain by equating the fundamental carrier phasor and the carrier phasor in (2.6) and (2.8), which is expressed by

$$\exp\left(j\omega_c t(l-2k)\right) = \exp\left(\pm j\omega_c t\right). \tag{2.10}$$

The equation in (2.10) can only be satisfied for $l \in \mathbb{N}_o$ and $k = (l \pm 1)/2$. Therefore, only the odd orders $l = 2k + 1$ of the passband nonlinearity contribute to the spectral components around the fundamental carrier $\pm\omega_c$. The filtered output signal of the first nonlinearity $\mathbf{F}[u_1(t)]$ is given with (2.6) and (2.10) by

$$\begin{aligned}\mathbf{F}[u_1(t)] = \sum_{l=1,\, l\in\mathbb{N}_o}^{L} \frac{b_l}{2^l} \Bigg\{ &\binom{l}{\frac{l+1}{2}} \left[\tilde{x}(t)\right]^{\frac{l-1}{2}} \left[\tilde{x}^*(t)\right]^{\frac{l+1}{2}} \exp\left(-j\omega_c t\right) \\ &+ \binom{l}{\frac{l-1}{2}} \left[\tilde{x}(t)\right]^{\frac{l+1}{2}} \left[\tilde{x}^*(t)\right]^{\frac{l-1}{2}} \exp\left(j\omega_c t\right) \Bigg\}. \end{aligned} \tag{2.11}$$

If we apply the identities $\tilde{x}(t)\,\tilde{x}^*(t) = |\tilde{x}(t)|^2$ and $\binom{l}{\frac{l+1}{2}} = \binom{l}{\frac{l-1}{2}}$ we can rewrite (2.11)

in the following compact form

$$\begin{aligned}\mathbf{F}[u_1(t)]=&\sum_{l=1,\,l\in\mathbb{N}_o}^{L}\frac{b_l}{2^l}\left\{\binom{l}{\frac{l+1}{2}}|\tilde{x}(t)|^{l-1}\,\tilde{x}^*(t)\exp\left(-j\omega_c t\right)\right.\\&\left.+\binom{l}{\frac{l+1}{2}}|\tilde{x}(t)|^{l-1}\,\tilde{x}(t)\exp\left(j\omega_c t\right)\right\}\\=&\mathrm{Re}\left\{\sum_{l=1,\,l\in\mathbb{N}_o}^{L}\frac{b_l}{2^{l-1}}\binom{l}{\frac{l+1}{2}}|\tilde{x}(t)|^{l-1}\,\tilde{x}(t)\exp\left(j\omega_c t\right)\right\}.\end{aligned}\tag{2.12}$$

If we apply the linear filter **F** to the output signal $u_2(t)$ in (2.8) we obtain

$$\begin{aligned}\mathbf{F}[u_2(t)]=&\sum_{l=1,\,l\in\mathbb{N}_o}^{L}\frac{c_l}{(j2)^l}\left\{\binom{l}{\frac{l+1}{2}}(-1)^{\frac{l+1}{2}}|\tilde{x}(t)|^{l-1}\,\tilde{x}^*(t)\exp\left(-j\omega_c t\right)\right.\\&\left.+\binom{l}{\frac{l+1}{2}}(-1)^{\frac{l-1}{2}}|\tilde{x}(t)|^{l-1}\,\tilde{x}(t)\exp\left(j\omega_c t\right)\right\}\\=&\mathrm{Im}\left\{\sum_{l=1,\,l\in\mathbb{N}_o}^{L}\frac{c_l}{2^{l-1}}\binom{l}{\frac{l+1}{2}}|\tilde{x}(t)|^{l-1}\,\tilde{x}(t)\exp\left(j\omega_c t\right)\right\}.\end{aligned}\tag{2.13}$$

To calculate the output signal of the nonlinear passband system $y(t)=\mathbf{F}[u_1(t)]+\mathbf{F}[u_2(t)]$, we express the signal in (2.13) in terms of its real part with $\mathrm{Im}\left\{\tilde{x}(t)\exp\left(j\omega_c t\right)\right\}=\mathrm{Re}\left\{-j\tilde{x}(t)\exp\left(j\omega_c t\right)\right\}$ by

$$\mathbf{F}[u_2(t)]=\mathrm{Re}\left\{\sum_{l=1,\,l\in\mathbb{N}_o}^{L}-j\frac{c_l}{2^{l-1}}\binom{l}{\frac{l+1}{2}}|\tilde{x}(t)|^{l-1}\,\tilde{x}(t)\exp\left(j\omega_c t\right)\right\}.\tag{2.14}$$

With (2.12) and (2.14), the real passband output signal is obtained with the variable substitution $l=2k+1$ and the complex parameters $d_{2k+1}=b_{2k+1}-jc_{2k+1}$ by

$$\begin{aligned}y(t)=&\mathbf{H}[x(t)]\\=&\mathrm{Re}\left\{\sum_{k=0}^{\lceil L/2\rceil-1}\frac{d_{2k+1}}{2^{2k}}\binom{2k+1}{k+1}|\tilde{x}(t)|^{2k}\,\tilde{x}(t)\exp\left(j\omega_c t\right)\right\}.\end{aligned}\tag{2.15}$$

Except for the carrier phasor, the expression within the braces of (2.15) represents the baseband output signal $\tilde{y}(t)$ of the real nonlinear passband system in Fig. 2.3 and Fig. 2.4, which is expressed by [8, 51]

$$\begin{aligned}\tilde{y}(t)=&\tilde{\mathbf{H}}[\tilde{x}(t)]\\=&\sum_{k=0}^{\lceil L/2\rceil-1}\frac{d_{2k+1}}{2^{2k}}\binom{2k+1}{k+1}|\tilde{x}(t)|^{2k}\,\tilde{x}(t)\\=&\sum_{k=0}^{\lceil L/2\rceil-1}\hat{d}_{2k+1}\,|\tilde{x}(t)|^{2k}\,\tilde{x}(t),\end{aligned}\tag{2.16}$$

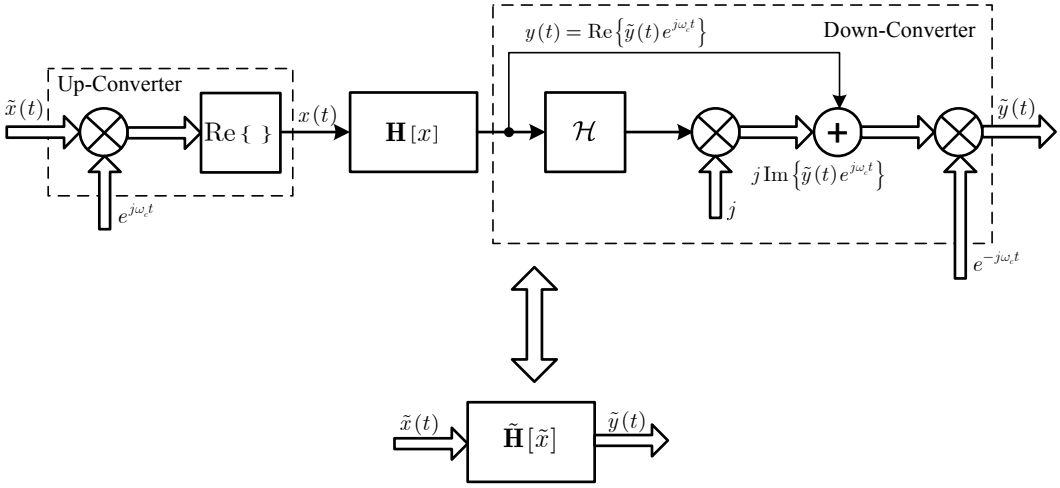


**Figure 2.6:** Equivalence between the nonlinear passband system which is composed of the nonlinear operator **H** and a frequency up- and down-conversion unit and the complex baseband system $\tilde{\mathbf{H}}$.

where $\hat{d}_{2k+1} = \frac{d_{2k+1}}{2^{2k}} \binom{2k+1}{k+1}$. The operator $\tilde{\mathbf{H}}$ in (2.16) describes the equivalent nonlinear complex baseband operator of the real nonlinear passband operator **H**. The complex baseband system is memoryless because only a static nonlinear function appears in (2.16), although the passband system in Fig. 2.3 itself contains memory which is implicitly introduced by the Hilbert transformer in Fig. 2.3. Therefore, we denote this model as quasi-memoryless as long as the parameters $d_{2k+1}$ in (2.16) are complex valued. If these parameters are real valued, we are not able to change the phase of the baseband output signal $\tilde{y}(t)$. In this case we denote the baseband model in (2.16) as memoryless. Fig. 2.6 depicts the block diagrams of a nonlinear passband system **H** embedded between a frequency up-conversion unit, a circuit to generate the analytic signal $\tilde{y}(t)\exp(j\omega_c t) = \mathrm{Re}\{\tilde{y}(t)\exp(j\omega_c t)\} + j\mathrm{Im}\{\tilde{y}(t)\exp(j\omega_c t)\}$ and a frequency down-conversion unit and the equivalent complex baseband system $\tilde{\mathbf{H}}$ [39] (cf. Appendix A). An alternative derivation with additional insights is given in the Appendix C.

### 2.2.1 AM/AM- and AM/PM-Conversion

To see that the quasi-memoryless model in (2.16) can be fully represented by the AM/AM-conversion and AM/PM-conversion (cf. Fig. 2.2), we expand (2.16) with $\tilde{x}(t) =$

$a(t)\exp(j\phi_0(t))$, which results in

$$\begin{aligned}\tilde{y}(t)=&\tilde{\mathbf{H}}[\tilde{x}(t)]\\ =&\exp(j\phi_0(t))\sum_{k=0}^{\lceil L/2\rceil-1}\hat{d}_{2k+1}[a(t)]^{2k+1}\\ =&|v(a(t))|\,\exp\left(j\left(\phi_0(t)+\arg\{v(a(t))\}\right)\right),\end{aligned}\tag{2.17}$$

where the complex function

$$v(a(t))=\sum_{k=0}^{\lceil L/2\rceil-1}\hat{d}_{2k+1}[a(t)]^{2k+1}\tag{2.18}$$

depends purely on the magnitude $a$ of the complex input signal $\tilde{x}(t)$. The function $|v(a)|$ in (2.17) describes the AM/AM-conversion and the function $\arg\{v(a)\}$ in (2.17) describes the AM/PM-conversion. These nonlinear functions are calculated by

$$|v(a)|=\left[\sum_{k=0}^{\lceil L/2\rceil-1}\sum_{l=0}^{\lceil L/2\rceil-1}\hat{d}_{2k+1}\hat{d}^{*}_{2l+1}a^{2(k+l+1)}\right]^{\frac{1}{2}},\tag{2.19}$$

and

$$\arg\{v(a)\}=\arctan\left\{\frac{\sum_{k=0}^{\lceil L/2\rceil-1}\mathrm{Im}\left\{\hat{d}_{2k+1}\right\}a^{2k+1}}{\sum_{k=0}^{\lceil L/2\rceil-1}\mathrm{Re}\left\{\hat{d}_{2k+1}\right\}a^{2k+1}}\right\}.\tag{2.20}$$

respectively. Figure 2.7 depicts the quasi-memoryless complex baseband model $\tilde{\mathbf{H}}$ which is equivalent, ($y(t)=\mathrm{Re}\{\tilde{y}(t)e^{j\omega_c t}\}$) to the real nonlinear passband system in Fig. 2.3.

### 2.2.2 Frequency-Domain Representation

To express the output signal of the quasi-memoryless system $\tilde{y}(t)$ in (2.16) in the frequency domain, we apply the Fourier transform denoted by $\mathcal{F}$ to (2.16), which yields

$$\begin{aligned}\tilde{Y}(\omega)=&\mathcal{F}\{\tilde{y}(t)\}\\ =&\sum_{k=0}^{\lceil L/2\rceil-1}\frac{\hat{d}_{2k+1}}{(2\pi)^{2k}}\underbrace{\tilde{X}(\omega)\star\ldots\star\tilde{X}(\omega)}_{(k+1)\times}\star\underbrace{\tilde{X}^{*}(-\omega)\star\ldots\star\tilde{X}^{*}(-\omega)}_{k\times},\end{aligned}\tag{2.21}$$

where $\tilde{X}(\omega)=\mathcal{F}\{\tilde{x}(t)\}$, and $\star$ denotes the convolution operator.

If we consider stationary stochastic signals, we cannot calculate the Fourier transform because of their infinite energy. In this case, the spectral characteristics of the output signal $\tilde{y}(t)$ is obtained by computing the Fourier transform of the auto-covariance function of $\tilde{y}(t)$ in terms of its power spectrum density [47, 49, 44]. In [74], a closed form expression for the quasi-memoryless system in (2.16) is given for a stationary complex Gaussian distributed input signal.

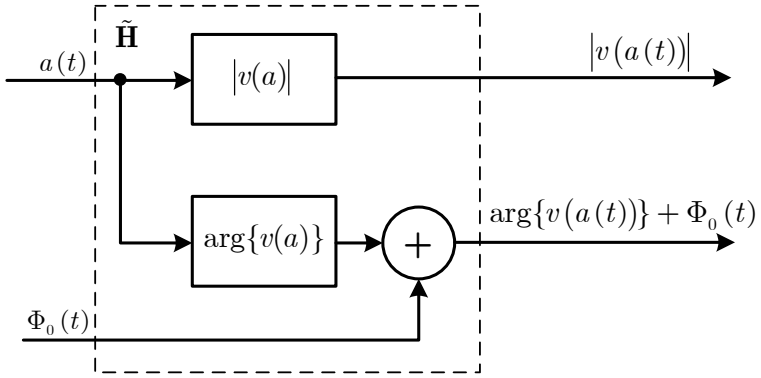


**Figure 2.7:** Baseband model of a quasi-memoryless system, which is composed of two static nonlinear functions described by the AM/AM-conversion $|v(a)|$ and AM/PM-conversion $\arg\{v(a)\}$. Although the baseband model is memoryless, the model is called quasi-memoryless because the corresponding passband model in Fig. 2.3 contains memory (Hilbert transformer).

### 2.2.3 Two-Tone Response of a Quasi-Memoryless System

If we apply a two-tone signal $x(t) = a/2\cos[(\omega_c + \omega_m)t] + a/2\cos[(\omega_c - \omega_m)t] = \mathrm{Re}\{a\cos(\omega_m t)\exp(j\omega_c t)\}$ to a nonlinear passband system, where $\omega_m$ denotes the modulation frequency, we obtain a discrete output spectrum at the odd multiples of the modulation frequency $\pm n\omega_m, n \in \mathbb{N}_o$ centered around $\omega_c$. Such a power spectrum is shown in Fig. 2.8 for a modulation frequency of 10 MHz at the output of a simulated RF PA. We notice that the spectral components around the center frequency are not symmetric regarding their output power. For the particular simulation example of a 2.2-GHz, 90-W RF PA we obtain a power difference of 7 dB if we consider the 3rd-order intermodulation frequency at $\omega_c \pm 3\omega_m$. If we reduce the modulation frequency $\omega_m/(2\pi)$ from 10 MHz to 1 MHz, the RF PA output power spectrum is almost symmetric around the center frequency $\omega_c$ (cf. Fig. 2.9). This bandwidth dependent effect is caused by the electrical and thermo-electrical memory effects of the RF PA, which are considered in detail in [70, 69, 11]. These memory effects make the complex baseband modeling of the nonlinear passband system difficult if we consider wideband applications with modern modulation formats such as OFDM or WCDMA [27].

To further analyze this effect, we calculate the output signal of the quasi-memoryless system in Fig.2.3 for the mentioned two-tone signal which is described in the complex

baseband domain by $\tilde{x}(t) = a\cos(\omega_m t)$. The output signal is given with (2.16) by

$$\begin{aligned}\tilde{y}(t) &= \sum_{k=0}^{\lceil L/2\rceil-1} \hat{d}_{2k+1}\left(\frac{a}{2}\right)^{2k+1} \sum_{l=0}^{2k+1} \binom{2k+1}{l} \exp\left(j\left(2l-2k-1\right)\omega_m t\right) \\ &= \sum_{k=0}^{\lceil L/2\rceil-1} \hat{d}_{2k+1}\left(\frac{a}{2}\right)^{2k+1} \sum_{l=0}^{k} \left\{ \binom{2k+1}{l} \exp\left(j\left(2l-2k-1\right)\omega_m t\right) \right. \\ &\qquad \left. + \binom{2k+1}{-l+2k+1} \exp\left(-j\left(2l-2k-1\right)\omega_m t\right) \right\}. \end{aligned} \tag{2.22}$$

Because of the binomial coefficient in (2.22) $\binom{2k+1}{l} = \binom{2k+1}{-l+2k+1}$, the magnitude and the phase of the output signal spectrum of the quasi-memoryless baseband model must be symmetric because every pair of the phasors $\exp(\pm jn\omega_m t)$, for $n = \pm 1, \pm 3, \ldots, \pm(2k+1)$ is weighted with the same complex constants. The output signal $\tilde{y}(t)$ in (2.22) can be simplified with real trigonometric functions to

$$\tilde{y}(t) = \sum_{k=0}^{\lceil L/2\rceil-1} 2\hat{d}_{2k+1}\left(\frac{a}{2}\right)^{2k+1} \sum_{l=0}^{k} \binom{2k+1}{l} \cos\left[(2k-2l+1)\omega_m t\right]. \tag{2.23}$$

From the derivation above, we notice that we cannot model an asymmetric power spectrum as depicted in Fig. 2.8 with the memoryless or the quasi-memoryless model in Fig. 2.3.

## 2.3 Complex Baseband Modeling with Volterra Series

To overcome the problem of generating an asymmetric power spectrum at the output of a quasi-memoryless model (if the magnitude of the input signal spectrum is symmetric) as shown in Fig. 2.8, we have to introduce some memory into the complex baseband model. Volterra series are a powerful mathematical tool to describe weak nonlinear systems with memory effects. For a thorough introduction to Volterra series and their classical input-output relation the reader is referred to [56, 52, 40].

### 2.3.1 Time-Domain Representation

We replace the nonlinear passband operator **G** of Fig.2.3, which is composed of two polynomial series and a Hilbert transformer, by a more general operator **G** whose functional description is given by the Volterra series

$$\begin{aligned} u(t) &= \mathbf{G}[\,x(t)] = \sum_{l=1}^{L} u_l(t) \\ u_l(t) &= \int_0^\infty \cdots \int_0^\infty h_l(\tau_1,\ldots,\tau_n) \prod_{i=1}^{l} x(t-\tau_i)\, d\tau_i, \end{aligned} \tag{2.24}$$

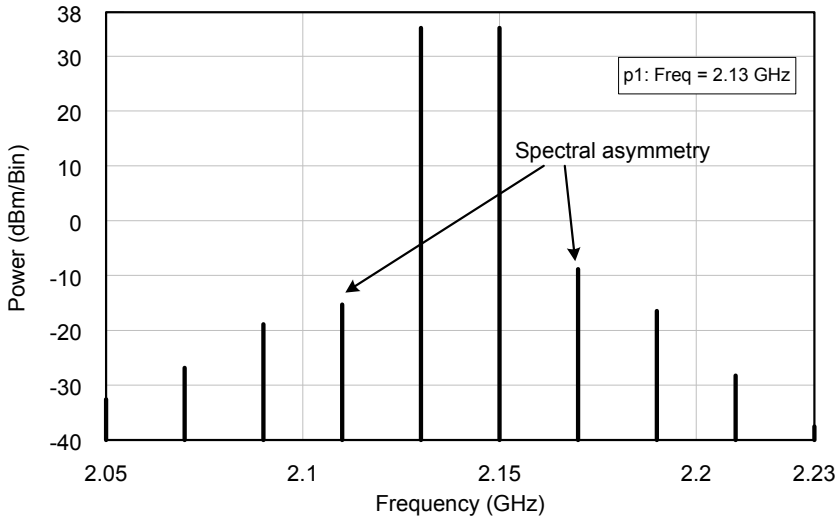


**Figure 2.8:** RF power amplifier output signal power spectrum for a two-tone excitation with $\omega_c = 2\pi \times 2.14$ GHz and $\Delta\omega = \omega_2 - \omega_1 = 2\omega_m = 2\pi \times 20$ MHz. The spectrum around the carrier frequency is highly asymmetric which is caused by the inherent memory of the RF power amplifier.

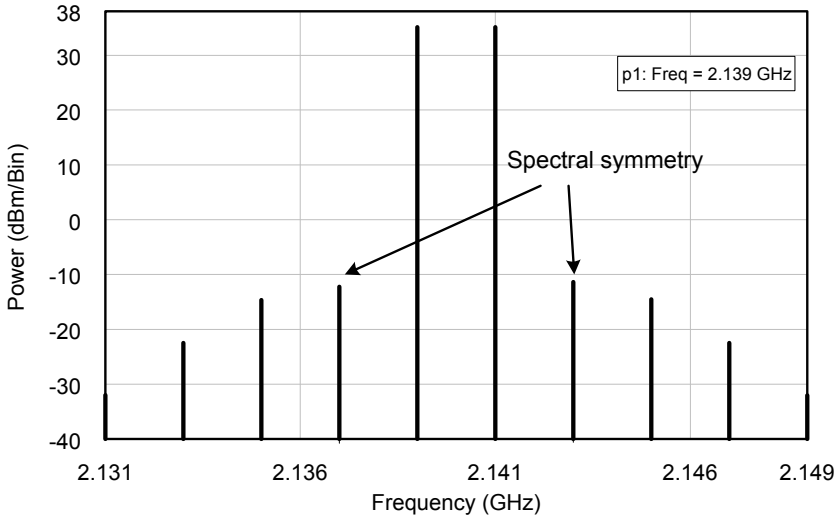


**Figure 2.9:** RF power amplifier output signal power spectrum for a two-tone excitation with $\omega_c = 2\pi \times 2.14$ GHz and $\Delta\omega = \omega_2 - \omega_1 = 2\omega_m = 2\pi \times 2$ MHz. The spectrum around the carrier frequency is almost symmetric because the inherent memory of the RF power amplifier does not affect the signal due to the small frequency difference of the two excitation components.

where $h_l$ is the $l$th-order time-domain Volterra kernel and $L$ is the highest order of the real passband nonlinearity. The output signal is filtered by a linear 1st-zonal filter described by the linear operator $\mathbf{F}$ to suppress the unwanted spectral components located around the multiples of the carrier frequency $\pm\omega_c$ [8, 10]. Therefore the output signal of the linear passband filter in Fig. 2.4

$$\begin{aligned} y(t) &= (\,\mathbf{F} \circ \mathbf{G}\,)\,[\,x(t)] \\ &= \mathbf{H}\,[\,x(t)] = \sum_{l=1}^{L} \mathbf{F}\,[\,u_l(t)] \end{aligned} \tag{2.25}$$

incorporates only the spectral components of interest which are located around the carrier frequency $\pm\omega_c$. To express the $l$th-order term of the output signal of the passband Volterra system $u_l(t)$ in (2.24), the product in (2.24) is expressed with the time delayed version of the passband input signals in (2.4) in a mathematical closed form by

$$\begin{aligned} \prod_{i=1}^{l} x(t-\tau_i) = \frac{1}{2^l} \sum_{k_1=1}^{2} \cdots \sum_{k_l=1}^{2} \left( \prod_{i=1}^{l} x_{k_i}(t-\tau_i) \right) \exp\left( j\omega_c \sum_{i=1}^{l} (-1)^{k_i}\,\tau_i \right) \\ \times \exp\left( j\omega_c\, t \sum_{i=1}^{l} (-1)^{k_i+1} \right), \end{aligned} \tag{2.26}$$

where the signals $x_1(t) = \tilde{x}(t)$ and $x_2(t) = \tilde{x}^*(t)$ in (2.26) are introduced for a convenient representation. The $l$th-order output signal of the passband Volterra system in (2.24) is expressed with (2.26) by

$$\begin{aligned} u_l(t) = \frac{1}{2^l} \sum_{k_1=1}^{2} \cdots \sum_{k_l=1}^{2} \int_0^{\infty} \cdots \int_0^{\infty} h_l(\tau_1,\ldots,\tau_l) \left( \prod_{i=1}^{l} x_{k_i}(t-\tau_i) \right) \\ \times \exp\left( j\omega_c \sum_{i=1}^{l} (-1)^{k_i}\,\tau_i \right) d\tau_1 \cdots d\tau_l \\ \times \exp\left( j\omega_c\, t \sum_{i=1}^{l} (-1)^{k_i+1} \right), \end{aligned} \tag{2.27}$$

where the product in (2.27) is composed of the permutations of the baseband signal $x_1(t) = \tilde{x}(t)$ and its conjugate $x_2(t) = \tilde{x}^*(t)$, respectively.

The overall output signal $y(t)$ in Fig. 2.4 is calculated with (2.25) by applying the linear operator $\mathbf{F}$ to the $l$th-order output signals of the passband Volterra system in (2.27) for $l = 1, \ldots, L$.

Each of the $2^l$ $l$-fold convolution integrals in (2.27) which contributes to the $l$th-order output signal $u_l(t)$ is multiplied by a phasor which corresponds to integer multiples of the carrier frequency. Therefore, the spectra of the convolution integrals are shifted in the frequency-domain to the corresponding multiples of the carrier frequency $\omega_c \sum_{i=1}^{l} (-1)^{k_i+1}$. If the order of the nonlinearity $l \in \mathbb{N}_o$, the spectra can only be located

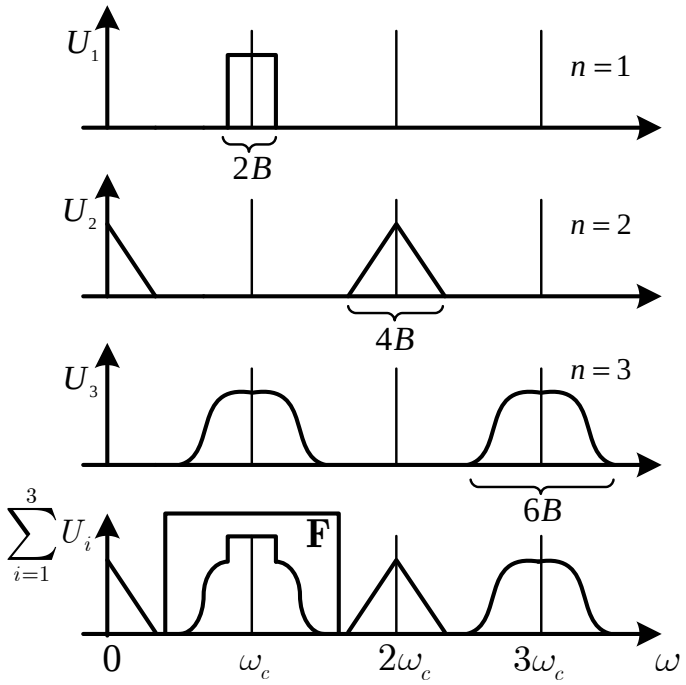


**Figure 2.10:** Frequency-domain output signal spectra of a Volterra series model, with contributions from the different orders of the nonlinearity up to $L = 3$.

around the odd multiples of the carrier frequency up to $l\omega_c$. If the order of the nonlinearity $l \in \mathbb{N}_e$, the spectra can only be located around the even multiples of the carrier up to $l\omega_c$.

The bandwidths of the individual contributions to (2.27) are $2\,l$ times the bandwidth $B$ of the complex baseband signal $\tilde{x}(t)$. If the carrier frequency satisfies $\omega_c \geq B(2L-1)$ the spectra of the individual contributions from (2.27) remain separate (c.f. Fig. 2.10). Therefore the output signal passed by the linear 1st-zonal filter **F** in Fig. 2.4 can be calculated from (2.27) if the carrier phasor in (2.27) is constraint to be

$$\exp\left(j\omega_c\, t \sum_{i=1}^{l} (-1)^{k_i+1}\right) = \exp\left(\pm j\omega_c\, t\right). \tag{2.28}$$

This equality can only be satisfied for the odd orders of the nonlinearity $l \in \mathbb{N}_o$. Therefore, solely the odd orders of the nonlinearity contribute to the filtered output signal centered around the carrier frequency $\pm\omega_c$ (c.f. Fig. 2.10). For the even orders of the nonlinearity $l \in \mathbb{N}_e$, the filtered output signal $F[\,u_l(t)] = 0$. From the $2^l$ contributions in (2.27) only $2\binom{l}{(l-1)/2}$ terms fulfill (2.28).

Without any loss of generality, the passband Volterra kernels $h_l$ in (2.27) are assumed to be symmetric [56, 40, 52] and, therefore, the permutations of the product in (2.27) are identical for $\binom{l}{(l-1)/2}$ terms. The same is obtained for the second group of terms which

are the conjugate of the first one. Therefore the filtered output signal is given by

$$\begin{aligned} F\left[u_l(t)\right] &= \frac{1}{2^l}\binom{l}{(l-1)/2}\left(f_l(t)+f_l^*(t)\right) \\ &= 2\,\mathrm{Re}\left\{\frac{1}{2^l}\binom{l}{(l-1)/2} f_l(t)\right\}, \end{aligned} \tag{2.29}$$

where the function $f_l$ in (2.29) is expressed with $l \in \mathbb{N}_o$ by

$$\begin{aligned} f_l(t) = &\int_0^\infty \cdots \int_0^\infty h_l(\tau_1,\ldots,\tau_l)\exp\left(-j\omega_c\left(\sum_{i=1}^{(l+1)/2}\tau_i - \sum_{i=(l+3)/2}^{l}\tau_i\right)\right) \\ &\times \prod_{i=1}^{(l+1)/2} x_1(t-\tau_i) \prod_{i=(l+3)/2}^{l} x_2(t-\tau_i)\, d\tau_1\cdots d\tau_l \exp\left(j\omega_c\, t\right). \end{aligned} \tag{2.30}$$

The final output signal passed by the linear 1st-zonal filter **F** in Fig. 2.4 is given with (2.25) by

$$\begin{aligned} y(t) = &\sum_{k=0}^{\lceil L/2\rceil-1} F[u_{2k+1}(t)] \\ &= \mathrm{Re}\left\{\sum_{k=0}^{\lceil L/2\rceil-1}\int_0^\infty\cdots\int_0^\infty \tilde{h}_{2k+1}(\tau_1,\ldots,\tau_{2k+1})\prod_{i=1}^{k+1}\tilde{x}(t-\tau_i)\prod_{i=k+2}^{2k+1}\tilde{x}^*(t-\tau_i)\right. \\ &\left.\times\, d\tau_1\cdots d\tau_{2k+1}\exp\left(j\omega_c\, t\right)\right\}, \end{aligned} \tag{2.31}$$

where the variable substitution $k=(l-1)/2$ is introduced for a more convenient representation of (2.31). The baseband-equivalent Volterra kernels in (2.31) are defined with (2.30) by

$$\begin{aligned} \tilde{h}_{2k+1}(t_1,\ldots,t_{2k+1}) = &\frac{1}{2^{2k}}\binom{2k+1}{k} h_{2k+1}(t_1,\ldots,t_{2k+1}) \\ &\times\exp\left(-j\omega_c\left(\sum_{i=1}^{k+1}t_i - \sum_{i=k+2}^{2k+1}t_i\right)\right). \end{aligned} \tag{2.32}$$

The term baseband-equivalent means that the frequency-domain representation of the kernels in (2.32) contains some frequency components around the zero frequency (baseband) and $-2\omega_c$. The latter one do not contribute to the output signal $y(t)$ in (2.31), because the frequency-domain representations of the baseband signals $\tilde{x}(t)$ and $\tilde{x}^*(t)$ are zero around $-2\omega_c$.

Except for the carrier phasor $\exp(j\omega_c\, t)$, the signal within the braces of (2.31) represents the nonlinear passband output signal $\tilde{y}(t)$ in the baseband domain because $y(t) =$

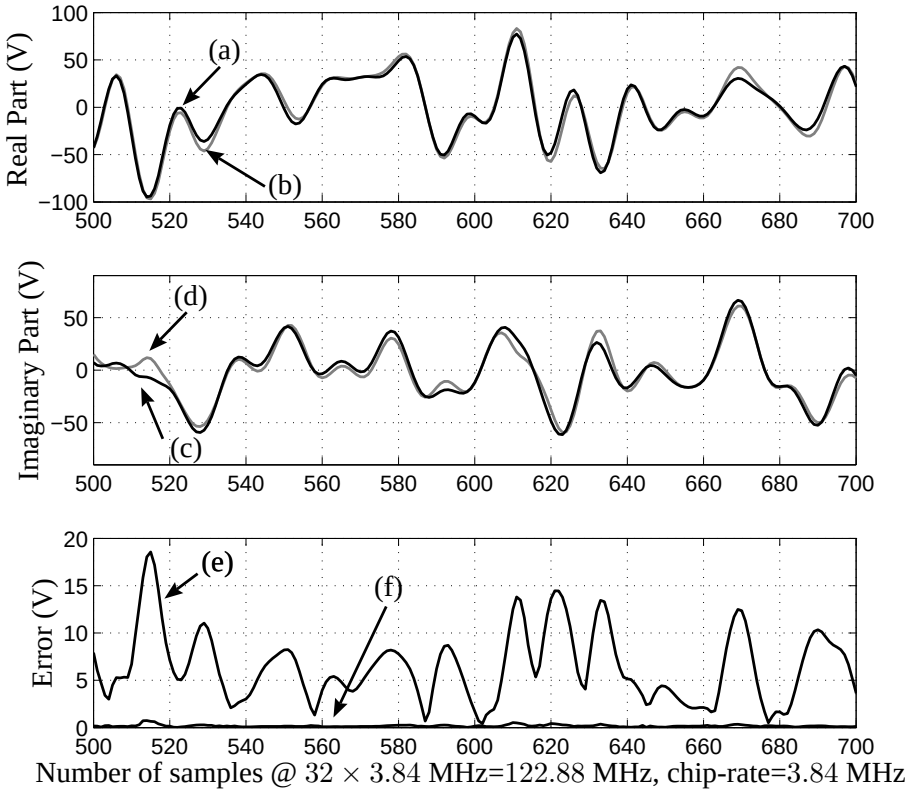


**Figure 2.11:** Complex baseband time-domain output signals of a 2.2-GHz, 90-W, Class-AB, RF PA, a quasi-memoryless PA model and a Volterra PA model. (a) and (c) real and imaginary parts of the output signals of the PA and the Volterra model, (b) and (d) real and imaginary parts of the output signals of the quasi-memoryless PA model, (e) error signal for the quasi-memoryless PA model, (f) error signal for the Volterra PA model.

Re $\{\tilde{y}(t)\exp(j\omega_c t)\}$. Therefore the complex baseband Volterra series [7]

$$\begin{aligned}\tilde{y}(t) &= \tilde{\mathbf{H}}[\tilde{x}(t)] \\ &= \sum_{k=0}^{\lceil L/2\rceil-1} \int_0^\infty \cdots \int_0^\infty \tilde{h}_{2k+1}(\tau_1,\ldots,\tau_{2k+1}) \\ &\quad \times \prod_{i=1}^{k+1} \tilde{x}(t-\tau_i) \prod_{i=k+2}^{2k+1} \tilde{x}^*(t-\tau_i)\, d\tau_1 \cdots d\tau_{2k+1}. \end{aligned} \tag{2.33}$$

relates the baseband input and output signals without considering the frequency up- and frequency down-conversion units in Fig. 2.6.

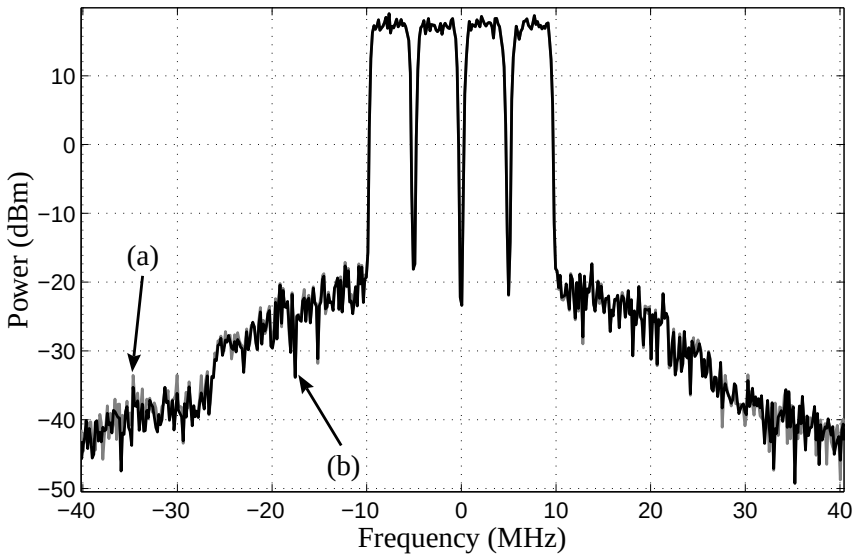


**Figure 2.12:** Power spectrum of a $2.2$-GHz, $90$-W, Class-AB, RF PA and a $9$th-order Volterra PA model with $43$ parameters for a four-carrier WCDMA input signal with $B = 20$ MHz. (a) RF PA, (b) Volterra PA model.

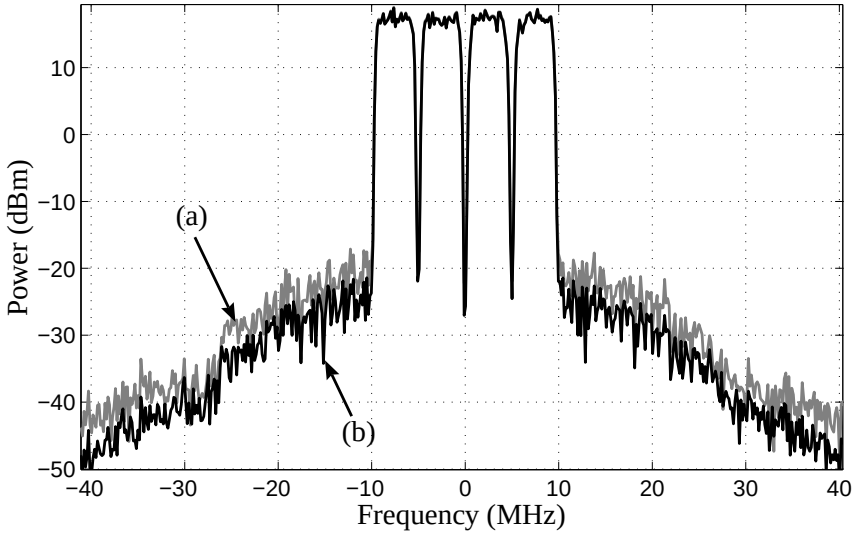


**Figure 2.13:** Power spectrum of a $2.2$-GHz, $90$-W, Class-AB, RF PA and a quasi-memoryless PA model for a four-carrier WCDMA input signal with $B = 20$ MHz. (a) RF PA, (b) quasi-memoryless PA model.

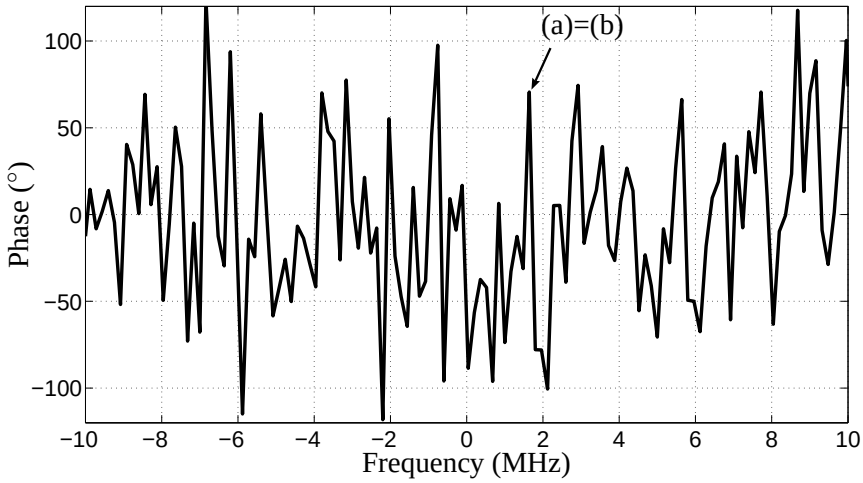


**Figure 2.14:** Phase response of a $2.2$-GHz, $90$-W, Class-AB, RF PA and a $9$th-order Volterra PA model with $43$ parameters within the input signal bandwidth of $\pm 10$ MHz for a four-carrier WCDMA input signal with $B = 20$ MHz. (a) RF PA, (b) Volterra PA model (no visible difference between the two graphs).

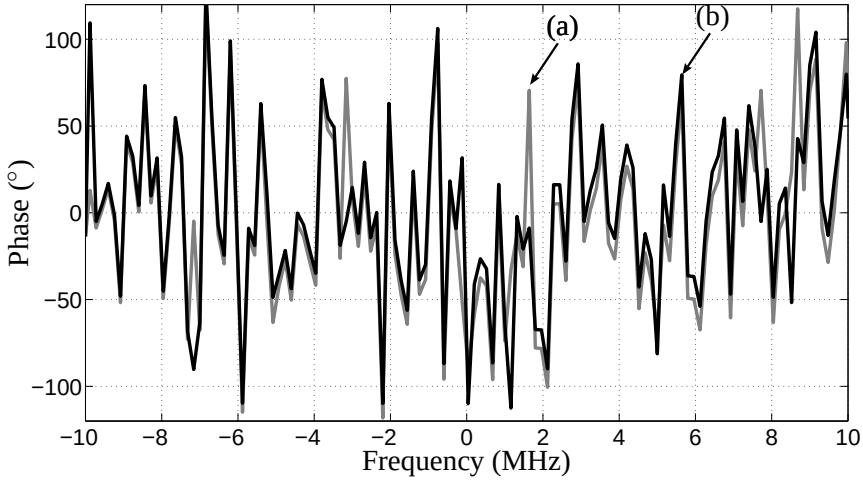


**Figure 2.15:** Phase response of a $2.2$-GHz, $90$-W, Class-AB, RF PA and a quasi-memoryless PA model within the input signal bandwidth of $\pm 10$ MHz for a four-carrier WCDMA input signal with $B = 20$ MHz. (a) RF PA, (b) quasi-memoryless PA model.

Figure 2.11 depicts the real and the imaginary parts of the complex baseband time-domain output signals from a $2.2$-GHz, $90$-W, Class-AB, RF PA (The RF PA output signal is down-converted as shown in Fig. 2.6), a quasi-memoryless PA model and a Volterra PA model. The RF PA and the two PA models are excited with a four carrier WCDMA signal with a bandwidth of approximately $20$ MHz. We see that the output signals of the quasi-memoryless PA model (curve (b) and (d)), which is implemented as in Fig. 2.7 with the AM/AM and AM/PM-conversion depicted in Fig. 2.2, are quite different from the RF PA baseband output signals. This is because the quasi-memoryless PA model is not able to model the long-term memory effects of the RF PA. If we reduce the bandwidth of the input signal to zero, the output signals of the RF PA and the quasi-memoryless PA model are exactly the same, because the AM/AM and AM/PM-conversion in Fig. 2.2 is measured with a single RF tone (bandwidth is zero). The resulting magnitude of the complex error (difference between the RF PA output signal and quasi-memoryless output signal) is shown in the lower plot of Fig. 2.11 in curve (e). The mean value is $6.2$ V. This error can be considerably reduced if we model the RF PA with a complex baseband Volterra model because this model is able to consider the long-term memory effects. In the two upper plots of Fig. 2.11 (curve (a) and curve (b)), we do not see any difference between the RF PA output signals and the output signals of the Volterra PA model. For this reason, we show the magnitude of the complex error in the lower plot of Fig. 2.11 in curve (f), which is $0.15$ V. Therefore we can improve the modeling error by approximately $33$ dB, if we employ a $9$th-order Volterra PA model with $43$ parameters instead of the quasi-memoryless PA model.

The power spectrum of the output signals of the RF PA and the $9$th-order Volterra PA model for a four-carrier WCDMA input signal with $B = 20\ MHz$ are depicted in Fig. 2.12. As expected from the error signal (curve (f)) in the lower plot of Fig. 2.11, the frequency-domain output signals are almost identical. On the other hand, if we compare the frequency-domain output signals of the RF PA and the quasi-memoryless PA model, the two spectra are quite different as expected from the time-domain error in the lower plot (curve (e)) of Fig. 2.11. The phase responses of the RF PA, the Volterra model and the quasi-memoryless model are depicted in Fig. 2.14 and Fig. 2.15 within the input signal bandwidth of $\pm 10$ MHz.

### 2.3.2 Frequency-Domain Representation

If we consider the frequency-domain representation of the complex baseband Volterra model in (2.33), we transform the one-dimensional nonlinear system (2.33) to a multi-dimensional linear system [56, 40] and apply a multi-dimensional Fourier transform. For this reason we span the one-dimensional time-domain signals

$$\tilde{y}_{2k+1}(t) = \int_0^\infty \cdots \int_0^\infty \tilde{h}_{2k+1}(\tau_1, \ldots, \tau_{2k+1}) \times \prod_{i=1}^{k+1} \tilde{x}(t-\tau_i) \prod_{i=k+2}^{2k+1} \tilde{x}^*(t-\tau_i)\, d\tau_1 \cdots d\tau_{2k+1}. \tag{2.34}$$

in (2.33) in $2k+1$ time-domain variables $\tilde{y}_{2k+1}(t) \rightarrow \tilde{y}_{(2k+1)}(t_1, \ldots, t_{2k+1})$, which yields

$$\tilde{y}_{(2k+1)}(t_1, \ldots, t_{2k+1}) = \int_0^\infty \cdots \int_0^\infty \tilde{h}_{2k+1}(\tau_1, \ldots, \tau_{2k+1}) \times \prod_{i=1}^{k+1} \tilde{x}(t_i - \tau_i) \prod_{i=k+2}^{2k+1} \tilde{x}^*(t_i - \tau_i)\, d\tau_1 \cdots d\tau_{2k+1}. \quad (2.35)$$

If we apply a $(2k+1)$-dimensional Fourier transform to (2.35) we obtain the $(2k+1)$-dimensional frequency-domain output signal as

$$\begin{aligned} \tilde{Y}_{(2k+1)}(\omega_1, \ldots, \omega_{2k+1}) &= \int_0^\infty \cdots \int_0^\infty \tilde{y}_{(2k+1)}(t_1, \ldots, t_{2k+1}) \\ &\quad \times \exp\left(-j \sum_{i=1}^{2k+1} \omega_i t_i\right) dt_1 \cdots dt_{2k+1} \\ &= \tilde{H}_{2k+1}(\omega_1, \ldots, \omega_{2k+1}) \prod_{i=1}^{k+1} \tilde{X}(\omega_i) \prod_{i=k+2}^{2k+1} \tilde{X}^*(-\omega_i), \end{aligned} \quad (2.36)$$

where $\tilde{X}(\omega) = \mathcal{F}\{\tilde{x}(t)\}$ denotes the frequency-domain baseband input signal and $\tilde{H}_{2k+1}(\omega_1, \ldots, \omega_{2k+1}) = \mathcal{F}\{\tilde{h}_{2k+1}(t_1 \ldots, t_{2k+1})\}$ denotes the $(2k+1)$-dimensional frequency-domain Volterra kernel. The multi-dimensional time-domain signals in (2.35) can also be expressed through the corresponding multi-dimensional frequency-domain signals in (2.36) by [56]

$$\begin{aligned} \tilde{y}_{(2k+1)}(t_1, \ldots, t_{2k+1}) &= \frac{1}{(2\pi)^{2k+1}} \int_{-\infty}^\infty \cdots \int_{-\infty}^\infty \tilde{Y}_{(2k+1)}(\omega_1, \ldots, \omega_{2k+1}) \\ &\quad \times \exp\left(j \sum_{i=1}^{2k+1} \omega_i t_i\right) d\omega_1 \cdots d\omega_{2k+1}. \end{aligned} \quad (2.37)$$

If we undo the process of spanning the one-dimensional time-domain signals into $(2k+1)$ time-domain variables by $\tilde{y}_{(2k+1)}(t_1, \ldots, t_{2k+1}) \rightarrow \tilde{y}_{2k+1}(t)$, (2.37) can be rewritten as

$$\begin{aligned} \tilde{y}_{2k+1}(t) &= \frac{1}{(2\pi)^{2k+1}} \int_{-\infty}^\infty \cdots \int_{-\infty}^\infty \tilde{Y}_{(2k+1)}(\omega_1, \ldots, \omega_{2k+1}) \\ &\quad \times \exp\left(j\left(\omega_1 + \cdots + \omega_{2k+1}\right) t\right) d\omega_1 \cdots d\omega_{2k+1}. \end{aligned} \quad (2.38)$$

If we make a change of the variables $\omega_1 + \cdots + \omega_{2k+1}$ in (2.38) by letting $\omega = \omega_1 + \cdots + \omega_{2k+1}$ we can rewrite the time-domain output signal in (2.38) by [56]

$$\begin{aligned} \tilde{y}_{2k+1}(t) = \frac{1}{2\pi} \int_{-\infty}^\infty \left[\frac{1}{(2\pi)^{2k}} \int_{-\infty}^\infty \cdots \int_{-\infty}^\infty \tilde{Y}_{(2k+1)}(\omega - v_1, v_1 - v_2, \ldots, v_{2k})\, dv_1 \cdots dv_{2k}\right] \\ \times \exp\left(j\omega t\right) d\omega. \end{aligned} \quad (2.39)$$

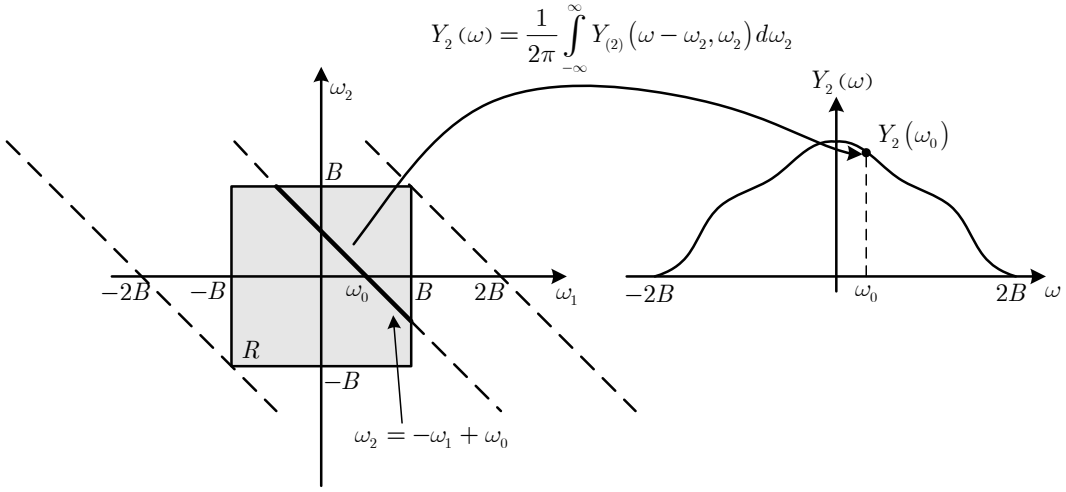


**Figure 2.16:** Frequency-domain convolution for a 2nd-order Volterra system. The output signal spectrum for a 2nd-order Volterra system is given by the integral expression $Y_2(\omega) = \int_{-\infty}^{\infty} Y_{(2)}(\omega - \omega_2, \omega_2) d\omega_2$, which evaluates the two-dimensional output signal $Y_{(2)}(\omega_1, \omega_2)$ along the straight lines $\omega_2 = -\omega_1 + \omega_0$ within the area $R$. If $|\omega| > 2B$, the output signal spectrum $Y_2(\omega)$ becomes zero, because the integration path (dotted lines) does not cross the area $R$ anymore. Therefore, the output signal bandwidth becomes twice the input signal bandwidth.

The $2k$-fold convolution integral within the braces of (2.39) represents the frequency-domain signal for $k > 0$ by

$$\tilde{Y}_{2k+1}(\omega) = \frac{1}{(2\pi)^{2k}} \int_{-\infty}^{\infty} \cdots \int_{-\infty}^{\infty} \tilde{Y}_{(2k+1)}(\omega - v_1, v_1 - v_2, \ldots, v_{2k})\, dv_1 \cdots dv_{2k}. \quad (2.40)$$

The final output spectrum of the complex baseband Volterra model in (2.33) is calculated by the summation of the individual contributions from the different orders in (2.40) which results in

$$\tilde{Y}(\omega) = \sum_{k=0}^{\lceil L/2 \rceil - 1} \tilde{Y}_{2k+1}(\omega) \quad (2.41)$$

From (2.40) and (2.41), we recognize that the frequency-domain output signal of the Volterra system is broadened by the convolution operation in (2.40). This process is depicted in Fig. 2.16 for a 2nd-order system (in complex baseband systems we do not have even orders, but this example demonstrates the convolution process in a simple way). The bandwidth of the output signal $\tilde{Y}(\omega)$ is $(2\lceil L/2 \rceil - 1)2B$, where $2B$ is the bandwidth of the complex input signal $\tilde{X}(\omega)$.

### 2.3.3 Two-Tone Response of a Complex Baseband Volterra model

If we apply a baseband two-tone signal $\tilde{x}(t) = a\cos(\omega_m t)$ to the complex baseband Volterra model described in (2.33) we obtain

$$\tilde{y}(t) = \sum_{k=0}^{\lceil L/2\rceil-1} \left(\frac{a}{2}\right)^{2k+1} \int_0^\infty \cdots \int_0^\infty \tilde{h}_{2k+1}(\tau_1,\ldots,\tau_{2k+1}) \times \prod_{i=1}^{2k+1} \left(\exp\left(j\omega_m(t-\tau_i)\right) + \exp\left(-j\omega_m(t-\tau_i)\right)\right) d\tau_1 \cdots d\tau_{2k+1}, \quad (2.42)$$

where the product in (2.42) can be expressed in a closed mathematical form by

$$\prod_{i=1}^{2k+1} \left(\exp\left(j\omega_m(t-\tau_i)\right) + \exp\left(-j\omega_m(t-\tau_i)\right)\right) = \sum_{n_1=1}^{2} \cdots \sum_{n_{2k+1}=1}^{2} \exp\left(j \sum_{i=1}^{2k+1} (-1)^{n_i+1}\omega_m(t-\tau_i)\right). \quad (2.43)$$

The response of the complex baseband Volterra model in (2.42) can be calculated with (2.43) which, after an interchange of the order of the integrals and summations yields

$$\tilde{y}(t) = \sum_{k=0}^{\lceil L/2\rceil-1} \left(\frac{a}{2}\right)^{2k+1} \sum_{n_1=1}^{2} \cdots \sum_{n_{2k+1}=1}^{2} \exp\left(j \sum_{i=1}^{2k+1} (-1)^{n_i+1}\omega_m t\right) \times \int_0^\infty \cdots \int_0^\infty \tilde{h}_{2k+1}(\tau_1,\ldots,\tau_{2k+1}) \exp\left(-j \sum_{i=1}^{2k+1} (-1)^{n_i+1}\omega_m \tau_i\right) \times d\tau_1 \cdots d\tau_{2k+1}. \quad (2.44)$$

The $(2k+1)$-dimensional integral expression in (2.44) represents the $(2k+1)$-dimensional frequency-domain baseband Volterra kernel $\tilde{H}_{2k+1}$ evaluated on the modulation frequency $\pm\omega_m$, which yields

$$\int_0^\infty \cdots \int_0^\infty \tilde{h}_{2k+1}(\tau_1,\ldots,\tau_{2k+1}) \exp\left(-j \sum_{i=1}^{2k+1} (-1)^{n_i-1}\omega_m \tau_i\right) d\tau_1 \cdots d\tau_{2k+1} = \tilde{H}_{2k+1}\left((-1)^{n_1+1}\omega_m, \ldots, (-1)^{n_{2k+1}+1}\omega_m\right). \quad (2.45)$$

With the frequency-domain Volterra kernels in (2.45), we can express the baseband output signal in (2.44) by

$$\tilde{y}(t) = \sum_{k=0}^{\lceil L/2\rceil-1} \left(\frac{a}{2}\right)^{2k+1} \sum_{n_1=1}^{2} \cdots \sum_{n_{2k+1}=1}^{2} \exp\left(j \sum_{i=1}^{2k+1} (-1)^{n_i+1}\omega_m t\right) \times \tilde{H}_{2k+1}\left((-1)^{n_1+1}\omega_m, \ldots, (-1)^{n_{2k+1}+1}\omega_m\right). \quad (2.46)$$

If we compare the two-tone responses of the quasi-memoryless system in (2.22) and the Volterra system in (2.46), we realize that the spectral components in (2.46) are weighted by the frequency-domain Volterra kernels $\tilde{H}_{2k+1}$ while the spectral components in (2.22) are weighted by the complex constants $\hat{d}_{2k+1}$. Because the magnitudes of the frequency-domain kernels are in general not symmetric (Fourier transform of the complex time-domain kernels $\tilde{h}_{2k+1}$), we are able to model the spectral asymmetries in Fig. 2.8 with a complex baseband Volterra model in (2.33).

## 2.4 Relationship Between Complex Volterra Models and Quasi-Memoryless Models

If the bandwidth of the input signal $\tilde{X}(\omega)$ in (2.36) becomes so small (ultra-narrowband assumption) that the frequency-domain kernels $\tilde{H}_{2k+1}(\omega_1, \ldots, \omega_{2k+1})$ are approximately constant over the input signal bandwidth, as we have shown in Fig. 2.9 for an RF PA, we can replace the baseband frequency-domain kernels $\tilde{H}_{2k+1}(\omega_1, \ldots, \omega_{2k+1}) \rightarrow \tilde{H}_{2k+1}(0, \ldots, 0)$. Therefore (2.36) can be rewritten by

$$\tilde{Y}_{(2k+1)}(\omega_1, \ldots, \omega_{2k+1}) = \tilde{H}_{2k+1}(0, \ldots, 0) \prod_{i=1}^{k+1} \tilde{X}(\omega_i) \prod_{i=k+2}^{2k+1} \tilde{X}^*(-\omega_i). \tag{2.47}$$

If we apply the $(2k+1)$-dimensional inverse Fourier transform $\mathcal{F}^{-1}$ to (2.47), we obtain the $(2k+1)$-dimensional time-domain output signal given by

$$\begin{aligned} \tilde{y}_{(2k+1)}(t_1, \ldots, t_{2k+1}) &= \frac{1}{(2\pi)^{2k+1}} \int_0^\infty \cdots \int_0^\infty \tilde{Y}_{(2k+1)}(\omega_1, \ldots, \omega_{2k+1}) \\ &\quad \times \exp\left( j \sum_{i=1}^{2k+1} \omega_i t_i \right) d\omega_1 \ldots d\omega_{2k+1} \\ &= \tilde{H}_{2k+1}(0, \ldots, 0) \prod_{i=1}^{k+1} \tilde{x}(t_i) \prod_{i=k+2}^{2k+1} \tilde{x}^*(t_i). \end{aligned} \tag{2.48}$$

If we transform the multi-dimensional linear system in (2.48) back to a one-dimensional nonlinear system by letting $t_1, \ldots, t_{2k+1} \rightarrow t$ we obtain

$$\tilde{y}_{2k+1}(t) = \tilde{H}_{2k+1}(0, \ldots, 0) \, |\tilde{x}(t)|^{2k} \, \tilde{x}(t). \tag{2.49}$$

After a summation of the different order signals in (2.49) for $k = 0, \ldots, \lceil L/2 \rceil - 1$, we obtain the quasi-memoryless system

$$\tilde{y}(t) = \sum_{k=0}^{\lceil L/2 \rceil - 1} \tilde{H}_{2k+1}(0, \ldots, 0) \, |\tilde{x}(t)|^{2k} \, \tilde{x}(t), \tag{2.50}$$

which is similar to the quasi-memoryless system in (2.16) which was derived from the nonlinear passband model in Fig. 2.3. This narrowband model can also be derived in the time-domain by replacing the delayed input baseband signals $\tilde{x}(t-\tau_i) \rightarrow \tilde{x}(t)$ in the complex baseband Volterra system (2.33) [51]. To relate these two quasi-memoryless systems, we calculate the baseband frequency-domain Volterra kernels $\tilde{H}$ in terms of the corresponding passband frequency-domain Volterra kernels by applying the $(2k+1)$-dimensional Fourier transform $\mathcal{F}$ to (2.32), which yields

$$\begin{aligned}\tilde{H}_{2k+1}(\omega_1,\ldots,\omega_{2k+1}) &= \int_0^\infty \cdots \int_0^\infty \tilde{h}_{2k+1}(t_1,\ldots,t_{2k+1}) \\ &\quad \times \exp\left(-j\sum_{i=1}^{2k+1}\omega_1 t_i\right) dt_1 \ldots dt_{2k+1} \\ &= \frac{1}{2^{2k}}\binom{2k+1}{k} H_{2k+1}\left(\omega_c+\omega_1,\ldots,\omega_c+\omega_{k+1},\right. \\ &\qquad \left. -\omega_c+\omega_{k+2},\ldots,-\omega_c+\omega_{2k+1}\right).\end{aligned} \tag{2.51}$$

Therefore the quasi-memoryless system in (2.50) is expressed with (2.51) by

$$\begin{aligned}\tilde{y}(t) = &\sum_{k=0}^{\lceil L/2\rceil-1} \frac{1}{2^{2k}}\binom{2k+1}{k} H_{2k+1}(\underbrace{\omega_c,\ldots,\omega_c}_{(k+1)\times},\underbrace{-\omega_c,\ldots,-\omega_c}_{k\times}) \\ &\times |\tilde{x}(t)|^{2k}\,\tilde{x}(t).\end{aligned} \tag{2.52}$$

After equating the output signals of the quasi-memoryless systems in (2.16) and (2.52), we can determine the odd parameters $b_{2k+1}$ and $c_{2k+1}$ of the polynomial functions of the passband model in Fig. 2.3 in terms of the corresponding frequency-domain passband Volterra kernels $H$, which results in

$$b_{2k+1} = \mathrm{Re}\{H_{2k+1}(\underbrace{\omega_c,\ldots,\omega_c}_{(k+1)\times},\underbrace{-\omega_c,\ldots,-\omega_c}_{k\times})\} \tag{2.53}$$

and

$$c_{2k+1} = -\mathrm{Im}\{H_{2k+1}(\underbrace{\omega_c,\ldots,\omega_c}_{(k+1)\times},\underbrace{-\omega_c,\ldots,-\omega_c}_{k\times})\}. \tag{2.54}$$

The even parameters $b_{2k}$ and $c_{2k}$ in Fig. 2.3 can be chosen arbitrarily from the set of the real numbers $\mathbb{R}$, because the spectral components caused by the even-order nonlinearities are filtered out by the 1st-zonal filter in Fig. 2.3 and do not contribute to the baseband output signal $\tilde{y}(t)$.

## 2.5 Frequency-Dependent AM/AM-Conversion and AM/PM-Conversion

In Sec. 2.2.1, we have considered the AM/AM-conversion and the AM/PM-conversion for a quasi-memoryless nonlinear system. Both nonlinear functions were purely dependent on the input signal magnitude $a$. In this section we extend the concept of the AM/AM-conversion and the AM/PM-conversion for the case of a Volterra system.

### 2.5.1 Measurement Setup

If we pass the two-tone response of a Volterra model in (2.46) through a complex linear filter (to observe the magnitude and the phase of the fundamental frequency at $\omega_m$) and sweep both the magnitude $a$ and the angular frequency $\omega_m$ of the input signal (see Fig. 2.17), we obtain

$$\begin{aligned}\tilde{y}_f(t) = \exp(j(\omega_m t + \phi)) \sum_{k=0}^{\lceil L/2\rceil-1} \left(\frac{a}{2}\right)^{2k+1} \binom{2k+1}{k+1} \\ \times \tilde{H}_{2k+1}(\underbrace{\omega_m, \ldots, \omega_m}_{(k+1)\times}, \underbrace{-\omega_m, \ldots, -\omega_m}_{k\times}),\end{aligned} \tag{2.55}$$

where we have assumed, without losing generality, that the Volterra kernels $\tilde{h}_{2k+1}(\tau_1, \ldots, \tau_{2k+1})$ in (2.42) are symmetric [56, 52]. The two-tone response of the complex Volterra model in (2.55) can be rewritten in the following form

$$\tilde{y}_f(t) = |v(a, \omega_m)| \exp(j(\omega_m t + \phi + \arg\{v(a, \omega_m)\})) \tag{2.56}$$

where

$$v(a, \omega_m) = \sum_{k=0}^{\lceil L/2\rceil-1} \left(\frac{a}{2}\right)^{2k+1} \binom{2k+1}{k+1} \tilde{H}_{2k+1}(\underbrace{\omega_m, \ldots, \omega_m}_{(k+1)\times}, \underbrace{-\omega_m, \ldots, -\omega_m}_{k\times}) \tag{2.57}$$

describes a complex function which depends on both, the signal amplitude $a$ and the modulation frequency $\omega_m$ of the input signal. The two-tone response of the complex Volterra system in (2.56) is similar to the response of the quasi-memoryless system in (2.17). For this reason we define $|v(a, \omega)|$ in (2.56) as the frequency-dependent AM/AM-conversion and $\arg\{v(a, \omega)\}$ in (2.56) as the frequency-dependent AM/PM-conversion. It is important to note that the described concept of the frequency-dependent AM/AM-conversion and of the AM/PM-conversion does not fully describe the Volterra system, because we only consider the frequency-domain Volterra kernels along the diagonals and not the full Volterra kernels. However, we are able to test a nonlinear system, e.g., an RF power amplifier whether memory is incorporated or not, which is important for linearization issues [11, 33, 36]. The frequency-dependent AM/AM-conversion and AM/PM-conversion can not only be considered for the fundamental frequency of the output signal spectrum at $\omega_m$, it can also be derived for the harmonics of the input signal, e.g. the

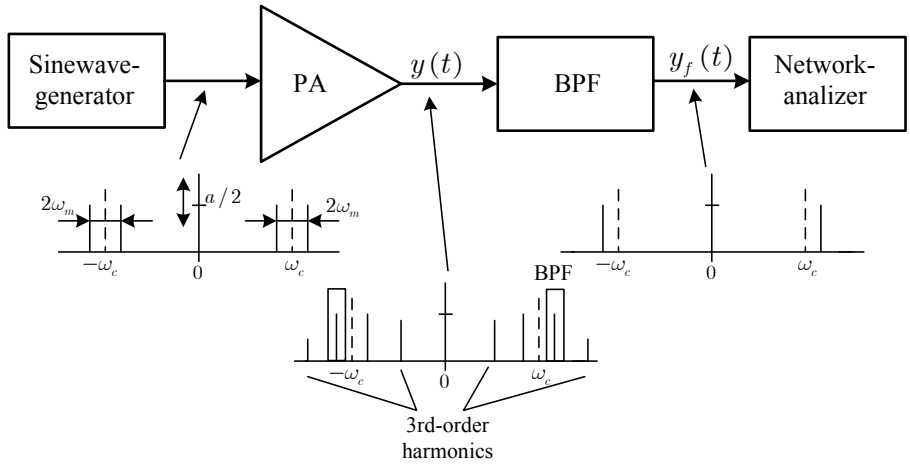


**Figure 2.17:** Setup for the measurement of the frequency-dependent AM/AM-conversion and AM/PM-conversion of the RF PA. The input signal magnitude $a$ and the modulation frequency $\omega_m$ are varied, where the fundamental frequency at $\pm(\omega_c + \omega_m)$ is observed to determine the frequency-dependent AM/AM- and AM/PM-conversion.

third-order intermodulation distortion (IMD3) at $3\omega_m$. Practical RF measurement methods and results for frequency-dependent IMD3 are reported e.g. in [36, 11, 73]. In Fig. 2.18, we show the power of the simulated frequency-dependent AM/AM-conversion $P_O = 10\log(|v(a,\omega)|^2/(2R\times 10^{-3}))$ of a 2.2-GHz, 90-W Class AB RF PA excited with a passband two-tone signal $x(t) = a[\cos((\omega_c+\omega_m)t) + \cos((\omega_c-\omega_m)t)]$, over the input signal power range of $P_I = 10\log(a^2/(2R\times 10^{-3})) = (-10\ldots 42)$ dBm, where $R = 50\ \Omega$ denotes the input impedance of the RF PA, and the modulation frequency ranges from $\omega_m/(2\pi) = (6\ldots 60)$ MHz. The corresponding frequency-dependent AM/PM-conversion is depicted in Fig.2.19. Figure 2.20 to Fig. 2.23 depict the two-dimensional plots of the AM/AM-conversion and AM/PM-conversion in Fig. 2.18 and Fig. 2.19 , if we cut them along the $P_I$-axes and the $\omega/(2\pi)$-axes respectively.

### 2.5.2 Constructing Memory-Polynomial Models from Frequency-Dependent AM/AM and AM/PM Measurements

In this section we use the concept of the frequency-dependent AM/AM-conversion and the AM/PM-conversion to construct a nonlinear model with memory. This model is based on memory-polynomials [33, 18] and can be calculated from two-tone measurements. If we assume that the Volterra kernels of the complex baseband Volterra model in (2.33) $\tilde{h}_{2k+1}(\tau_1,\ldots,\tau_{2k+1}) \equiv 0$, for $\tau_1 \neq \tau_2 \neq \cdots \neq \tau_{2k+1}$, we obtain the continuous-time

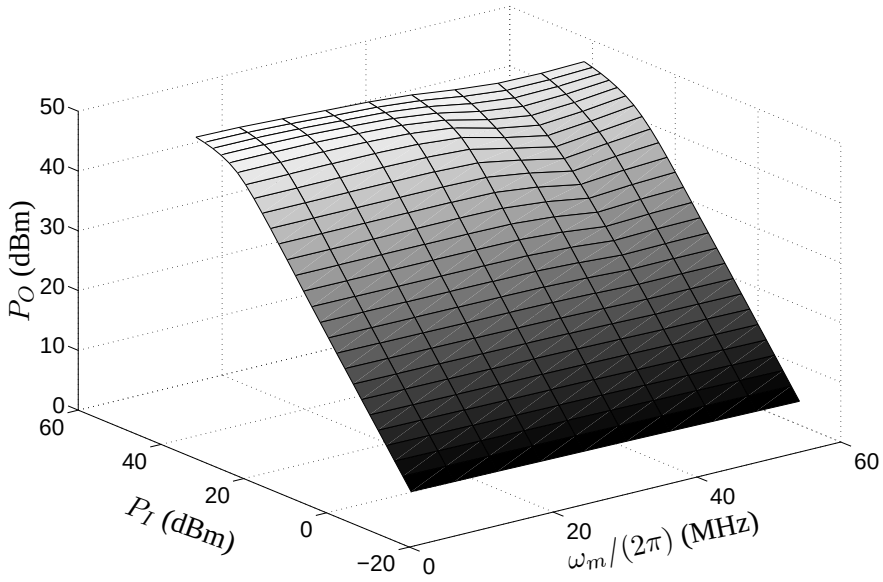


**Figure 2.18:** Frequency-dependent AM/AM-conversion of a 2.2-GHz, 90-W Class AB RF power amplifier excited with a two-tone signal $x(t) = a[\cos((\omega_c+\omega_m)t)+\cos((\omega_c-\omega_m)t)]$, with the angular carrier-frequency of $\omega_c = 2\pi\times 2.17$ GHz. $P_I = 10\log(a^2/(2R\times 10^{-3}))$ and $P_O = 10\log(|v(a,\omega_m)|^2/(2R\times 10^{-3}))$ denotes the input and output signal power respectively, where $R = 50\ \Omega$ is the input impedance of the RF PA.

memory-polynomial model with (2.33) as

$$\begin{aligned}\tilde{y}(t) &= \sum_{k=0}^{\lceil L/2\rceil-1} \int_0^\infty \tilde{g}_{2k+1}(\tau)\,|\tilde{x}(t-\tau)|^{2k}\,\tilde{x}(t-\tau)\,d\tau \\ &= \sum_{k=0}^{\lceil L/2\rceil-1} \tilde{g}_{2k+1}(t)\star|\tilde{x}(t)|^{2k}\,\tilde{x}(t)\end{aligned} \tag{2.58}$$

where $\tilde{g}_{2k+1}(\tau) \equiv \tilde{h}_{2k+1}(\tau,\ldots,\tau)$, describes the time-domain Volterra kernels along the diagonals in a multi-dimensional space. Figure 2.24 illustrates a two-dimensional kernel (although even order kernels do not exist in the baseband Volterra representation, it simply shows the concept of diagonal kernels) $\tilde{h}_2(\tau_1,\tau_2)$, and the cut along the diagonal $\tau_1 = \tau_2$ and the corresponding diagonal kernel $\tilde{g}_2(\tau) \equiv \tilde{h}_2(\tau,\tau)$. If we apply a baseband two-tone

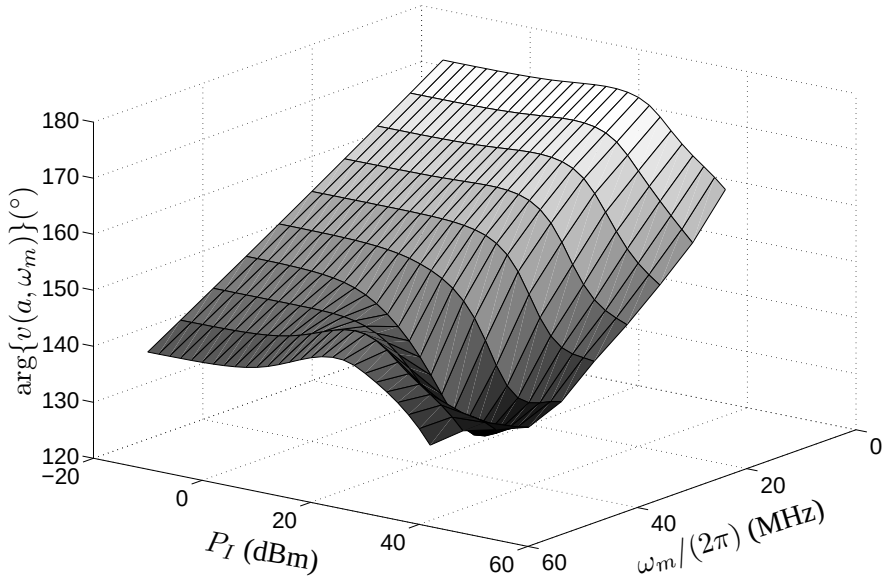


**Figure 2.19:** Frequency-dependent AM/PM-conversion of a 2.2-GHz, 90-W Class AB RF power amplifier excited with a two-tone signal $x(t) = a[\cos((\omega_c + \omega_m)t) + \cos((\omega_c - \omega_m)t)]$, with the angular carrier-frequency of $\omega_c = 2\pi \times 2.17$ GHz. $P_I = 10\log(a^2/(2R \times 10^{-3}))$ denotes the input signal power, where $R = 50\ \Omega$ is the input impedance of the RF PA.

signal $\tilde{x}(t) = a\cos(\omega_m t + \phi)$ to the memory-polynomial model in (2.58), we obtain

$$\tilde{y}(t) = \sum_{k=0}^{\lceil L/2 \rceil - 1} \left(\frac{a}{2}\right)^{2k+1} \int_0^\infty \tilde{g}_{2k+1}(\tau) \Big[\exp(j(\omega_m(t-\tau)+\phi)) + \exp(-j(\omega_m(t-\tau)+\phi))\Big]^{2k+1} d\tau. \tag{2.59}$$

If we evaluate the $(2k+1)$-th power of the expression within the brackets of (2.59), we can rewrite (2.59) as

$$\tilde{y}(t) = \sum_{k=0}^{\lceil L/2 \rceil - 1} \left(\frac{a}{2}\right)^{2k+1} \sum_{n=0}^{2k+1} \binom{2k+1}{n} \exp\Big[j((2n-2k-1)\omega_m t + (2n-2k-1)\phi)\Big] \times \int_0^\infty \tilde{g}_{2k+1}(\tau) \exp\big(-j(2n-2k-1)\omega_m \tau\big)\, d\tau, \tag{2.60}$$

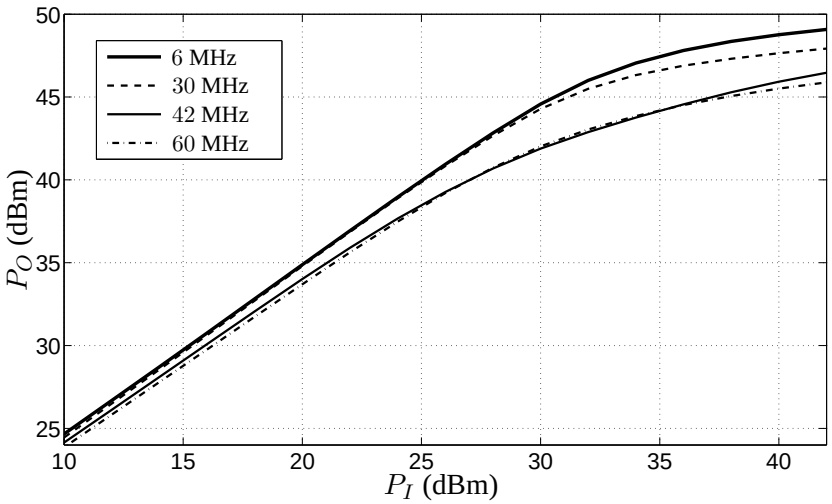


**Figure 2.20:** AM/AM-conversion of a 2.2-GHz, 90-W Class AB RF power amplifier excited with a two-tone signal $x(t) = a[\cos((\omega_c + \omega_m)t) + \cos((\omega_c - \omega_m)t)]$ for four different frequencies $\omega_m$ (cuts through Fig. 2.18 along the $P_I$-axis), with the angular carrier-frequency of $\omega_c = 2\pi \times 2.17$ GHz.

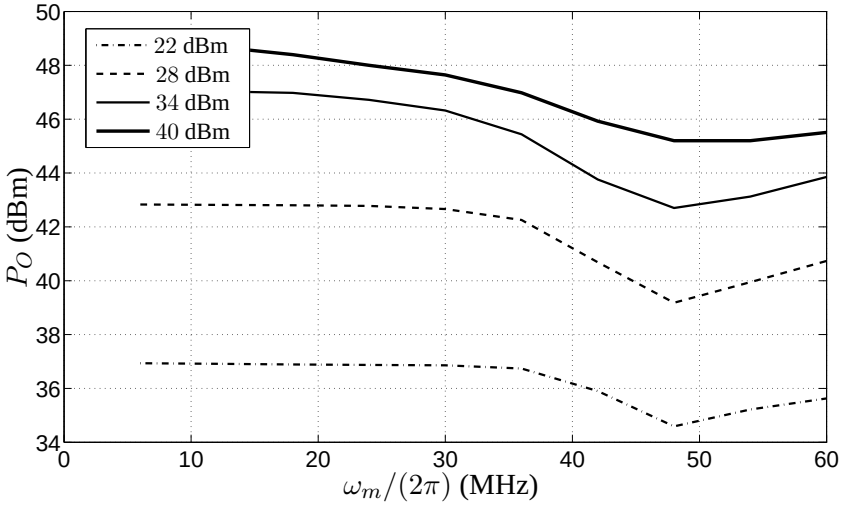


**Figure 2.21:** AM/AM-conversion of a 2.2-GHz, 90-W Class AB RF power amplifier excited with a two-tone signal $x(t) = a[\cos((\omega_c + \omega_m)t) + \cos((\omega_c - \omega_m)t)]$ for four different input signal power levels (cuts through Fig. 2.18 along the $\omega_m/(2\pi)$-axis), with the angular carrier-frequency of $\omega_c = 2\pi \times 2.17$ GHz.

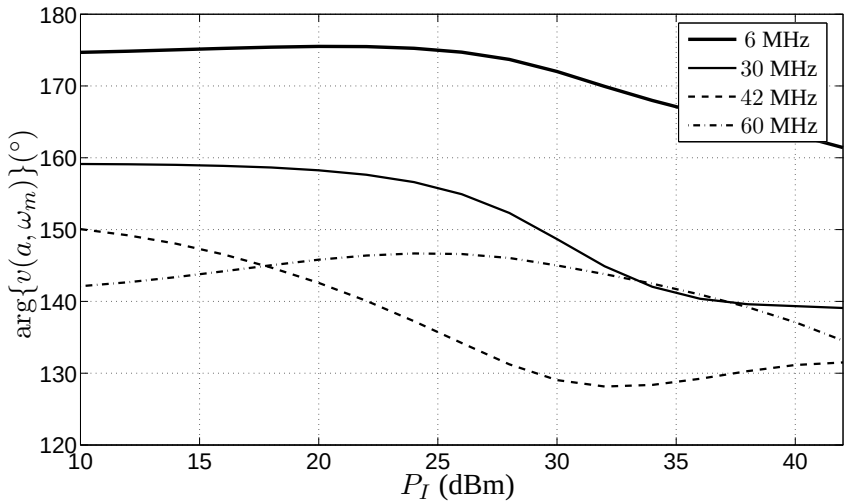


**Figure 2.22:** AM/PM-conversion of a 2.2-GHz, 90-W Class AB RF power amplifier excited with a two-tone signal $x(t) = a[\cos((\omega_c+\omega_m)t)+\cos((\omega_c-\omega_m)t)]$ for four different frequencies (cuts through $\arg\{v(a,\omega_m)\}$ in Fig. 2.19 along the $P_I$-axis), with the angular carrier-frequency of $\omega_c = 2\pi \times 2.17$ GHz.

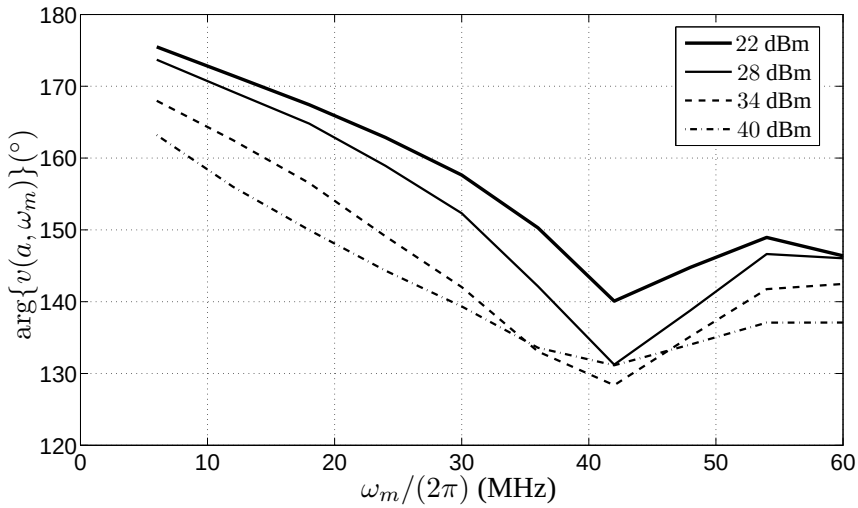


**Figure 2.23:** AM/PM-conversion of a 2.2-GHz, 90-W Class AB RF power amplifier excited with a two-tone signal $x(t) = a[\cos((\omega_c+\omega_m)t)+\cos((\omega_c-\omega_m)t)]$ for four different input signal magnitudes (cuts through $\arg\{v(a,\omega_m)\}$ in Fig. 2.19 along the frequency-axis), where the carrier-frequency $\omega_c = 2\pi \times 2.17$ GHz.

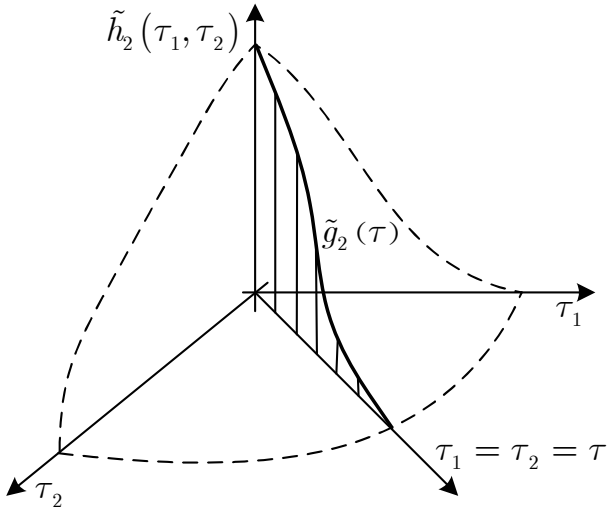


**Figure 2.24:** Two-dimensional time-domain Volterra kernel $\tilde{h}_2(\tau_1, \tau_2)$, and the corresponding diagonal kernel $\tilde{g}_2(\tau) \equiv \tilde{h}_2(\tau, \tau)$.

which yields for the fundamental angular frequency at $\omega_m$ ($n = k + 1$)

$$\tilde{y}_f(t) = \exp(j(\omega_m t + \phi)) \sum_{k=0}^{\lceil L/2 \rceil - 1} \left(\frac{a}{2}\right)^{2k+1} \binom{2k+1}{k+1} \tilde{G}_{2k+1}(\omega_m), \tag{2.61}$$

where $\tilde{G}_{2k+1}(\omega_m) = \mathcal{F}\{\tilde{g}_{2k+1}(t)\}$ denotes the Fourier transform of the diagonal time-domain Volterra kernels in (2.58). The filtered two-tone response of the complex memory-polynomial model in (2.61), can be rewritten in the following form

$$\tilde{y}_f(t) = |v(a, \omega_m)| \exp(j(\omega_m t + \phi + \arg\{v(a, \omega_m)\})) \tag{2.62}$$

where

$$v(a, \omega_m) = \sum_{k=0}^{\lceil L/2 \rceil - 1} \left(\frac{a}{2}\right)^{2k+1} \binom{2k+1}{k+1} \tilde{G}_{2k+1}(\omega_m) \tag{2.63}$$

describes a complex function which depends on both the signal amplitude $a$ and the modulation frequency $\omega_m$ of the input signal. Because the memory-polynomial model in (2.58) is purely dependent on the $\lceil L/2 \rceil$ complex linear filters (diagonal frequency-domain Volterra kernels) $\tilde{G}_{2k+1}(\omega_m)$ (see Fig.2.25), we can estimate them from the measured frequency-dependent AM/AM-conversion and AM/PM-conversion in (2.63) for $\lceil L/2 \rceil$ different input signal magnitudes $a_i$, for $i = 1, \ldots, \lceil L/2 \rceil$. As in practical applications, these measurements are noisy (imperfect measurements, model inaccuracies), we formulate a classical linear least squares problem [26] to estimate the unknown linear filters $\tilde{G}_{2k+1}(\omega_m)$ in (2.63) by

$$\hat{\mathbf{G}}(\omega_m) = (\mathbf{A}^T \mathbf{A})^{-1} \mathbf{A}^T \hat{\mathbf{v}}(\omega_m), \tag{2.64}$$

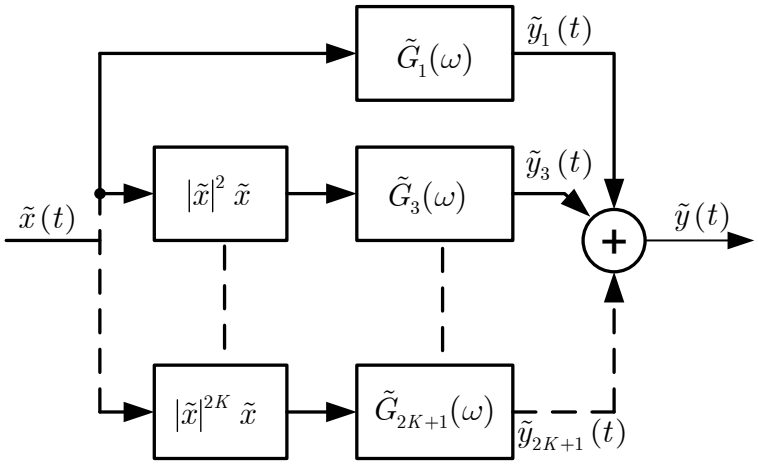


**Figure 2.25:** Complex baseband model built with memory-polynomials. The model is composed of a bank of known static nonlinearities and the unknown linear filters $\tilde{G}_{2k+1}(\omega)$ for $k = 0, \ldots, K$ where $K = \lceil L/2 \rceil - 1$, which can be estimated from frequency-dependent AM/AM and AM/PM-conversion measurements.

where

$$\hat{\mathbf{v}}(\omega_m) = [\hat{v}(a_1, \omega_m), \hat{v}(a_2, \omega_m), \ldots, \hat{v}(a_N, \omega_m)]^T, \tag{2.65}$$

denotes an $N \times 1$ vector ($N > \lceil L/2 \rceil$), whose components are the measured (noisy) versions of the frequency-dependent AM/AM and AM/PM-conversion entries in (2.63), and the $\lceil L/2 \rceil \times 1$ vector

$$\hat{\mathbf{G}}(\omega_m) = [\hat{G}_1(\omega_m), \hat{G}_3(\omega_m), \ldots, \hat{G}_{2\lceil L/2 \rceil - 1}(\omega_m)]^T \tag{2.66}$$

describes the estimated linear filters in Fig. 2.25 for the modulation frequency $\omega_m$. The $N \times \lceil L/2 \rceil$ observation matrix $\mathbf{A}$ in (2.64) is defined by

$$\mathbf{A} = \begin{pmatrix} \frac{a_1}{2} & 3(\frac{a_1}{2})^3 & \ldots & \binom{2\lceil \frac{L}{2} \rceil - 1}{\lceil \frac{L}{2} \rceil} (\frac{a_1}{2})^{2\lceil \frac{L}{2} \rceil - 1} \\ \vdots & \vdots & & \vdots \\ \frac{a_N}{2} & 3(\frac{a_N}{2})^3 & \ldots & \binom{2\lceil \frac{L}{2} \rceil - 1}{\lceil \frac{L}{2} \rceil} (\frac{a_N}{2})^{2\lceil \frac{L}{2} \rceil - 1} \end{pmatrix}. \tag{2.67}$$

To obtain the frequency-responses of the unknown linear filters $\hat{G}_{2k+1}(\omega)$ over the frequency-range of interest, we solve the least squares problem in (2.64) for different modulation frequencies $\omega_m$. The calculated complex linear filters $G_1(\omega)$ and $G_3(\omega)$ are shown in Fig. 2.26 and Fig.2.27, where we have assumed the highest order of the nonlinearity three. To evaluate the memory-polynomial model, we excite an 2.2-GHz, 90-W, Class AB RF power amplifier with a discrete multi-tone (DMT) signal with $B = 20$ MHz and

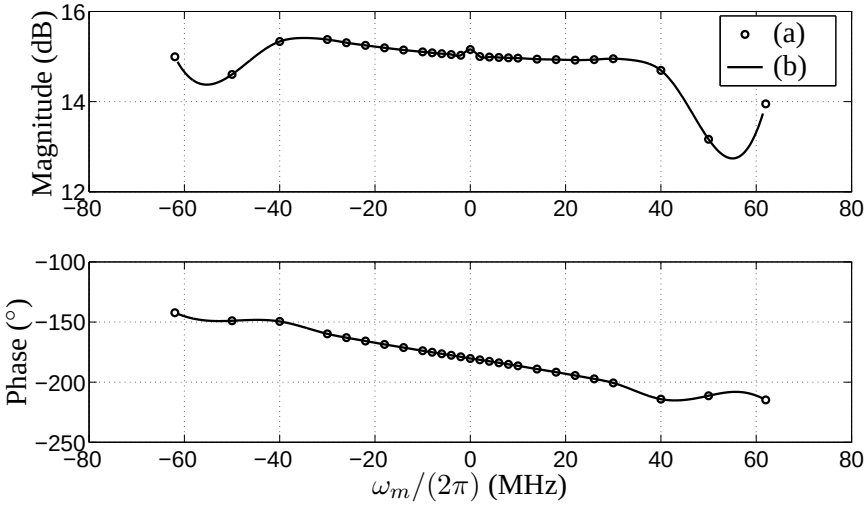


**Figure 2.26:** Frequency-response of the complex linear filter $\tilde{G}_1(\omega)$ of the memory-polynomial model in Fig.2.25. The filter is calculated with (2.64) and the simulated frequency-dependent AM/AM and AM/PM-surfaces depicted in Fig. 2.18 and Fig.2.19. (a) Calculated values, (b) Cubic spline interpolated.

$P_I = 27$ dBm and compare the complex baseband output signal of the amplifier and the 3rd-order memory-polynomial model (see Fig. 2.28 and Fig. 2.29). The modeling error ($10\log(|\tilde{y}_{\text{PA}}(t) - \tilde{y}(t)|^2 \,/\, |\tilde{y}_{\text{PA}}(t)|^2)$) for the linear memory-polynomial model (only $\tilde{G}_1(\omega)$ in Fig.2.25) is approximately $-22$ dB, where the modeling error of the 3rd-order model is approximately $-29$ dB. The modeling error can be further reduced by increasing the polynomial order of the memory-polynomial model.

## 2.6 Conclusion

We have reviewed the concept of memoryless and quasi-memoryless nonlinear baseband systems which are equivalent to the corresponding real nonlinear passband systems described by two static nonlinearities and a linear 1st-zonal filter. We have shown that these nonlinear models are not sufficient to describe a general nonlinear passband system such as an RF PA under a wideband excitation. The reason for this is that the memory effects (electrical and electro-thermal) of the nonlinear passband system generate spectral asymmetries which cannot be generated by the mentioned static nonlinear models.

Therefore we have replaced the static nonlinear passband system by a real Volterra system and transformed the cascade of this real Volterra system and a linear 1st-zonal filter to the baseband domain. As the resulting complex baseband Volterra series model contains memory we are able to generate spectral asymmetries. We have shown that the memoryless and quasi-memoryless models are special cases of the complex Volterra series model, which are obtained from the complex baseband Volterra model if the bandwidth of the complex

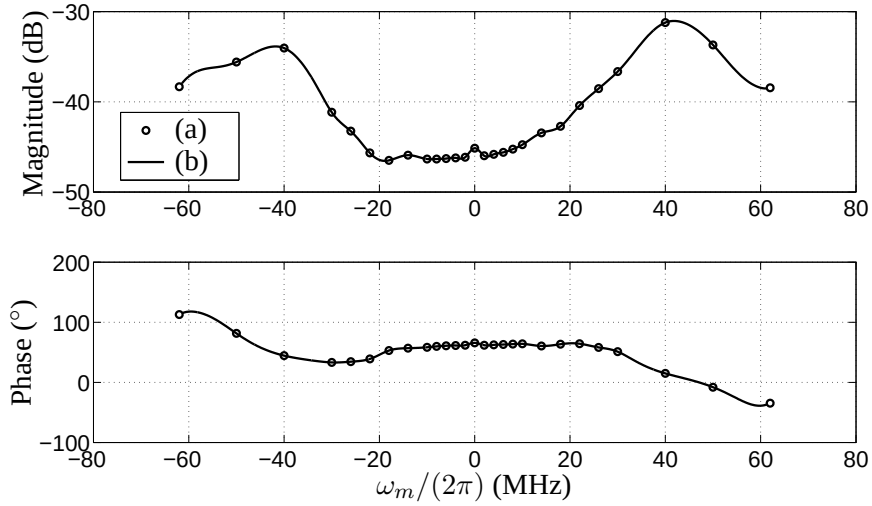


**Figure 2.27:** Frequency-response of the complex linear filter $\tilde{G}_3(\omega)$ of the memory-polynomial model in Fig.2.25. The filter is calculated with (2.64) and the simulated frequency-dependent AM/AM and AM/PM-surfaces depicted in Fig. 2.18 and Fig.2.19. (a) Calculated values, (b) Cubic spline interpolated.

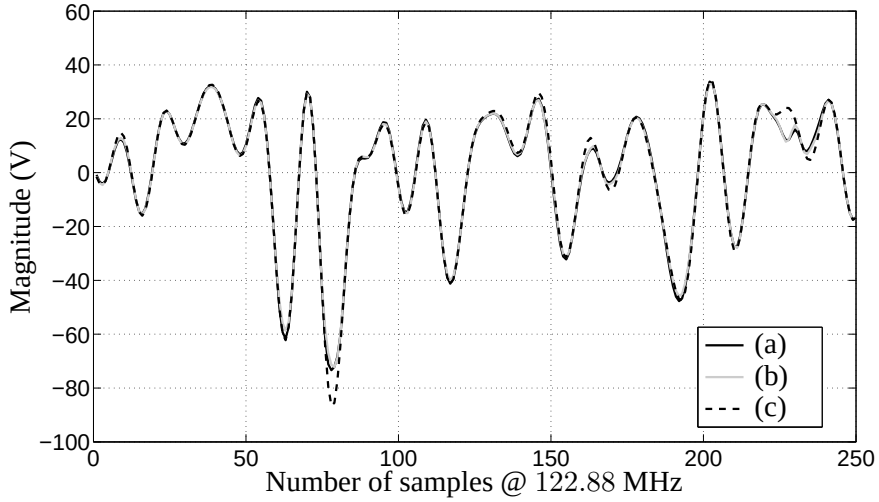


**Figure 2.28:** (a) Real output signal magnitude of a 2.2-GHz, 90-W, Class AB RF power amplifier excited with a DMT signal with $B = 20$ MHz, $P_I = 27$ dBm.(b) Real output signal magnitude of a 3rd-order memory-polynomial model in Fig.2.25,(c) Real output signal magnitude of a linear memory-polynomial model in Fig.2.25 (the graphs for (a) and (b) essentially coincide).

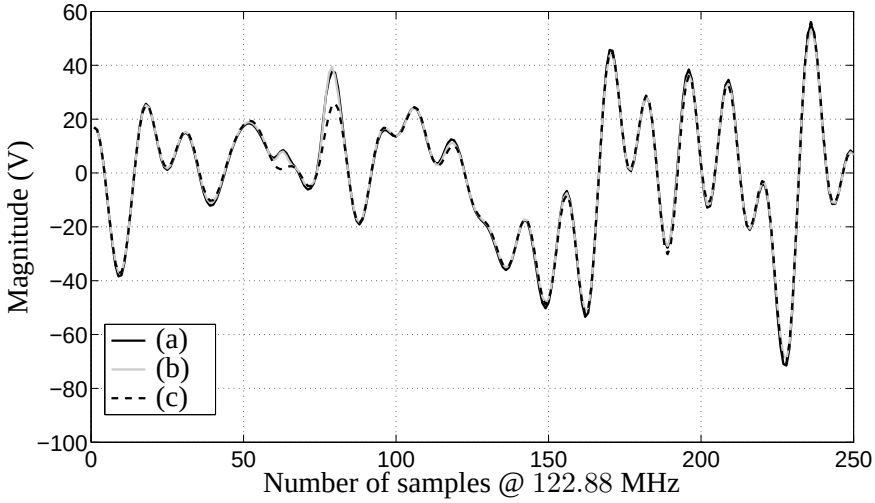


**Figure 2.29:** (a) Imaginary output signal magnitude of a 2.2-GHz, 90-W, Class AB RF power amplifier excited with a DMT signal with $B = 20$ MHz, $P_I = 27$ dBm.(b) Real output signal magnitude of a 3rd-order memory-polynomial model in Fig.2.25,(c) Real output signal magnitude of a linear memory-polynomial model in Fig.2.25 (the graphs for (a) and (b) essentially coincide).

baseband input signal becomes so small that the frequency-domain Volterra kernels are constant over the input signal bandwidth (ultra-narrowband assumption).

Furthermore, we have extended the concept of the AM/AM and AM/PM-conversion in order to reflect the dependence on the modulation frequency. The resulting frequency-dependent AM/AM and AM/PM surfaces can be employed to calculate the unknown complex linear filters in a memory-polynomial model (simplified Volterra model). This new characterization of nonlinear passband systems can be obtained from simple measurements and its one-to-one correspondence with the memory-polynomial system structure. On the other hand memory-polynomial systems can be fully characterized by frequency-dependent AM/AM and AM/PM measurements and are often sufficiently accurate approximations of a full Volterra kernel model for RF PA's.

# Chapter 3

# Frequency-Domain Expansion of Volterra Kernels

In Chap. 2 we have developed complex baseband Volterra series models for wideband and narrowband applications. A serious drawback of Volterra series models is the large number of parameters which grows immensely with the order of the nonlinearity and the memory depth if the Volterra model is implemented in the discrete-time domain. However in many practical wideband applications, the frequency-domain Volterra kernels vary quite smoothly over the input signal bandwidth if the carrier frequency is much larger than the input signal bandwidth (e.g., $\omega_c \approx 100 \times B$ in a four carrier UMTS). Therefore, it could be reasonable to expand the multi-dimensional frequency-domain Volterra kernels and approximate them with multi-dimensional orthogonal polynomials. This results in general in a complex RF PA baseband model with a lower number of parameters and a performance which is comparable to Volterra series models. In Sec. 3.1 we consider the required basic steps to obtain a time-domain complex baseband model with approximated frequency-domain Volterra kernels in the baseband and passband domains. In Sec. 3.2 we expand the frequency-domain kernels of a complex baseband Volterra series model with multi-dimensional orthogonal polynomials and build a complex baseband model which is composed of a bank of linear filters, conjugate operators and a multi-variate polynomial series, whose parameters determine the particular RF PA baseband model. If the RF PA input signal becomes narrowband, the complex baseband model reduces exactly to the narrowband model as discussed in Chap. 2, which can be described by the AM/AM and AM/PM conversion. In Sec. 3.3, we transform the complex baseband model with the approximated frequency-domain Volterra kernels back to the passband domain, which gives us some useful insights about passband modeling without explicit 1st-zonal filtering. In Sec. 3.4, we consider the discrete-time implementation and parameter estimation for the developed complex baseband models.

## 3.1 Introduction

Figure 3.1 depicts the basic steps which are required to develop a Volterra-based nonlinear model with approximated frequency-domain kernels in the baseband and passband domains. The first operation, which is denoted by $\mathcal{P}$, transforms the cascade of a real passband Volterra model and a 1st-zonal filter (bandpass filter centered around the carrier frequency $\omega_c$ [10, 8]) to the baseband domain. The resulting complex baseband Volterra model is equivalent to the corresponding model in the passband domain, which means

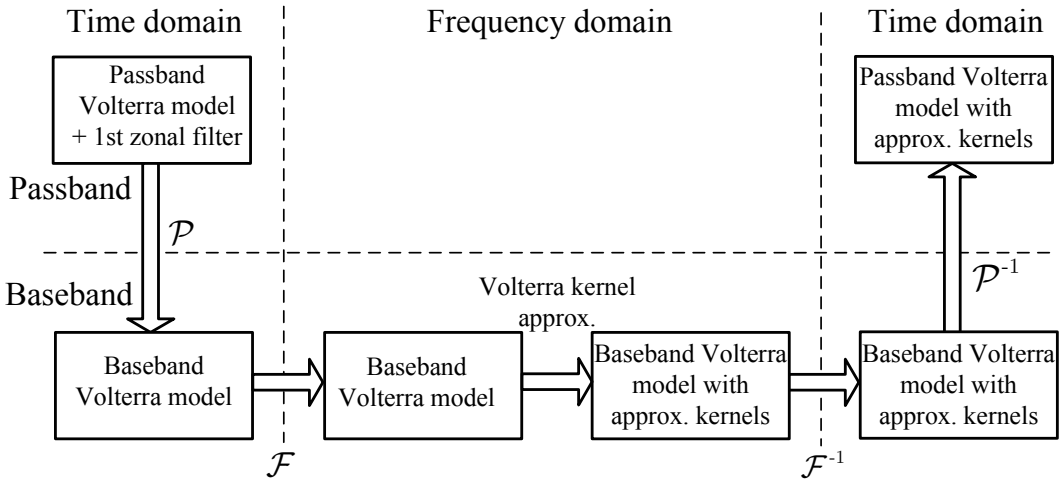


**Figure 3.1:** Development of a baseband and a passband Volterra model with approximated frequency-domain Volterra kernels. The symbols $\mathcal{F}$ and $\mathcal{F}^{-1}$ denote the Fourier transform and its inverse. The symbols $\mathcal{P}$ and $\mathcal{P}^{-1}$ denote the transform from a passband model to a baseband model and vice versa.

that the output signal of the complex baseband Volterra model $\tilde{y}(t)$ and the output signal of the cascade of the passband Volterra model and the 1st-zonal filter $y(t)$ are related by $y(t) = Re\{\tilde{y}(t)\exp(j\omega_c t)\}$. If we transform this complex baseband Volterra model to the frequency domain by applying the Fourier transform $\mathcal{F}$ to the time-domain output signal of the complex baseband Volterra model, we obtain a useful relationship of the multi-linear frequency-domain output signal representations and the frequency-domain Volterra kernels. As a next step, we expand these kernels with multi-dimensional orthogonal polynomials and approximate the frequency-domain Volterra kernels within the input signal bandwidth with a moderate number of parameters (low approximation order). The resulting complex baseband Volterra model with the approximated frequency-domain kernels have in general a lower number of parameters but a performance comparable to the corresponding Volterra model. In the final step of Fig. 3.1, we transform the baseband Volterra model with the approximated kernels back to the passband domain by applying a baseband to passband transform denoted by $\mathcal{P}^{-1}$. This transform leads to an interesting representation of nonlinear passband systems, where the passband output signal $y(t)$ is generated without any explicit 1st-zonal filtering.

## 3.2 Volterra Kernel Expansion with Orthogonal Polynomials

If we consider the $(2k+1)$-dimensional frequency-domain output signal of a complex Volterra model $\tilde{Y}_{(2k+1)}(\omega_1, \ldots, \omega_{2k+1})$ in (2.36), we notice that the frequency-domain Volterra kernels $\tilde{H}_{2k+1}(\omega_1, \ldots, \omega_{2k+1})$ are masked out by the band-limited $(2k+1)$-

dimensional input signal $\prod_{i=1}^{k+1} \tilde{X}(\omega_i) \prod_{i=k+2}^{2k+1} \tilde{X}^*(-\omega_i)$. Therefore we can expand and approximate the frequency-domain Volterra kernels $\tilde{H}_{2k+1}(\omega_1, \ldots, \omega_{2k+1})$ over the input signal bandwidth of $\pm B$ with a multi-dimensional orthogonal polynomial series [56, 35, 54]

$$\hat{H}_{2k+1}(\omega_1, \ldots, \omega_{2k+1}) = \sum_{m_1=0}^{M_{2k+1}} \cdots \sum_{m_{2k+1}=0}^{M_{2k+1}} c_{m_1,\ldots,m_{2k+1}} \times T_{m_1}(\omega_1) \cdots T_{m_{2k+1}}(\omega_{2k+1}), \tag{3.1}$$

with $M_{2k+1} + 1$ members of a complete set of real orthogonal polynomials $T_i$, for $0 \leq i \leq M_{2k+1}$ and the complex valued parameters $c_{m_1,\ldots,m_{2k+1}}$. The orthogonality condition is expressed by

$$\int_{-B}^{B} p(\omega)\, T_n(\omega)\, T_m(\omega)\, d\omega = \begin{cases} \lambda_n & \text{if } m = n \\ 0 & \text{if } m \neq n \end{cases} \tag{3.2}$$

where the real function $p(\omega) > 0$ is a certain weight, which defines the particular set of orthogonal polynomials. To calculate the optimum parameters $c_{m_1,\ldots,m_{2k+1}}$ in (3.1), the integral-square error

$$E = \int_{-B}^{B} \ldots \int_{-B}^{B} p(\omega_1) \cdots p(\omega_{2k+1}) \cdot \left| \tilde{H}_{2k+1}(\omega_1, \ldots, \omega_{2k+1}) - \hat{H}_{2k+1}(\omega_1, \ldots, \omega_{2k+1}) \right|^2 d\omega_1 \ldots d\omega_{2k+1} \tag{3.3}$$

is minimized with respect to the complex coefficients $c_{m_1,\ldots,m_{2k+1}}$. If the approximation order of the multi-dimensional polynomial series in (3.1) $M_{2k+1} \to \infty$, the numerical value in (3.3) tends to zero, if the set of orthogonal polynomials is complete and the multi-dimensional frequency-domain kernels $\tilde{H}_{2k+1}(\omega_1, \ldots, \omega_{2k+1})$ are square-integrable in sense (cf. Appendix B)

$$\int_{-B}^{B} \ldots \int_{-B}^{B} p(\omega_1) \cdots p(\omega_{2k+1}) \left| \tilde{H}_{2k+1}(\omega_1, \ldots, \omega_{2k+1}) \right|^2 d\omega_1, \ldots, d\omega_{2k+1} < \infty. \tag{3.4}$$

With (3.1), (3.2) and (3.3), the optimum complex parameters for the multi-dimensional polynomial series in (3.1) are calculated by (cf. Appendix B)

$$c_{o(m_1,\ldots,m_{2k+1})} = \frac{1}{\lambda_{m_1} \cdots \lambda_{m_{2k+1}}} \int_{-B}^{B} \cdots \int_{-B}^{B} p(\omega_1) \cdots p(\omega_{2k+1})\, \tilde{H}_{2k+1}(\omega_1, \ldots, \omega_{2k+1}) \times T_{m_1}(\omega_1) \cdots T_{m_{2k+1}}(\omega_{2k+1})\, d\omega_1 \ldots d\omega_{2k+1}. \tag{3.5}$$

If we insert the optimum complex parameters from (3.5) in (3.1) and evaluate the integral square error in (3.3) we obtain the minimum integral square error (cf. Appendix B)

$$E_{min} = \int_{-B}^{B} \cdots \int_{-B}^{B} p(\omega_1) \cdots p(\omega_{2k+1}) \left| \tilde{H}_{2k+1}(\omega_1, \ldots, \omega_{2k+1}) \right|^2 d\omega_1 \ldots d\omega_{2k+1} - \sum_{m_1=0}^{M_{2k+1}} \cdots \sum_{m_{2k+1}=0}^{M_{2k+1}} \lambda_{m_1} \cdots \lambda_{m_{2k+1}} \left| c_{o(m_1,\ldots,m_{2k+1})} \right|^2 . \quad (3.6)$$

Because the minimum error and right-hand side expressions in (3.6) are all nonnegative, the following kind of Bessel's inequality [35] holds

$$\sum_{m_1=0}^{M_{2k+1}} \cdots \sum_{m_{2k+1}=0}^{M_{2k+1}} \lambda_{m_1} \cdots \lambda_{m_{2k+1}} \left| c_{o(m_1,\ldots,m_{2k+1})} \right|^2 \leq \int_{-B}^{B} \cdots \int_{-B}^{B} p(\omega_1) \cdots p(\omega_{2k+1}) \times \left| \tilde{H}_{2k+1}(\omega_1, \ldots, \omega_{2k+1}) \right|^2 d\omega_1 \ldots d\omega_{2k+1}, \quad (3.7)$$

which implies equality if the approximation order $M_{2k+1} \to \infty$.

The frequency-domain approximation with orthogonal polynomials is demonstrated in Figure 3.2 for the linear kernel of a simple 1st-order low-pass filter which is described by $\tilde{H}_1(\omega) = 1/(1 + j\omega/\omega_c)$, where $\omega_c$ denotes the 3-dB cut-off frequency. The upper plots in Fig. 3.2 depict the real and the imaginary parts of the linear kernel $\tilde{H}_1(\omega)$, and the 1st- and 2nd-order approximation polynomials $\hat{H}_1(\omega)$ in (3.1) for $k = 0$, $M_1 = 1$ and $M_1 = 2$, respectively. The lowest plot shows the optimum approximation error $|\tilde{H}_1(\omega) - \hat{H}_1(\omega)|^2$ for the 1st- and 2nd-order approximation polynomials.

If we express the multi-dimensional frequency-domain signal in (2.36) with the multi-dimensional polynomial series in (3.1) ($\tilde{H}_{2k+1} \to \hat{H}_{2k+1}$), we are able to transform the approximate signal

$$\hat{Y}_{(2k+1)}(\omega_1, \ldots, \omega_{2k+1}) = \sum_{m_1=0}^{M_{2k+1}} \cdots \sum_{m_{2k+1}=0}^{M_{2k+1}} c_{m_1,\ldots,m_{2k+1}} T_{m_1}(\omega_1) \cdots T_{m_{2k+1}}(\omega_{2k+1}) \times \prod_{i=1}^{k+1} \tilde{X}(\omega_i) \prod_{i=k+2}^{2k+1} \tilde{X}^*(-\omega_i), \quad (3.8)$$

into the time-domain by a multi-dimensional inverse Fourier transform

$$\hat{y}_{(2k+1)}(t_1, \ldots, t_{2k+1}) = \mathcal{F}^{-1} \left\{ \hat{Y}_{(2k+1)}(\omega_1, \ldots, \omega_{2k+1}) \right\} \quad (3.9)$$

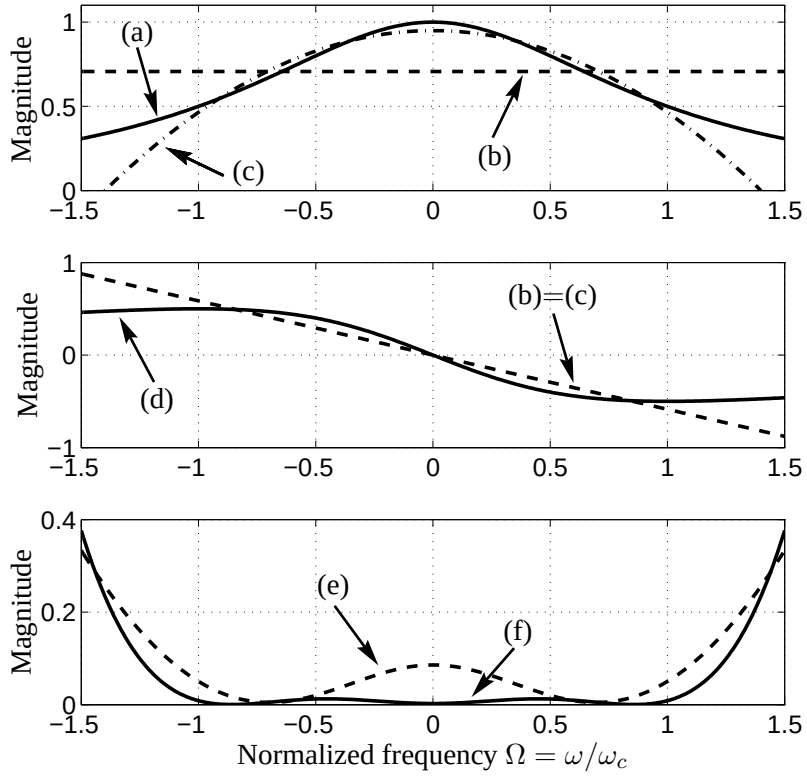


**Figure 3.2:** Approximation of a linear frequency-domain Volterra kernel with Chebyshev polynomials over the normalized frequency range of $\Omega \in [-1, 1]$. (a) shows $\mathrm{Re}\{\tilde{H}_1(\Omega)\}$ and (d) shows $\mathrm{Im}\{\tilde{H}_1(\Omega)\}$, where (b) and (c) are the 1st- and 2nd-order approximations. The lowest figure shows the optimum approximation squared-magnitude error in (e) and (f) for the 1st- and 2nd-order approximations.

which results in

$$\begin{aligned}\hat{y}_{(2k+1)}(t_1,\ldots,t_{2k+1}) = \sum_{m_1=0}^{M_{2k+1}} \cdots \sum_{m_{2k+1}=0}^{M_{2k+1}} c_{m_1,\ldots,m_{2k+1}} \mathcal{F}^{-1}\left\{T_{m_1}(\omega_1)\,\tilde{X}(\omega_1)\right\}\cdots \\ \times \mathcal{F}^{-1}\left\{T_{m_{k+1}}(\omega_{k+1})\,\tilde{X}(\omega_{k+1})\right\} \\ \times \mathcal{F}^{-1}\left\{T_{m_{k+2}}(\omega_{k+2})\,\tilde{X}^*(-\omega_{k+2})\right\}\cdots \\ \times \mathcal{F}^{-1}\left\{T_{m_{2k+1}}(\omega_{2k+1})\,\tilde{X}^*(-\omega_{2k+1})\right\}. \end{aligned} \tag{3.10}$$

If we now undo the process of spanning the time-domain function in $2k+1$ dimensions in (2.35), the final approximate baseband output signal of the order $2k+1$ is given by

$$\begin{aligned}\hat{y}_{2k+1}(t) &= \hat{y}_{(2k+1)}(t,\ldots,t) \\ &= \sum_{m_1=0}^{M_{2k+1}} \cdots \sum_{m_{2k+1}=0}^{M_{2k+1}} c_{m_1,\ldots,m_{2k+1}} \tilde{w}_{m_1}(t)\cdots\tilde{w}_{m_{k+1}}(t) \\ &\quad \times \tilde{u}_{m_{k+2}}(t)\cdots\tilde{u}_{m_{2k+1}}(t), \end{aligned} \tag{3.11}$$

where the time-domain signals $\tilde{w}_i(t)$ and $\tilde{u}_i(t)$ in (3.11) are defined for $0 \le i \le M_{2k+1}$ by

$$\begin{aligned}\tilde{w}_i(t) &= \mathcal{F}^{-1}\left\{T_i(\omega)\,\tilde{X}(\omega)\right\} \\ \tilde{u}_i(t) &= \mathcal{F}^{-1}\left\{T_i(\omega)\,\tilde{X}^*(-\omega)\right\}. \end{aligned} \tag{3.12}$$

The overall output signal is obtained by summing up all contributions from (3.11), which yields

$$\hat{y}(t) = \sum_{k=0}^{\lceil N/2\rceil-1} \hat{y}_{2k+1}(t). \tag{3.13}$$

The time-domain signals in (3.12) are calculated by applying the inverse Fourier operator on the product of the frequency-domain input signals $\tilde{X}(\omega)$ and the $i$th-order orthogonal polynomials $T_i(\omega) = \sum_{k=0}^{i} a_{ki}\omega^k$, where the real coefficients $a_{ki}$ are defined by the particular set of orthogonal polynomials. This leads to a series with complex-scaled and differentiated time-domain input signals of different orders, expressed by

$$\begin{aligned}\tilde{w}_i(t) &= \sum_{k=0}^{i} a_{ki}\mathcal{F}^{-1}\left\{\omega^k\tilde{X}(\omega)\right\} \\ &= \sum_{k=0}^{i} a_{ki}\frac{1}{j^k}\frac{d^k\tilde{x}(t)}{dt^k} \end{aligned} \tag{3.14}$$

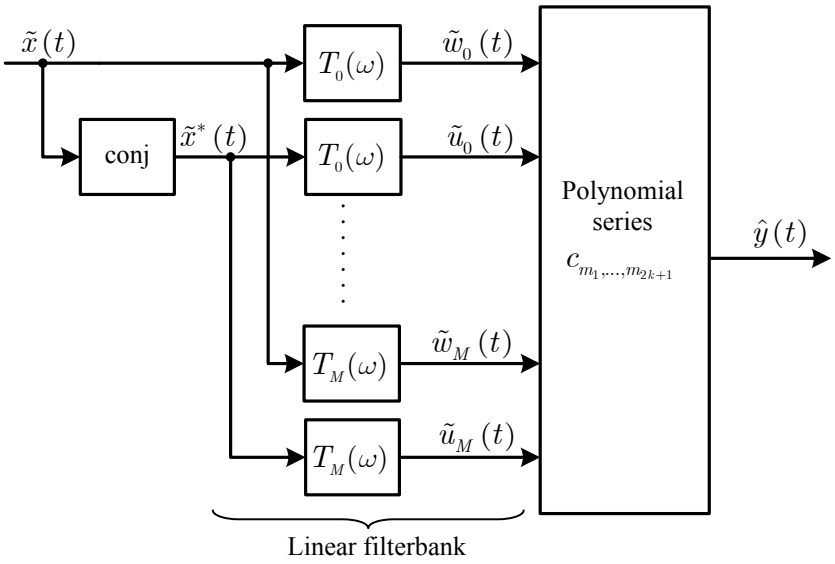


**Figure 3.3:** Complex RF power amplifier model with approximated frequency-domain Volterra kernels. The model is composed of a bank of linear filters (differentiators) and a static nonlinearity represented by a polynomial series.

and

$$\begin{aligned}\tilde{u}_i(t) &= \sum_{k=0}^{i} a_{ki}\mathcal{F}^{-1}\left\{\omega^k \tilde{X}^*(-\omega)\right\} \\ &= \sum_{k=0}^{i} a_k \frac{1}{j^{ki}}\frac{d^k\tilde{x}^*(t)}{dt^k}.\end{aligned} \tag{3.15}$$

The complex baseband PA model from (3.11) to (3.15) is depicted in Fig. 3.3. The system consists of a bank of $2(M+1)$ complex linear filters described by the orthogonal polynomials $T_i(\omega)$ (generalized complex differentiators) for $0 \leq i \leq M$, where $M = \max\left\{M_1, M_3, \ldots, M_{2\lceil N/2\rceil-1}\right\}$ for $M \neq M_1$, and a static nonlinear system represented by a polynomial series. If the linear term in (3.13) ($k=0$) leads to the maximum $M = M_1$, we only need $M+K+2$ linear filters where $K = \max\left\{M_3, M_5, \ldots, M_{2\lceil N/2\rceil-1}\right\}$, because the linear terms in (3.13) do not incorporate the signals $\tilde{u}_i(t)$.

### 3.2.1 Chebyshev Approximation

In this section we focus on the frequency-domain Volterra kernel approximation with a particular set of orthogonal polynomials which allows us to develop a practical model for a given nonlinear system, e.g., an RF PA. For this reason, we consider the complete set of Chebyshev polynomials [35], which are linearly transformed to be orthogonal over the desired frequency-domain interval of $[-B, B]$ with respect to the weighting function

$p(\omega) = \frac{1}{\sqrt{1-(\omega/B)^2}}$, because they have a simple representation [35, 72]. It is important to note that any kind of orthogonal polynomials which are orthogonal on a finite domain (e.g., Legendre polynomials) can be used for the approximation of frequency-domain Volterra kernels $\tilde{H}_{2k+1}(\omega_1, \ldots, \omega_{2k+1})$ as we have shown in the previous section. The squared norm $\lambda_n$ in (3.2) of the transformed Chebyshev polynomial is $\pi B$ for $n = 0$ and $\frac{\pi B}{2}$ for $n \neq 0$. From the recursive definition of the Chebyshev polynomials, $C_0(\omega) = 1$, $C_1(\omega) = \frac{\omega}{B}$, and $C_{n+1}(\omega) = \frac{2\omega}{B} C_n(\omega) - C_{n-1}(\omega)$, the Chebyshev polynomials are expressed in a closed form for $i > 0$ by

$$C_i(\omega) = \frac{i}{2} \sum_{k=0}^{\lfloor i/2 \rfloor} \frac{(-1)^k}{i-k} \binom{i-k}{k} \left(\frac{2\,\omega}{B}\right)^{i-2k}. \tag{3.16}$$

The time-domain signals $\tilde{w}_i(t)$ and $\tilde{u}_i(t)$ in (3.12) are expressed with $T_i(\omega) \rightarrow C_i(\omega)$ and (3.16) by

$$\tilde{w}_i(t) = \frac{i}{2} \sum_{k=0}^{\lfloor i/2 \rfloor} \frac{(-1)^k}{i-k} \binom{i-k}{k} \left(\frac{2}{j\,B}\right)^{i-2k} \frac{d^{(i-2k)}\tilde{x}(t)}{dt^{(i-2k)}} \tag{3.17}$$

with the complex baseband input signal $\tilde{x}(t)$ and

$$\tilde{u}_i(t) = \frac{i}{2} \sum_{k=0}^{\lfloor i/2 \rfloor} \frac{(-1)^k}{i-k} \binom{i-k}{k} \left(\frac{2}{j\,B}\right)^{i-2k} \frac{d^{(i-2k)}\tilde{x}^*(t)}{dt^{(i-2k)}} \tag{3.18}$$

with the conjugate of the input signal $\tilde{x}^*(t)$. The quantity $(i-2k)$ within the superscript parentheses of the time-domain signals denotes the order of the derivative. All these orders within the series in (3.17) and (3.18) are even, if $i$ is even, and odd, if $i$ is odd because the term $2k$ is always even. For the even orders, it does not matter whether the sign of the imaginary unit $j$ in (3.17) and (3.18) is positive or negative and the constant values within the series always result in real quantities and, therefore, the signals $\tilde{u}_i(t)$ can be obtained from the signals $\tilde{w}_i(t)$ by a simple conjugation. If the order $i$ is odd, the constants within the series in (3.17) and (3.18) are purely imaginary and, therefore, the signals $\tilde{u}_i(t)$ can be obtained from a simple inversion of (the real part of) $\tilde{w}_i(t)$. For this reason the signals $\tilde{u}_i(t)$ in (3.18) can be expressed for even and odd orders of $i$ by

$$\tilde{u}_i(t) = (-1)^i\, \tilde{w}_i^*(t). \tag{3.19}$$

Figure 3.4 depicts the RF PA model of Fig. 3.3, where the general orthogonal polynomials $T_i(\omega)$ are replaced by the particular set of Chebyshev polynomials $C_i(\omega)$. Because of the equality (3.19), the linear filters in Fig. 3.3, which generate the signals $\tilde{u}_i(t)$ from $\tilde{x}^*(t)$, can be replaced by $M+1$ (if $M \neq M_1$) or $K+1$ (if $M = M_1$) complex conjugate operators and constant multipliers which can be more easily implemented than filters.

### 3.2.2 Narrowband Modeling

In the last section, we have modeled an RF PA in the complex baseband domain by expanding the frequency-domain Volterra kernels with Chebyshev polynomials. This concept

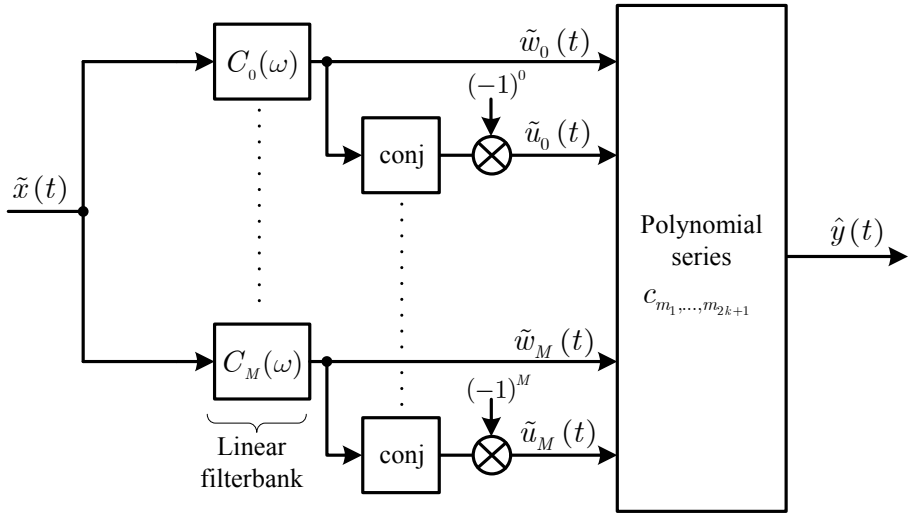


**Figure 3.4:** Complex RF power amplifier model with Chebyshev Volterra kernel approximation in the frequency domain. The model is composed of a bank of linear filters (generalized differentiators), complex conjugate operators, sign multipliers and a static nonlinearity represented by a polynomial series.

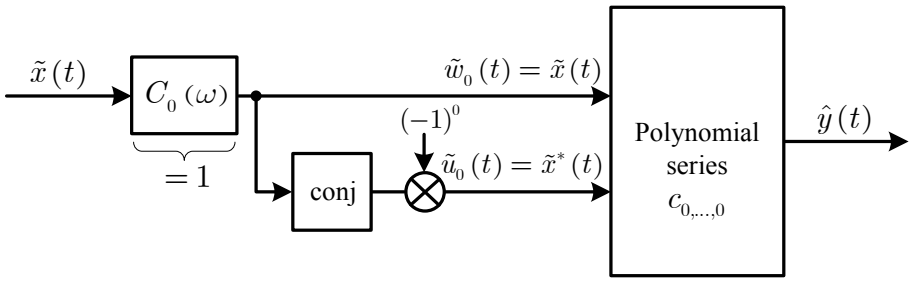


**Figure 3.5:** Complex RF power amplifier baseband model with zero-order Chebyshev Volterra kernel approximation in the frequency-domain for ultra-narrowband applications. The model is quasi-memoryless and can be described by an AM/AM-conversion and an AM/PM-conversion.

results in a complex baseband model which is composed of a cascade of a linear filterbank, complex conjugate operators with sign multipliers and a static nonlinearity which is represented by a polynomial series as depicted in Fig. 3.4.

If the passband-signal $x(t)$ becomes ultra-narrowband (see Ch. 2), the complex baseband model in Fig. 3.4 is reduced to a simple system which incorporates solely two static nonlinearities, described by the AM/AM- and AM/PM-conversion (see Ch. 2).

Because of the ultra-narrowband assumption, the approximation order $M_{2k+1}$ in (3.1) can be set to zero for all $k$'s and, therefore, the approximate $(2k+1)$-dimensional frequency-domain Volterra kernels $\hat{H}_{2k+1}(\omega_1, \ldots, \omega_{2k+1})$ in (3.1) (with $T_i(\omega) \rightarrow C_i(\omega)$) can be simplified with $C_0(\omega_i) = 1$ to $\hat{H}_{2k+1}(\omega_1, \ldots, \omega_{2k+1}) = c_{0,\ldots,0}$. The optimum complex parameters $c_{o(0,\ldots,0)}$ are given with (3.2), (3.5) and $\tilde{H}_{2k+1}(\omega_1 \ldots, \omega_{2k+1}) \rightarrow \tilde{H}_{2k+1}(0, \ldots, 0)$ (because the bandwidth $B$ tends to zero) by

$$\begin{aligned} c_{o(0,\ldots,0)} &= \frac{\tilde{H}_{2k+1}(0,\ldots,0)}{\lambda_0^{2k+1}} \int_{-B}^{B} \cdots \int_{-B}^{B} p(\omega_1) \cdots p(\omega_{2k+1})\, d\omega_1 \cdots d\omega_{2k+1} \\ &= \tilde{H}_{2k+1}(0,\ldots,0). \end{aligned} \tag{3.20}$$

The $(2k+1)$th order time-domain output signal $\hat{y}_{2k+1}(t)$ in (3.11) is given with (3.20) and the approximation order $M_{2k+1} = 0$, for $0 \leq k \leq \lceil N/2 \rceil - 1$ by

$$\begin{aligned} \hat{y}(t) &= \tilde{H}_{2k+1}(0,\ldots,0)\, \tilde{w}_0(t)^{k+1}\, \tilde{u}_0(t)^k \\ &= \tilde{H}_{2k+1}(0,\ldots,0)\, |\tilde{x}(t)|^{2k}\, \tilde{x}(t). \end{aligned} \tag{3.21}$$

The output signal $\hat{y}(t)$ in (3.13), which is obtained with (3.21) by a summation over all $k$'s

$$\begin{aligned} \hat{y}(t) &= \sum_{k=0}^{\lceil N/2 \rceil - 1} \tilde{H}_{2k+1}(0,\ldots,0)\, \tilde{w}_0(t)^{k+1}\, \tilde{u}_0(t)^k \\ &= \sum_{k=0}^{\lceil N/2 \rceil - 1} \tilde{H}_{2k+1}(0,\ldots,0)\, |\tilde{x}(t)|^{2k}\, \tilde{x}(t), \end{aligned} \tag{3.22}$$

is identical to the quasi-memoryless PA model in (2.50), and can therefore be described by the AM/AM-conversion and the AM/PM-conversion as we have shown in Chap. 2. Fig. 3.5 depicts the RF PA model from Fig. 3.4 with an approximation order $M_{2k+1} = 0$ for ultra-narrowband applications. Because the zero-order Chebyshev polynomial $C_0(\omega) = 1$, only the signals $\tilde{w}_i(t) = \tilde{x}(t)$ and $\tilde{u}_i(t) = \tilde{x}^*(t)$ are used to build the time-domain output signal $\hat{y}(t)$ in (3.22) within the polynomial series block in Fig. 3.5.

## 3.3 Baseband to Passband Transform

To calculate the time-domain passband Volterra model with the Chebyshev polynomial expanded frequency-domain Volterra kernels in Fig. 3.1, we use the relationship $y(t) =$

$\mathrm{Re}\{\hat{y}(t)\exp(j\omega_c t)\}$, which yields with (3.13), (3.11) and (3.19)

$$y(t) = \mathrm{Re}\left\{ \sum_{k=0}^{\lceil N/2\rceil-1} \sum_{m_1=0}^{M_{2k+1}} \cdots \sum_{m_{2k+1}=0}^{M_{2k+1}} c_{m_1,\ldots,m_{2k+1}} (-1)^{m_{k+2}+\cdots+m_{2k+1}} \right.$$
$$\left. \times \prod_{i=1}^{k+1} \tilde{w}_{m_i}(t) \prod_{i=k+2}^{2k+1} \tilde{w}^*_{m_i}(t)\exp(j\omega_c t) \right\}. \tag{3.23}$$

To express the passband output signal $y(t)$ in (3.23), with the passband input signals

$$\begin{aligned} w_{m_i}(t) &= \mathrm{Re}\left\{\tilde{w}_{m_i}(t)\exp(j\omega_c t)\right\} \\ &= |\tilde{w}_{m_i}(t)|\cos\left(\omega_c t + \psi_{m_i}(t)\right) \end{aligned} \tag{3.24}$$

of the corresponding baseband input signals of the polynomial series block in Fig. 3.4 and Fig. 3.5, we use the identity $\exp(j\omega_c t) = (\exp(j\omega_c t))^{k+1}\,(\exp(-j\omega_c t))^k$, which yields

$$y(t) = \mathrm{Re}\left\{ \sum_{k=0}^{\lceil N/2\rceil-1} \sum_{m_1=0}^{M_{2k+1}} \cdots \sum_{m_{2k+1}=0}^{M_{2k+1}} c_{m_1,\ldots,m_{2k+1}} (-1)^{m_{k+2}+\cdots+m_{2k+1}} \right.$$
$$\left. \times \prod_{i=1}^{k+1} \Big(\tilde{w}_{m_i}(t)\exp(j\omega_c t)\Big) \prod_{i=k+2}^{2k+1} \Big(\tilde{w}^*_{m_i}(t)\exp(-j\omega_c t)\Big) \right\}, \tag{3.25}$$

where the phase in (3.24) is defined by $\psi_{m_i}(t) = \arg\{\tilde{w}_{m_i}(t)\}$. The product terms within the braces of (3.25) can be expanded with $\tilde{w}_{m_i}(t) = |\tilde{w}_{m_i}(t)|\exp(j\psi_{m_i}(t))$ and the well known Euler formula $\exp(\pm j\theta) = \cos(\theta) \pm j\sin(\theta)$ by

$$\prod_{i=1}^{k+1} \Big(\tilde{w}_{m_i}(t)\exp(j\omega_c t)\Big) \prod_{i=k+2}^{2k+1} \Big(\tilde{w}^*_{m_i}(t)\exp(-j\omega_c t)\Big) = \sum_{l_1=0}^{1} \cdots \sum_{l_{2k+1}=0}^{1}$$
$$\times (-1)^{l_{k+2}+\cdots+l_{2k+1}}\, j^{\,l_1+\cdots+l_{2k+1}} \prod_{i=1}^{2k+1} |\tilde{w}_{m_i}(t)|\, f_{l_i}(t) \tag{3.26}$$

where the phase-modulated carrier $f_{l_i}(t)$ in (3.26) is expressed by

$$f_{l_i}(t) = \begin{cases} \cos\big(\omega_c t + \psi_{m_i}(t)\big) & \text{if } l_i = 0 \\ \sin\big(\omega_c t + \psi_{m_i}(t)\big) & \text{if } l_i = 1 \end{cases} \tag{3.27}$$

Therefore the real passband signals $|\tilde{w}_{m_i}(t)|\, f_{l_i}(t)$ in (3.26) can be expressed with (3.24) and (3.27) by (see Appendix A)

$$|\tilde{w}_{m_i}(t)|\, f_{l_i}(t) = \begin{cases} w_{m_i}(t) & \text{if } l_i = 0 \\ \mathcal{H}\{w_{m_i}(t)\} & \text{if } l_i = 1 \end{cases}. \tag{3.28}$$

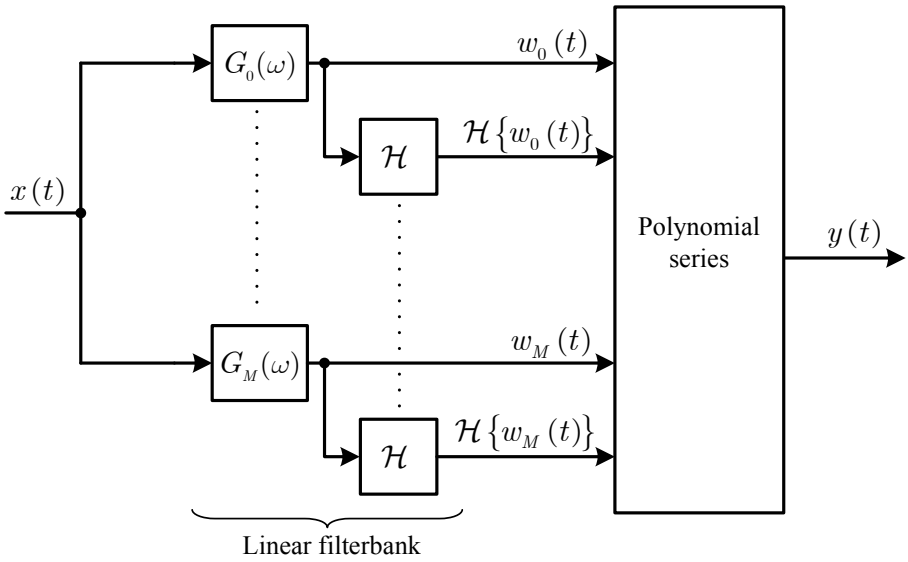


**Figure 3.6:** Passband RF power amplifier model with approximated frequency-domain Volterra kernels. The model is composed of a bank of linear passband filters (generalized differentiators and Hilbert transformers) and a static nonlinearity which is represented by a polynomial series.

The real passband output signal $y(t)$ in (3.25) can be expressed with (3.26) by the polynomial series

$$\begin{aligned} y(t) = \sum_{k=0}^{\lceil N/2\rceil-1} \sum_{m_1=0}^{M_{2k+1}} \cdots \sum_{m_{2k+1}=0}^{M_{2k+1}} \sum_{l_1=0}^{1} \cdots \sum_{l_{2k+1}=0}^{1} \mathrm{Re}\Big\{ j^{\,l_1+\cdots+l_{2k+1}} \mathrm{Re}\left\{c_{m_1,\ldots,m_{2k+1}}\right\} \\ + j^{\,l_1+\cdots+l_{2k+1}+1} \mathrm{Im}\left\{c_{m_1,\ldots,m_{2k+1}}\right\}\Big\} (-1)^{\,l_{k+2}+\cdots+l_{2k+1}+m_{k+2}+\cdots+m_{2k+1}} \\ \times \prod_{i=1}^{2k+1} |\tilde{w}_{m_i}(t)|\, f_{l_i}(t), \end{aligned} \tag{3.29}$$

which results in the passband model shown in Fig. 3.6. While in the baseband model of Fig. 3.4 the input signals of the polynomial series block are the output signals of the baseband differentiators $C_i(\omega)$ and the conjugate operators, the input signals of the polynomial series block in Fig. 3.6 are the corresponding passband signals and their Hilbert transforms. To express the passband signals $w_{m_i}(t)$ and $\mathcal{H}\{w_{m_i}(t)\}$ in (3.29) as a function of the passband input signal $x(t)$, we constrain the frequency responses of the baseband filters $C_i(\omega)$ in Fig. 3.4 and Fig. 3.5 to

$$C_i'(\omega) = \begin{cases} C_i(\omega) & -B \le \omega \le B \\ 0 & \text{otherwise} \end{cases}, \tag{3.30}$$

which is important to ensure that the frequency-shifted baseband filters $C_i'(\omega-\omega_c)$ are analytical ($C_i'(\omega-\omega_c) = 0$ for $\omega < 0$) [29, 49]. Therefore with (3.24), we can use the

following identity

$$\begin{aligned} w_{m_i}(t) &= \mathrm{Re}\left\{(\tilde{x}(t) \star c'_{m_i}(t))\exp(j\omega_c t)\right\} \\ &= \underbrace{\mathrm{Re}\left\{\tilde{x}(t)\exp(j\omega_c t)\right\}}_{x(t)} \star \underbrace{2\mathrm{Re}\left\{c'_{m_i}(t)\exp(j\omega_c t)\right\}}_{\text{Bandpass-filter}}, \end{aligned} \tag{3.31}$$

to express the passband filter $G_i(\omega)$ in Fig. 3.6 with the baseband filter $C_i(\omega)$ in (3.30), where $c'_i(t) = \mathcal{F}^{-1}\left\{C'_i(\omega)\right\}$, which yields

$$\begin{aligned} G_i(\omega) &= \mathcal{F}\left\{2\mathrm{Re}\left\{c'_i(t)\exp(j\omega_c t)\right\}\right\} \\ &= C'_i(\omega-\omega_c) + C'_i(-\omega-\omega_c). \end{aligned} \tag{3.32}$$

It is important to note that the spectral components of the output signal $y(t)$ in Fig. 3.6 are only located around the carrier frequency $\pm\omega_c$. The spectral components around the multiples of the carrier frequency will be canceled by the $2^{2k+1}$ contributions of the inner sums of the polynomial series in (3.29) without any explicit 1st-zonal filtering.

### 3.3.1 Narrowband Modeling

If the frequency-domain Volterra kernels $\tilde{H}_{2k+1}(\omega_1,\ldots,\omega_{2k+1})$ are constant over the input signal bandwidth of $\pm B$ or the input-signal bandwidth tends to zero, the nonlinear passband model in (3.29) (Fig. 3.6) can be simplified by setting the approximation order of the multivariate Chebyshev polynomials $M_{2k+1} = 0$, for $0 \le k \le \lceil N/2\rceil - 1$. Therefore (3.29) combined with (3.17) ($\tilde{w}_0(t) = \tilde{x}(t)$) reduces to

$$\begin{aligned} y(t) = \sum_{k=0}^{\lceil N/2\rceil-1} \sum_{l_1=0}^{1} \cdots \sum_{l_{2k+1}=0}^{1} \mathrm{Re}\Big\{ & j^{\,l_1+\cdots+l_{2k+1}} \mathrm{Re}\left\{c_{0,\ldots,0}\right\} \\ & + j^{\,l_1+\cdots+l_{2k+1}+1} \mathrm{Im}\left\{c_{0,\ldots,0}\right\}\Big\} (-1)^{\,l_{k+2}+\cdots+l_{2k+1}} \prod_{i=1}^{2k+1} |\tilde{x}(t)|\, f_{l_i}(t). \end{aligned} \tag{3.33}$$

Because the product in (3.33) is solely composed of the passband signals $x(t)$ and $\mathcal{H}\{x(t)\}$, the narrowband model can be simplified to create the model depicted in Fig. 3.7.

To see the equivalence of the narrowband model in (3.33) and the quasi-memoryless model in Fig. 2.3, we rewrite (3.33) with (3.26) in the following form

$$\begin{aligned} y(t) = & \sum_{k=0}^{\lceil N/2\rceil-1} \mathrm{Re}\left\{c_{0,\ldots,0}\right\} |\tilde{x}(t)|^{2k+1} \cos\big(\omega_c t + \psi_0(t)\big) \\ & - \sum_{k=0}^{\lceil N/2\rceil-1} \mathrm{Im}\left\{c_{0,\ldots,0}\right\} |\tilde{x}(t)|^{2k+1} \sin\big(\omega_c t + \psi_0(t)\big), \end{aligned} \tag{3.34}$$

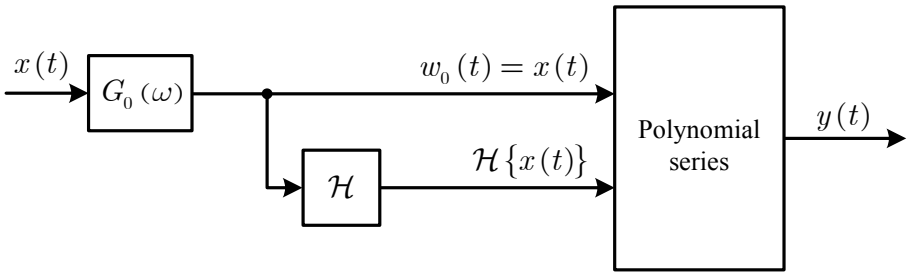


**Figure 3.7:** RF power amplifier passband model with zero-order Chebyshev Volterra kernel approximation in the frequency domain for ultra-narrowband applications. This passband model without any explicit 1st-zonal filtering is equivalent to the quasi-memoryless model in Fig. 2.3 and achieves implicit 1st-zonal filtering.

which underlines the fact that the output signal spectra are solely located around the carrier frequency $\pm\omega_c$. To introduce the real passband signals $x(t)$ and $\mathcal{H}\{x(t)\}$ in (3.34), we compute the $(2k+1)$th power from the magnitude and the phase-modulated carriers in (3.34), which yields $[|\tilde{x}(t)|\cos(\omega_c t+\psi_0(t))]^{2k+1}$ and $[|\tilde{x}(t)|\sin(\omega_c t+\psi_0(t))]^{2k+1}$, where

$$\cos^{2k+1}\big(\omega_c t+\psi_0(t)\big) = \frac{1}{4^k}\sum_{n=0}^{k}\binom{2k+1}{n}\cos\big[(2k+1-2n)\,\omega_c t + (2k+1-2n)\,\psi_0(t)\big] \tag{3.35}$$

and

$$\sin^{2k+1}\big(\omega_c t+\psi_0(t)\big) = \frac{(-1)^k}{4^k}\sum_{n=0}^{k}(-1)^n\binom{2k+1}{n}\sin\big[(2k+1-2n)\,\omega_c t + (2k+1-2n)\,\psi_0(t)\big]. \tag{3.36}$$

From (3.35) and (3.36), we notice that the $(2k+1)$th power computation of the passband signals $x(t)$ and $\mathcal{H}\{x(t)\}$ generates additional spectral components which are located around the odd multiples of the carrier frequency. If we suppress these spectral components with a linear 1st-zonal filter **F** as depicted in Fig. 2.4, the output signal $y(t)$ in (3.34) could be expressed with (3.35) and (3.36) by

$$y(t) = \mathbf{F}\left[\sum_{k=0}^{\lceil N/2\rceil-1} 4^k\, 1/\binom{2k+1}{k}\,\mathrm{Re}\{c_{0,\ldots,0}\}\,\big(x(t)\big)^{2k+1} - \sum_{k=0}^{\lceil N/2\rceil-1} 4^k\, 1/\binom{2k+1}{k}\,\mathrm{Im}\{c_{0,\ldots,0}\}\,\big(\mathcal{H}\{x(t)\}\big)^{2k+1}\right] \tag{3.37}$$

which represents a quasi-memoryless model as we have shown in (3.37). The constant terms $4^k\, 1/\binom{2k+1}{k}$ in (3.37) compensate the scaling of the fundamental carrier frequency $\omega_c$ in (3.35) and (3.36) for $n=k$.

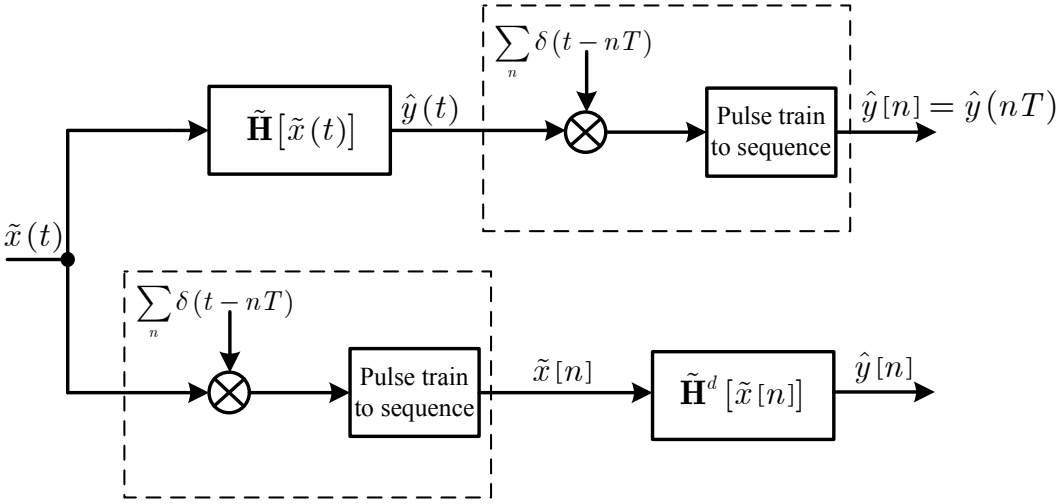


**Figure 3.8:** Block diagram which shows the equivalence of a continuous-time nonlinear system $\tilde{\mathbf{H}}[\tilde{x}(t)]$ and a discrete-time nonlinear system $\tilde{\mathbf{H}}^d[\tilde{x}[n]]$ if the input signal $\tilde{x}(t)$ is band-limited to $B \leq \pi/(NT)$.

## 3.4 Discrete-Time Modeling

In the preceding sections we have developed continuous-time baseband models for nonlinear RF power amplifiers. In this section, we focus on the discrete-time counterpart, which is of fundamental importance for the discrete-time implementation of a nonlinear model, e.g., digital predistortion, and for numerical simulation purposes.

To develop such a nonlinear discrete-time model, we sample the continuous-time output signal $\hat{y}(t)$ of the nonlinear system $\tilde{\mathbf{H}}$ in Fig. 3.8 with a sampling period of $T \leq \pi/(NB)$, where we have assumed that the Fourier transform of the baseband output signal $\hat{Y}^c(\omega) = 0$ for $|\omega| > NB$. The spectrum of the continuous-time sampled output signal is amplitude weighted with $1/T$ and periodically extended with $(2\pi)/T$ [45, 46]. After a conversion from the continuous-time impulse train to the discrete-time sequence $\hat{y}[n] = \hat{y}(nT)$, the spectrum will be normalized regarding the frequency-axis and therefore it will be periodic with $2\pi$. To generate the discrete-time signal $\hat{y}[n]$ in Fig. 3.8 directly in the discrete-time domain, we sample the continuous-time baseband input signal $\tilde{x}(t)$ and feed the resulting sequence $\tilde{x}[n]$ into the discrete-time model, which is described by the nonlinear operator $\tilde{\mathbf{H}}^d$.

### 3.4.1 Structure Derivation

The two systems in Fig. 3.8 produce the same discrete-time output signal $\hat{y}[n]$, if the discrete-time domain Volterra kernels are identical, e.g.,

$$\tilde{H}^d_{2k+1}(\exp(j\Omega_1), \ldots, \exp(j\Omega_{2k+1})) \equiv \tilde{H}_{2k+1}(j\Omega_1/T, \ldots, j\Omega_{2k+1}/T), \quad (3.38)$$

for $-BT \leq \Omega_i \leq BT$, where $\Omega_i = \omega_i T$ denotes the normalized frequencies (see Fig. 3.9 for $\tilde{\mathbf{H}}[\tilde{x}(t)] = (d\tilde{x}(t)/dt)^2$). The equality of the frequency-domain Volterra kernels over the normalized input signal bandwidth is sufficient because the output signal spectrum $\hat{Y}^c(\omega)$ is purely determined by the multi-dimensional Volterra kernels over the input signal bandwidth as we have shown in Chap. 2.

Because the continuous-time model in Fig. 3.4 is composed of a cascade of a linear filterbank and a multi-variate static nonlinear system, the discrete-time counterpart of Fig. 3.4 is obtained by replacing the continuous-time filters $C_i(\omega)$ in Fig. 3.4 by the corresponding discrete-time filters $C_i^d(\exp(j\Omega))$. The frequency responses of the discrete-time filters are given with (3.16) and (3.38) by

$$C_i^d(\exp(j\Omega)) = \frac{i}{2} \sum_{k=0}^{\lfloor i/2 \rfloor} \frac{(-1)^k}{i-k} \binom{i-k}{k} \left(\frac{2}{jB}\right)^{i-2k} \left(\frac{j\Omega}{T}\right)^{i-2k}. \tag{3.39}$$

which have to be periodically extended with $2\pi$ in the normalized frequency $\Omega$ after appropriate band limitation. The expression $j\Omega/T$ in (3.39) represents the frequency-response of a linear differentiator as depicted in Fig. 3.9 (curve (h) after periodic extension). The frequency-domain output signals of the linear filters in (3.39) are given by

$$\tilde{W}_i^d(\exp(j\Omega)) = C_i^d(\exp(j\Omega))\tilde{X}^d(\exp(j\Omega)) \tag{3.40}$$

where $\tilde{X}^d(\exp(j\Omega))$ denotes the discrete Fourier transform of the sampled baseband input signal $\tilde{x}[n] = \tilde{x}(nT)$. The discrete-time output signals of the generalized differentiators are given with (3.39), (3.40) and the convolution property by

$$\tilde{w}_i[n] = \frac{i}{2} \sum_{k=0}^{\lfloor i/2 \rfloor} \frac{(-1)^k}{i-k} \binom{i-k}{k} \left(\frac{2}{jB}\right)^{i-2k} \tilde{x}[n] \star \underbrace{h_D[n] \star \ldots \star h_D[n]}_{(i-2k)\times}. \tag{3.41}$$

where $h_D[n] = \mathcal{F}^{-1}(j\Omega/T)$ denotes the impulse response of an ideal (band-limited) differentiator. Because an ideal band-limited differentiator can not be implemented by using a causal discrete-time system [45, 48], we approximate the frequency-response $j\Omega/T$ over the normalized frequency-range of $-BT \leq \Omega \leq BT$. This leads to a causal discrete-time differentiator whose magnitude-response (FIR-filter with 5 parameters) is shown in Fig. 3.10. The number of parameters which are required to guaranty a maximum approximation error strongly depends on the highest order of the nonlinearity $N$. If $N$ is large, the normalized input signal bandwidth $BT = \pi/N$ becomes small (approximation range of the differentiator), and therefore, the number of the required FIR-filter parameters becomes low.

The discrete-time signals

$$\tilde{u}_i[n] = (-1)^i \, \tilde{w}_i^*[n], \tag{3.42}$$

are obtained from (3.19) by replacing the continuous-time signals $w_i(t)$ by the corresponding discrete-time signals $w_i[n]$ of (3.41). With (3.41) and (3.42), the discrete-time counter-

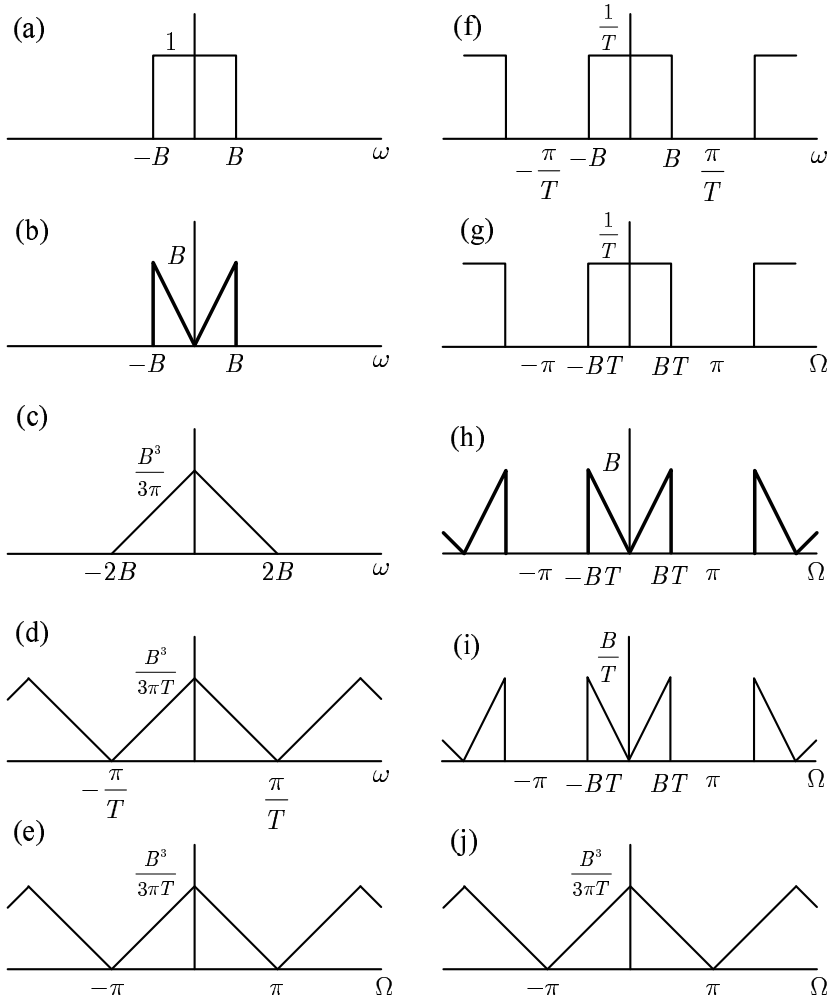


**Figure 3.9:** Frequency-domain signals generated by the sampling process of the nonlinear system $\tilde{\mathbf{H}}[\tilde{x}(t)] = (d\tilde{x}(t)/dt)^2$. (a) Band-limited input signal $|\bar{X}(\omega)|$ , (b) Frequency response $H(j\omega)$ of a band-limited linear differentiator $d\tilde{x}(t)/dt$, (c) $1/(2\pi)H(j\omega) \star H(j\omega)$ (simplified shape), (d) Periodically extended spectrum of (c) caused by the sampling with a continuous-time pulse train, (e) Frequency-axis normalization caused by the pulse-train to discrete-time sequence conversion, (f) Periodically extended spectrum of (a) caused by the sampling with a continuous-time pulse train, (g) Frequency-axis normalization caused by the pulse-train to discrete-time sequence conversion, (h) Frequency response of a band-limited discrete-time differentiator $H^d(\exp(j\Omega))$, (i) Product of (g) and (h), (j) Convolution of (i) with itself leads to the identical output signal as in (e) if $H^d(\exp(j\Omega)) \equiv H(j\Omega/T)$ for $-BT \leq \Omega \leq BT$.

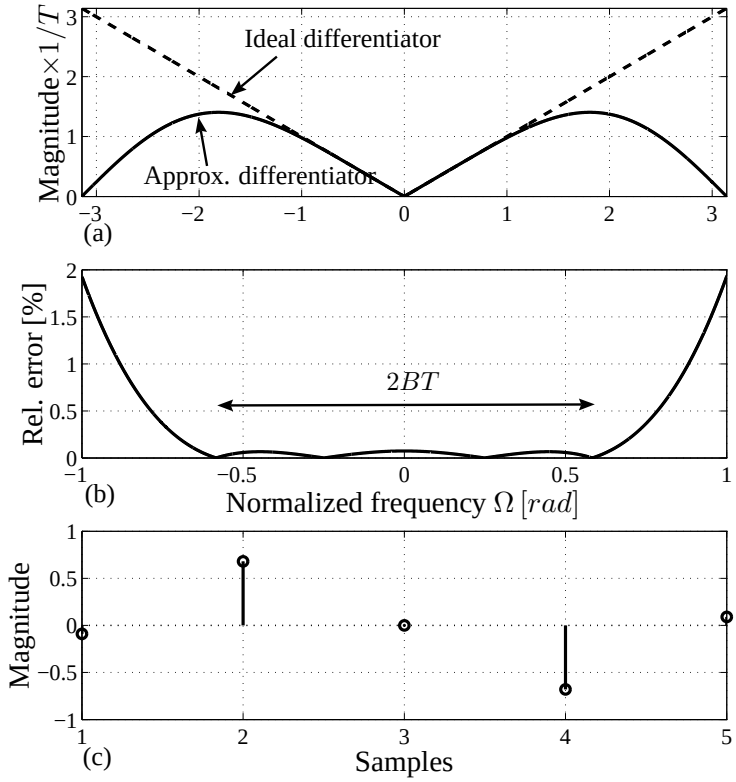


**Figure 3.10:** Band-limited discrete-time differentiator, (a) Magnitude response of an ideal and an approximated linear differentiator over $[-\pi, \pi]$, (b) Rel. error of the magnitude response within the input signal bandwidth $[-BT, BT]$, (c) Impulse response of the approximated differentiator (FIR-filter with $5$ parameters.)

part of the continuous-time model in Fig. 3.4 is described by

$$\hat{y}_{2k+1}[n] = \sum_{m_1=0}^{M_{2k+1}} \cdots \sum_{m_{k+1}=m_k}^{M_{2k+1}} \sum_{m_{k+2}=0}^{M_{2k+1}} \cdots \sum_{m_{2k+1}=m_{2k}}^{M_{2k+1}} c_{m_1,\ldots,m_{2k+1}} \tilde{w}_{m_1}[n] \cdots \tilde{w}_{m_{k+1}}[n] \times \tilde{u}_{m_{k+2}}[n] \cdots \tilde{u}_{m_{2k+1}}[n], \tag{3.43}$$

and

$$\hat{y}[n] = \sum_{k=0}^{\lceil N/2 \rceil - 1} \hat{y}_{2k+1}[n], \tag{3.44}$$

which is shown in Fig. 3.11.

The indices $m_i$ in (3.43) do not all start with zeros as in (3.11), because in (3.43), we only consider the $\binom{M_{2k+1}+1+k}{k+1} \times \binom{M_{2k+1}+k}{k}$ different permutations of the $2k+1$

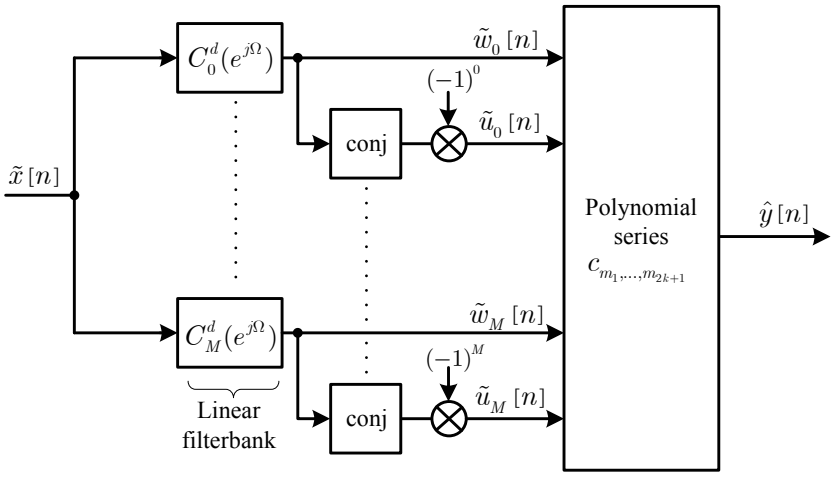


**Figure 3.11:** Discrete-time complex RF power amplifier model with approximated frequency-domain Volterra kernels. The model is composed of a bank of linear filters (generalized differentiators) and a static nonlinearity which generates a polynomial series.

products of the signals $\tilde{w}_{m_i}[n]$ and $\tilde{u}_{m_i}[n]$. This is important to save computational complexity on the one hand, and on the other hand we thereby avoid to use redundant information, which generally leads to numerical problems if we estimate the unknown parameters $c_{m_1,\ldots,m_{2k+1}}$ with least-squares methods [9, 25].

### 3.4.2 Parameter Estimation

The unknown parameters $c_{m_1,\ldots,m_{2k+1}}$ in (3.43) can be computed from the discrete-time counterpart of (3.5) only if the frequency-domain kernels are known. As, in general, they are unknown, we have to estimate these parameters. As the relationships in (3.43) and (3.44) are linear in the parameters we can formulate a classical linear least-squares problem [26, 40]. For this we rewrite (3.44) in vector form as

$$\hat{y}[n] = \mathbf{c}^H \tilde{\mathbf{w}}[n] \tag{3.45}$$

where the vectors

$$\mathbf{c}^H = \Big[c_0, \ldots, c_{M_1}, c_{0,0,0}, \ldots, c_{M_3,M_3,M_3}, c_{0,\ldots,0}, \ldots, \underbrace{c_{M_{2\lceil N/2\rceil-1},\ldots,M_{2\lceil N/2\rceil-1}}}_{(2\lceil N/2\rceil-1)\times}\Big] \tag{3.46}$$

and

$$\begin{aligned}\tilde{\mathbf{w}}^H[n] = \Big[&\tilde{w}_0^*[n], \ldots, \tilde{w}_{M_1}^*[n], \tilde{w}_0^*[n]\tilde{w}_0^*[n]\tilde{u}_0^*[n], \ldots, \tilde{w}_{M_3}^*[n]\tilde{w}_{M_3}^*[n]\tilde{u}_{M_3}^*[n], \\ &\ldots, \underbrace{\tilde{w}_{M_{2\lceil N/2\rceil-1}}^*[n]\cdots\tilde{w}_{M_{2\lceil N/2\rceil-1}}^*[n]}_{\lceil N/2\rceil\times}\underbrace{\tilde{u}_{M_{2\lceil N/2\rceil-1}}^*[n]\cdots\tilde{u}_{M_{2\lceil N/2\rceil-1}}^*[n]}_{(\lceil N/2\rceil-1)\times}\Big]\end{aligned} \tag{3.47}$$

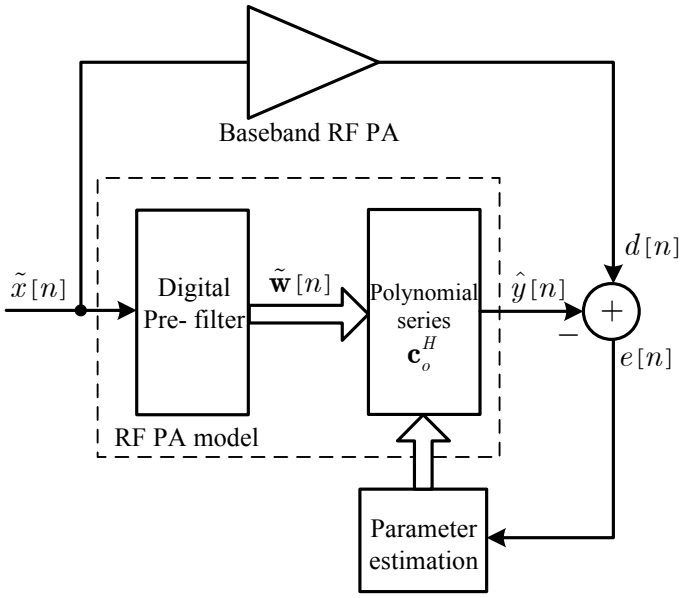


**Figure 3.12:** Parameter estimation setup for the discrete-time complex RF power amplifier model in Fig. 3.11. The error signal $e[n] = d[n] - \hat{y}[n]$ is used to perform an optimum parameter ($\mathbf{c}_o$) estimation for the RF PA model.

contain all $\sum_{k=0}^{\lceil N/2 \rceil - 1} \begin{pmatrix} M_{2k+1}+1+k \\ k+1 \end{pmatrix} \times \begin{pmatrix} M_{2k+1}+k \\ k \end{pmatrix}$ different permutations of the parameters and signals $\tilde{w}_i[n]$ and $\tilde{u}_i[n]$ in (3.43).

Now the error energy over the interval $[n_1, n_2]$

$$\mathcal{E} = \sum_{n=n_1}^{n_2} \left| e[n] \right|^2 \tag{3.48}$$

with $e[n] = d[n] - \hat{y}[n]$, where $d[n]$ is the discrete-time complex baseband output signal of the RF PA, is minimized to obtain the optimal parameter vector

$$\mathbf{c}_o = \left( \mathbf{A}^H \mathbf{A} \right)^{-1} \mathbf{A}^H \mathbf{d}. \tag{3.49}$$

The data matrix **A** and the data vector **d** in (3.49) are given by

$$\mathbf{A}^H = \left[ \tilde{\mathbf{w}}[n_1], \tilde{\mathbf{w}}[n_1+1], \ldots, \tilde{\mathbf{w}}[n_2] \right] \tag{3.50}$$

and

$$\mathbf{d}^H = \left[ d[n_1], d[n_1+1], \ldots, d[n_2] \right]. \tag{3.51}$$

Figure 3.12 depicts the parameter estimation setup for the discrete-time RF PA model with approximated frequency-domain Volterra kernels in Fig. 3.11. The output signal of the RF PA baseband system $d[n]$, and the output signal of the RF PA model $\hat{y}[n]$ (composed of the digital pre-filter and the polynomial series) is used to build the error signal $\tilde{e}[n]$, which is utilized to perform an optimum parameter estimation for the RF PA model.

## 3.5 Simulation Results

To validate the frequency-domain approximation developed in the last sections, we simulate an analytically tractable 3rd-order Wiener system which represents the RF PA. For of simplicity, we assume a complex linear frequency-domain kernel directly in the normalized frequency domain $\Omega$. The magnitude of this kernel $\tilde{H}_1^d(\exp(j\Omega))$ is depicted in Fig. 3.13 for $-\pi \leq \Omega \leq \pi$. The linear frequency-domain kernel is chosen in such a way, that the variation over the input signal bandwidth $2BT = 2\pi/N$, for $N = 5$ is moderate. Because the input signal signal bandwidth is 20% of the entire frequency range, it would be possible to consider nonlinearities up to the 5th-order, without aliasing effects.

Figure 3.14 depicts a complex baseband Wiener model of 3rd-order, which represents an RF PA in the baseband domain. The structure is chosen based on (2.32), (2.33) and with the assumption that the passband RF PA can be described by a Wiener system $\mathbf{H}[x(t)] = \int_0^\infty h_1(\tau)\, x(t-\tau)\, d\tau + [\int_0^\infty h_1(\tau)\, x(t-\tau)\, d\tau]^3$, where $h_1(t)$ represents a real linear passband kernel. The frequency response $\mathcal{F}\{h_1(t)\exp(-j\omega_c t)\}$, for $-\pi/T \leq \omega \leq \pi/T$, is identical to $\tilde{H}_1^d(\exp(j\Omega))$ in Fig. 3.13 for $-\pi \leq \Omega \leq \pi$. The frequency-domain baseband kernels in Fig. 3.14 are given by $\tilde{H}_1^d(\exp(j\Omega))$ and $\tilde{H}_3^d(\exp(j\,(\Omega_1+\Omega_2+\Omega_3))) = \tilde{H}_1^d(\exp(j\,\Omega_1))\,\tilde{H}_1^d(\exp(j\,\Omega_2))\,[\tilde{H}_1^d(exp\,(-j\,\Omega_3))]^*$. The 1st- and 2nd-order approximations ($M_1 = 1$, $M_1 = 2$) of the linear frequency-domain kernels are depicted in Fig. 3.13. These kernels are identical to the orthogonal polynomials which minimizes the integral square error in (3.6) within the normalized input signal bandwidth of $\pm\, B\, T$. Outside they are different because the frequency response magnitude of the approximated differentiator in Fig. 3.10 tends to zero. Therefore, the system model becomes noise insensitive because the noise power outside the signal band of $\pm\, B\, T$ will not monotonically increase with the model bandwidth. The 3rd-order kernel will be approximated with a 2nd-order Chebyshev polynomial ($M_3 = 2$) which is not explicitly depicted here. However we will see the full information about the kernel approximation in the error of the output spectra of the complex baseband Wiener system (baseband RF PA model) and the Volterra model with the approximated frequency-domain kernels (cf. Fig. 3.11) in Fig. 3.15. It is important to note that, although we only approximate the kernels within the input signal band, we obtain an accurate frequency response almost over the entire frequency range (see Ch. 2, Sec. 2.3.2). Due to the smooth frequency-domain kernels and the resulting low order approximation ($M_1, M_3 = 2$), the number of free parameters can be reduced from 120 for the complex basband Volterra model to 21 for the Volterra model with the approximated frequency-domain kernels.

## 3.6 Conclusion

Baseband modeling of nonlinear devices such as RF power amplifiers is of major concern in system level analysis. For this reason, we developed a novel efficient behavioral model which is based on a frequency-domain Volterra kernel approximation with multivariate orthogonal polynomials. The frequency-domain approximation results in a time-domain model which is composed of a bank of complex linear pre-filters and a static multi-

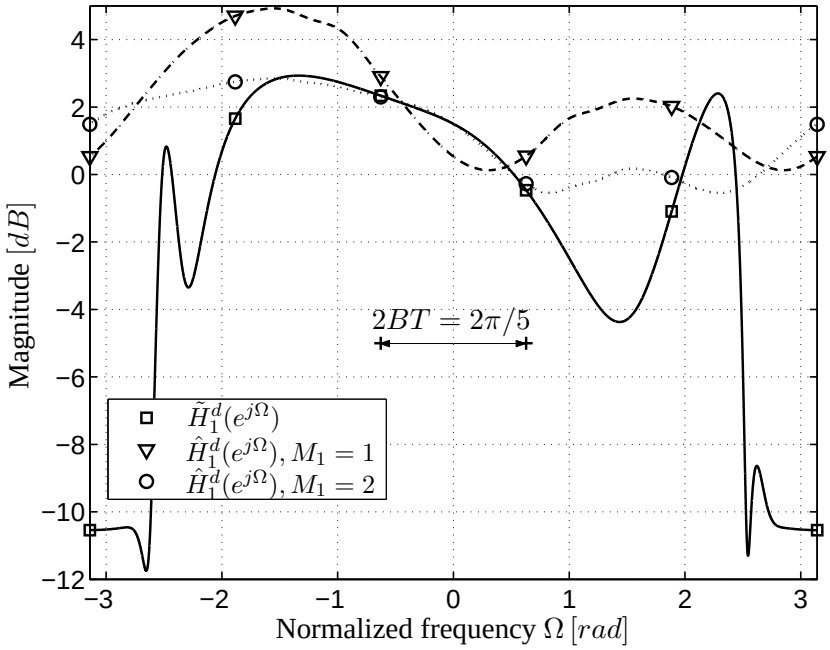


**Figure 3.13:** Linear frequency-domain kernel (magnitude) of the Wiener model in Fig. 3.14 and its 1st and 2nd-order approximations, the range of $2BT$ denotes the approximation region (input signal bandwidth), and $T$ denotes the sampling time.

variate polynomial series. The number of free parameters can be considerably reduced if the approximation order of the frequency-domain kernels can be kept low. This is generally reached, if the bandwidth of the excitation signal is much smaller than the bandwidth of the linear frequency-domain kernel (frequency response). We expect from the given simulation example an efficiency factor of approximately five in the number of required parameters. If the frequency-domain kernels are completely flat over the input signal bandwidth or the bandwidth of the input signal tends to zero, the approximation order becomes zero. This results in a well known quasi-memoryless model which is described by two different static nonlinear functions which are purely dependent on the input signal magnitude.

Furthermore we have developed a new passband representation of a complex nonlinear baseband system, whose frequency domain Volterra kernels are expanded with multi-variate orthogonal polynomials. This model does not incorporate an explicit 1st-zonal filter to pass only the spectral components of interest, which are located near the carrier frequency. This filtering is accomplished by combining the corresponding output signals of static nonlinear operators within a multi-variate polynomial function. If the frequency-domain kernels are completely flat over the input signal bandwidth or the bandwidth of the input signal tends to zero, the model reduces to a well known quasi-memoryless passband model as in the case of the baseband representation.

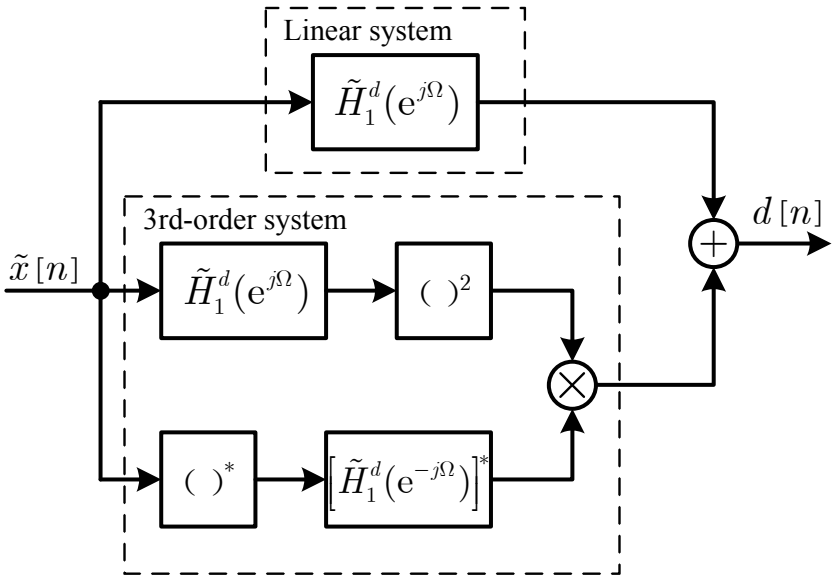


**Figure 3.14:** Complex baseband Wiener model of 3rd-order, which represents an RF PA in the baseband domain.

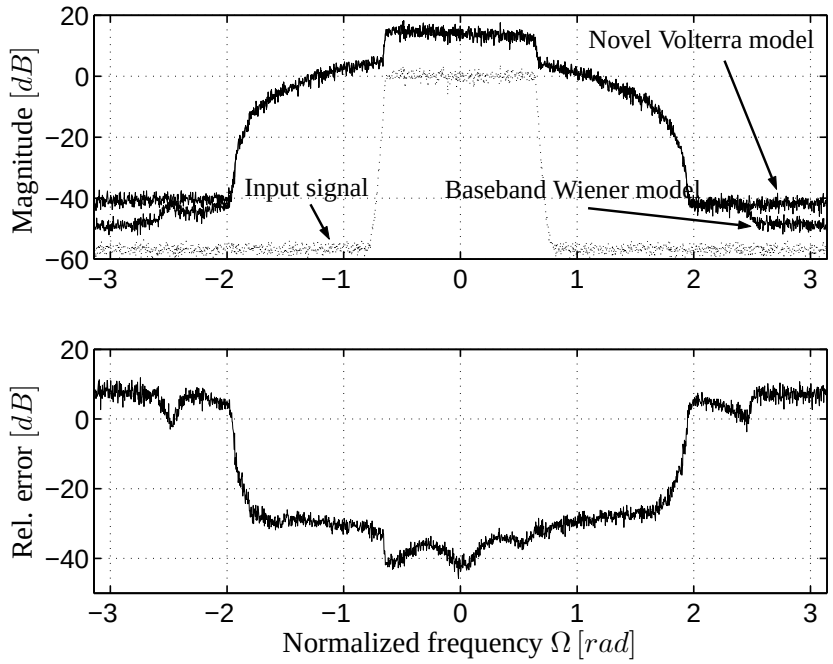


**Figure 3.15:** Frequency-domain output signals of the Volterra model with the approximated frequency-domain kernels in Fig. 3.11 and the complex baseband Wiener model (baseband RF PA) for a band-limited ($2BT$) white Gaussian noise excitation. The approximation order is $M_1 = M_3 = 2$.

# Chapter 4

# Volterra Kernel Interpolation for System Modeling and Predistortion Purposes

In this chapter we address the problem of nonlinear system identification and Volterra kernel interpolation for system modeling and digital predistortion purposes. In Sec. 4.1, we discuss the basic problems and requirements of nonlinear system identification with discrete-time Volterra models. In Sec. 4.2 we consider nonlinear system identification methods based on a sampling frequency which is at least twice the bandwidth of the output signal of the nonlinear baseband system. The major drawbacks of this identification method such as the high condition numbers, if we formulate a least squares problem, or the low convergence speed, if we use adaptive algorithms, and, of course, the demand for high sampling rate ADCs (corresponding to on the highest order of the baseband nonlinearity), motivate the investigation of more appropriate identification methods in Sec. 4.3. This schemes have the advantage that the sampling frequency only has to fulfill the Nyquist theorem regarding the input signal.

## 4.1 Introduction

In Ch. 2 and Ch. 3, we have shown that complex baseband modeling can be advantageously employed in system level simulations to predict the behavior of nonlinear passband systems such as RF PA's. With this concept, we can perform much faster simulations than with transistor-based models, which is important if we assess the performance (e.g., spectral transmission mask, bit error rate,...) of a whole communication transceiver. Nonlinear behavioral models can also be used to develop efficient(low number of parameters) structures to implement the approximate inverse [40] of a nonlinear passband system, which is important for linearization issues such as digital predistortion [32, 15, 16, 13, 33, 18, 20].

Because the behavior of nonlinear passband systems is generally unknown, we have to estimate it, e.g., from input and output signal measurements. Because the estimation is usually performed in the discrete-time domain [57], the sampling frequency of the down-converted input and output signals of the nonlinear passband system and the discrete-time nonlinear model plays a crucial role. It has be shown in [23, 76], that nonlinear system identification can usually be accomplished with a sampling frequency which is just twice the bandwidth of the input signal of the nonlinear system. This becomes clear if we consider the frequency-domain representation of Volterra systems of Ch. 2. If the input signal is band-limited to $\pm B$, than also the multi-dimensional output signal of the Volterra model

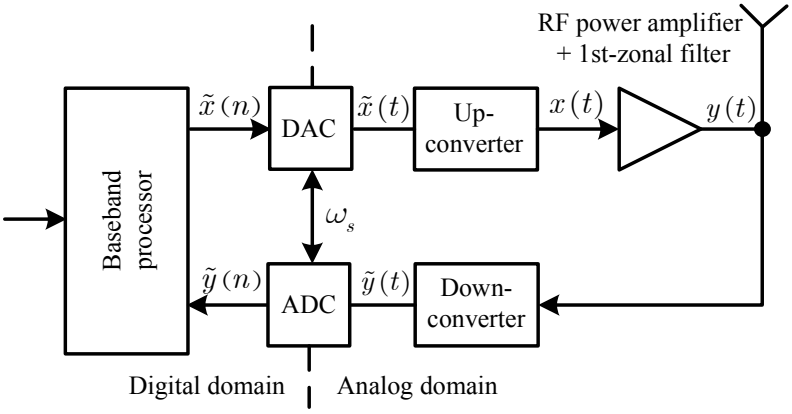


**Figure 4.1:** Block diagram of a wireless communication transmitter with a digital baseband processor for the identification and linearization (predistortion) of the RF power amplifier.

is band-limited, and therefore purely determined by the multi-dimensional Volterra kernels within $\pm B$ in each of the frequency dimensions.

The apparent advantage of this identification scheme is that we can use low sampling rate ADCs, which are cheaper and less power consuming as the high sampling rate counterparts which are needed in a Nyquist sampling identification scheme. Furthermore, because of the low sampling frequency which is just twice the bandwidth of the input signal, we achieve a persistent excitation of the discrete-time Volterra model. This leads to small condition numbers and, therefore, to accurate estimation results if we formulate a least squares problem, or to fast convergence speeds if we apply adaptive algorithms.

However in some applications as mentioned above, nonlinear discrete-time models which are able to generate the same spectral out-off-band components (spectral regrowth caused by the nonlinearity) as nonlinear continuous-time systems are required. For this reason it is important that the discrete-time nonlinear model is operated with a sampling frequency which fulfills the Nyquist theorem regarding the output signal of the RF PA baseband model. We will demonstrate that this can be accomplished by Volterra kernel interpolation with no additional computational costs.

Figure 4.1 depicts the block diagram of a wireless RF transmitter including the digital baseband processor. To identify the RF PA or its inverse from RF PA input and output signal measurements for predistortion purposes, we use a feedback path including a frequency down-converter and an ADC to provide the digital baseband processor with the output signal of the RF PA. Both the identification process of the RF PA baseband model or its inverse and the predistortion (see Ch. 5) is performed within the digital baseband processor.

If we build a complex baseband Volterra model for system modeling purposes to predict the generated distortion of the RF PA or to assess the transceiver performance, we can perform the identification process off-line with a mathematical software tool such as MATLAB® shown in Fig. 4.2.

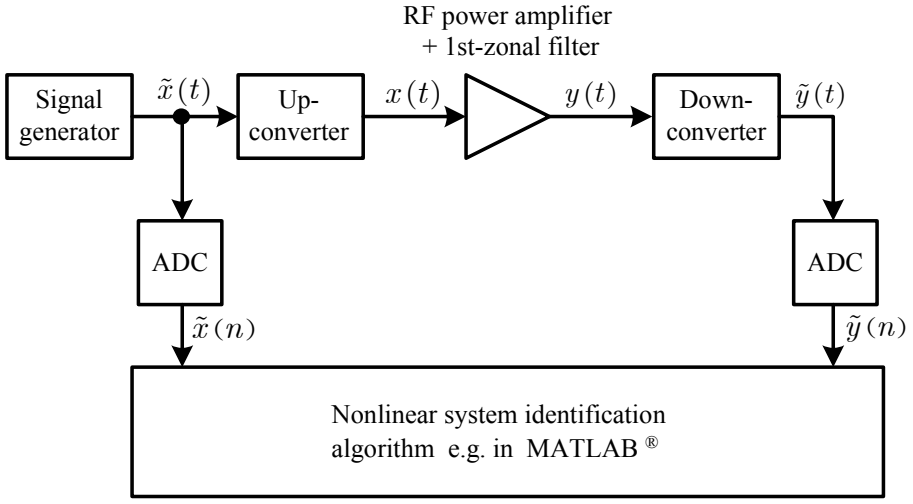


**Figure 4.2:** Block diagram of a nonlinear system identification scheme for the RF PA for system modeling purposes. The identification is performed off-line with a mathematical software tool such as MATLAB®.

## 4.2 Nonlinear System Identification Based on Nyquist Sampling

One method to identify a cascade of a nonlinear passband system e.g. an RF PA and a 1st-zonal filter in the complex baseband domain is shown in Fig. 4.3 and Fig. 4.4. Figure 4.4 is a simplified version of Fig. 4.3, where we have used the fact that the nonlinear passband system $(\mathbf{F} \circ \mathbf{G})[x]$ and the frequency down-converters can be represented in the complex baseband-domain by the equivalent baseband model $\tilde{\mathbf{H}}[\tilde{x}]$ as shown in Ch. 2. The spectrum of the complex baseband output signal $\tilde{y}(t)$ which is calculated with (2.40) and (2.41) is broadened to $B(2\lceil L/2\rceil - 1)$, where $B$ is the bandwidth of the complex baseband input signal $\tilde{x}(t)$ and $(2\lceil L/2\rceil - 1)$ the highest order of the baseband nonlinearity. Although we do not have the even orders of the nonlinearity in the baseband representation of Volterra models (see Ch. 2), we use them to illustrate the identification process, which can of course, also be applied to identify real systems which incorporate the even orders of the nonlinearity as well.

To perform the identification process in the discrete-time domain, we sample the complex baseband output signal $\tilde{y}(t)$ with an angular sampling frequency of $\omega_s = 2\pi/T \geq 2B(2\lceil L/2\rceil - 1)$ which satisfies the Nyquist theorem regarding the output signal $\tilde{y}(t)$ to avoid aliasing effects [45, 46, 48]. The broadening of the frequency-domain input signal $\tilde{X}^c(\omega) = \mathcal{F}\{\tilde{x}(t)\}$ of a 2nd-order model, which is caused by the integration of the two-dimensional output signal $\tilde{Y}^c_{(2)}(\omega_1, \omega_2) = \tilde{H}_2(\omega_1, \omega_2)\tilde{X}(\omega_1)\tilde{X}(\omega_2)$ along the integration path $\omega_2 = -\omega_1 + \omega$, and the periodic extension of the output signal spectrum $\tilde{Y}^c(\omega) = \mathcal{F}\{\tilde{y}(t)\}$ which is caused by the sampling process is depicted in Fig. 4.5 (a) and Fig. 4.5 (b). While the periodically extended spectrum in Fig. 4.5 (b) still incorporates the

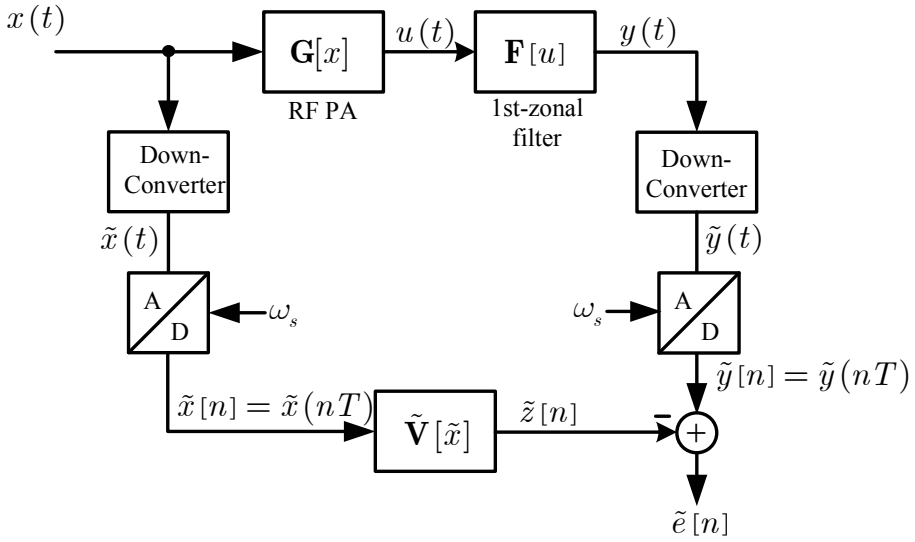


**Figure 4.3:** Nonlinear system identification scheme for the cascade of the RF PA and a 1st-zonal filter. The ADCs and the nonlinear discrete-time model $\tilde{\mathbf{V}}[\tilde{x}]$ are operated on a angular sampling frequency $\omega_s$, which is at least two times the bandwidth of the output signal $y(t)$.

sampling-time $T$ in the frequency scaling, the spectrum in Fig. 4.5 (c) does not so, because of the normalization of the discrete-time signals $\tilde{x}[n] = \tilde{x}(nT)$ and $\tilde{y}[n] = \tilde{y}(nT)$.

The goal of the nonlinear system identification in Fig. 4.4, is to determine the Volterra kernels $\tilde{v}_{2k+1}[n_1, \ldots, n_{2k+1}]$ of the discrete-time complex baseband Volterra model

$$\begin{aligned}\tilde{z}[n] &= \tilde{\mathbf{V}}\big[\tilde{x}[n]\big] \\ &= \sum_{k=0}^{\lceil L/2\rceil-1} \sum_{n_1=0}^{N_{2k+1}} \cdots \sum_{n_{2k+1}=0}^{N_{2k+1}} \tilde{v}_{2k+1}[n_1, \ldots, n_{2k+1}] \\ &\quad \times \prod_{i=1}^{k+1} \tilde{x}[n-n_i] \prod_{i=k+2}^{2k+1} \tilde{x}^*[n-n_i], \end{aligned} \tag{4.1}$$

in such a way that the periodic output signal spectrum $\tilde{Z}^d(\exp(j\Omega)) = \mathcal{F}\{\tilde{z}[n]\}$ of the discrete-time model in (4.1) is identical to the spectrum of the sampled RF PA baseband model output signal $\tilde{Y}^d(\exp(j\Omega)) = \mathcal{F}\{\tilde{y}[n]\}$. This is achieved if the frequency-domain Volterra kernels $\tilde{V}_{2k+1}$ of the discrete-time model in (4.1) satisfy

$$\tilde{V}_{2k+1}(\exp(j\Omega_1), \ldots, \exp(j\Omega_{2k+1})) \equiv \tilde{H}_{2k+1}\left(\frac{\Omega_1}{T}, \ldots, \frac{\Omega_{2k+1}}{T}\right), \tag{4.2}$$

for the frequency range of interest given by $|\Omega_i| \leq BT$, where $BT$ denotes the normalized bandwidth of the discrete-time input signal $\tilde{x}[n]$. Outside this frequency range ($BT < |\Omega_i| \leq \pi$), the kernels $\tilde{V}_{2k+1}$ in (4.2) can have arbitrary values.

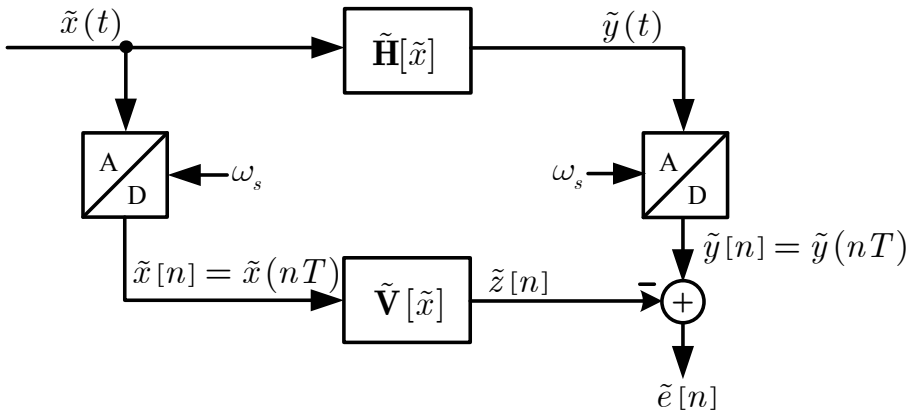


**Figure 4.4:** Nonlinear system identification scheme operating in the baseband which is equivalent to the scheme in Fig. 4.3. The ADCs and the nonlinear discrete-time model $\tilde{\mathbf{V}}[\tilde{x}]$ are operated on an angular sampling frequency $\omega_s$ which is at least two times the bandwidth of the output signal of the baseband power amplifier model $\tilde{y}(t)$.

To show this, we calculate the output signal spectrum of the discrete-time Volterra model in (4.1) with the discrete-time counterparts of (2.40) and (2.41) by

$$\tilde{Z}^d(\exp(j\Omega)) = \sum_{k=0}^{\lceil L/2\rceil-1} \frac{1}{(2\pi)^{2k}} \int_{-\pi}^{\pi} \cdots \int_{-\pi}^{\pi} \tilde{Z}^d_{(2k+1)}\big(\exp(j(\Omega-\Theta_1)), \exp(j(\Theta_1-\Theta_2)), \ldots, \exp(j\Theta_{2k})\big)\, d\Theta_1 \ldots d\Theta_{2k}, \tag{4.3}$$

where the multi-dimensional frequency-domain output signals

$$\tilde{Z}^d_{(2k+1)}\big(\exp(j\Omega_1), \ldots, \exp(j\Omega_{2k+1})\big) = \tilde{V}_{2k+1}\big(\exp(j\Omega_1), \ldots, \exp(j\Omega_{2k+1})\big) \times \prod_{i=1}^{k+1} \tilde{X}^d(\exp(j\Omega_i)) \prod_{i=k+2}^{2k+1} \tilde{X}^{d^*}(\exp(-j\Omega_i)) \tag{4.4}$$

with $\tilde{X}^d(\exp(j\Omega)) = \mathcal{F}\{\tilde{x}[n]\}$ are band-limited to $\pm BT$, and periodic with $2\pi$ in each of the $2k+1$ frequency variables (gray shaded areas in Fig. 4.6 (a)). The spectrum of the discrete-time input signal $\tilde{x}[n]$ in (4.4) is related to the spectrum of the continuous-time signal $\tilde{x}(t)$ by

$$\tilde{X}^d\big(\exp(j\Omega)\big) = \begin{cases} \frac{1}{T}\tilde{X}^c(\frac{\Omega}{T}) & |\Omega| \le BT \\ 0 & BT < |\Omega| \le \pi. \end{cases} \tag{4.5}$$

The multi-dimensional frequency-domain signal in (4.4) can be rewritten over one period with (4.2) and (4.5) by

$$\tilde{Z}^d_{(2k+1)}\big(\exp(j\Omega_1), \ldots, \exp(j\Omega_{2k+1})\big) = \frac{1}{T^{2k+1}} \tilde{Y}^c_{(2k+1)}\left(\frac{\Omega_1}{T}, \ldots, \frac{\Omega_{2k+1}}{T}\right), \tag{4.6}$$

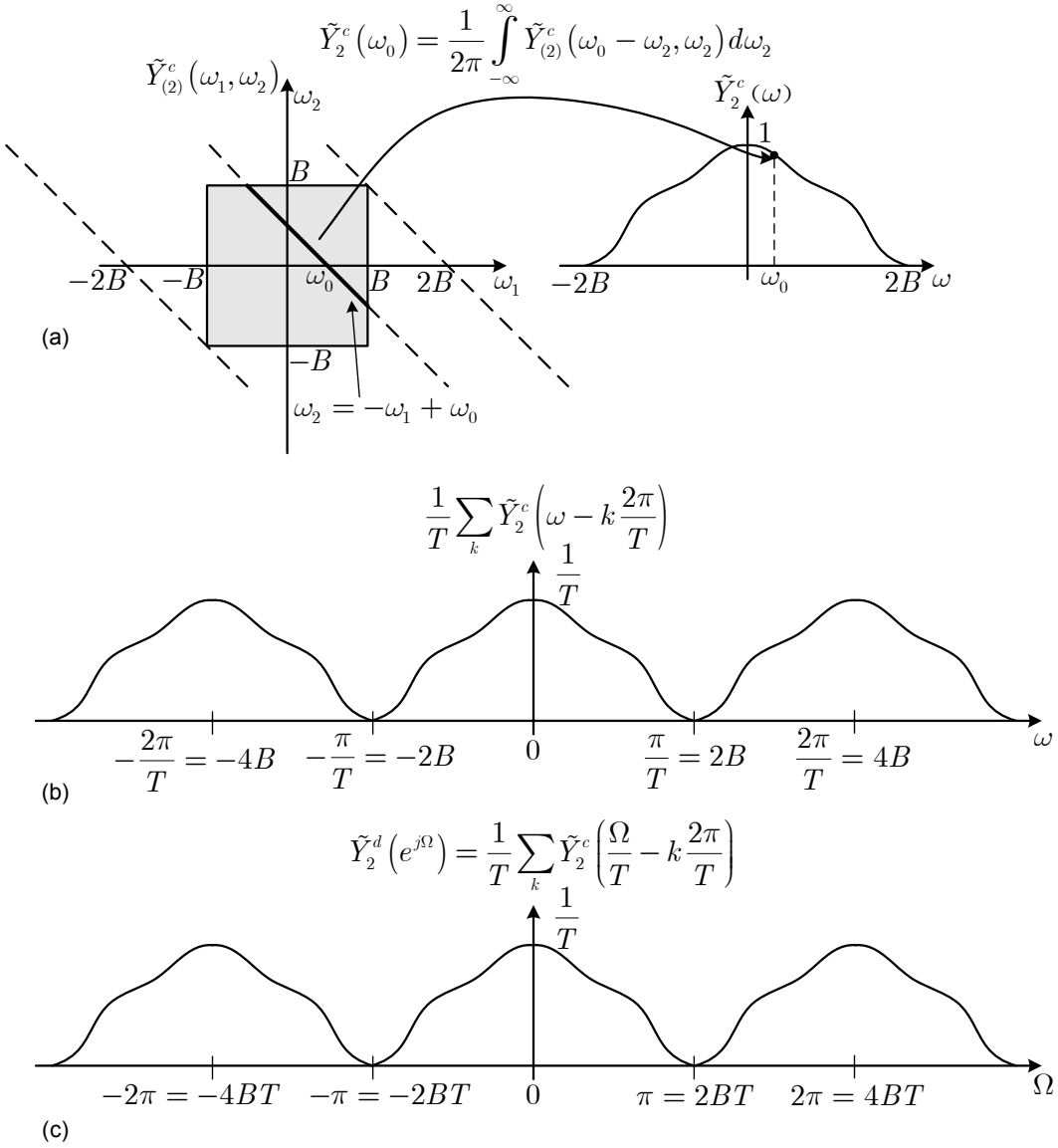


**Figure 4.5:** Output signal spectra of a 2nd-order Volterra system for the discrete-time identification process in Fig. 4.4. (a) Building the output signal spectrum $\tilde{Y}_2^c(\omega)$ by integrating the two-dimensional frequency-domain output signal $\tilde{Y}_{(2)}^c(\omega_1, \omega_2)$ along the integration path $\omega_2 = -\omega_1 + \omega$. (b) Magnitude-scaled and periodically extended output signal spectrum caused by the sampling process with $\omega_s = 2\pi/T = 4B$. (c) Frequency-scaled version of (b), caused by the sampling $\tilde{y}[n] = \tilde{y}(nT)$.

where $|\Omega_i| \leq \pi$. The spectrum in (4.6) is periodically extended with $2\pi$ in each of the $2k+1$ frequency variables $\Omega_i$. If we use the relationship in (4.6) to evaluate the integral expression in (4.3), we obtain with $\Omega = \omega T$ one period of the output signal spectrum of the discrete-time Volterra model in Fig. 4.6 (b) by

$$\tilde{Z}^d(\exp(j\Omega)) = \sum_{k=0}^{\lceil L/2 \rceil - 1} \frac{T^{2k}}{(2\pi)^{2k} T^{2k+1}} \int_{-\pi/T}^{\pi/T} \cdots \int_{-\pi/T}^{\pi/T} \tilde{Y}^c_{(2k+1)} \Big( \frac{\Omega}{T} - \theta_1, \theta_1 - \theta_2, \ldots, \theta_{2k} \Big) \, d\theta_1 \ldots d\theta_{2k}, \tag{4.7}$$

which is identical to one period of the spectrum $\tilde{Y}_2^d(\exp(j\Omega))$ in Fig. 4.5 (c). In practical applications, we are usually unable to identify the exact Volterra kernels $\tilde{H}_{2k+1}$ of the RF PA baseband model $\tilde{\mathbf{H}}[\tilde{x}]$ because of model uncertainties and noises. For this reason we estimate the discrete-time Volterra model $\tilde{\mathbf{V}}[\tilde{x}]$ e.g., with standard linear least squares methods (the estimation problem is linear in the parameters) [40] or adaptively with an LMS-algorithm [40] to minimize a particular cost-function defined on the discrete-time error signal $\tilde{e}[n]$.

With the concept in Fig. 4.3 and Fig. 4.4, unfortunately two major difficulties arise. The first one is the demand for high sampling rate ADCs (depending on the highest order of the RF PA nonlinearity $L$), which are expensive and high power consuming. The second one is that standard least squares algorithms tend to numerical unstable solutions [9, 25], if the input signal bandwidth is below half the sampling frequency (non-persistent excitation). This is caused by the oversampling of the input signal $\tilde{x}[n]$ by the factor of $2\lceil L/2 \rceil - 1$ to satisfy the Nyquist theorem regarding the output signal of the RF PA baseband model $\tilde{\mathbf{H}}[\tilde{x}]$ to avoid aliasing. Figure 4.7 depicts the ill-conditioning [25, 9] of the data matrix in terms of its condition number (the ratio between the largest and the smallest singular value) for three different orders of the RF PA nonlinearity $L$. If the excitation of the discrete-time baseband Volterra model becomes more persistent $2B/\omega_s \rightarrow 1$, the condition number decreases which improves the estimation accuracy considerably [25, 9].

## 4.3 Volterra Kernel Interpolation

To overcome the problems mentioned in the last section, we perform the nonlinear system identification process in Fig. 4.3 and Fig. 4.4 with an angular sampling frequency of $\omega_s^{'} = \omega_s / K$, where $K = 2\lceil L/2 \rceil - 1$ denotes the highest order of the baseband nonlinearity, which satisfies the Nyquist theorem only regarding the input signal $\tilde{x}(t)$. This is possible because the RF PA baseband model $\tilde{\mathbf{H}}[\tilde{x}]$ in Fig. 4.8 is purely determined by the corresponding multi-dimensional frequency-domain Volterra kernels $\tilde{H}_{2k+1}(\omega_1, \ldots, \omega_{2k+1})$ over the frequency range of $\pm B$ in each of the $2k+1$ frequency variables $\omega_i$ if the input signal $\tilde{x}(t)$ is band-limited to $\pm B$ (see Ch. 2).

It has been shown in [23] that if the equality in (4.2) holds, the output signal of the discrete-time model $\check{z}[n]$ in Fig. 4.8 is identical to the sampled and aliased output signal of

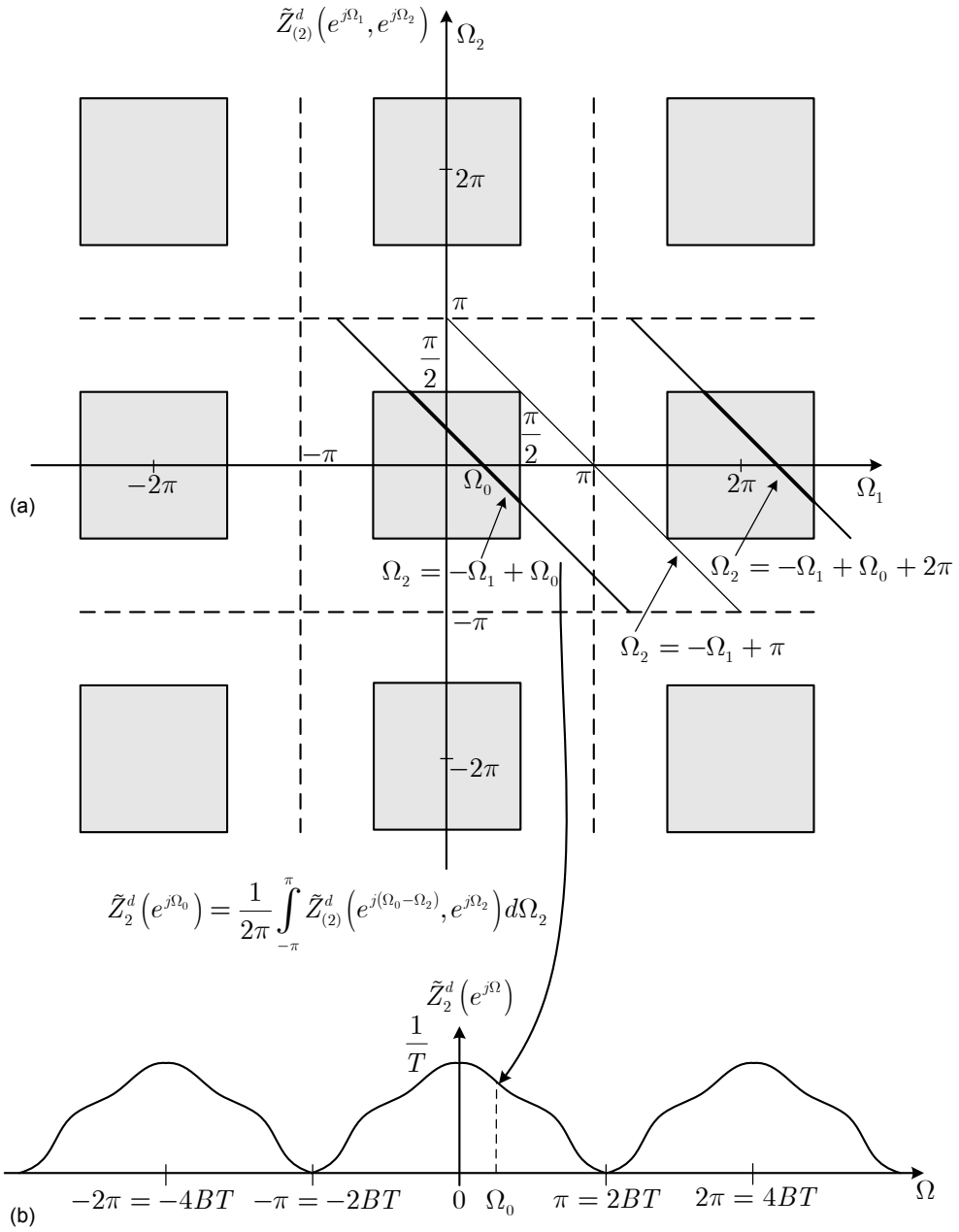


**Figure 4.6:** Output signal spectra for a 2nd-order discrete-time Volterra model $\tilde{\mathbf{V}}[\tilde{x}]$ in Fig. 4.4. (a) Building the output signal spectrum $\tilde{Z}^d_2(\exp(j\Omega))$ by integrating the two-dimensional periodic frequency-domain output signal $\tilde{Z}^d_{(2)}(\exp(j\Omega_1), \exp(j\Omega_2))$ along the integration path $\Omega_2 = -\Omega_1 + \Omega$. (b) Output signal spectrum $\tilde{Z}^d_2(\exp(j\Omega))$ of the discrete-time Volterra model $\tilde{\mathbf{V}}[\tilde{x}]$.

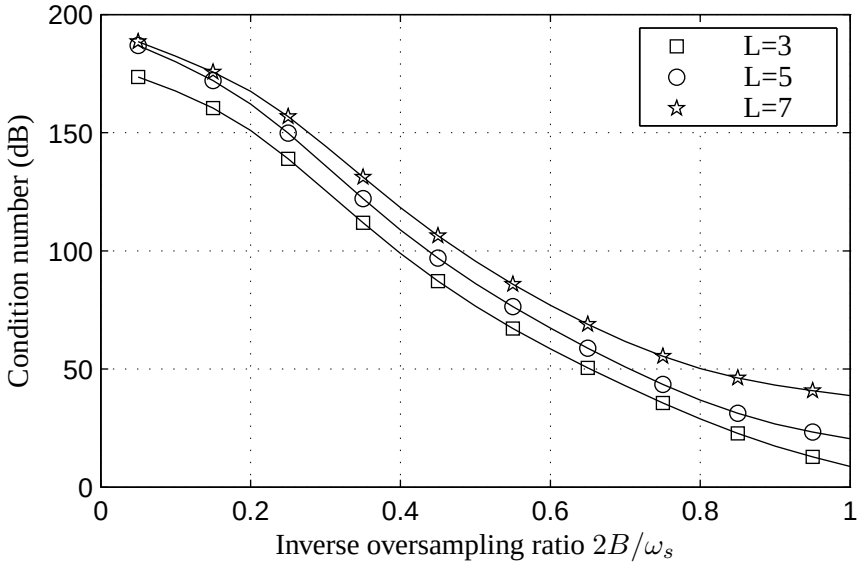


**Figure 4.7:** The condition number (ratio between largest and smallest singular value) for least squares problems determines the parameter estimation accuracy. If the excitation becomes more persistent (more wide-band), the condition number decreases.

the RF PA baseband model $\breve{y}[n] = \tilde{y}(nT')$, where $T' = KT$ denotes the new sampling time.

The output signal of the RF PA baseband model in (2.40) and (2.41) is illustrated for a 2nd-order model in Fig. 4.9 (a). The output signal spectrum for a particular frequency $\omega_0$ is given by the integration of the two-dimensional frequency-domain signal $\tilde{Y}^c_{(2)}(\omega_1, \omega_2)$ along the integration path of $\omega_2 = -\omega_1 + \omega_0$.

Because of the low angular sampling frequency $\omega_s = 2B$ (which fulfills the Nyquist theorem only regarding the input signal $\tilde{x}(t)$), the sampled output signal $\breve{y}[n]$ becomes aliased, and results in a spectrum which is composed of magnitude-scaled and overlapped spectral copies of $\tilde{Y}^c_2(\omega)$. The output signal spectrum for a particular frequency $\omega_0$ in Fig. 4.9 (b) is given by the non aliased component $\frac{1}{T'}\tilde{Y}^c_2(\omega_0)$ (integration along the path $\omega_2 = -\omega_1 + \omega_0$) and the aliased component $\frac{1}{T'}\tilde{Y}^c_2\left(\omega_0 - \frac{2\pi}{T'}\right)$ (integration along the path $\omega_2 = -\omega_1 - 2B + \omega_0$).

While the aliasing in the output signal $\breve{y}[n]$ is generated by the sampling of the continuous-time output signal $\tilde{y}(t)$ with the low angular sampling frequency $\omega_s'$, the pseudo-aliasing in the output signal of the discrete-time model

$$\begin{aligned}\breve{z}[n] &= \breve{\mathbf{V}}\big[\breve{x}[n]\big] \\ &= \sum_{k=0}^{\lceil L/2\rceil-1} \sum_{n_1=0}^{N_{2k+1}} \cdots \sum_{n_{2k+1}=0}^{N_{2k+1}} \breve{v}_{2k+1}[n_1, \ldots, n_{2k+1}] \\ &\quad \times \prod_{i=1}^{k+1} \breve{x}[n-n_i] \prod_{i=k+2}^{2k+1} \breve{x}^*[n-n_i], \end{aligned} \tag{4.8}$$

is introduced because the integration path $\Omega_2 = -\Omega_1 + \Omega_0$ in Fig. 4.10 (a) contains the spectral components of the first periodic extension of $\breve{Z}^d_{(2)}(\exp(j\Omega_1), \exp(j\Omega_2))$.

Therefore, the output signal spectrum of the 2nd-order discrete-time model in (4.8) which is calculated by (see Fig. 4.10)

$$\breve{Z}^d_2(\exp(j\Omega)) = \underbrace{\frac{1}{2\pi} \int_{-\pi}^{-\pi+\Omega} \breve{Z}^d_{(2)}(\exp(j(\Omega-\Omega_2)), \exp(j\Omega_2))\, d\Omega_2}_{\text{pseudo-aliasing}} + \frac{1}{2\pi} \int_{-\pi+\Omega}^{\pi} \breve{Z}^d_{(2)}(\exp(j(\Omega-\Omega_2)), \exp(j\Omega_2))\, d\Omega_2, \tag{4.9}$$

is identical to the aliased output signal spectrum $\breve{Y}^d_2(\exp(j\Omega))$ (see Fig. 4.9 (c)) of the sampled output signal $\breve{y}[n]$ of the RF PA baseband model [23].

Although, nonlinear system identification can be accomplished with a low angular sampling frequency $\omega_s$ (Nyquist theorem regarding the input signal), in many applications for example digital predistortion, the discrete-time model (the inverse of the RF PA baseband model $\tilde{\mathbf{H}}$) must be operated on a sufficiently high angular sampling frequency $\omega_s$ to generate the spectral out-off-band components required for the nonlinear compensation (see Ch. 5). This is also true if we use the discrete-time RF PA baseband model in a transmitter chain for overall system performance simulations.

To avoid pseudo-aliasing in the output signal of the low-rate identified discrete-time model $\breve{\mathbf{V}}[\breve{x}]$ in Fig. 4.8, we have to guarantee, that the integral operation in (4.3) is not performed over more than one of the periodically extended multi-dimensional spaces of (4.4). This can be accomplished by a frequency scaling of the multi-dimensional Volterra kernels $\breve{V}_{2k+1}(\exp(j\Omega_1), \ldots, \exp(j\Omega_{2k+1}))$, by the factor of $K$, which is equivalent to a multi-dimensional zero stuffing, in the time domain, and the masking of the unwanted spectral copies of the frequency scaled Volterra kernels by the multi-dimensional input signal spectrum $\prod_{i=1}^{k+1} \tilde{X}^d(\exp(j\Omega_i) \prod_{i=k+2}^{2k+1} \tilde{X}^{d*}(\exp(-j\Omega_i)$.

To see this, we first apply a multi-dimensional upsampling to the time-domain Volterra kernels $\breve{v}_{2k+1}[n_1, \ldots, n_{2k+1}]$ in (4.8), which yields

$$\tilde{u}_{2k+1}[n_1, \ldots, n_{2k+1}] = \sum_{l_1=0}^{N_{2k+1}} \cdots \sum_{l_{2k+1}=0}^{N_{2k+1}} \breve{v}_{2k+1}[l_1, \ldots, l_{2k+1}] \prod_{i=1}^{2k+1} \delta[n_i - K l_i] \tag{4.10}$$

where $\delta[n]$ denotes the discrete-time unit impulse [45, 46, 48]. The upsampling for a 2nd-order discrete-time Volterra kernel with a memory depth of two is depicted in Fig. 4.11.

If we calculate the multi-dimensional discrete Fourier transform of (4.10) by

$$\tilde{U}_{2k+1}(\exp(j\Omega_1), \ldots, \exp(j\Omega_{2k+1})) = \sum_{n_1=0}^{N_{2k+1}} \cdots \sum_{n_{2k+1}=0}^{N_{2k+1}} \tilde{u}_{2k+1}[n_1, \ldots, n_{2k+1}] \times \prod_{i=1}^{2k+1} \exp(-j\Omega_i n_i), \tag{4.11}$$

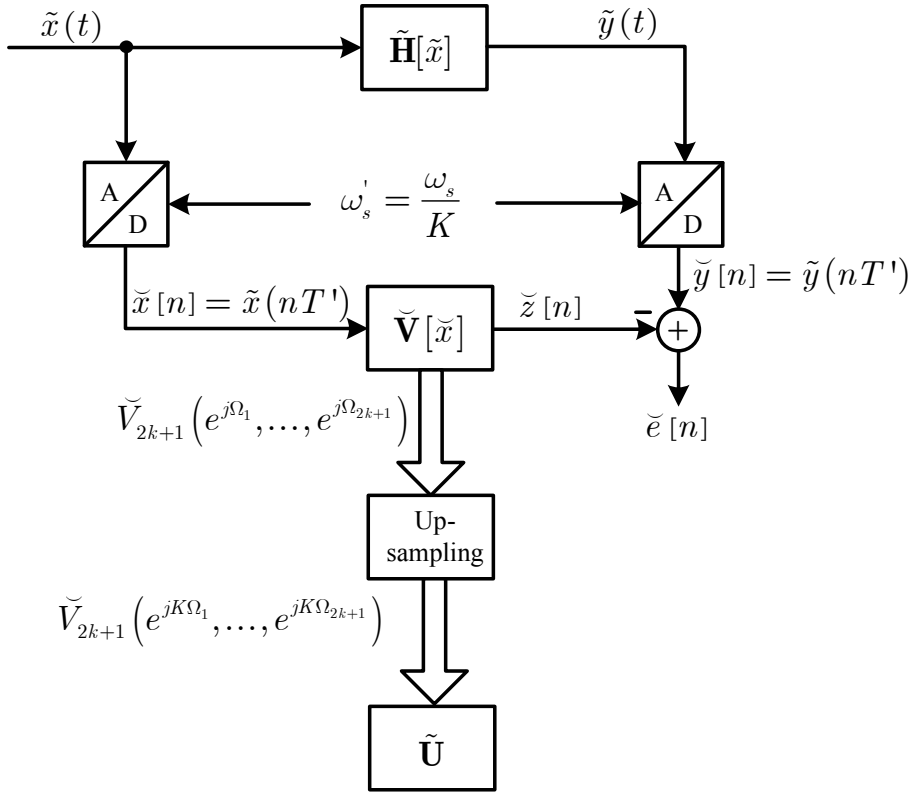


**Figure 4.8:** Nonlinear system identification scheme for the RF PA baseband system $\tilde{\mathbf{H}}[\tilde{x}]$ based on a low angular sampling frequency $\omega_s'$. The ADCs and the discrete-time Volterra model $\breve{\mathbf{V}}[\breve{x}]$ are operated with an angular sampling frequency $\omega_s'$, which is only two times the bandwidth of the input signal $\tilde{x}(t)$. The frequency-domain Volterra kernels of the resulting low-rate model $\breve{\mathbf{V}}[\breve{x}]$ are frequency scaled (multi-dimensional upsampling) to obtain a high-rate Volterra model $\tilde{\mathbf{U}}[\tilde{x}]$ which is able to generate the same spectral out-of-band components as the high-rate Volterra model $\tilde{\mathbf{V}}[\tilde{x}]$ in Fig. 4.4.

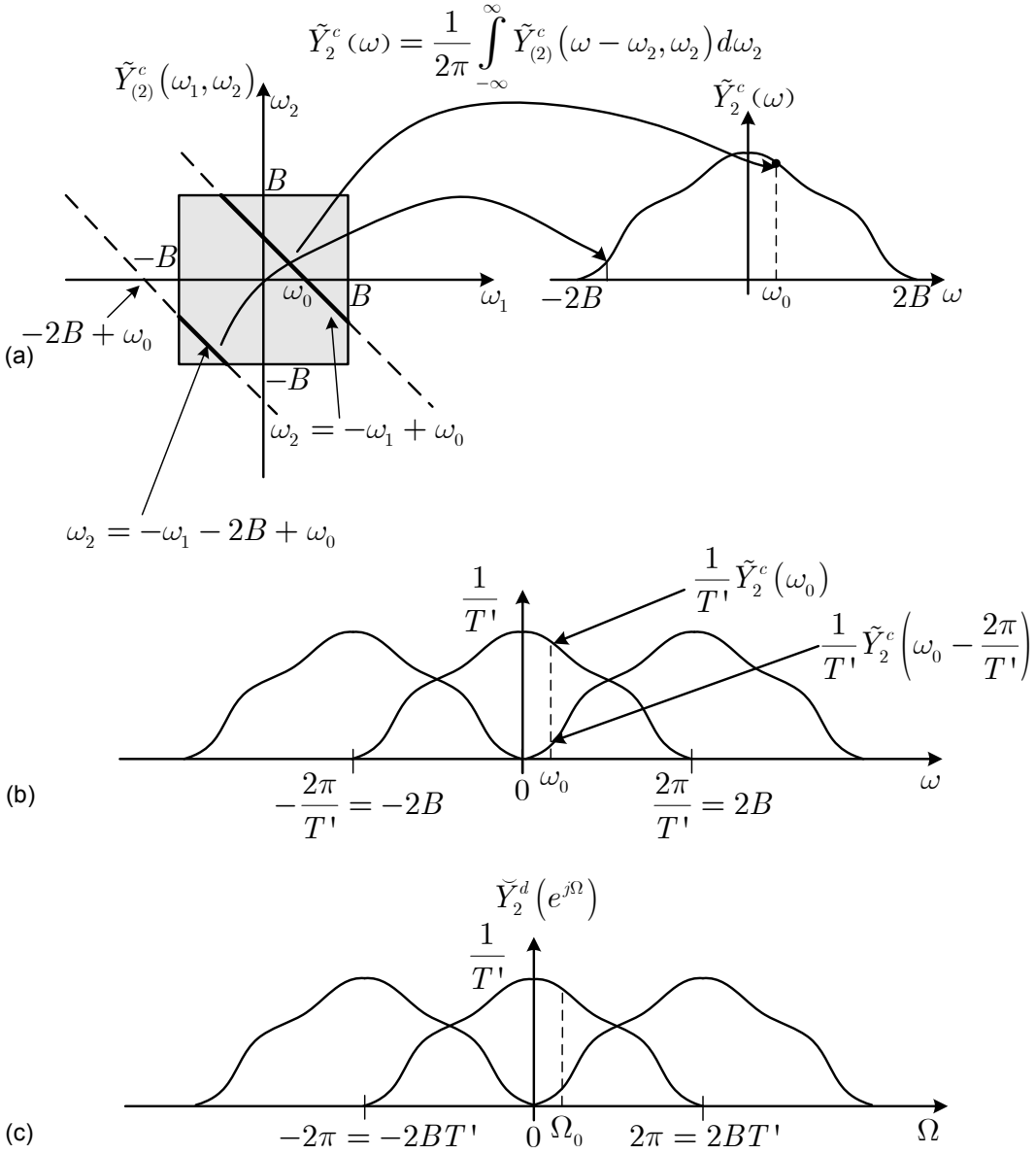


**Figure 4.9:** Output signal spectra of a 2nd-order RF PA baseband system for the discrete-time identification process in Fig. 4.8. (a) Building the output signal spectrum $\tilde{Y}_2^c(\omega)$ by integrating the two-dimensional frequency-domain output signal $\tilde{Y}_{(2)}^c(\omega_1,\omega_2)$ along the integration path $\omega_2 = -\omega_1 + \omega$. (b) Magnitude-scaled and periodically extended aliased output signal spectrum which is caused by the sampling process with $\omega_s = (2\pi)/T' = 2B$, where $T' = KT$. The factor $K$ denotes the highest order of the baseband nonlinearity. (c) Frequency-scaled version of (b), caused by the sampling $\tilde{y}[n] = \breve{y}(nT')$.

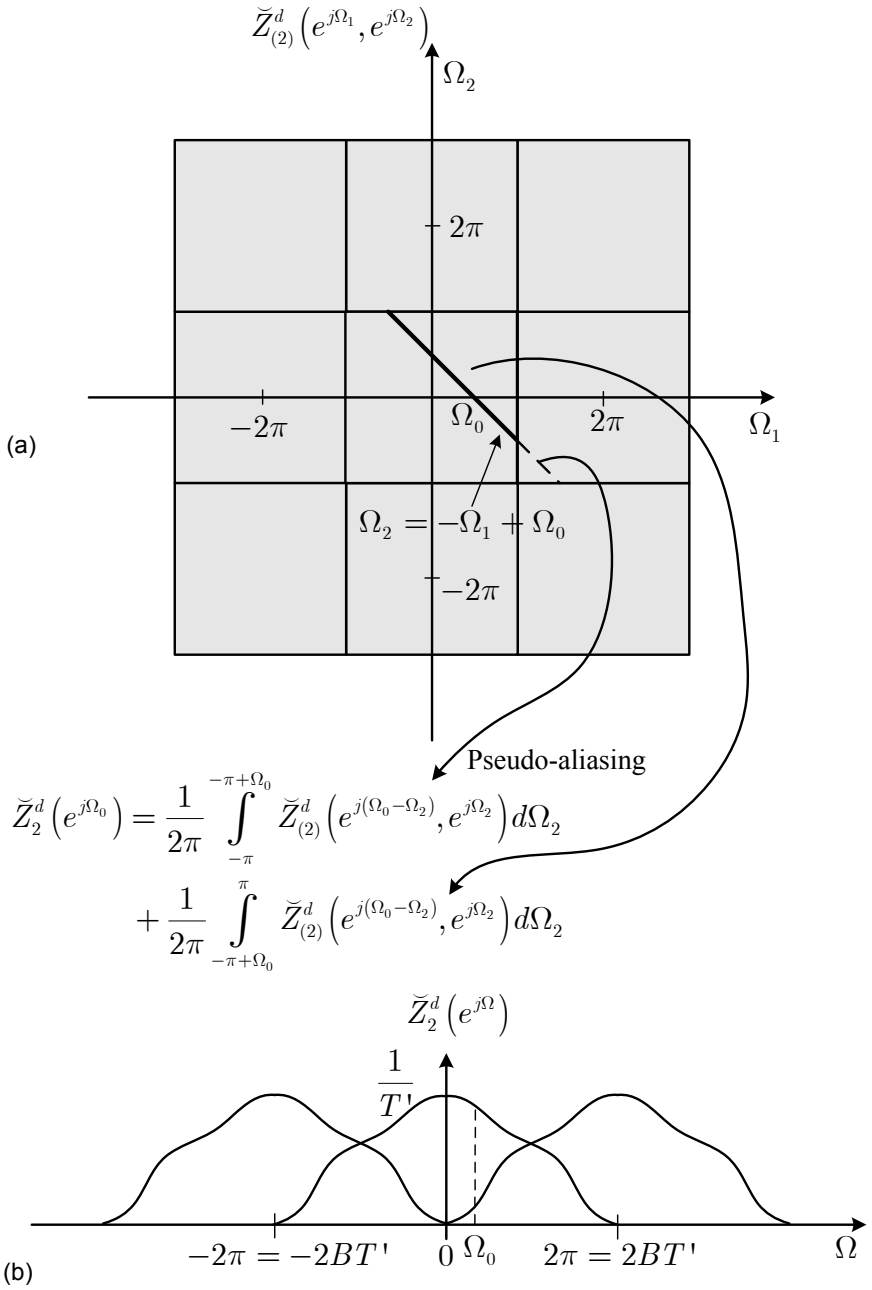


**Figure 4.10:** Output signal spectra of a 2nd-order Volterra model for the discrete-time RF PA identification process in Fig. 4.8. (a) Generation of pseudo-aliasing caused by the integration of the two-dimensional signal $\breve{Z}^d_{(2)}(\exp(j\Omega_1), \exp(j\Omega_2))$ along the integration path of $\Omega_2 = -\Omega_1 + \Omega$ which intersects the first periodic extension of $\breve{Z}^d_{(2)}(\exp(j\Omega_1), \exp(j\Omega_2))$. (b) Pseudo-aliased output signal spectrum of the Volterra model $\breve{\mathbf{V}}[\breve{x}]$, which is identical to the output signal spectrum in Fig. 4.9 (c).

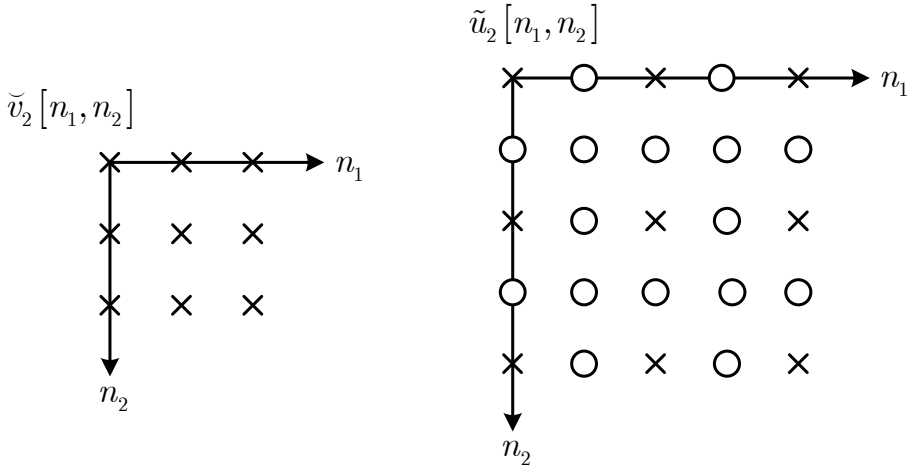


**Figure 4.11:** Time-domain kernels of a 2nd-order Volterra system with a memory depth of two. (a) Kernel of the low-rate (Nyquist theorem regarding the input signal) identified model $\breve{\mathbf{V}}[\breve{x}]$. (b) Upsampled kernels constructed from (a) by introducing zeros between the kernel entries of (a).

we obtain the frequency scaled Volterra kernels of the high sampling rate model $\tilde{\mathbf{U}}[\tilde{x}]$ in Fig. 4.8 by

$$\tilde{U}_{2k+1}(\exp(j\Omega_1), \ldots, \exp(j\Omega_{2k+1})) = \breve{V}_{2k+1}(\exp(jK\Omega_1), \ldots, \exp(jK\Omega_{2k+1})) \,. \tag{4.12}$$

It is important to note, that the multi-dimensional upsampling in (4.10) is accomplished with almost no additional costs, because we simply have to replace each unit-sample delay $z^{-1}$ in (4.8) by a $K$-sample delay $z^{-K}$.

To show that the RF PA baseband model $\tilde{\mathbf{U}}[\tilde{x}]$ in Fig. 4.8 generates the identical non-aliased output spectrum as the RF PA model $\tilde{\mathbf{V}}[\tilde{x}]$ in Fig. 4.4, it is sufficient to show that the equation

$$\tilde{U}_{2k+1}\big(\exp(j\Omega_1), \ldots, \exp(j\Omega_{2k+1})\big) \equiv \tilde{V}_{2k+1}\big(\exp(j\Omega_1), \ldots, \exp(j\Omega_{2k+1})\big) \tag{4.13}$$

holds for $|\Omega_i| \leq BT$. Outside this frequency range from $BT < |\Omega_i| \leq \pi$, the Volterra kernels in (4.13) differ because $\tilde{U}_{2k+1}$ is periodically extended with $\pi$ (see Fig. 4.13), where $\tilde{V}_{2k+1}$ can take arbitrary values. Because the Volterra kernels $\breve{V}_{2k+1}$ in Fig. 4.8 are related to the frequency-domain Volterra kernels of the RF PA baseband model $\tilde{\mathbf{H}}[\tilde{x}]$ by

$$\breve{V}_{2k+1}\big(\exp(j\Omega_1), \ldots, \exp(j\Omega_{2k+1})\big) \equiv \tilde{H}_{2k+1}\left(\frac{\Omega_1}{KT}, \ldots, \frac{\Omega_{2k+1}}{KT}\right) \tag{4.14}$$

for $|\Omega_i| \leq \pi$, we can rewrite (4.12) with (4.14) by

$$\tilde{U}_{2k+1}\big(\exp(j\Omega_1), \ldots, \exp(j\Omega_{2k+1})\big) \equiv \tilde{H}_{2k+1}\left(\frac{\Omega_1}{T}, \ldots, \frac{\Omega_{2k+1}}{T}\right), \tag{4.15}$$

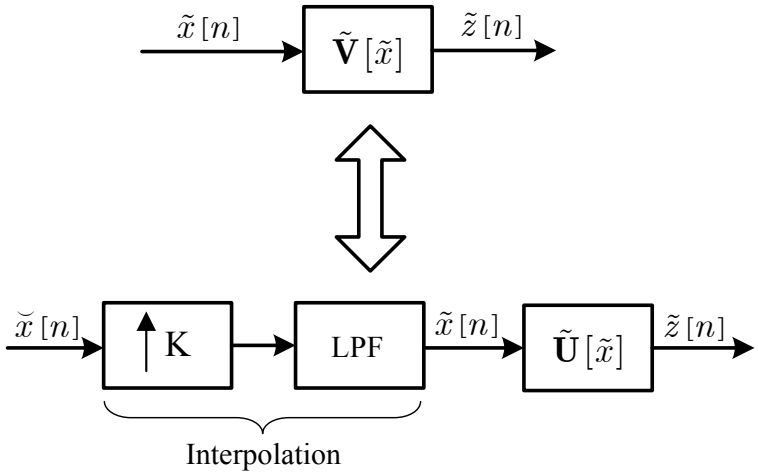


**Figure 4.12:** Equivalence between the discrete-time Volterra model $\tilde{\mathbf{V}}[\tilde{x}]$ which was identified at a sampling frequency which fulfills the Nyquist theorem regarding the output signal and the interpolated Volterra model $\tilde{\mathbf{U}}[\tilde{x}]$. This model is based on the discrete-time Volterra model $\breve{\mathbf{V}}[\breve{x}]$ which was identified on a sampling frequency which only fulfills the Nyquist theorem regarding the input signal. The equivalence holds only for band-limited input signals $\tilde{x}[n]$ with a bandwidth $B \leq \pi/K$.

where $|\Omega_i| \leq \pi/K = BT$, which proofs the equality given in (4.13). Figure 4.12 depicts the two equivalent block diagrams of the discrete-time nonlinear models $\tilde{\mathbf{V}}[\tilde{x}]$ and $\tilde{\mathbf{U}}[\tilde{x}]$, whose output signals $\tilde{z}[n]$ are in the ideal case (perfect kernel estimation) exactly the sampled non-aliased output signal from the RF PA baseband model $\tilde{\mathbf{H}}[\tilde{x}]$ in Fig. 4.3. While the model $\tilde{\mathbf{V}}[\tilde{x}]$ is identified on the high angular sampling frequency $\omega_s$, the model $\tilde{\mathbf{U}}[\tilde{x}]$ is obtained from the model $\breve{\mathbf{V}}[\breve{x}]$ identified at the low angular sampling frequency ($\omega_s^{'} = \omega_s/K$), and a Volterra kernel upsampling (multi-dimensional zero insertion) shown in Fig. 4.8. While the multi-dimensional upsampling only changes the scaling of the frequency variables of the low-rate identified model $\breve{\mathbf{V}}[\breve{x}]$, (as shown in Fig. 4.13), the interpolation (masking of the unwanted spectral copies) is accomplished by the multiplication with the spectra of the high-rate sampled input signal $\tilde{x}[n]$ as depicted in Fig. 4.13.

Figure 4.14 shows the output signal power spectra for a 3rd-order RF PA baseband model (see Fig. 3.14 in Ch. 3) $\tilde{\mathbf{H}}[\tilde{x}]$ and the nonlinear model $\tilde{\mathbf{U}}[\tilde{x}]$ in Fig. 4.12 which was obtained from the baseband model $\breve{\mathbf{V}}[\breve{x}]$ by applying a Volterra kernel interpolation. The relative frequency-domain error signal in Fig. 4.13 reflects the imperfect Volterra kernel estimation with a standard linear least squares algorithm, which is caused by the RF PA baseband model uncertainties and noise.

## 4.4 Conclusion

Although nonlinear systems can be identified with nonlinear discrete-time models on a sampling rate which is just twice the input signal bandwidth (Nyquist theorem regarding the

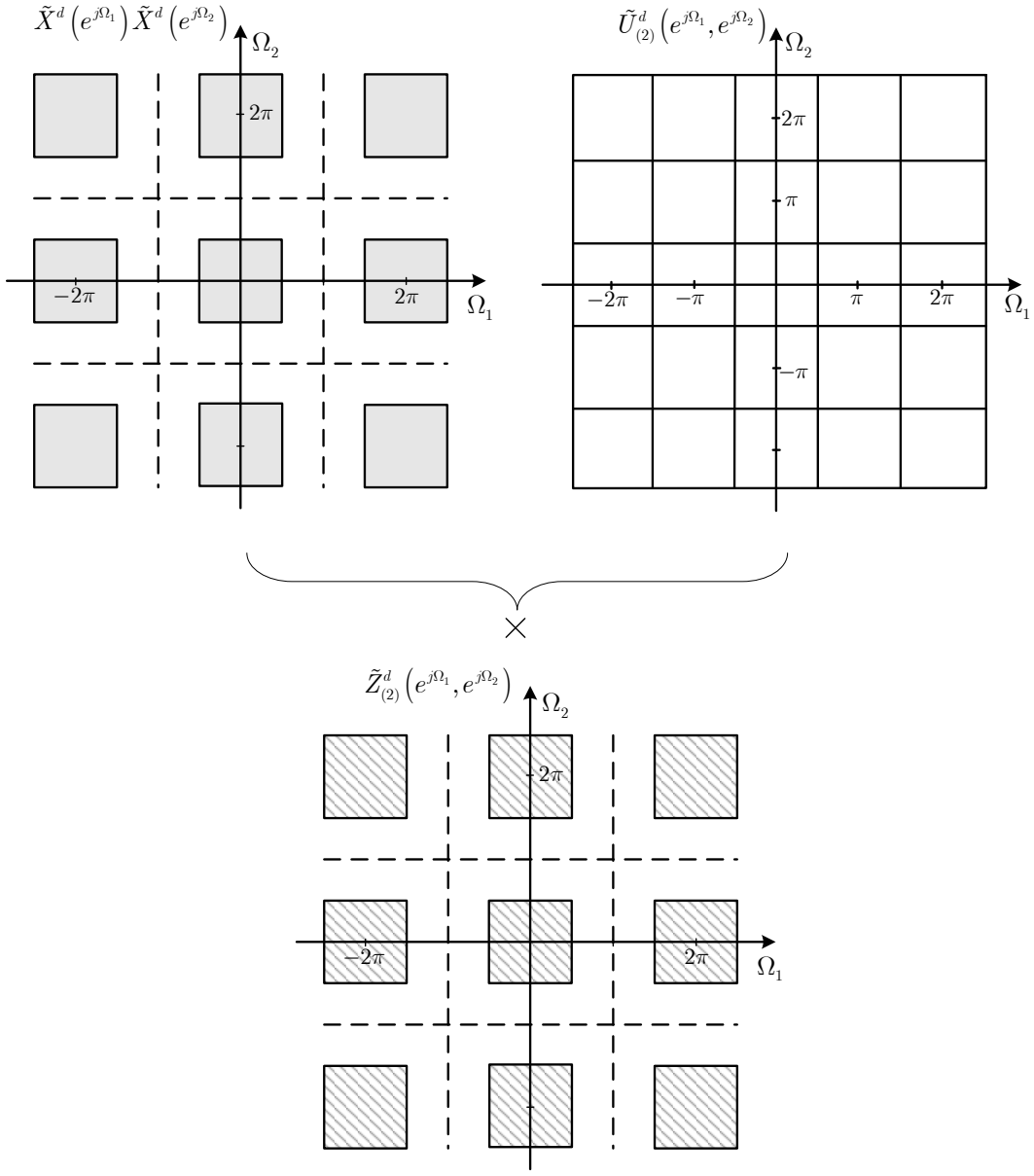


**Figure 4.13:** Volterra kernel interpolation of a 2nd-order Volterra model $\breve{\mathbf{V}}[\breve{x}]$, which was identified on the low sampling frequency $\omega_s^{'}$. The unwanted spectral copies of the two-dimensional frequency-domain output signal $\tilde{U}^d_{(2)}(\exp(j\Omega_1), \exp(j\Omega_2))$ are masked by the input signal spectrum $\tilde{X}^d(\exp(j\Omega_1))\tilde{X}^d(\exp(j\Omega_2))$. The resulting spectrum $\tilde{Z}^d_{(2)}(\exp(j\Omega_1), \exp(j\Omega_2))$ is exactly the same as we obtain with the high sampling frequency identification scheme in Fig. 4.4.

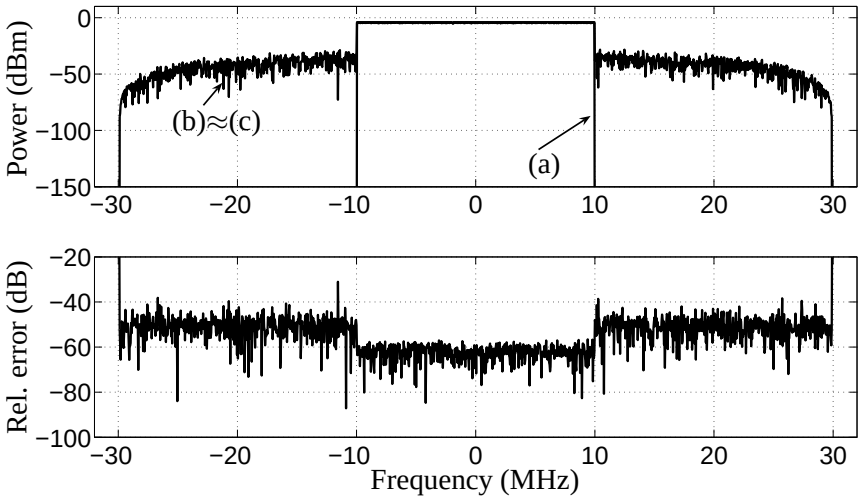


**Figure 4.14:** Frequency-domain input and output signals from the two equivalent Volterra models in Fig. 4.12. (a) Input signal power spectrum. (b) Output signal power spectrum of a 3rd-order RF PA baseband model $\tilde{\mathbf{H}}[\tilde{x}]$ (see Fig. 3.14 in Ch. 3). (c) Output signal power spectrum of the interpolated Volterra model $\tilde{\mathbf{U}}[\tilde{x}]$. The (relative) frequency-domain error signal does not vanish due to the imperfect Volterra kernel estimation.

input signal), for some applications, nonlinear discrete-time models which are operated on a sampling frequency which is at least twice the output signal bandwidth are necessary.

One of these applications is digital predistortion. A predistorter is a functional block which precedes the RF PA in the digital baseband domain in order to linearize the overall transmitter chain. Such discrete-time models are also required for overall system simulations of communication systems to predict their performance without the full computational complexity of a transistor-based circuit simulation.

One method to build such nonlinear discrete-time models is to identify a complex baseband RF PA with a sampling frequency which satisfies the Nyquist theorem regarding the output signal bandwidth (Nyquist sampling). One of the inherent problems with this method is the ill-conditioned data matrix (large condition number) if we formulate a linear least squares problem. This become especially serious, if we model high-order nonlinearities with large memory depths, because this leads in general to bad kernel estimates.

Another difficulty is the demand for high sampling rate ADCs (depends on the highest order of the baseband nonlinearity) which are in general expensive and high power consuming. To overcome these major drawbacks, we employ a Volterra kernel interpolation to the nonlinear discrete-time model which was identified with a sampling frequency below the Nyquist theorem. This is possible because the nonlinear system is purely determined by the frequency-domain Volterra kernels within the bandwidth of the input signal in each of the frequency variables.

The Volterra kernel interpolation is accomplished by a multi-dimensional zero-insertion

of the discrete-time model mentioned above. This procedure requires almost no additional computational complexity, because we only have to replace each unit-sample delay in the complex baseband Volterra model (predistorter or RF PA baseband model) by a $K$-sample delay. This operation leads to a frequency scaling of the multi-dimensional frequency-domain Volterra kernels, which results in a change of the primitive period from $2\pi \rightarrow 2\pi/K$. The unwanted spectral copies of the frequency-domain Volterra kernels are interpolated by a spectral masking with the discrete-time input signal which was sampled with a frequency which is at least twice the bandwidth of the RF PA baseband output signal (Nyquist theorem regarding the output signal).

# Chapter 5

# Digital Baseband Predistortion for RF Power Amplifiers

In this chapter, we address the problem of digital predistortion for RF power amplifiers. This complex baseband method is one of the most efficient ways to linearize an RF PA. The digital predistortion is implemented by introducing a nonlinear functional block (approximate inverse of the RF PA) which precedes the RF block (frequency up-converter, pre-driver and PA) in order to obtain an almost linear overall system with a higher efficiency. In Sec. 5.2, we compare three different predistorter architectures (Volterra series, memory polynomials and static predistorters) regarding their linearization performance measured by the adjacent channel power ratio (ACPR) and their complexities regarding the number of free parameters. In all cases the predistorters are determined by a direct estimation of the post-inverse of the RF PA baseband system. In Sec.5.3, we consider the sampling requirements for predistorters based on a $p$th-order inverse. In Sec.5.4, we develop a predistortion scheme based on a low sampling-rate RF PA baseband system identification. This architecture saves computational complexity (low-rate ADCs) and avoids possible numerical problems during parameter estimation.

## 5.1 Introduction

To obtain a sufficient output power level covering the range within a mobile communication cell, high power amplifiers are needed. As this device is one of the most cost intensive components (large chip area) within a basestation, it is of fundamental importance to operate the RF PA in the region of compression to obtain the highest possible efficiency (efficiency is approximately inverse proportional to the linearity of the RF PA) [15, 16, 32]. The region of compression is defined by the RF PA input power level where the real and the ideal RF PA output power levels differs by $1$ dB. The main problem with this concept is the dynamic nonlinear behavior of the RF PA in combination with the high peak-to-average power ratio (PAPR $> 10$ dB) in the envelope of the transmission signal. This generally leads to spectral regrowth and intermodulation distortion in the signal band (see Ch. 2). The spectral regrowth leads to adjacent channel interference which may not exceed some levels imposed by the regulatory bodies. On the other hand, intermodulation distortion increases the bit-error rate on the receiver side if we make no attempt to linearize or back-off the RF PA, where the latter one results in a very poor efficiency.

Several state of the art methods like feed-forward [15, 16, 32] are used in today's power

amplifier products which have a tremendous expense in RF components (additional error amplifier, directional couplers, delay lines and amplitude- and phase shifting networks). The overall efficiency of feed-forward transmitters is in the range of 10 percent for typical multi-carrier signals [15, 16, 32, 50].

Digital predistortion is a more powerful linearization technique, which exploits the considerable processing power now available from DSP devices. This technique allows us to perform the predistortion and all other required operations such as system identification (RF PA or its inverse) and parameter adaptation (RF PA is slightly time-variant due to temperature and power supply drifts, aging effects,...) with digital algorithms without the difficulties which occur in feed-forward concepts. The efficiency of digital predistorters can be increased to approximately 20 percent for typical multi-carrier signals [15, 16, 32, 50].

Digital predistorters can be classified either into static predistorters for low memory requirements or predistorters with memory which are also suitable for wideband RF PAs. The first group is based on the assumption that RF PAs can be described by the two static nonlinearities called AM/AM-conversion and AM/PM-conversion (see Ch. 2). Such predistorters can be implemented with look-up table techniques. Because both, the AM/AM-conversion and the AM/PM-conversion purely depends on the magnitude of the transmission signal, the magnitude can be used to find the look-up table entries with the corresponding complex correction parameters. Static digital predistorters based on this concept are reported, e.g., in [13, 15, 16, 32, 50]. Unfortunately, these digital predistorters have a very limited performance if we apply them to RF PAs excited with wideband signals such as a four carrier WCDMA. The reason for this performance loss are the memory effects (electrical and thermo-electrical [11, 69, 70]) of the RF PA which are not considered in static predistorters.

To overcome this problem, Volterra series [56, 52, 40] based predistorters which incorporate memory can be advantageously used to improve the predistorter performance considerably. The drawback of Volterra series predistorters is in general the large number of parameters which increases immensely with the order of the nonlinearity and the memory length [40]. For this reason several different predistorter structures with a lower number of parameters such as Hammerstein, Wiener, Parallel-Wiener or Memory-polynomial predistorters are proposed in the literature [51, 20, 18].

## 5.2 Complex Baseband Predistorters Identified with an Indirect Learning Architecture

A digital predistorter is a nonlinear functional block implemented in the baseband discrete-time domain which precedes the RF transmitter chain in order to linearize the transmitter (nonlinearity is mainly caused by the RF PA). Because the behavior of an RF PA is generally unknown, we have to identify either the RF PA itself and calculate the approximate inverse, or we directly identify the approximate inverse of the RF PA. Figure 5.1 depicts the block diagram of a wireless transmitter including a digital predistortion processor to the transmitter chain and a feedback path (receiver) for system identification and adaptation. Unfortunately only a small class of nonlinear systems possesses an exact inverse [40]. One

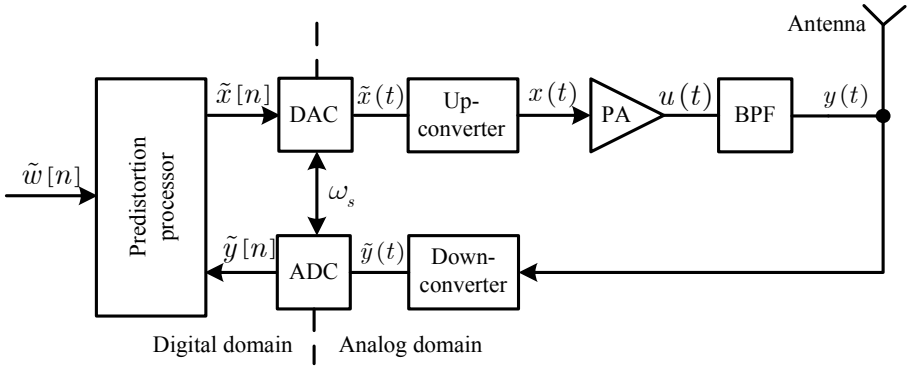


**Figure 5.1:** Block diagram of a wireless communication transmitter incorporating a digital baseband predistortion processor. The predistortion processor identifies the approximate inverse of the transmitter chain and linearizes it by cascading the identified inverse and the transmitter in order to reduce the nonlinear distortion of the transmission signal $y(t)$.

method to find the approximate inverse of a nonlinear system described by Volterra series is the theory of pth-order inverses.

It has be shown in [56, 40, 55] that a Volterra system can be linearized either with a Volterra pre- or a postdistorter (Volterra system of $p$th-order.) up to the order of $p$. Therefore the output signal of the cascade of the nonlinear system (RF PA) and the pre- or postdistorter is composed of the input signal and a nonlinear distortion which is caused by the nonzero Volterra kernels of higher order than $p$. If we calculate the $p$th-order postdistorter of a Volterra system, this system is also the predistorter of the Volterra system. The difference between the two different cascaded systems is the remaining nonlinear distortion.

Unfortunately, the theory of $p$th-order inverses leads to complicated structures for the predistorter on the one hand, and on the other hand it is difficult (Volterra systems are not orthogonal) to identify the different Volterra kernels of the RF PA to build the predistorter.

One method to overcome this difficulty is to identify directly an approximate post-inverse of the RF PA with an indirect learning architecture [33]. This identification architecture is shown in the upper part of Fig. 5.3 (part of the predistortion processor in Fig. 5.1). The postdistorter will be identified by minimizing a cost function defined on the error signal $\tilde{e}[n]$. If the nonlinear model described by the operator $\tilde{\mathbf{L}}$ is linear in the parameters, we can use a standard linear optimization algorithm (LMS, RLS,...) [26, 40] to find the optimum parameters of the postdistorter. If we have found the optimum parameters, we copy them into the predistorter which precedes the DAC and the RF PA baseband model $\tilde{\mathbf{H}}$ in Fig. 5.3 (lower part), in order to linearize the transmitter chain (mainly the RF PA). The indirect learning architecture is based on the assumption that if we have found the optimum post-inverse , this post-inverse is a good approximation for the pre-inverse (pre-inverse and the post-inverse of a nonlinear system are in general different), which seems to be true (verified from simulations) if the cost function converges to a small value. [22, 40, 33, 18].

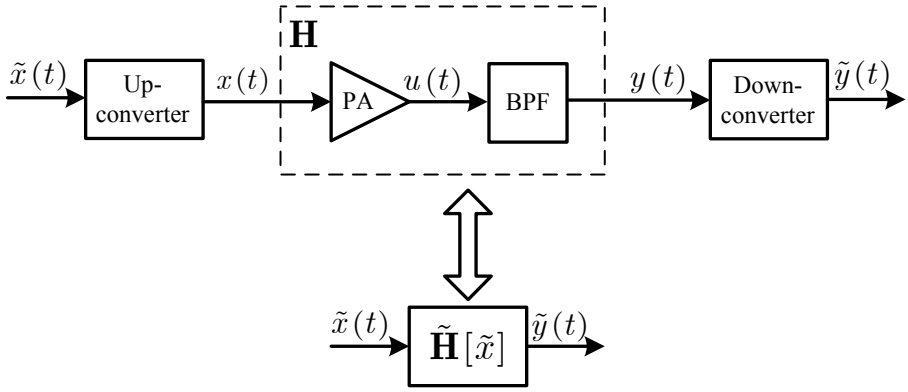


**Figure 5.2:** Block-diagram of the transmitter and receiver chain of the wireless transmitter in Fig. 5.1 and the equivalent representation by the complex baseband power amplifier model described by the nonlinear operator $\tilde{\mathbf{H}}$.

### 5.2.1 Volterra Predistorter

We have shown in Ch. 2, that RF PAs can be successfully described in the complex baseband domain with nonlinear models which are based on Volterra series (Volterra, memory-polynomials, AM/AM-conversion and AM/PM-conversion,...). The most apparent method to realize a digital predistorter with an indirect learning architecture as shown in Fig. 5.1 and Fig. 5.3 is to implement the postdistorter described by the nonlinear operator $\tilde{\mathbf{L}}$ as one of these models.

If we discretize the complex baseband Volterra series model in (2.33) and apply it to the predistortion setup in Fig. 5.1 and Fig. 5.3 we obtain

$$\begin{aligned}\tilde{z}[n] &= \tilde{\mathbf{L}}[\tilde{y}[n]] \\ &= \sum_{k=0}^{K-1} \sum_{m_1=0}^{M_{2k+1}-1} \cdots \sum_{m_{2k+1}=0}^{M_{2k+1}-1} \tilde{l}_{2k+1}[m_1, \ldots, m_{2k+1}] \\ &\quad \times \prod_{i=1}^{k+1} \tilde{y}[n-m_i] \prod_{i=k+2}^{2k+1} \tilde{y}^*[n-m_i], \end{aligned} \tag{5.1}$$

where $\tilde{l}_{2k+1}[m_1, \ldots, m_{2k+1}]$ denotes the unknown discrete-time Volterra kernels, $M_{2k+1}$ is the memory length of the different orders of the nonlinearity of the discrete-time Volterra model and $2K-1$ is the highest order of the postdistorter nonlinearity. Figure 5.4 shows a 3rd-order discrete-time Volterra postdistorter with a memory length of $M_3 = 3$. The Volterra system is implemented as a static nonlinear block which builds the different combinations of the delayed and conjugate input signals and a bank of complex linear filters to

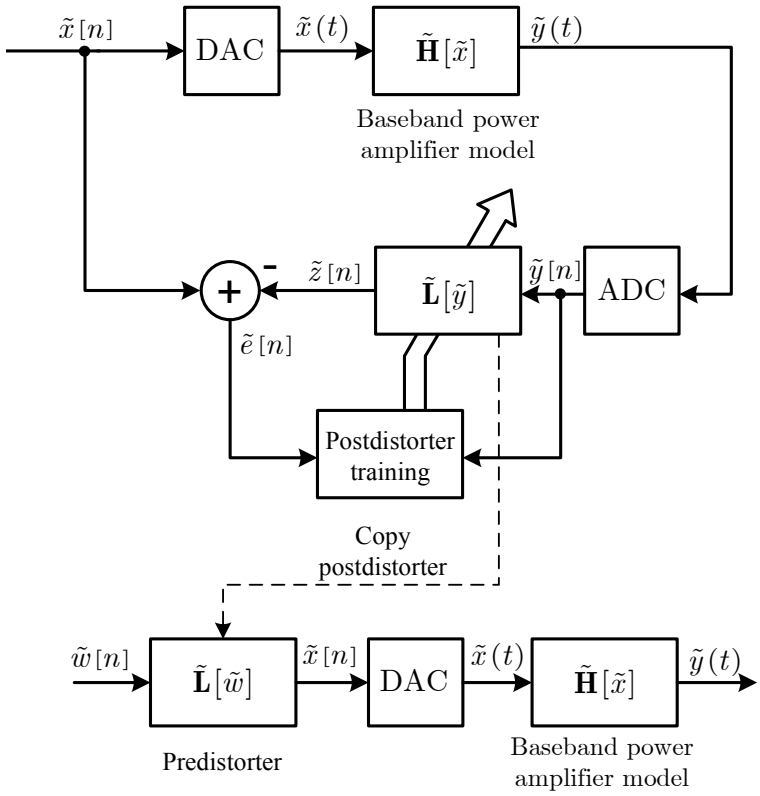


**Figure 5.3:** Detailed illustration of the predistortion processor depicted in Fig. 5.1. The upper part shows the identification (postdistorter training) of the post-inverse of the baseband power amplifier model $\tilde{\mathbf{L}}$ with an adaptive algorithm (LMS, RLS, ...). This structure is called indirect learning architecture, because we directly identify the inverse of the baseband power amplifier instead of the baseband power amplifier itself (direct learning architecture). After the postdistorter training, the postdistorter $\tilde{\mathbf{L}}$ is cascaded as predistorter with the ADC and the baseband power amplifier $\tilde{\mathbf{H}}$ to linearize the transmitter chain as depicted on the lower part.

perform the convolution operations in (5.1) in the following way

$$\begin{aligned}\tilde{z}[n] &= \tilde{\mathbf{L}}[\tilde{y}[n]] \\ &= \sum_{m=0}^{M_1-1} \tilde{l}_1[m]\tilde{y}[n-m] \\ &\quad + \sum_{m=0}^{M_3-1} \tilde{l}_3[m,m,m]\,|\tilde{y}[n-m]|^2\,\tilde{y}[n-m] \\ &\quad + \sum_{m=0}^{M_3-2} \tilde{l}_3[m,m,m+1]y^2[n-m]y^*[n-m-1] \\ &\quad \vdots \end{aligned} \tag{5.2}$$

The big drawback of the Volterra series model in (5.1) and (5.2) is the large number of unknown parameters (Volterra kernel entries, e.g., $\tilde{l}_1[0]$, $\tilde{l}_1[1]$, $\tilde{l}_3[1,0,2]$,...) which increases immensely with the order of the nonlinearity and the memory length and which is expressed for the $(2k+1)$th-order by

$$P_{2k+1} = (M_{2k+1})^{2k+1}, \tag{5.3}$$

where the total number of parameters is is given by

$$P = \sum_{k=0}^{K-1} P_{2k+1}. \tag{5.4}$$

The number of parameters in (5.3) can be reduced if we exploit the commutative property of the products of the delayed input signals in the discrete-time Volterra series in (5.1)

$$\prod_{i=1}^{k+1} \tilde{y}[n-m_i] \prod_{i=k+2}^{2k+1} \tilde{y}^*[n-m_i] = \prod_{i=1}^{k+1} \tilde{y}[n-m_{\pi_1(i)}] \prod_{i=k+2}^{2k+1} \tilde{y}^*[n-m_{\pi_2(i)}], \tag{5.5}$$

where $\pi_1(i)$ and $\pi_2(i)$ denotes the distinct permutations of the indices $m_1,\ldots,m_{k+1}$ and $m_{k+2},\ldots,m_{2k+1}$ respectively. Therefore the discrete-time Volterra series model in (5.1) can be simplified with (5.5), which results in

$$\begin{aligned}\tilde{z}[n] &= \tilde{\mathbf{L}}[\tilde{y}[n]] \\ &= \sum_{k=0}^{K-1} \sum_{m_1=0}^{M_{2k+1}-1} \cdots \sum_{m_{k+1}=m_k}^{M_{2k+1}-1} \sum_{m_{k+2}=0}^{M_{2k+1}-1} \cdots \sum_{m_{2k+1}=m_{2k}}^{M_{2k+1}-1} \\ &\quad \times \tilde{l}_{2k+1}[m_1,\ldots,m_{2k+1}] \prod_{i=1}^{k+1} \tilde{y}[n-m_i] \prod_{i=k+2}^{2k+1} \tilde{y}^*[n-m_i], \end{aligned} \tag{5.6}$$

which reduces the number of parameters for the $(2k+1)$th-order of the discrete-time

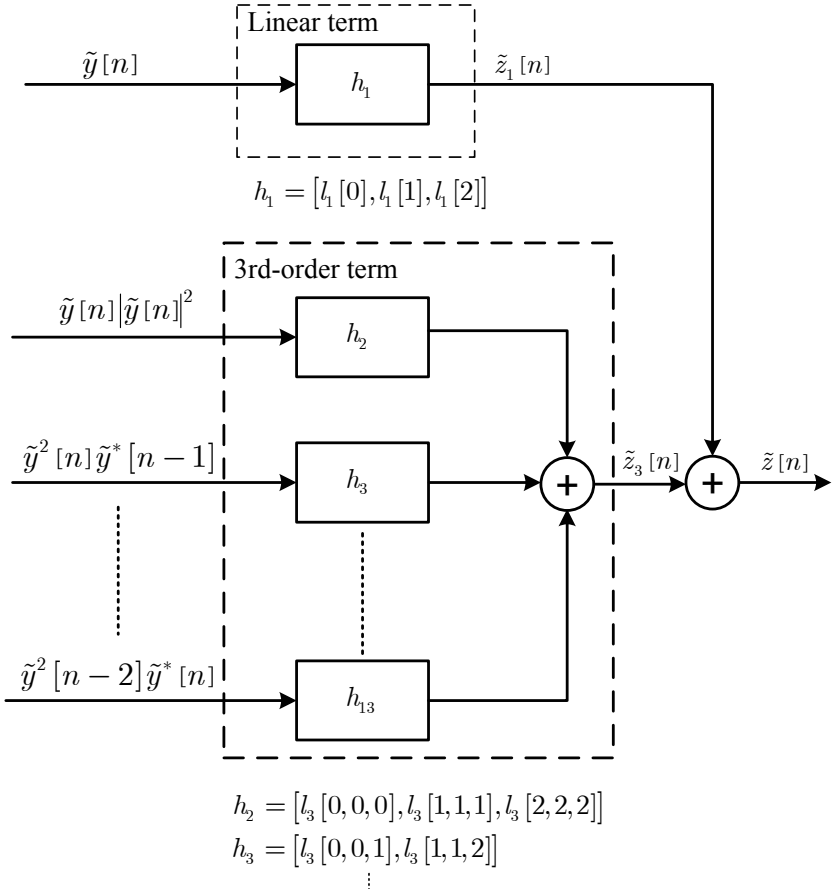


**Figure 5.4:** 3rd-order discrete-time Volterra postdistorter with a memory length of $M_3 = 3$. The postdistorter is composed of a static nonlinear block which builds the different combinations of the delayed input signals and its conjugate and a bank of linear complex filters to perform the convolution operations in (5.1).

Volterra series model in (5.6) to [40]

$$P_{2k+1} = \binom{M_{2k+1}+k}{k+1}\binom{M_{2k+1}+k-1}{k} = \frac{M_{2k+1}+k}{k+1}\left[\frac{(M_{2k+1}+k-1)!}{k!(M_{2k+1}-1)!}\right]^2. \tag{5.7}$$

### 5.2.2 Memory-Polynomial Predistorter

Although, the number of parameters of discrete-time Volterra series models can be reduced if we exploit some symmetry properties, the number of parameters $P = \sum_{k=0}^{K-1} P_{2k+1}$, where $P_{2k+1}$ is given by (5.7), are in general still quite large (e.g. $P_3 = 18$ with $M_3 = 3$). In Ch. 2 we have considered a special case of a continuous-time Volterra series model called

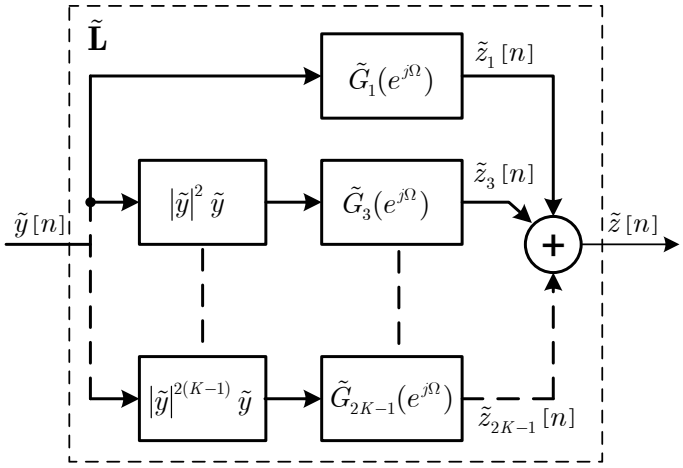


**Figure 5.5:** A complex baseband postdistorter described by the nonlinear operator $\tilde{\mathbf{L}}$ in Fig. 5.3 is built with discrete-time memory-polynomials. The postdistorter is composed of a bank of static nonlinearities and the linear discrete-time filters $\tilde{G}_{2k+1}(\exp(j\Omega))$.

memory-polynomial model where the off-diagonal Volterra kernels are assumed to be zero. In this section we apply a discretized version of this memory-polynomial to linearize the RF PA baseband model of Fig. 5.3 in an indirect-learning architecture setup. If we constrain the discrete-time Volterra kernels in (5.6) $\tilde{l}_{2k+1}[m_1,\ldots,m_{2k+1}] \equiv 0$, for $m_1 \neq m_2 \neq \cdots \neq m_{2k+1}$, we obtain the discrete-time memory-polynomial model given by

$$\begin{aligned}\tilde{z}[n] &= \tilde{\mathbf{L}}[\tilde{y}[n]] \\ &= \sum_{k=0}^{K-1} \sum_{m=0}^{M_{2k+1}-1} \tilde{g}_{2k+1}[m]\,|\tilde{y}[n-m]|^{2k}\,\tilde{y}[n-m] \\ &= \sum_{k=0}^{K-1} \tilde{g}_{2k+1}[n] \star |\tilde{y}[n]|^{2k}\,\tilde{y}[n] \end{aligned} \tag{5.8}$$

where $\tilde{g}_{2k+1}[m] \equiv \tilde{l}_{2k+1}[m_1,\ldots,m_{2k+1}]$ describes the discrete-time Volterra kernels along the diagonals in a multi-dimensional space. The memory-polynomial postdistorter in (5.8) is shown in Fig. 5.5, where $\tilde{G}_{2k+1}(\exp(j\Omega)) = \mathcal{F}\{\tilde{g}_{2k+1}[n]\}$.

The postdistorter is composed of a bank of static nonlinearities (monomials), where each of these nonlinear systems is cascaded with a complex linear filter $\tilde{G}_{2k+1}(\exp(j\Omega))$ as given by the convolution operation in (5.8). The output signals $\tilde{z}_{2k+1}[n]$ of these filters are summed up to build the final output signal $\tilde{z}[n]$. The number of parameters for the $(2k+1)$th-order term is now purely determined by the corresponding memory length of the linear filters in Fig. 5.5, given by

$$P_{2k+1} = M_{2k+1}, \tag{5.9}$$

where the total number of parameters is given with (5.9) and (5.4) by $P = \sum_{k=0}^{K-1} M_{2k+1}$.

If we compare the number of parameters for the memory-polynomial postdistorter in (5.9) with the number of parameters for the Volterra series based postdistorter in (5.7), we realize a considerable reduction of parameters for $k > 0$ (factor of 6 for $P_3 = M_3 = 3$). This parameter reduction can of course result in a poorer linearization performance if the assumption regarding the off-diagonal Volterra kernel entries is not satisfied.

### 5.2.3 Static Predistorter

Static predistorters are based on the assumption that the RF PA which should be linearized can be sufficiently described by the two static nonlinearities called AM/AM-conversion and AM/PM-conversion (see Ch. 2 and Ch. 3). This kind of linearization has been successfully applied by many researchers to linearize low-power RF PAs (hand-sets) or high-power RF PAs (basestations) with narrowband transmission signals [13, 50, 32, 15].

If the memory length in (5.1) is constraint to be $M_{2k+1} = 1$ for $0 \leq k \leq K-1$, the complex baseband Volterra postdistorter in (5.1) reduces to the well known case of a complex static polynomial function given by (see Ch. 2)

$$\begin{aligned}\tilde{z}[n] &= \tilde{\mathbf{L}}[\tilde{y}[n]] \\ &= \sum_{k=0}^{K-1} \tilde{c}_{2k+1} \prod_{i=1}^{k+1} \tilde{y}[n] \prod_{i=k+2}^{2k+1} \tilde{y}^*[n] \\ &= \sum_{k=0}^{K-1} \tilde{c}_{2k+1} \, |\tilde{y}[n]|^{2k} \, \tilde{y}[n], \end{aligned} \tag{5.10}$$

where $\tilde{c}_{2k+1} = \tilde{g}_{2k+1}[0] \equiv \tilde{l}_{2k+1}[0, \ldots, 0]$ describes the Volterra kernel entries for the time-lag of zero. The structure of this static postdistorter is shown in Fig. 5.6, where the complex linear filters in Fig. 5.5 have been replaced by simple complex constants. Therefore the number of unknown parameters for the $(2k+1)$th-order term in (5.10) reduces to

$$P_{2k+1} = 1, \tag{5.11}$$

which results with (5.4) in a total number of parameters given by $P = K$.

As by using this kind of postdistorter, we do not consider any memory effects of the RF PA, we usually have a very limited linearization performance if the transmission signal is not narrowband. This is caused by the approximation of the frequency-domain Volterra kernels with complex constants over the input signal frequency range (see Ch. 3). If this kernels are almost flat (low-power RF PAs) or the transmission signal bandwidth becomes small, the approximation with complex constants is more accurate, which generally yields an acceptable linearization performance [13].

### 5.2.4 Simulation Results of Different Predistorters in an Indirect Learning Architecture

In this section we simulate the performance of three different complex Volterra series based predistorters (Volterra, memory-polynomial and static predistorter) which are applied to a

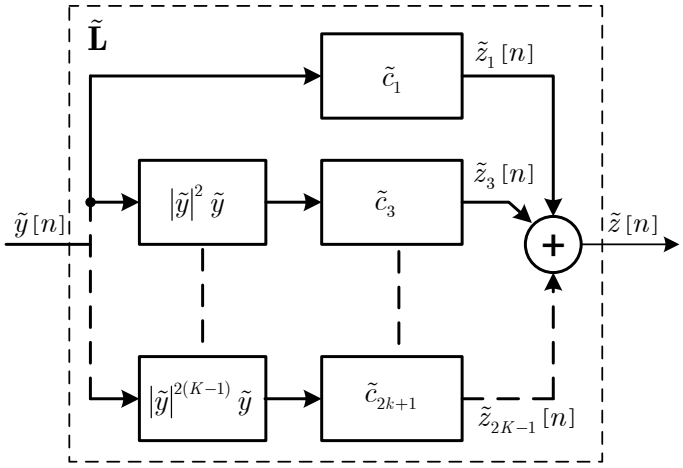


**Figure 5.6:** Complex baseband linearizer described by the nonlinear operator $\tilde{\mathbf{L}}$ in Fig. 5.3 for the case of static polynomials. The postdistorter is composed of a bank of static nonlinearities and the variable complex valued constants $\tilde{c}_{2k+1}$.

2.2-GHz 90-W Class AB RF power amplifier with an Infineon PTF210901 LDMOS transistor [28]. The identification of the unknown parameters is performed with an indirect learning architecture as shown in Fig. 5.3, where the optimum post-inverse (postdistorter) is determined by solving a linear optimization problem. Once we have found the optimum post-inverse (postdistorter) we copy the postdistorter parameters into the predistorter and hope that the post-inverse is a good approximation for the pre-inverse of the RF PA. This is in general satisfied if the error signal $\tilde{e}[n]$ in Fig. 5.3 becomes sufficiently small during the optimization process [22, 33]. A direct identification of the optimum pre-inverse would be more difficult because in this case we have to solve a nonlinear optimization problem [2], even if we use predistorters which are linear in their parameters.

In this simulation setup we employ a linear least-squares algorithm with truncated singular value decomposition [25, 9, 26] to find the optimum parameters of the post-inverse and to avoid the numerical instabilities as discussed in Chap. 4. The RF PA is simulated with the microwave circuit simulator Microwave Office® in harmonic balance mode, where the optimization and predistortion is performed in a MATLAB® environment.

To test the performance of the three different predistorters we use a four-carrier WCDMA signal with a bandwidth of approximately 20 MHz (to see the impact of memory effects) and a carrier frequency of 2.17 GHz. After the output signal of the RF PA is passed trough the 1st-zonal filter (BPF) in Fig. 5.2 to filter out the frequency components around the angular carrier frequency of $\omega_c$, the input signal $x(t)$ and the output signal $y(t)$ are down converted to the complex baseband domain.

Both signals are sampled with $\omega_c/(2\pi) = 122.88$ Mhz ($32 \times c$, where $c$ is the chip-rate of 3.84 MHz) which is sufficiently high to consider the out-off-band spectrum caused by the PA nonlinearity up to frequencies where the absolute power level becomes negligibly low.

To compare the performance of the different predistorters we measure the adjacent chan-

| | ACPR ($-5$ MHz) | ACPR ($+5$ MHz) | Number of parameters $P$ |
|---|---|---|---|
| Volterra predistorter | 20 dB | 20 dB | 42 |
| Static predistorter | 4 dB | 6 dB | 4 |
| Memory-polynomial predistorter | 17 dB | 16 dB | 11 |

**Table 5.1:** Adjacent channel power ratios (ACPR) between the linearized $2.2$-GHz $90$-W Class AB RF power amplifiers [28] and the RF power amplifier without linearization. The ACPR is evaluated with a root raised cosine filter ($B = 5$ MHz, roll off factor $R = 0.22$).

nel power ratio (ACPR $= 10\log(P_{in}/P_{adj})$, where $P_{in}$ and $P_{adj}$ denotes the inband and adjacent channel power respectively) of the linearized RF PA and the RF PA without linearization (highest nonlinear order of the post- and predistorter is assumed to be seven, root raised cosine filter with $B = 5$ MHz (consider only one carrier), roll off factor $R = 0.22$) in a frequency distance of $\pm 5$ Mhz from the centers of the 1st and 4th carrier respectively. The memory length $M_{2k+1}$ for the different orders of the nonlinearities of the postdistorters are chosen in such a way that we increase the memory length step by step beginning with the lowest order of the nonlinearity until the cost function becomes a minimum. If we use the Volterra predistorter in (5.1) with the memory length of $M_1 = 4$ for the 1st-order term, $M_3 = 2$ for the 3rd-order term and $M_5 = M_7 = 2$ respectively, we obtain the linearization performance depicted in Fig. 5.7, curve (d). The adjacent channel power can be considerably reduced (20 dB) compared to the RF PA without linearization. Although, the Volterra predistorters offer a good linearization performance, the number of parameters is large ($P = 42$) (see Tab. 5.1). To overcome this drawback, we can use static predistorters given in (5.10) to linearize the RF PA. In this case the number of parameters can be reduced to $P = 4$ (see Tab. 5.1). Nevertheless, as expected from the theory, the static predistorter performance is poor if we use a four-carrier WCDMA signal ($B = 20$ MHz), because we do not consider any memory effects of the RF PA (frequency-domain Volterra kernels are approximated with complex constants). The normalized power spectrum of this predistorter is shown in Fig. 5.7, curve (b). The memory-polynomial predistorter in (5.8) offers a good trade-off between complexity ($P = 11$) and linearization performance as shown in Fig. 5.7, curve (c) and Tab. 5.1 for the memory length of $M_1 = 4$, $M_3 = 3$, $M_5 = 2$ and $M_7 = 2$.

Figure 5.8 and Fig. 5.9 show the magnitude and phase responses of the complex linear filters (up to the 7th-order with the memory length given above) of the memory-polynomial post- and predistorter depicted in Fig. 5.5. The frequency responses are calculated by applying a Fourier transform to the identified complex impulse responses given in Tab. 5.2.

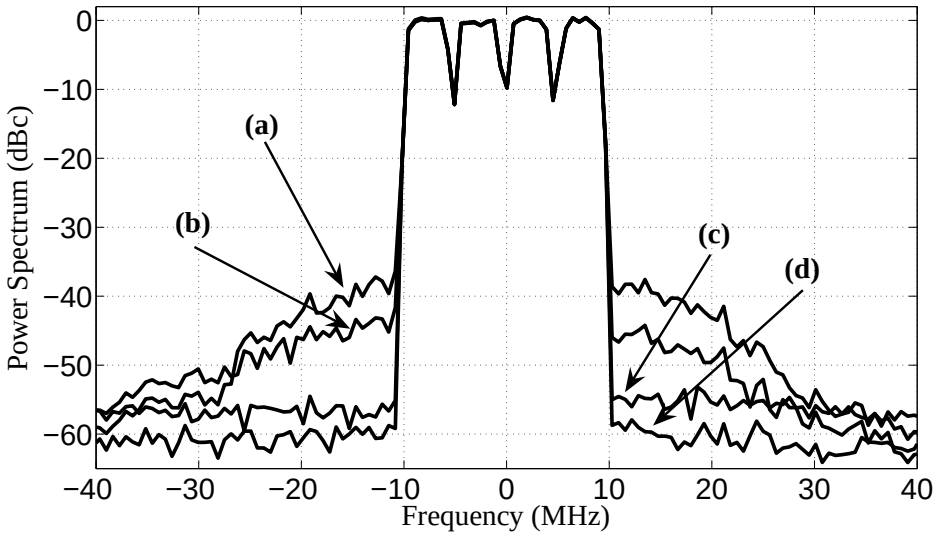


**Figure 5.7:** Comparison of the normalized power spectrum (PS) of the linearized (Volterra , memory-polynomial and static predistorter) 2.2-GHz 90-W Class AB RF power amplifiers [28] and the RF power amplifier without linearization. (a) PS of the RF PA without linearization, (b) PS of the static predistorter linearized RF PA , (c) PS of the memory-polynomial predistorter linearized RF PA , (d) PD of the Volterra predistorter linearized RF PA.

| $\tilde{g}_1[n]$ | $\tilde{g}_3[n]$ | $\tilde{g}_5[n]$ | $\tilde{g}_7[n]$ |
|---|---|---|---|
| $-1.144 + j\,0.322$ | $(-17 + j\,56)E^{-4}$ | $(-27 - j\,3)E^{-4}$ | $(285.8 - j\,45.1)E^{-6}$ |
| $0.324 - j\,0.04$ | $(147 + j\,17)E^{-4}$ | $(-12 + j)E^{-4}$ | $(43.2 + j\,1.7)E^{-6}$ |
| $(-54 - j\,73)E^{-3}$ | $(-15 - j\,17)E^{-4}$ | $0$ | $0$ |
| $(-20 + j\,45)E^{-3}$ | $0$ | $0$ | $0$ |

**Table 5.2:** Complex impulse responses of the linear filters (identified parameters of the post-inverse) of the memory-polynomial predistorter in Fig. 5.5.

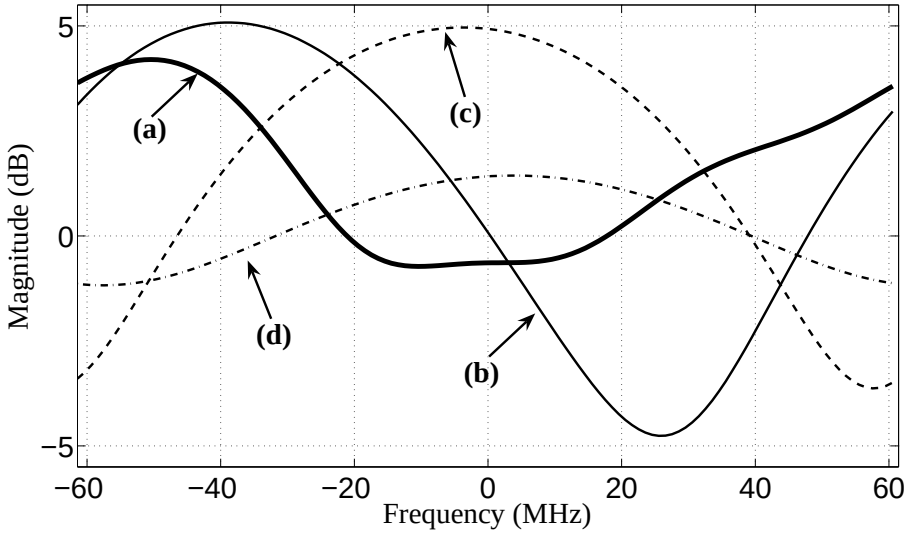


**Figure 5.8:** Normalized magnitude responses of the complex linear filters of the polynomial-predistorter depicted in Fig. 5.5, (a) $20\log\left|\tilde{G}_1(\exp(j\Omega/(2\pi T)))\right|$, (b) $20\log\left|\tilde{G}_3(\exp(j\Omega/(2\pi T)))\right| + 38$ dB, (c) $20\log\left|\tilde{G}_5(\exp(j\Omega/(2\pi T)))\right| + 53$ dB, (d) $20\log\left|\tilde{G}_7(\exp(j\Omega/(2\pi T)))\right| + 71$ dB.

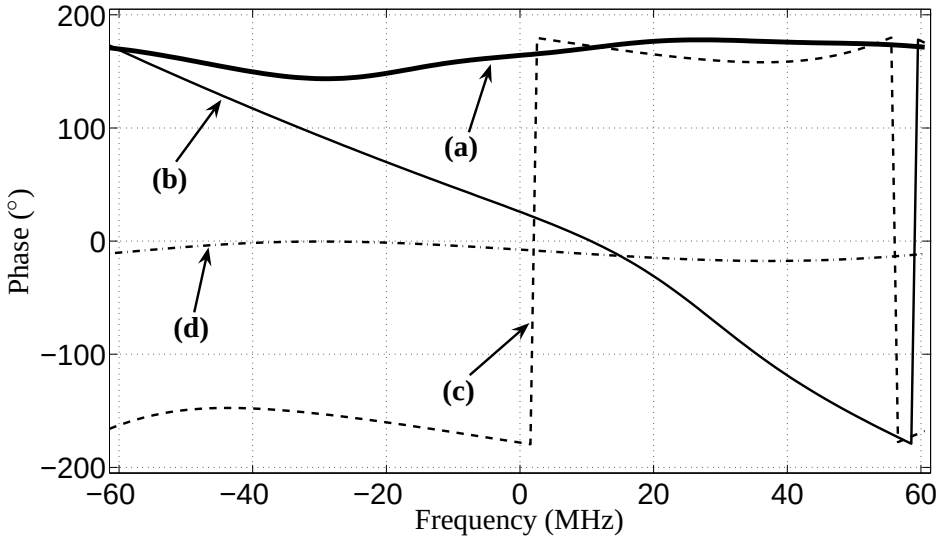


**Figure 5.9:** Phase responses of the complex linear filters of the polynomial-predistorter depicted in Fig. 5.5, (a) $\arg\{\tilde{G}_1(j\Omega/(2\pi T))\}$, (b) $\arg\{\tilde{G}_3(j\Omega/(2\pi T))\}$, (c) $\arg\{\tilde{G}_5(j\Omega/(2\pi T))\}$, (d) $\arg\{\tilde{G}_7(j\Omega/(2\pi T))\}$.

## 5.3 Sampling-Rate Requirements for Volterra Predistorters Based on a pth-Order Inverse

The identification of the Volterra postdistorter in an indirect-learning architecture shown in Fig. 5.3 is accomplished at a sampling frequency which fulfills the Nyquist theorem regarding the output signal bandwidth. Unfortunately we cannot perform in general a low-rate system identification and a Volterra kernel interpolation afterwards, as discussed in Ch. 4. To see this, we consider a cascade of two continuous-time complex baseband Volterra systems $\tilde{\mathbf{Q}}[\tilde{x}] = (\tilde{\mathbf{H}} \circ \tilde{\mathbf{R}})[\tilde{x}]$ as shown in Fig. 5.10, where $\tilde{\mathbf{R}}[\tilde{x}]$ and $\tilde{\mathbf{H}}[\tilde{z}]$ describe the predistorter and the RF PA baseband system respectively. The output signals of the predistorter and the RF PA baseband model in Fig. 5.10 are given by [56, 52].

$$\begin{aligned} \tilde{z}(t) &= \tilde{\mathbf{R}}[\tilde{x}(t)] \\ &= \sum_{k=0}^{K} \underbrace{\tilde{\mathbf{R}}_{2k+1}[\tilde{x}(t)]}_{\tilde{z}_{2k+1}(t)}, \end{aligned} \tag{5.12}$$

and

$$\begin{aligned} \tilde{y}(t) &= \tilde{\mathbf{H}}[\tilde{z}(t)] \\ &= \sum_{m=0}^{M} \tilde{\mathbf{H}}_{2m+1}[\tilde{z}(t)], \end{aligned} \tag{5.13}$$

where $2K+1$ and $2M+1$ denote the highest orders of the predistorter and RF PA baseband nonlinearities (see Fig. 5.11). The cascade of these Volterra series results in a new Volterra series, whose response to the scaled input signal $c\tilde{x}(t)$ is given by

$$\begin{aligned} \tilde{y}(t) &= \tilde{\mathbf{Q}}[c\tilde{x}(t)] \\ &= \sum_{k=0}^{N} c^{2k+1} \tilde{\mathbf{Q}}_{2k+1}[\tilde{x}(t)]. \end{aligned} \tag{5.14}$$

This system is depicted in Fig. 5.12, where the highest order of the nonlinearity of the cascade of the two Volterra systems is given by the product of the corresponding orders of the Volterra systems $2N+1 = (2K+1)(2M+1)$. The output signal $\tilde{y}(t)$ in (5.13) can be expressed with (5.12) and $\tilde{x}(t) \rightarrow c\tilde{x}(t)$ by

$$\begin{aligned} \tilde{y}(t) &= \tilde{\mathbf{H}}[\tilde{z}(t)] \\ &= \sum_{m=0}^{M} \tilde{\mathbf{H}}_{2m+1} \left[ \sum_{k=0}^{K} c^{2k+1} \tilde{z}_{2k+1}(t) \right] \\ &= \sum_{m=0}^{M} \underbrace{\sum_{n_1=1}^{2K+1} \cdots \sum_{n_{2m+1}=1}^{2K+1}}_{n_i \in \mathbb{N}_o} c^{n_1+\cdots+n_{2m+1}} \tilde{\mathbf{H}}_{2m+1} \left\{ \tilde{z}_{n_1}(t), \ldots, \tilde{z}_{2m+1}(t) \right\}, \end{aligned} \tag{5.15}$$

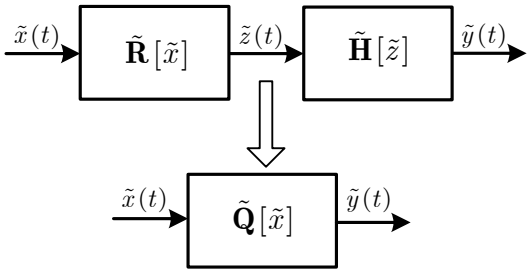


**Figure 5.10:** Cascade of two continuous-time Volterra systems where $\tilde{\mathbf{H}}[\tilde{z}]$ and $\tilde{\mathbf{R}}[\tilde{x}]$ describe the baseband RF power amplifier and the predistorter, respectively. The cascade of the two Volterra systems results in a new Volterra system described by $\tilde{\mathbf{Q}}[\tilde{x}] = (\tilde{\mathbf{H}} \circ \tilde{\mathbf{R}})[\tilde{x}]$.

where the $(2m+1)$st-linear operator in (5.15) can be expressed as a complex Volterra functional given by

$$\tilde{\mathbf{H}}_{2m+1}\{\tilde{z}_{n_1}(t), \ldots, \tilde{z}_{2m+1}(t)\} = \int_0^\infty \cdots \int_0^\infty \tilde{h}_{2m+1}(\tau_1, \ldots, \tau_{2m+1}) \times \prod_{i=1}^{m+1} \tilde{z}_{n_i}(t-\tau_i) \prod_{i=m+2}^{2m+1} \tilde{z}^*_{n_i}(t-\tau_i)\, d\tau_1 \cdots d\tau_{2m+1}. \tag{5.16}$$

The Volterra operators $\tilde{\mathbf{Q}}_{2k+1}$ in Fig. 5.12 can be expressed in terms of the Volterra operators $\tilde{\mathbf{R}}_{2m+1}$ and $\tilde{\mathbf{H}}_{2l+1}$ by equating the corresponding powers of $c$ in (5.14) and (5.15) [55, 52]. The resulting Volterra system is illustrated in Fig. 5.13 for $M = K = 1$, where the 1st and 3rd-order operators are expressed by

$$\begin{aligned} \tilde{\mathbf{Q}}_1[\tilde{x}] &= (\tilde{\mathbf{H}}_1 \circ \tilde{\mathbf{R}}_1)[\tilde{x}] \\ \tilde{\mathbf{Q}}_3[\tilde{x}] &= (\tilde{\mathbf{H}}_1 \circ \tilde{\mathbf{R}}_3)[\tilde{x}] + (\tilde{\mathbf{H}}_3 \circ \tilde{\mathbf{R}}_1)[\tilde{x}]. \end{aligned} \tag{5.17}$$

To remove the 3rd-order nonlinear distortion of the RF PA baseband system $\tilde{\mathbf{H}}$, we set the 3rd-order operator in (5.17), $\tilde{\mathbf{Q}}_3[\tilde{x}] = 0$. If we preserve the linear response of the RF PA baseband model ($\tilde{\mathbf{Q}}_1[\tilde{x}] = \tilde{\mathbf{H}}_1[\tilde{x}]$) we obtain the 3rd-order predistorter with (5.17) given by

$$\begin{aligned} \tilde{\mathbf{R}}_1[\tilde{x}] &= 1 \\ \tilde{\mathbf{R}}_3[\tilde{x}] &= (-\tilde{\mathbf{H}}_1^{-1} \circ \tilde{\mathbf{H}}_3)[\tilde{x}]. \end{aligned} \tag{5.18}$$

The higher order operators $\tilde{\mathbf{Q}}_5, \ldots, \tilde{\mathbf{Q}}_9$ in Fig. 5.13 are not explicitly calculated because they represent the added higher order nonlinear distortion (was not present without predistortion), which cannot be adjusted independently once the predistorter has been determined.

If we insert the calculated predistorter operators from (5.18) into the operators in (5.17), we obtain a Volterra system where the 3rd-order nonlinear distortion has been completely removed (see Fig. 5.14).

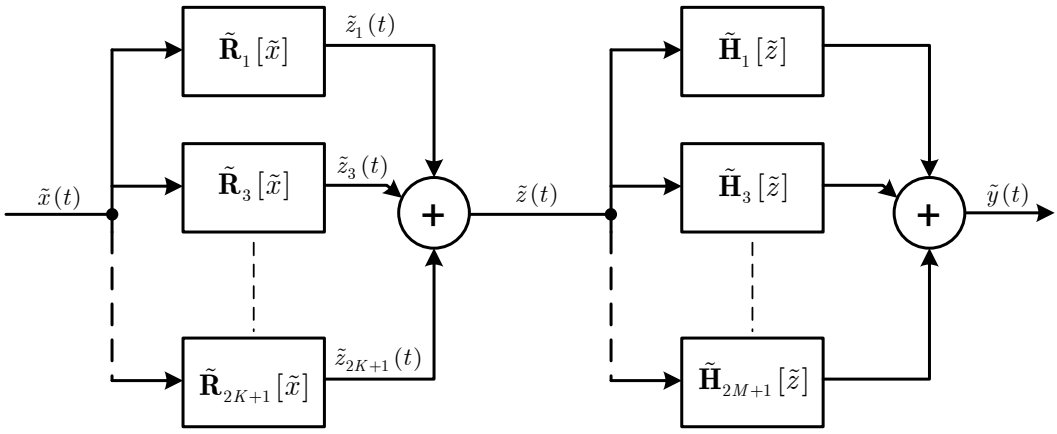


**Figure 5.11:** Detailed block diagram of the cascade of two complex baseband Volterra systems (predistorter and RF PA baseband system). Both systems are purely described by odd-order nonlinear operators.

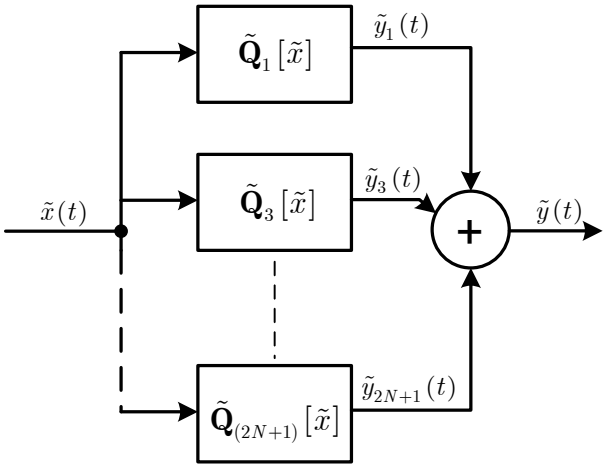


**Figure 5.12:** Complex baseband Volterra system which develops from the cascade in Fig. 5.10 and Fig. 5.11. The highest order of nonlinearity is given by $2N+1 = (2K+1)(2M+1)$ where $2K+1$ and $2M+1$ are the highest nonlinear orders of the predistorter and RF power amplifier, respectively.

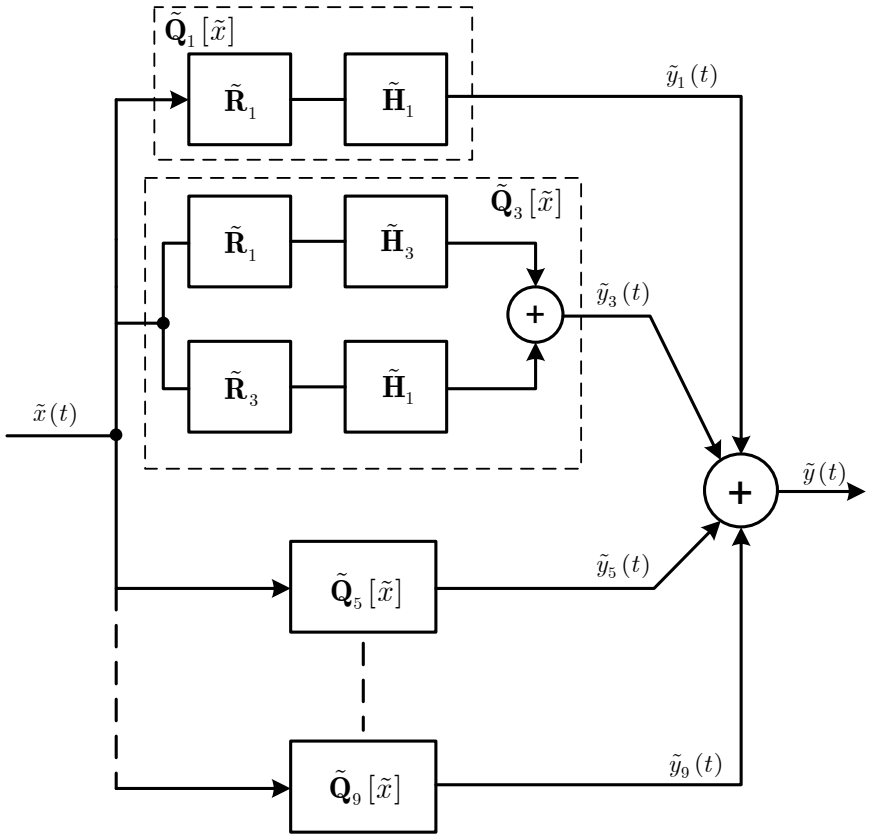


**Figure 5.13:** Complex baseband Volterra system from Fig. 5.12 which develops from the cascade connection of two 3rd-order Volterra systems. The system is implemented in terms of the corresponding Volterra operators $\tilde{\mathbf{H}}_{2k+1}$ of the RF PA baseband system and the Volterra operators $\tilde{\mathbf{R}}_{2k+1}$ of the predistorter, respectively.

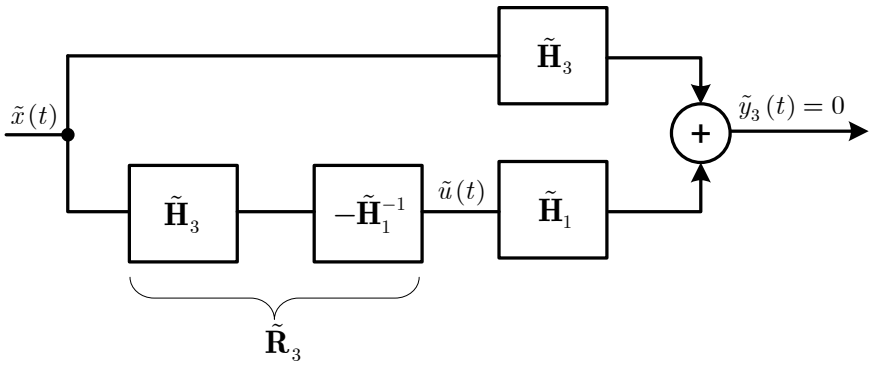


**Figure 5.14:** Block diagram of the 3rd-order Volterra operator $\tilde{\mathbf{Q}}_3$ from Fig. 5.13 which incorporates the implemented 3rd-order term of the predistorter $\tilde{\mathbf{R}}_3 = -\tilde{\mathbf{H}}_1^{-1} \circ \tilde{\mathbf{H}}_3$ in terms of the RF PA baseband system operators.

As predistorters are usually implemented in the discrete-time domain, they must operate on a sufficiently high sampling frequency $\omega_s \geq 2B(2K+1)$. The term $(2K+1)$ denotes the highest order of the nonlinear distortion caused by the RF PA baseband system which should be removed, and $B$ denotes again the bandwidth of the input signal.

If we consider the time-domain output signal of the 3rd-order predistorter in Fig. 5.14

$$\begin{aligned}\tilde{u}(t) &= \tilde{\mathbf{R}}_3[\tilde{x}(t)] \\ &= \int_0^\infty \int_0^\infty \int_0^\infty \tilde{r}_3(\tau_1,\tau_2,\tau_3)\,\tilde{x}(t-\tau_1)\,\tilde{x}(t-\tau_2)\,\tilde{x}^*(t-\tau_3)\,d\tau_1\,d\tau_2\,d\tau_3 \end{aligned} \tag{5.19}$$

in the three-dimensional frequency space, we obtain the output signal

$$\tilde{U}_{(3)}(\omega_1,\omega_2,\omega_3) = \tilde{R}_3(\omega_1,\omega_2,\omega_3)\,\tilde{X}(\omega_1)\,\tilde{X}(\omega_2)\,\tilde{X}^*(-\omega_3) \tag{5.20}$$

which is band-limited to $\pm B$ in each of the three frequency variables. Therefore, it seems that the 3rd-order nonlinear system $\tilde{\mathbf{R}}_3$ in Fig. 5.14 could be identified on a sampling frequency which is just twice the input signal bandwidth because the function in (5.20) is zero outside the cube shown in Fig. 5.15. But if we consider the frequency-domain Volterra kernel of the cascade connection $-\tilde{\mathbf{H}}_1^{-1} \circ \tilde{\mathbf{H}}_3$ in (5.18) we obtain the new frequency-domain Volterra kernel given by [52] $\tilde{R}_3(\omega_1,\omega_2,\omega_3) = -\tilde{H}_3(\omega_1,\omega_2,\omega_3)\tilde{H}_1^{-1}(\omega_1+\omega_2+\omega_3)$, which yields with (5.20)

$$\tilde{U}_{(3)}(\omega_1,\omega_2,\omega_3) = -\tilde{H}_3(\omega_1,\omega_2,\omega_3)\tilde{H}_1^{-1}(\omega_1+\omega_2+\omega_3)\,\tilde{X}(\omega_1)\,\tilde{X}(\omega_2)\,\tilde{X}^*(-\omega_3). \tag{5.21}$$

From (5.21), we realize that even if $|\omega_i| \leq B$ for $i = 1,2,3$ (point inside the cube of Fig. 5.15), we generally need the frequency response of the inverse linear system $\tilde{H}_1^{-1}(\omega)$ for $\omega > B$. Unfortunately, this information cannot be obtained from a system identification scheme whose input signal bandwidth is below $3B$.

If we consider the time-domain signal in (5.19) and calculate the corresponding frequency-domain signal with (2.40) and (5.21), we obtain

$$\begin{aligned}\tilde{U}(\omega) = -H_1^{-1}(\omega)\frac{1}{(2\pi)^2}\int_{-\infty}^{\infty}\int_{-\infty}^{\infty} &\tilde{H}_3(\omega-v_1,v_1-v_2,v_2)\tilde{X}(\omega-v_1)\tilde{X}(v_1-v_2) \\ &\times\tilde{X}^*(-v_2)\,dv_1\,dv_2. \end{aligned} \tag{5.22}$$

From (5.22), we realize that the output signal $\tilde{U}(\omega)$ is determined as expected by the product of the frequency-domain output signal of the 3rd-order nonlinear part of the RF PA baseband system (integral expression) and the frequency response of the linear part of the RF PA baseband system. This can also be explained graphically, cf. Fig. 5.15. The integrand within the double-integral in Fig. 5.15 describes a plane inside a cube which depends on the angular frequency $\omega$. The frequency-domain output signal $\tilde{U}(\omega)$ is calculated by integrating the three dimensional function $\tilde{U}_{(3)}(\omega_1,\omega_2,\omega_3)$ along this plane.

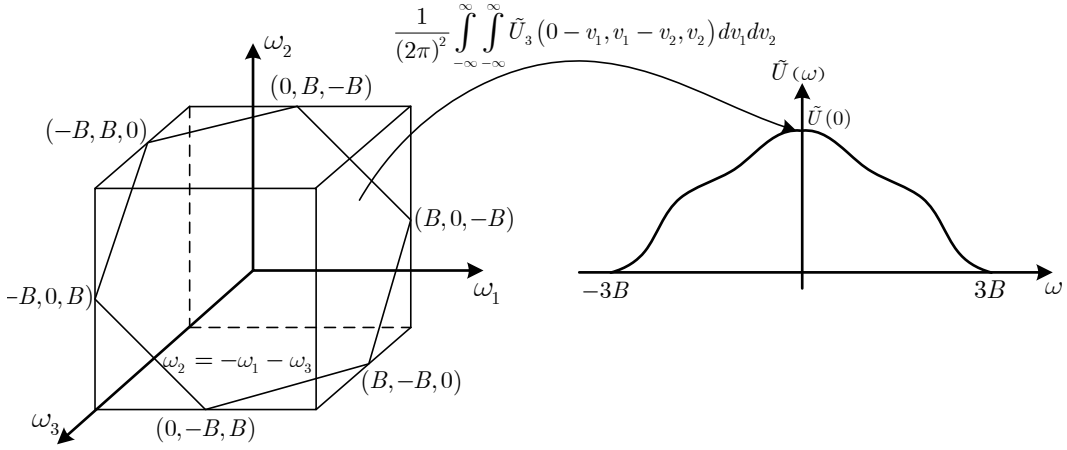


**Figure 5.15:** Frequency-domain output signal of a 3rd-order nonlinear system. Depending on the frequency $\omega$, we have different planes within a cube with an edge-length of $2B$ (determined by the input signal bandwidth). The integration of $\tilde{U}_{(3)}(\omega_1,\omega_2,\omega_3)$ along these planes yields the corresponding frequency response $\tilde{U}(\omega)$.

## 5.4 Predistorters Based on Low Sampling Frequency Identification and Volterra Kernel Interpolation

In this section, we focus on a simple predistortion architecture proposed in [24], which makes it possible to apply the low sampling rate system identification and Volterra kernel interpolation as shown in Ch. 4. The discrete-time predistorter $\tilde{\mathbf{L}}$ is composed of a parallel structure of a delay operator $z^{-\delta}$ and a cascade of the purely nonlinear part $\breve{\mathbf{H}}_P$ with the inverse of the linear part $\breve{\mathbf{H}}_1$ of an operator $\breve{\mathbf{H}}$, described by the equation $\tilde{\mathbf{L}} \equiv z^{-\delta}+\breve{\mathbf{H}}_1^{-1}\circ\breve{\mathbf{H}}_P$. The architecture of $\tilde{\mathbf{L}}$ as part of the overall system is shown in Fig. 5.16, where $\tilde{\mathbf{H}}$ describes the RF PA baseband model in terms of its linear operator $\tilde{\mathbf{H}}_1$ and its nonlinear operator $\tilde{\mathbf{H}}_P$ in the discrete-time domain. The highest order of the RF PA baseband model is denoted by $P \in \mathbb{N}_o$. The composition of the predistorter and the RF PA baseband system in Fig. 5.16

$$\tilde{\mathbf{V}} = \underbrace{\left(\tilde{\mathbf{H}}_1+\tilde{\mathbf{H}}_P\right)}_{\tilde{\mathbf{H}}} \circ \underbrace{\left(z^{-\delta}+\breve{\mathbf{H}}_1^{-1}\circ\breve{\mathbf{H}}_P\right)}_{\tilde{\mathbf{L}}} \tag{5.23}$$

yields a linearization if $\left\|\tilde{\mathbf{H}}_P\right\| \ll \left\|\tilde{\mathbf{H}}_1\right\|$ with $\breve{\mathbf{H}}_1 = -\tilde{\mathbf{H}}_1$ and $\breve{\mathbf{H}}_P = \tilde{\mathbf{H}}_P$, where the operator norm corresponds to the signal norm with $\left\|\tilde{\mathbf{H}}_1\right\| \equiv \sup_{\|u\|<1}\left\|\tilde{\mathbf{H}}_1 u\right\|$. Qualitatively this becomes clear by decomposing (5.23) as

$$\tilde{\mathbf{V}} = z^{-\delta}\circ\tilde{\mathbf{H}}_1 - z^{-\delta}\circ\tilde{\mathbf{H}}_P + \tilde{\mathbf{H}}_P\circ(z^{-\delta}-\tilde{\mathbf{H}}_1^{-1}\circ\tilde{\mathbf{H}}_P) \tag{5.24}$$

where we used the fact that the delay operator commutes with all time-invariant operators and $\tilde{\mathbf{H}}_1\circ\tilde{\mathbf{H}}_1^{-1} = z^{-\delta}$.

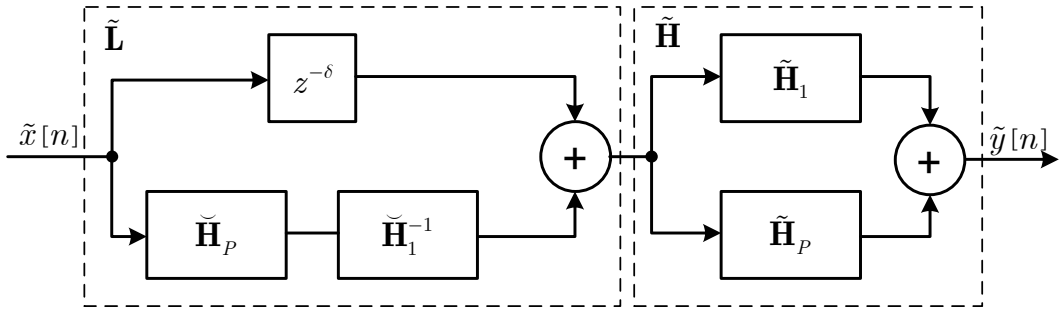


**Figure 5.16:** Cascade of a simple predistorter $\tilde{\mathbf{L}}$ and the RF power amplifier baseband model $\tilde{\mathbf{H}}$. The amplifier is composed of its linear and nonlinear parts with the highest order of nonlinearity of $P$. If the nonlinearity is weak, which is expressed by $\|\tilde{\mathbf{H}}_P\| \ll \|\tilde{\mathbf{H}}_1\|$, the RF power amplifier baseband model can be linearized with $\tilde{\mathbf{L}}$ ($\breve{\mathbf{H}}_1 = -\tilde{\mathbf{H}}_1$ and $\breve{\mathbf{H}}_P = \tilde{\mathbf{H}}_P$), which yields $\tilde{y}[n] \approx \tilde{\mathbf{H}}_1[\tilde{x}[n-\delta]]$.

The above assumption on weak nonlinearity implies $\|\tilde{\mathbf{H}}_P \circ \tilde{\mathbf{H}}_1^{-1} \circ \tilde{\mathbf{H}}_P\| \ll \|\tilde{\mathbf{H}}_P\|$, such that we can approximate the last term in (5.24) as $\tilde{\mathbf{H}}_P \circ (z^{-\delta} - \tilde{\mathbf{H}}_1^{-1} \circ \tilde{\mathbf{H}}_P) \approx \tilde{\mathbf{H}}_P \circ z^{-\delta}$. Thus the overall system response is obtained as $\tilde{\mathbf{V}} \approx z^{-\delta} \circ \tilde{\mathbf{H}}_1$. Therefore the time-domain output signal of the cascade of the predistorter $\tilde{\mathbf{L}}$ and the RF PA baseband system $\tilde{\mathbf{H}}$ in Fig. 5.16 yields $\tilde{y}[n] \approx \tilde{\mathbf{H}}_1[\tilde{x}[n-\delta]]$.

A quantitative analysis of the linearization performance of the architecture in Fig. 5.16 can be done if we employ the Volterra series representation of the involved operators. Subsequently, the set of frequency-domain Volterra kernels $\tilde{V}_{2p+1}(z_1, \ldots, z_{2p+1})$ for $p = 0, 1, 2, \ldots, (P^2-1)/2$ of $\tilde{\mathbf{V}}$ is expressed in terms of the Volterra kernels of the operators according to the composition in (5.23). If we apply the $\mathcal{Z}$-domain cascade rule for discrete-time Volterra series [52] to $\tilde{\mathbf{V}} = \tilde{\mathbf{H}} \circ \tilde{\mathbf{L}}$ and arrange the indices in order to consider only the present odd-order Volterra kernels, we obtain

$$\tilde{V}_{2p+1}(z_1, \ldots, z_{2p+1}) = \sum_{n=0}^{p} \underbrace{\sum_{m_1=1} \cdots \sum_{m_{2n+1}=1}}_{\substack{u(2n+1)=2p+1 \\ m_i \in \mathbb{N}_o}} \Big\{ \tilde{H}_{2n+1}(z_{l(1)} \cdots z_{u(1)}, \ldots, z_{l(2n+1)} \cdots z_{u(2n+1)}) \prod_{k=1}^{2n+1} \tilde{L}_{m_k}(z_{l(k)}, \ldots, z_{u(k)}) \Big\}, \tag{5.25}$$

where the lower and upper index bound functions are defined by $l(k) \equiv l(m_1, \ldots, m_{k-1}) = 1 + \sum_{j=1}^{k-1} m_j$, and $u(k) \equiv u(m_1, \ldots, m_k) = \sum_{j=1}^{k} m_j$, respectively with $l(1) = 1$. If we substitute the Volterra kernels of the cascade of the nonlinear operator $\breve{\mathbf{H}}_P$ and the linear operator $\breve{\mathbf{H}}_1^{-1}$ given by (see Fig. 5.17)

$$\tilde{L}_{2p+1}(z_1, \ldots, z_{2p+1}) = \breve{H}_{2p+1}(z_1, \ldots, z_{2p+1}) \breve{H}_1^{-1}(z_1 \cdots z_{2p+1}) \tag{5.26}$$

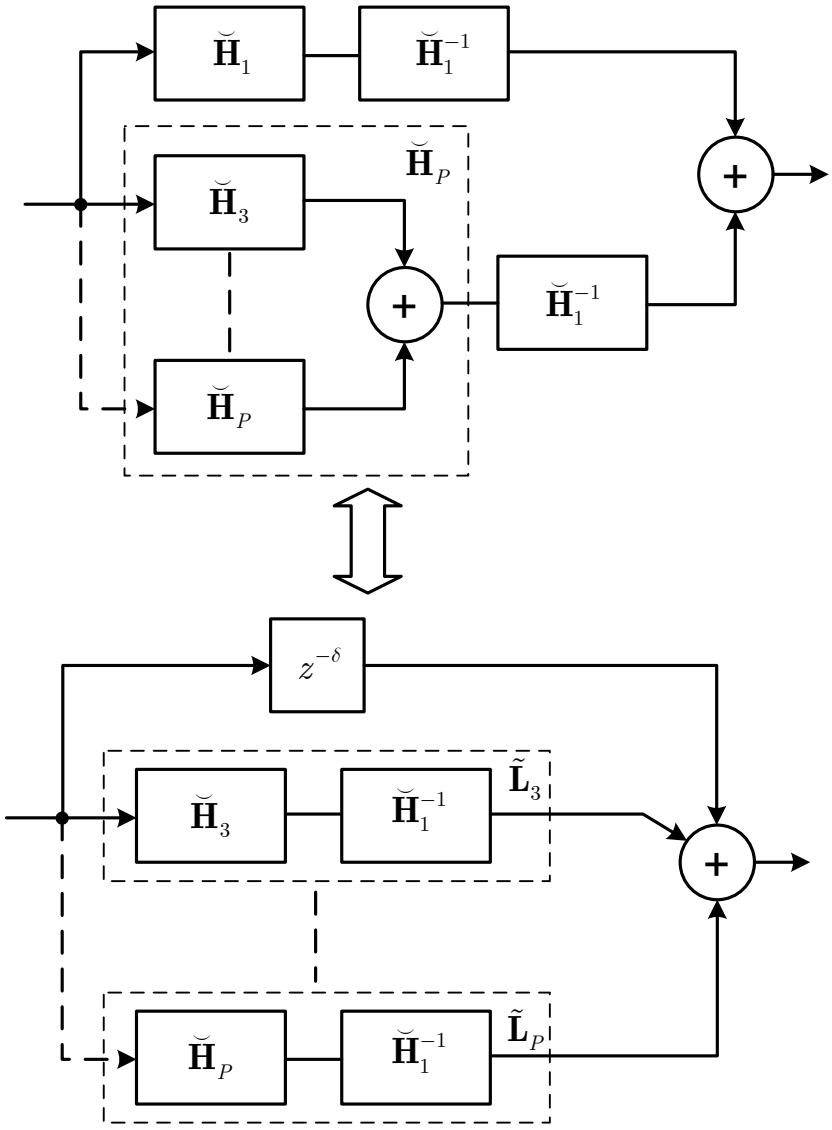


**Figure 5.17:** Equivalent representations of the predistorter structure $\tilde{\mathbf{L}}$ in Fig. 5.16 which is based on the superposition property of the linear operator $\breve{\mathbf{H}}_1^{-1}$. The resulting Volterra kernels $\tilde{\mathbf{L}}_{2p+1}$ are determined by the cascade connection of the kernels $\breve{\mathbf{H}}_{2p+1}$ and the linear kernel $\breve{\mathbf{H}}_1^{-1}$.

with $\tilde{L}_1(z) = \breve{H}_1(z)\breve{H}_1^{-1}(z) = z^{-\delta}$ into (5.25), we obtain

$$\tilde{V}_{2p+1}(z_1,\ldots,z_{2p+1}) = \sum_{n=0}^{p} \underbrace{\sum_{m_1=1} \cdots \sum_{m_{2n+1}=1}}_{\substack{u(2n+1)=2p+1 \\ m_i\in\mathbb{N}_o}} \Big\{ \tilde{H}_{2n+1}(z_{l(1)}\cdots z_{u(1)},\ldots,z_{l(2n+1)}\cdots \cdots z_{u(2n+1)}) \prod_{k=1}^{2n+1} \breve{H}_{m_k}(z_{l(k)},\ldots,z_{u(k)})\breve{H}_1^{-1}(z_{l(k)}\cdots z_{u(k)}) \Big\}. \tag{5.27}$$

Figure 5.17 depicts the expanded predistorter structure $\tilde{\mathbf{L}}$ from Fig. 5.16 and its equivalent structure (based on the superposition principle of the linear operator $\breve{\mathbf{H}}_1^{-1}$) which is used in (5.27).

If we separate the terms in (5.27) for $n = 0$ and $n = p$, (5.27) results in

$$\begin{aligned}\tilde{V}_{2p+1}(z_1,\ldots,z_{2p+1}) = {} & \tilde{H}_1(z_1\cdots z_{2p+1})\breve{H}_1^{-1}(z_1\cdots z_{2p+1})\breve{H}_{2p+1}(z_1,\ldots,z_{2p+1}) \\ & + \tilde{H}_{2p+1}(z_1,\ldots,z_{2p+1})(z_1\cdots z_{2p+1})^{-\delta} \\ & + \sum_{n=1}^{p-1} \underbrace{\sum_{m_1=1} \cdots \sum_{m_{2n+1}=1}}_{\substack{u(2n+1)=2p+1 \\ m_i\in\mathbb{N}_o}} \Big\{ \tilde{H}_{2n+1}(z_{l(1)}\cdots z_{u(1)},\ldots,z_{l(2n+1)} \\ & \cdots z_{u(2n+1)}) \prod_{k=1}^{2n+1} \breve{H}_1^{-1}(z_{l(k)}\cdots z_{u(k)})\breve{H}_{m_k}(z_{l(k)},\ldots,z_{u(k)}) \Big\},\end{aligned} \tag{5.28}$$

where the first two summands in (5.28) equalize if the linear frequency-domain Volterra kernel is given by

$$\breve{H}_1^{-1}(z) = -\tilde{H}_1^{-1}(z)z^{-\delta}, \tag{5.29}$$

and the higher order frequency-domain Volterra kernels for $p \geq 1$ are

$$\breve{H}_{2p+1}(z_1,\ldots,z_p) = \tilde{H}_{2p+1}(z_1,\ldots,z_p). \tag{5.30}$$

Thus a system with a perfectly adjusted predistorter results in the following odd-order

frequency-domain Volterra kernels

$$
\begin{aligned}
&\tilde{V}_1(z) = \tilde{H}_1(z)z^{-\delta} \\
&\tilde{V}_3(z_1, z_2, z_3) = 0 \\
&\qquad\vdots \\
&\tilde{V}_{2p+1}(z_1, \ldots, z_{2p+1}) = -\sum_{n=1}^{p-1} \underbrace{\sum_{m_1=1} \cdots \sum_{m_{2n+1}=1}}_{\substack{u(2n+1)=2p+1 \\ m_i \in \mathbb{N}_o}} \Big\{ \tilde{H}_{2n+1}(z_{l(1)} \cdots z_{u(1)}, \ldots, z_{l(2n+1)} \\
&\qquad\qquad \cdots z_{u(2n+1)}) \prod_{k=1}^{2n+1} \tilde{H}_1^{-1}(z_{l(k)} \cdots z_{u(k)})(z_{l(k)} \cdots z_{u(k)})^{-\delta} \\
&\qquad\qquad \times \tilde{H}_{m_k}(z_{l(k)}, \ldots, z_{u(k)}) \Big\}.
\end{aligned}
\tag{5.31}
$$

Although perfect equalization is only possible for the third order Volterra kernel $\tilde{V}_3(z_1, z_2, z_3)$, the resulting distortion of the predistorted PA output signal is much lower compared to the non-compensated PA if $\left\|\tilde{\mathbf{H}}_P\right\| \ll \left\|\tilde{\mathbf{H}}_1\right\|$, because all the kernels $\tilde{V}_{2p+1}(z_1, \ldots, z_{2p+1})$ for $p \geq 2$ in (2.32) incorporate the multiplicative inverse of the linear kernel $\tilde{H}_1^{-1}(z)$.

To establish a relation to the more general linearization method of the $p$th-order inverse [56] we consider the special case of the 3rd-order inverse for a system described by the operator decomposition $\tilde{\mathbf{H}} = \tilde{\mathbf{H}}_1 + \tilde{\mathbf{H}}_3 + \tilde{\mathbf{H}}_P$, where the operator $\tilde{\mathbf{H}}_P$ contains all odd-order operator components with $p > 3$. The predistorter based on the 3rd-order inverse, where the linear frequency response is not equalized, is given with (5.18) by $\breve{\mathbf{L}} = z^{-\delta} \circ (1 - \tilde{\mathbf{H}}_1^{-1} \circ \tilde{\mathbf{H}}_3)$, while according to (5.23) the applied predistorter is $\tilde{\mathbf{L}} = z^{-\delta} \circ (1 - \tilde{\mathbf{H}}_1^{-1} \circ (\tilde{\mathbf{H}}_3 + \tilde{\mathbf{H}}_P))$. From that, it is obvious that for a 3rd-order nonlinear model $\tilde{\mathbf{H}}$, the two predistortion schemes coincide. The comparison of the two schemes in case of a higher-order inverse of a system e.g. the 5th-order $\tilde{\mathbf{H}} = \tilde{\mathbf{H}}_1 + \tilde{\mathbf{H}}_3 + \tilde{\mathbf{H}}_5 + \tilde{\mathbf{H}}_P$ will point out an essential difference of which the important consequences for a low-rate implementation are discussed in the next subsection.

### 5.4.1 Predistortion and Upsampling

As shown in Ch. 4, the low sampling-rate identified RF PA baseband model $\breve{\mathbf{V}} = \breve{\mathbf{V}}_1 + \breve{\mathbf{V}}_P$ can be upsampled to a higher sampling frequency such that it exactly reproduces the output of the RF PA baseband system $\tilde{\mathbf{H}}$. The natural question posed in this section is whether or not we can apply the upsampled model of Ch. 4 for the predistortion architecture shown in Fig. 5.16 with $\breve{H}_1^{-1}(z) = -\breve{V}_1^{-1}(z^P)z^{-\delta}$ and $\breve{H}_{2p+1}(z_1, \ldots, z_{2p+1}) = \breve{V}_{2p+1}(z_1^P, \ldots, z_{2p+1}^P)$ such that it yields the identical result as the corresponding application of kernels of $\tilde{\mathbf{H}}$ in (5.29) and (5.30). As the model is able to reproduce the exact output of the RF PA baseband system, one is tempted to answer this question positively. Unfortu-

nately, they do not perform in the same way when applied to the predistortion architecture. To see this, first note that the kernels of the upsampled model and the RF PA baseband system coincide only over the input signal bandwidth. Reconsidering the structure of the predistorter $\tilde{\mathbf{L}} = z^{-\delta} + \breve{\mathbf{H}}_1^{-1} \circ \breve{\mathbf{H}}_P$ reveals that, due to the spectral regrowth of $\breve{\mathbf{H}}_P$, the linear operator $\breve{\mathbf{H}}_1^{-1}$ acts on a signal with a bandwidth that is in general $P$ times the input signal bandwidth. Thus, the output signal of the upsampled version of $\breve{\mathbf{H}}_1^{-1}$ differs from the correct version given in (5.29) and (5.30) by an amount that depends on the flatness of the linear frequency response of the RF PA baseband system. The flatter the response is, the less the effect of the periodic extension in the upsampled version outside the input signal bandwidth. Once we have copied the linear kernel of the upsampled inverse $\breve{V}_1^{-1}(z^P)$ of the RF PA into the predistorter, we can correct the periodic extensions (caused by the low-rate identification) of $\breve{H}_1^{-1}(z)$ by adapting the corresponding filter parameters with standard linear optimization algorithms (e.g. least-mean-square algorithm). Although, the linear filter $\breve{H}_1^{-1}$ is operated on the high sampling rate, the modification of the filter parameters is accomplished on the low sampling rate. The initialization is taken to be the upsampled response $-\breve{V}_1^{-1}(z^P)z^{-\delta}$. The adaptation process is depicted in Fig. 5.18.

In this context, an important property of the applied predistortion architecture $\tilde{\mathbf{L}} = z^{-\delta} + \breve{\mathbf{H}}_1^{-1} \circ \breve{\mathbf{H}}_P$ becomes evident. As the operator $\breve{\mathbf{H}}_P$ with the kernels $\breve{H}_{2p+1}(z_1, \ldots, z_{2p+1}) = \breve{V}_{2p+1}(z_1^P, \ldots, z_{2p+1}^P)$ operates on the input signal bandwidth, its response is identical to the response of $\breve{\mathbf{H}}_P$ with $\tilde{H}_{2p+1}(z_1, \ldots, z_{2p+1})$ and thus requires no adaptation.

This feature allows for efficient low-rate adaptive predistortion, where only the few parameters of $\breve{H}_1^{-1}(z)$ need to be tuned, while the mass of parameters from the higher-order frequency responses require no adaptation. This stands in contrast to the application of the upsampled kernels $\breve{V}_{2p+1}(z_1^P, \ldots, z_{2p+1}^P)$ to the $p$th-order inverse architecture.

In the case of upsampled kernels, every composition of operators where a nonlinear operator $\tilde{\mathbf{H}}_{2k+1}$ with $k > 0$ precedes one or more operators, an adaptation of all consecutive operators following $\tilde{\mathbf{H}}_{2k+1}$ is necessary to yield equivalent performance to a $5$th-order inverse utilizing the correct high-rate kernels of the RF PA baseband system $\tilde{\mathbf{H}}$.

The overall system including the identification of the low-rate model $\breve{\mathbf{V}}$ of the system $\tilde{\mathbf{H}}$, predistorter $\tilde{\mathbf{L}}$ with its optional adaptation, and the kernel upsampling is shown in Fig. 5.18. The switch in Fig. 5.18 indicates that for the initial identification of the low-rate model $\breve{\mathbf{V}}$ the predistorter is bypassed. Note that simultaneous low-rate identification and predistortion is generally not possible, because of the spectral regrowth at the output of the predistorter.

In the derivations above we have focused on Volterra predistorters, although we can employ other nonlinear models as e.g. memory-polynomials or models based on frequency-domain expansion, if they are sufficient to model the RF PA who should be linearized.

### 5.4.2 Application and Simulation Results

To evaluate the performance of the proposed low-rate predistortion scheme in Fig. 5.18, the linearization of two different PAs for wireless and wireline transmission systems are performed. The $5$th-order complex baseband Volterra model in Fig. 5.19 is used to simulate the behavior of an RF PA for wireless applications.

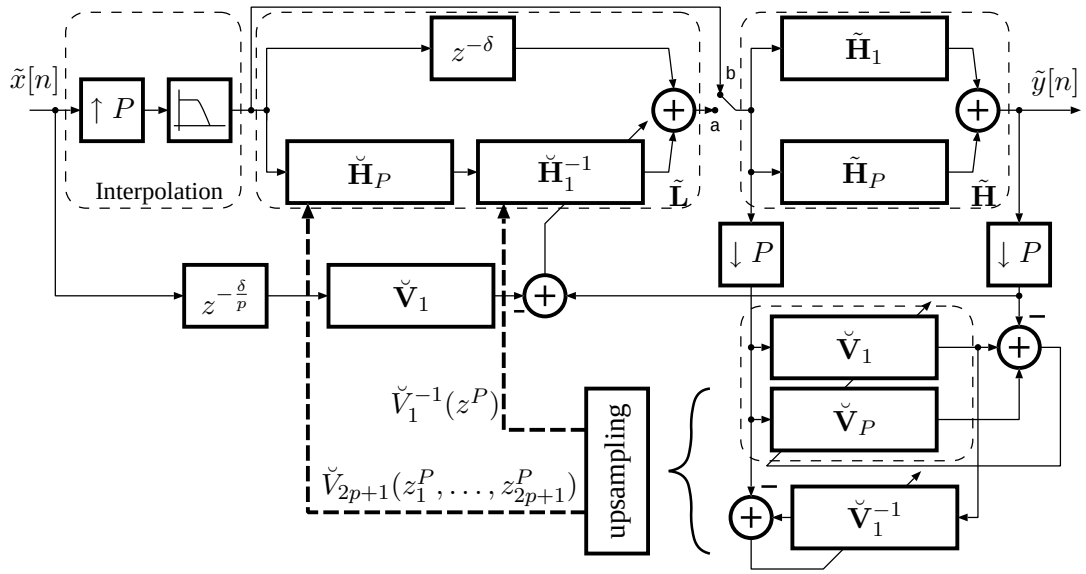


**Figure 5.18:** Multi-rate digital predistortion architecture $\tilde{\mathbf{H}} \circ \tilde{\mathbf{L}}$ composed of a high-rate system $\tilde{\mathbf{H}}$, a high-rate predistorter $\tilde{\mathbf{L}} = z^{-\delta} + \breve{\mathbf{H}}_1^{-1} \circ \tilde{\mathbf{H}}_P$ with an optional low-rate adaptation of the linear operator $\breve{\mathbf{H}}_1^{-1}$, a low-rate system identification $\breve{\mathbf{V}}$, and Volterra kernel upsampling (zero insertion); switch position $b$ for identification and position $a$ for predistortion; with $\delta = nP$

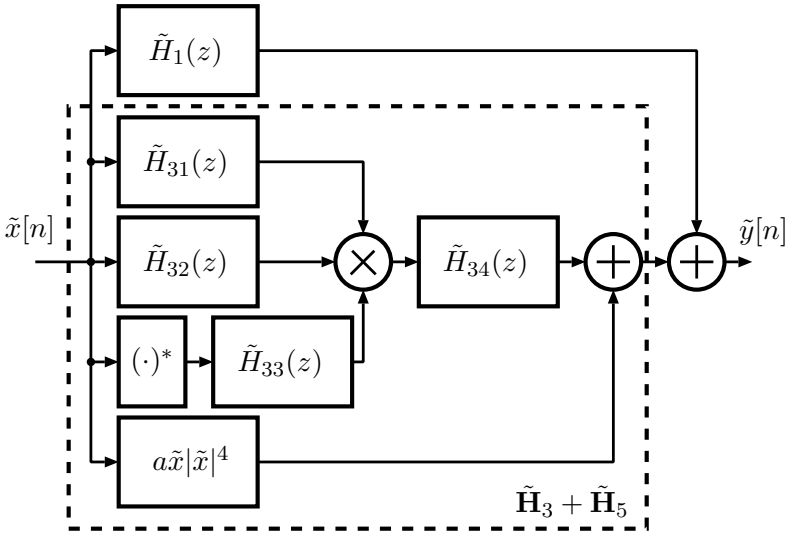


**Figure 5.19:** Complex baseband Volterra model of a 5th-order RF power amplifier for wireless applications, $\tilde{\mathbf{H}} = \tilde{\mathbf{H}}_1 + \tilde{\mathbf{H}}_3 + \tilde{\mathbf{H}}_5$.

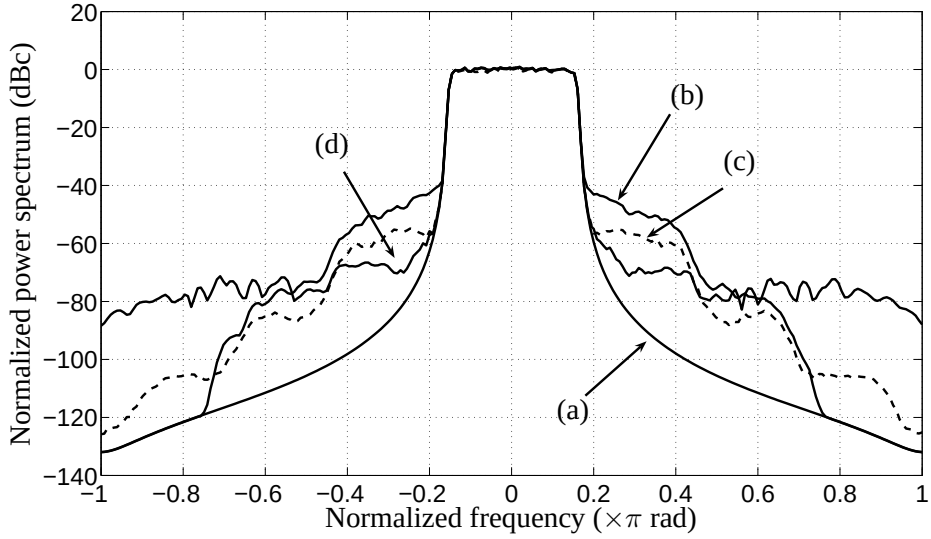


**Figure 5.20:** Normalized power spectra for the RF PA baseband model (a) Input signal power spectrum, (b) Output signal power spectrum for the RF PA baseband model without linearization, (c) Output signal power spectrum for the linearized RF PA baseband model (without adaptation of the linear kernel), (d) Output signal power spectrum for the linearized RF PA baseband model (with adaptation of the linear kernel).

The frequency-domain Volterra kernels in this example are chosen as $\tilde{H}_1(z)$, $\tilde{H}_3(z_1, z_2, z_3) = \tilde{H}_{34}(z_1 z_2 z_3)\tilde{H}_{31}(z_1)\tilde{H}_{32}(z_2)\tilde{H}^*_{33}(z_3)$ and $\tilde{H}_5(z_1, \ldots, z_5) = a$ (cf. Fig. 5.19). Following the exposition of the previous sections, the normalized bandwidth of the discrete-time input signal $\tilde{x}[n]$ has to be lower than $\pi/5$. If we apply the low-rate predistortion scheme in Fig. 5.18 we can reduce the nonlinear distortion measured by the adjacent channel power ratio (ACPR) depending on the flatness of the linear frequency-domain Volterra kernel $\tilde{H}_1(z)$ as discussed in the previous section. In this simulation we have applied a linear kernel with magnitude variations around $1.5$ dB (pessimistic assumption see Ch. 2). For this case we obtain an ACPR of approximately $10$ dB (see Fig. 5.20) if we apply the predistorter with the upsampled (zero insertion) Volterra kernels without any adaptation of the system $\breve{\mathbf{H}}_1^{-1}$. The ACPR can be further increased to approximately $20$ dB, if we additionally adjust the linear system with a low-rate adaptive algorithm.

The predistortion scheme in Fig. 5.18 is not restricted to wireless RF PAs which are described in the equivalent complex baseband domain, it can also be applied to wireline transmission systems where the predistorter is applied to real-valued signals. For this case we also incorporate the even-order operators to describe nonlinear devices such as PAs . To evaluate the performance of the proposed low-rate predistortion scheme, the linearization of a PA for a wireline transmission system is performed. The system $\tilde{\mathbf{H}}$ is taken to be a high-rate discrete-time model of a PA for a VDSL analog front-end [71] that complies with the distortion ratios of the standard [1]. To be able to apply predistortion over a realistic distortion range, the circuit was mistuned to yield a harmonic distortion ratio of $40$ dB. The model

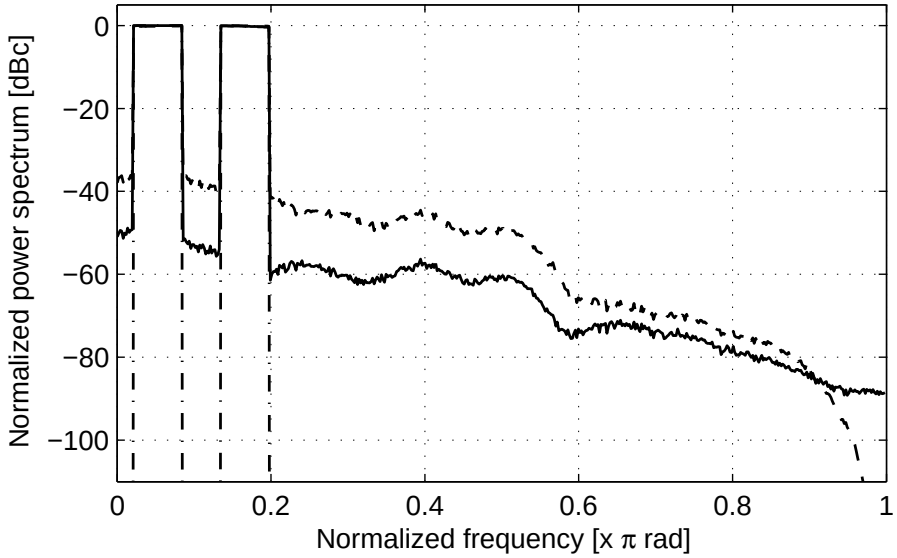


**Figure 5.21:** Normalized power spectrum at $\omega_s$ for the output of the power amplifier $\tilde{\mathbf{H}}$ (dashed), the output of the linearization $\tilde{\mathbf{H}} \circ \tilde{\mathbf{L}}$ applying the upsampled kernels for the predistortion (solid), and the ideal linear response (dashed-dotted); results averaged over $50$ different randomly chosen DMT input signals.

has been obtained by fitting a simple $5$th-order Volterra model to the I/O measurement of a transistor-level circuit simulation. The standard 4-band VDSL system can utilize a bandwidth of up to $12$ MHz, where each band is DMT modulated. The frequency allocation for this simulation according to the standard [1] (Band Plan 998) consists of two downstream bands with bandwidth of each $2.59$ MHz, located at center frequencies $2.225$ MHz and $6.885$ MHz. Following the exposition of the previous sections the sampling rate of digital predistortion for that system has to be at least $\omega_s = 2\pi \times 81.8$ MHz. Conventionally, this directly translates to the sampling requirements of the ADC in the feedback path (refer to 5.1) used for the parameterization of the predistorter. The proposed approach requires an ADC sampling rate of only $\omega_f = 2\pi \times 16.36$ MHz.

The following results are all obtained by averaging over 50 different DMT signals with constant peak-to-average power ratio (PAPR) but randomly chosen phase constellation. The constant PAPR corresponds to the average PAR occurring if the phase constellations are drawn from the uniform distribution $\mathcal{U}[0, 2\pi)^N$, with $N$ being the number of carriers. In Fig. 5.21 the average power spectrum of the output of the amplifier and its linearized version using the upsampled kernels of the low-rate identification is depicted. The corresponding results with an additional low-rate adaptation of $\breve{\mathbf{V}}_1^{-1}$ where the initialization is taken to be $\breve{\mathbf{V}}_1^{-1}(z^P)$, are shown in Fig. 5.22.

The graph in Fig. 5.21 indicates the general result that for systems with a flat frequency response over the input signal bandwidth, such as power amplifiers, the application of the upsampled kernels already yields a good linearization performance. It is evident from Fig. 5.22 that a gain in linearization can be achieved by the low-rate adaptation of $\breve{\mathbf{V}}_1^{-1}$

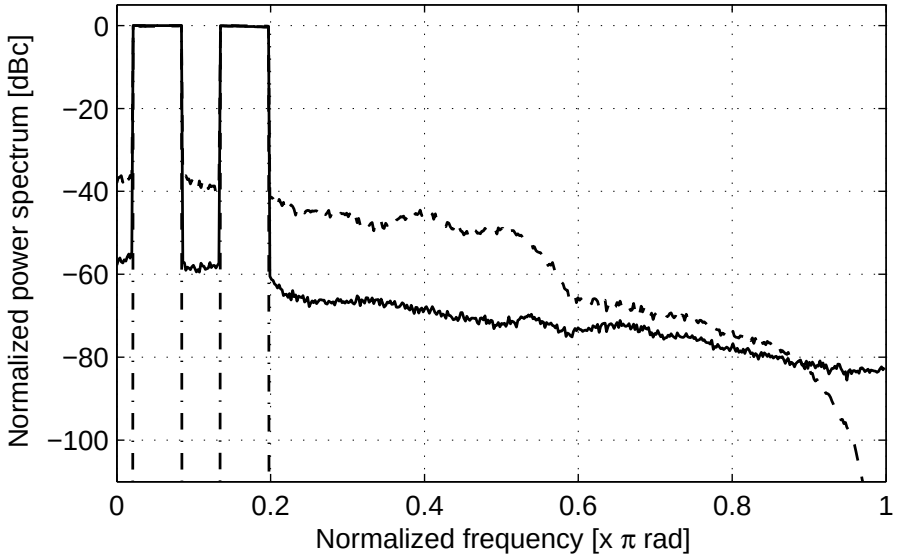


**Figure 5.22:** Normalized power spectrum at $\omega_s$ for the output of the power amplifier $\tilde{\mathbf{H}}$ (dashed), the output of the linearization $\tilde{\mathbf{H}} \circ \tilde{\mathbf{L}}$ applying a low-rate adaptation for $\breve{\mathbf{H}}_1^{-1}$ in the predistorter (solid), and the ideal linear response (dashed-dotted); results averaged over $50$ different randomly chosen DMT input signals.

initialized with $\breve{\mathbf{V}}_1^{-1}(z^P)$. The underlying optimization problem for the adaptive $\breve{\mathbf{V}}_1^{-1}$ is nonlinear because its output signal passes through the nonlinear operator $\tilde{\mathbf{H}}$ to generate the low-rate error signal for the adaptation. Although good initialization is necessary for such problems in general, extensive simulations have not shown any critical dependence of the performance on the initialization.

## 5.5 Conclusion

We have shown that state-of-the art digital predistorters which are based on static nonlinearities are not sufficient to linearize RF PAs for wideband applications, because they do not consider memory effects. Volterra series based predistorters are able to consider such memory effects and have in general a very good linearization performance. The drawback of Volterra series predistorters is the large number of required parameters especially for the higher orders of the nonlinearity. Therefore many different models based on a reduction of Volterra series models such as Memory polynomials (only the diagonal entries of the time-domain Volterra kernels are considered) can be used for digital predistorters. The number of parameters for these simplified predistorters can be considerably reduced compared to the full Volterra predistorter, while the linearization performance is still acceptable for most applications.

Although nonlinear systems such as RF PAs can be identified on a sampling rate which is just twice the input signal bandwidth, for digital predistortion a sampling rate which

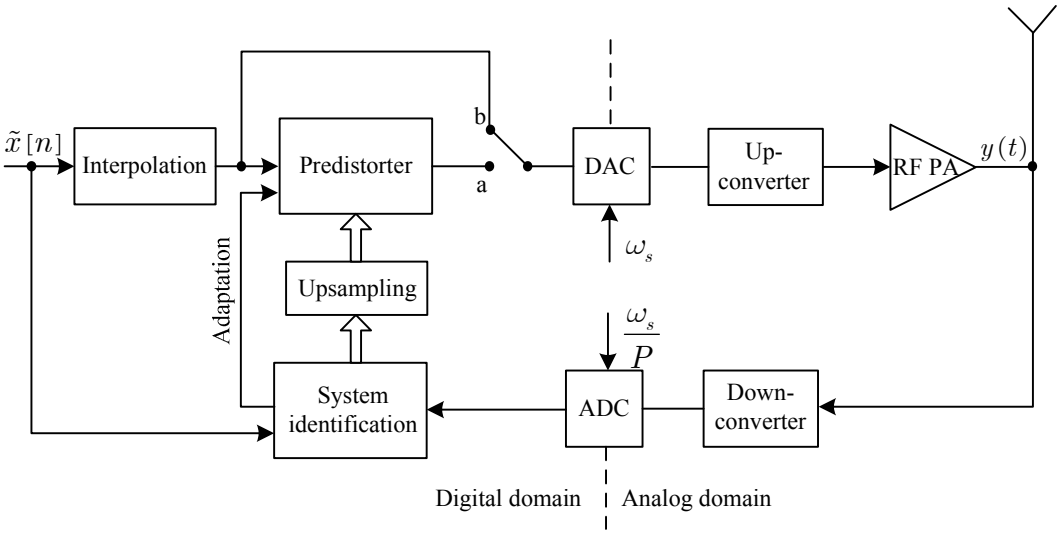


**Figure 5.23:** Block diagram of a wireless transmitter including digital predistortion and low sampling-rate system identification (equivalent to the digital baseband system in Fig. 5.18).

is at least twice the output signal bandwidth is required. However we have shown for a particular predistortion architecture that it is sufficient to interpolate the nonlinear kernels of the low-rate identified PA and copy these high-rate kernels into the predistorter. The unwanted spectral copies of the higher order kernels are masked out by the band-limited input signals. This multi-rate predistorter works perfectly (compared to the purely high-rate system) if the linear kernel of the RF PA is completely flat over the input signal bandwidth (interpolated linear kernel is equal to the high-rate identified kernel), otherwise we have a sub-optimal solution which can be improved upon, if we apply an additional low-rate adaptive algorithm to adjust the frequency response of the interpolated linear kernel in the predistorter over the whole frequency band. With a typical smooth linear kernel for the PA (magnitude variation is approximately 1.5 dB) we obtain a neighbor channel power suppression of approximately 10 dB if we solely apply Volterra kernel interpolation on the low-rate identified kernels, and 20 dB if we additionally adjust the frequency response of the interpolated linear kernel over the whole frequency band. This performance can be obtained, although we only employ a low-cost, low-rate ADC in the analog front-end of the transmitter feedback path. Figure 5.23, depicts a block diagram of a wireless transmitter including the digital predistortorter, the low sampling-rate system identification and the Volterra kernel upsampling block from the multi-rate predistortion architecture in Fig. 5.18 in a real world environment.

# Chapter 6

# Concluding Remarks

In this thesis we analyzed different methods to describe nonlinear passband systems such as RF PAs with input-output behavior models in the complex baseband domain. These models can be advantageously used in system-level simulations to predict the overall performance (spectral masks, bit error rate,...) of wireless communication systems (including the nonlinear RF PA) without the full computational complexity of transistor based circuit simulations. In Ch. 2 we started with the well known description of RF PAs with two different static nonlinearities called AM/AM-conversion and AM/PM-conversion. Models based on this concept are unfortunately not able to describe memory effects (thermal and electrothermal) [70, 69, 11] of RF PAs, which are important for wideband applications such as four-carrier WCDMA. For this reason we used the concept of complex baseband Volterra series models introduced by S. Benedetto [7] for the modeling of nonlinear satellite links and applied them to Class-AB RF PAs for basestation applications. The drawback of such Volterra series models is that the complexity grows immensely with the order of the nonlinearity and the memory length of the RF PA. In Ch. 3, we developed a more efficient representation of complex baseband Volterra series models which is based on frequency-domain Volterra kernel expansion with orthogonal polynomials. If the bandwidth of the wideband input signal is still small compared to the carrier frequency, the kernels vary in general quite smoothly over the input signal band. In this case we can often reduce the number of parameters considerably. One of the key issues in system modeling is nonlinear system identification. Although we know from the work of W. A. Franck [23], that nonlinear system identification can be accomplished efficiently at a sampling-rate which only fulfills the Nyquist theorem regarding the input signal, the identified model is in general not sufficient for system modeling where the spectral out-of-band components plays a crucial role. For this reason, we developed the concept of Volterra kernel interpolation in Ch. 4, which allows nonlinear identification on a low sampling rate as considered in [23]. After the low-rate identification (reduced hardware costs), we transform the model to a new model which is operated on a sufficiently high sampling rate to be able to generate the spectral out-of-band components generated by a nonlinear system. It has been shown that this transformation can be accomplished with almost no additional computational complexity by simple zero insertion.

The second topic of this thesis is the linearization of nonlinear RF PAs with digital predistortion. State of the art digital predistorters are primarily based on static nonlinear functions implemented with look-up table techniques. With this method the complex baseband input signal will be multiplied with a complex correction factor, in order to obtain a linear

transmitter in the ideal case[13]. As discussed above, such static nonlinear functions are not sufficient to describe memory effects of RF PAs, which become important for basestations operated with wideband signals such as four-carrier WCDMA. In Ch. 5 we investigated different predistorter structures and nonlinear identification methods based on direct or indirect methods, with a special focus on implementation complexity. Furthermore we have shown that special predistorter structures are applicable to apply low-rate nonlinear system identification in combination with Volterra kernel interpolation to obtain a sufficient linearization performance with an adequate hardware complexity.

# Appendix A

# Hilbert Transform of Complex Modulated Passband Signals

If we consider the amplitude and phase modulated passband signal $x(t) = a(t)\cos(\omega_c t + \phi_0(t)) = \mathrm{Re}\{\tilde{x}(t)e^{j\omega_c t}\}$ in the frequency-domain, where we assume that the angular carrier frequency $\omega_c > B$, and $\tilde{x}(t)$ is band-limited to $\pm B$, we obtain with [46]

$$\begin{aligned} X(\omega) &= \mathcal{F}\{x(t)\} \\ &= \frac{1}{2}\left[\tilde{X}(\omega-\omega_c) + \tilde{X}^*(-(\omega+\omega_c))\right], \end{aligned} \tag{A.1}$$

where $\tilde{X}(\omega) = \mathcal{F}\{\tilde{x}(t)\}$ denotes the Fourier transform of the complex baseband signal $\tilde{x}(t) = a(t)e^{j\phi_0(t)}$. The complex transfer function of a Hilbert transformer is given in the frequency-domain by [46, 48, 29]

$$H_{\mathcal{H}}(\omega) = -j\mathrm{sgn}(\omega), \tag{A.2}$$

where

$$\mathrm{sgn}(\omega) = \begin{cases} 1 & \text{for } \omega \geq 0 \\ -1 & \text{for } \omega < 0 \end{cases} \tag{A.3}$$

If we apply this complex transfer function to the frequency-domain signal in (A.1), we obtain

$$\begin{aligned} X_s(\omega) &= H_{\mathcal{H}}(\omega)X(\omega) \\ &= \frac{1}{2}\left[-j\tilde{X}(\omega-\omega_c) + j\tilde{X}^*(-(\omega+\omega_c))\right]. \end{aligned} \tag{A.4}$$

If we transform $X_s(\omega)$ back to the time domain by applying the inverse Fourier transform $\mathcal{F}^{-1}$, we obtain

$$\begin{aligned} x_s(t) &= \mathcal{F}^{-1}\{X_s(\omega)\} \\ &= \frac{j}{2}\left[-\tilde{x}(t)e^{j\omega_c t} + \tilde{x}^* e^{-j\omega_c t}\right] \\ &= \mathrm{Im}\left\{\tilde{x}(t)e^{j\omega_c t}\right\}, \end{aligned} \tag{A.5}$$

where $\mathrm{Im}\left\{\tilde{x}(t)e^{j\omega_c t}\right\} = a(t)\sin(\omega_c t + \phi_0(t))$. Therefore the Hilbert transformer shifts the carrier of the passband signal at $90°$, where the amplitude $a(t)$ and the phase $\phi_0(t)$ of the passband input signal $x(t)$ are preserved.

# Appendix B

# Optimum Parameter Calculation of Multi-Variate Orthogonal Polynomials

To calculate the optimum parameters of the multi-dimensional orthogonal polynomial series in (3.1), we first evaluate the integral square error in (3.3) with the identity $|\tilde{H}_{2k+1} - \hat{H}_{2k+1}|^2 = (\tilde{H}_{2k+1} - \hat{H}_{2k+1})(\tilde{H}^*_{2k+1} - \hat{H}^*_{2k+1})$, which results with (3.1) in

$$E = \int_{-B}^{B} \dots \int_{-B}^{B} p(\omega_1) \cdots p(\omega_{2k+1}) \Bigg( \tilde{H}_{2k+1}(\boldsymbol{\omega}_{2k+1}) - \sum_{m_1,\dots,m_{2k+1}=0}^{M_{2k+1}} c_{m_1,\dots,m_{2k+1}} \times T_{m_1}(\omega_1) \cdots T_{m_{2k+1}}(\omega_{2k+1}) \Bigg) \Bigg( \tilde{H}^*_{2k+1}(\boldsymbol{\omega}_{2k+1}) - \sum_{m_1,\dots,m_{2k+1}=0}^{M_{2k+1}} c^*_{m_1,\dots,m_{2k+1}} \times T_{m_1}(\omega_1) \cdots T_{m_{2k+1}}(\omega_{2k+1}) \Bigg) \boldsymbol{d\omega}_{2k+1}. \tag{B.1}$$

where $\boldsymbol{\omega}_{2k+1} = [\omega_1, \dots, \omega_{2k+1}]^T$ and $\boldsymbol{d\omega}_{2k+1} = d\omega_1 \cdots d\omega_{2k+1}$ are introduced for a more compact notation. If we evaluate the product terms in (B.1) we obtain

$$\begin{aligned} E = & \int_{-B}^{B} \dots \int_{-B}^{B} p(\omega_1) \cdots p(\omega_{2k+1}) \left| \tilde{H}_{2k+1}(\boldsymbol{\omega}_{2k+1}) \right|^2 \boldsymbol{d\omega}_{2k+1} \\ & - \sum_{m_1,\dots,m_{2k+1}=0}^{M_{2k+1}} c_{m_1,\dots,m_{2k+1}} \int_{-B}^{B} \dots \int_{-B}^{B} p(\omega_1) \cdots p(\omega_{2k+1}) \tilde{H}^*_{2k+1}(\boldsymbol{\omega}_{2k+1}) \\ & \qquad \times T_{m_1}(\omega_1) \cdots T_{m_{2k+1}}(\omega_{2k+1}) \, \boldsymbol{d\omega}_{2k+1} \\ & - \sum_{m_1,\dots,m_{2k+1}=0}^{M_{2k+1}} c^*_{m_1,\dots,m_{2k+1}} \int_{-B}^{B} \dots \int_{-B}^{B} p(\omega_1) \cdots p(\omega_{2k+1}) \tilde{H}_{2k+1}(\boldsymbol{\omega}_{2k+1}) \\ & \qquad \times T_{m_1}(\omega_1) \cdots T_{m_{2k+1}}(\omega_{2k+1}) \, \boldsymbol{d\omega}_{2k+1} \end{aligned}$$

$$+\sum_{m_1,\ldots,m_{2k+1}=0}^{M_{2k+1}}\sum_{n_1,\ldots,n_{2k+1}=0}^{M_{2k+1}} c_{m_1,\ldots,m_{2k+1}} c^*_{n_1,\ldots,n_{2k+1}} \int_{-B}^{B} p(\omega_1) T_{m_1}(\omega_1) T_{n_1}(\omega_1) d\omega_1 \cdots \int_{-B}^{B} p(\omega_{2k+1}) T_{m_{2k+1}}(\omega_{2k+1}) T_{n_{2k+1}}(\omega_{2k+1}) d\omega_{2k+1}. \tag{B.2}$$

If we apply the orthogonality condition in (3.2) to the last summation term in (B.2), the integral square error reduces to

$$\begin{aligned} E = & \int_{-B}^{B} \cdots \int_{-B}^{B} p(\omega_1) \cdots p(\omega_{2k+1}) \left| \tilde{H}_{2k+1}(\boldsymbol{\omega}_{2k+1}) \right|^2 \boldsymbol{d\omega}_{2k+1} \\ & - \sum_{m_1,\ldots,m_{2k+1}=0}^{M_{2k+1}} c_{m_1,\ldots,m_{2k+1}} \int_{-B}^{B} \cdots \int_{-B}^{B} p(\omega_1) \cdots p(\omega_{2k+1}) \tilde{H}^*_{2k+1}(\boldsymbol{\omega}_{2k+1}) \\ & \qquad \times T_{m_1}(\omega_1) \cdots T_{m_{2k+1}}(\omega_{2k+1}) \, \boldsymbol{d\omega}_{2k+1} \\ & - \sum_{m_1,\ldots,m_{2k+1}=0}^{M_{2k+1}} c^*_{m_1,\ldots,m_{2k+1}} \int_{-B}^{B} \cdots \int_{-B}^{B} p(\omega_1) \cdots p(\omega_{2k+1}) \tilde{H}_{2k+1}(\boldsymbol{\omega}_{2k+1}) \\ & \qquad \times T_{m_1}(\omega_1) \cdots T_{m_{2k+1}}(\omega_{2k+1}) \, \boldsymbol{d\omega}_{2k+1} \\ & + \sum_{m_1,\ldots,m_{2k+1}=0}^{M_{2k+1}} \left| c_{m_1,\ldots,m_{2k+1}} \right|^2 \lambda_{m_1} \cdots \lambda_{m_{2k+1}}. \end{aligned} \tag{B.3}$$

By completing the magnitude square in (B.3), the final expression for the integral square error is given by

$$\begin{aligned} E = & \int_{-B}^{B} \cdots \int_{-B}^{B} p(\omega_1) \cdots p(\omega_{2k+1}) \left| \tilde{H}_{2k+1}(\boldsymbol{\omega}_{2k+1}) \right|^2 \boldsymbol{d\omega}_{2k+1} \\ & + \sum_{m_1,\ldots,m_{2k+1}=0}^{M_{2k+1}} \left| c_{m_1,\ldots,m_{2k+1}} \sqrt{\lambda_{m_1} \cdots \lambda_{m_{2k+1}}} - \frac{1}{\sqrt{\lambda_{m_1} \cdots \lambda_{m_{2k+1}}}} \right. \\ & \times \left. \int_{-B}^{B} \cdots \int_{-B}^{B} p(\omega_1) \cdots p(\omega_{2k+1}) \tilde{H}_{2k+1}(\boldsymbol{\omega}_{2k+1}) T_{m_1}(\omega_1) \cdots T_{m_{2k+1}}(\omega_{2k+1}) \, \boldsymbol{d\omega}_{2k+1} \right|^2 \end{aligned}$$

$$- \sum_{m_1,\ldots,m_{2k+1}=0}^{M_{2k+1}} \left| \frac{1}{\sqrt{\lambda_{m_1} \cdots \lambda_{m_{2k+1}}}} \int_{-B}^{B} \cdots \int_{-B}^{B} p(\omega_1) \cdots p(\omega_{2k+1}) \tilde{H}_{2k+1}(\boldsymbol{\omega}_{2k+1}) \right.$$
$$\left. \times T_{m_1}(\omega_1) \cdots T_{m_{2k+1}}(\omega_{2k+1})\, \boldsymbol{d\omega}_{2k+1} \right|^2, \quad \text{(B.4)}$$

where only the middle summation term depends on the unknown complex parameters $c_{m_1,\ldots,m_{2k+1}}$. Because this term is always nonnegative, the integral square error is minimized by

$$c_{o(m_1,\ldots,m_{2k+1})} \sqrt{\lambda_{m_1} \cdots \lambda_{m_{2k+1}}} - \frac{1}{\sqrt{\lambda_{m_1} \cdots \lambda_{m_{2k+1}}}} \int_{-B}^{B} \cdots \int_{-B}^{B} p(\omega_1) \cdots p(\omega_{2k+1})$$
$$\times \tilde{H}_{2k+1}(\boldsymbol{\omega}_{2k+1}) T_{m_1}(\omega_1) \cdots T_{m_{2k+1}}(\omega_{2k+1})\, \boldsymbol{d\omega}_{2k+1} = 0, \quad \text{(B.5)}$$

which yields the optimum complex parameters in (3.5)

$$c_{o(m_1,\ldots,m_{2k+1})} = \frac{1}{\lambda_{m_1} \cdots \lambda_{m_{2k+1}}} \int_{-B}^{B} \cdots \int_{-B}^{B} p(\omega_1) \cdots p(\omega_{2k+1})$$
$$\times \tilde{H}_{2k+1}(\boldsymbol{\omega}_{2k+1}) T_{m_1}(\omega_1) \cdots T_{m_{2k+1}}(\omega_{2k+1})\, \boldsymbol{d\omega}_{2k+1}. \quad \text{(B.6)}$$

# Appendix C

# Quasi-Memoryless Systems Based on Fourier Series Expansion

If we consider the nonlinear passband model in Fig. 2.3 with $\mathbf{G}[x] = v(x)$, the output signal $u(t)$ can be rewritten in the following form

$$u(t) = v[a(t)\cos\psi(t)], \tag{C.1}$$

where $\psi(t) = \omega_c t + \phi_0(t)$. Because the expression in (C.1) is periodic in $\psi(t)$ with $2\pi$, we can expand (C.1) in a Fourier series [10]

$$u(t) = m_0(a(t)) + \sum_{k=1}^{\infty} 2\mathrm{Re}\{m_k(a(t))\exp(jk\psi(t))\}, \tag{C.2}$$

where the complex magnitude dependent Fourier coefficients are expressed by

$$m_k(a) = \frac{1}{2\pi}\int_0^{2\pi} v(a\cos\psi)\exp(-j\psi)d\psi. \tag{C.3}$$

The 1st-zonal filter $\mathbf{F}[u]$ in Fig. C.1 passes only the frequency components which are located near the carrier frequency. Therefore the filtered output signal is given with (C.2) by

$$y(t) = 2\mathrm{Re}\{m_1(a(t))\exp(j\psi(t))\}. \tag{C.4}$$

The complex Fourier coefficient $m_1(a)$ can be calculated with (C.3) and $v(a\cos\psi) = \sum_{l=1}^{L} b_l[a\cos\psi]^l + \sum_{l=1}^{L} c_l[a\sin\psi]^l$ (see Fig. 2.3) by

$$m_1(a) = \sum_{l=1}^{L} b_l a^l \frac{1}{2\pi}\int_0^{2\pi}[\cos\psi]^l\exp(-j\psi)d\psi + \sum_{l=1}^{L} c_l a^l \frac{1}{2\pi}\int_0^{2\pi}[\sin\psi]^l\exp(-j\psi)d\psi. \tag{C.5}$$

The evaluation of the integral expressions in (C.5) yields

$$\frac{1}{2\pi}\int_0^{2\pi}[\cos\psi]^l\exp(-j\psi)d\psi = \begin{cases} \frac{1}{2^l}\binom{l}{(l+1)/2} & \text{for } l \in \mathbb{N}_o \\ 0 & \text{otherwise} \end{cases} \tag{C.6}$$

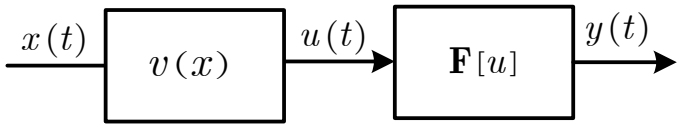


**Figure C.1:** Memoryless nonlinear passband system from Fig. 2.3, where the nonlinear operator $\mathbf{G}[x]$ is represented by the static nonlinear function $v(x)$.

and

$$\frac{1}{2\pi}\int_0^{2\pi}[\sin\psi]^l\exp(-j\psi)d\psi=\begin{cases}-j\frac{1}{2^l}\binom{l}{(l+1)/2} & \text{for } l\in\mathbb{N}_o\\ 0 & \text{otherwise}\end{cases} \tag{C.7}$$

Therefore the complex Fourier coefficient in (C.5) can be expressed with (C.6) and (C.7) by

$$m_1(a)=\sum_{k=0}^{\lceil L/2\rceil-1}a^{2k+1}\frac{1}{2^{2k+1}}\binom{2k+1}{k+1}\underbrace{(b_{2k+1}-jc_{2k+1})}_{d_{2k+1}}. \tag{C.8}$$

If we express (C.4) with (C.8), we obtain with $\tilde{x}(t)=a(t)\exp(j\phi_0(t))$ the desired result given by

$$y(t)=\mathrm{Re}\left\{\sum_{k=0}^{\lceil L/2\rceil-1}\frac{d_{2k+1}}{2^{2k}}\binom{2k+1}{k+1}|\tilde{x}(t)|^{2k}\,\tilde{x}(t)\exp\left(j\omega_c t\right)\right\}. \tag{C.9}$$

# Bibliography


[1] "European Telecommunication Standards Institute, 1999 ETSI TM, TS 101 270-1 V.1.2.1 (1999-10), Transmission and Multiplexing (TM)." 5.4.2

[2] W. Alt, *Nichtlineare Optimierung*. Wiesbaden, Germany: Vieweg, 2002. 5.2.4

[3] Anritsu, "Application note, Adjacent Channel Power Ratio (ACPR)," http://www.us.anritsu.com/, 2001. 1.2

[4] E. Aschbacher and M. Rupp, "Identification of a nonlinear power-amplifier L-N-L structure for pre-distortion purposes," in *IEEE Proceedings on Personal, Indoor and Mobile Radio Communications PIMRC*, Sept. 2003, pp. 2102–2106. 1.1

[5] ——, "Modelling and identification of nonlinear power-amplifier with memory for nonlinear digital adaptive pre-distortion," in *IEEE Workshop on Signal Processing Advances in Wireless Communications*, June 2003, pp. 658–662. 1.1

[6] ——, "Robustness analysis of gradient identification method for a nonlinear Wiener system," in *IEEE Workshop on Statistical Signal Processing*, July 2005, pp. 103–108. 1.1

[7] S. Benedetto, E. Biglieri, and R. Daffara, "Modeling and performance evaluation of nonlinear satellite links—a Volterra series approach," *IEEE Trans. Aerosp. Electron. Syst.*, vol. 15, pp. 494–507, July 1979. 2.1, 2.2, 2.3.1, 6

[8] S. Benedetto and E. Biglieri, *Principles of digital transmission with wireless applications*. Dordrecht, The Netherlands: Kluwer academic / Plenium Publishers, 1999. 1.1, 1.2, 2.1, 2.2, 2.2, 2.2, 2.3.1, 3.1

[9] A. Björck, *Numerical methods for least squares problems*. Philadelphia: Siam, 1996. 3.4.1, 4.2, 5.2.4

[10] N. M. Blachman, "Detectors, bandpass nonlinearities, and their optimization: Inversion of the Chebyshev transform," *IEEE Trans. Inform. Theory*, vol. 17, pp. 398–404, July 1971. 2.1, 2.2, 2.3.1, 3.1, C

[11] W. Boesch and G. Gatti, "Measurement and simulation of memory effects in predistortion linearizers," *IEEE Trans. Microwave Theory Tech.*, vol. 37, pp. 1885–1890, Dec. 1989. 1.1, 2.1, 2.2.3, 2.5.1, 5.1, 6

[12] A. Carini, G. L. Sicuranza, and V. J. Mathews, "On the inversion of certain nonlinear systems," *IEEE Signal Processing Lett.*, vol. 4, pp. 334–336, Dec. 1997. 1.1

[13] J. K. Cavers, "Amplifier linearization using a digital predistorter with fast adaption and low memory requirements," *IEEE Trans. Veh. Technol.*, vol. 37, pp. 1885–1890, Dec. 1989. 1.1, 1.1, 4.1, 5.1, 5.2.3, 5.2.3, 6

[14] ——, "Amplifier linearization by adaptive predistortion," U.S. Patent 5049832, September 1991. 1.1

[15] S. C. Cripps, *RF power amplifiers for wireless communications*. Boston, London: Artech House, 1999. 1, 1.1, 2.1, 2.2, 4.1, 5.1, 5.2.3

[16] ——, *Advanced techniques in RF power amplifier design*. Boston, London: Artech House, 2002. 1, 1.1, 2.1, 2.2, 4.1, 5.1

[17] A. N. D'Andrea, V. Lottici, and R. Reggiannini, "A digital approach to efficient RF power amplifier linearization," in *IEEE Global Telecommunications Conference, GLOBECOM 97, Phoenix, USA*, vol. 1, Nov. 1997, pp. 77–81. 1.1

[18] L. Ding, G. T. Zhou, D. R. Morgan, Z. Ma, S. Kenney, J. Kim, and C. R. Giardina, "A robust digital baseband predistorter constructed using memory polynomials," *IEEE Trans. Commun.*, vol. 52, pp. 159–165, Jan. 2004. 2.5.2, 4.1, 5.1, 5.2

[19] L. Ding, R. Raich, and G. T. Zhou, "A Hammerstein predistortion linearization design based on the indirect learning architecture," in *IEEE International Conference on Acoustics, Speech and Signal Processing*, May 2002, pp. 2689–2692. 1.1

[20] ——, "A Hammerstein predistortion linearization design based on the indirect learning architecture," in *IEEE International Conference on Acoustics, Speech, and Signal Processing, 2002. Proceedings. (ICASSP '02)*, May 2002, pp. 2689–2692. 1.1, 4.1, 5.1

[21] L. Ding, G. T. Zhou, D. R. Morgan, Z. Ma, and S. Kenney, "Memory polynomial predistorter based on the indirect learning architecture," in *IEEE Global Telecommunications Conference GLOBECOM*, Nov. 2002, pp. 967–971. 1.1

[22] C. Eun and E. J. Powers, "A new Volterra predistorter based on the indirect learning architecture," *IEEE Trans. Signal Processing*, vol. 45, pp. 223–227, Jan. 1997. 1.1, 5.2, 5.2.4

[23] W. A. Frank, "Sampling requirements for Volterra system identification," *IEEE Signal Processing Letters*, vol. 3, pp. 266–268, Sept. 1996. 4.1, 4.3, 4.3, 6

[24] X. Y. Gao and W. M. Snelgrove, "Adaptive linearization schemes for weakly nonlinear systems using adaptive linear and nonlinear FIR filters," in *Midwest Symposium on Circuits and Systems*, Aug. 1990, pp. 9–12. 5.4

[25] P. C. Hansen, *Rank-deficient and discrete ill-posed problems*. Philadelphia: Siam, 1998. 3.4.1, 4.2, 5.2.4

[26] S. Haykin, *Adaptive Filter Theory*. Upper Saddle River, New Jersey: Prentice Hall, Inc., 2002. 1.1, 2.5.2, 3.4.2, 5.2, 5.2.4

[27] C. L. Henrik Schulze, *Theory and Applications of OFDM and CDMA*. John Wiley & Sons, Inc., New York, 2005. 2.1, 2.2.3

[28] Infineon Technologies, "Data sheet PTF210901, LDMOS RF Power Field Effect Transistor $90$ W, $2110 - 2170$ MHz," http://www.infineon.com/, 2004. 1.2, 5.2.4, 5.1, 5.7

[29] K. Kammeyer, *Nachrichtenübertragung*. Stuttgart: B.G. Teubner, 1996. 2.2, 3.3, A

[30] H. W. Kang, Y. S. Cho, and D. H. Youn, "On compensating nonlinear distortions of an OFDM system using an efficient adaptive predistorter," *IEEE Trans. Commun.*, vol. 47, pp. 522–526, Apr. 1999. 1.1

[31] A. Kaye, D. George, and M. Eric, "Analysis and compensation of bandpass nonlinearities for communication," *IEEE Trans. Commun.*, vol. 20, pp. 965–972, Oct. 1972. 2.1, 2.2

[32] P. B. Kennington, *High linearity RF amplifier design*. Boston, London: Artech House, 2000. 1, 1.1, 2.1, 2.2, 4.1, 5.1, 5.2.3

[33] J. Kim and K. Konstantinou, "Digital predistortion of wideband signals based on power amplifiers with memory," *Electronics Letters*, vol. 37, pp. 1417–1418, Nov. 2001. 1.1, 2.5.1, 2.5.2, 4.1, 5.2, 5.2.4

[34] H. Koeppl and P. Singerl, "An efficient scheme for nonlinear modeling and predistortion in mixed signal systems," *IEEE Trans. Circuits Syst.*, Dec. 2006, to be published. 1.3

[35] E. Kreyszig, *Advanced engineering mathematics*. New York: John Wiley & Sons, Inc., 605 Third Avenue, New York, 1999. 3.2, 3.2, 3.2.1

[36] H. Ku, M. D. McKinley, and J. Kenney, "Quantifying memory effects in RF power amplifiers," *IEEE Trans. Microwave Theory Tech.*, vol. 50, pp. 2843–2849, Dec. 2002. 1.1, 2.1, 2.5.1

[37] K. S. Kundert, J. K. White, and A. Sangiovanni-Vincentelli, *Steady-state methods for simulating analog and microwave circuits*. Boston, London: Kluwer Academic Publishers, 1990. 1.2, 2.2

[38] S. Marsili, "Algorithm for peak to average power ratio reduction operating at symbol rate," in *IEEE International Symposium on Circuits and Systems (ISCAS 2005)*, May 2005, pp. 5497–55 002. 1.1

[39] K. W. Martin, "Complex signal processing is not complex," *IEEE Trans. Circuits Syst.*, vol. 51, pp. 1823–1836, Sept. 2004. 1.1, 2.2

[40] V. J. Mathews and G. L. Sicuranza, *Polynomial signal processing*. New York: John Wiley & Sons, Inc., 605 Third Avenue, New York, 2000. 1.1, 1.1, 2.1, 2.3, 2.3.1, 2.3.2, 3.4.2, 4.1, 4.2, 5.1, 5.2, 5.2.1

[41] K. Mekechuk, W.-J. Kim, and S. P. Stapleton, "Linearizing power amplifiers using digital predistortion, EDA tools and test hardware," *High Frequency Electronics,Summit Technical Media, LLC*, 2004. 1.1

[42] O. Mendoza, *Measurement of EVM (Error Vector Magnitude) for 3G Receiver*. Chalmers University of Technology, Gotheburg, Sweden: Master Thesis, 2002. 1.2

[43] K. J. Muhonen, M. Kavehrad, and R. Krishnamoorthy, "Look-up table techniques for adaptive digital predistortion: a development and comparison," *IEEE Trans. Veh. Technol.*, vol. 49, pp. 1995–2002, Sept. 2000. 1.1

[44] C. L. Nikias and A. P. Petropulu, *Higher-order spectral analysis*. Englewood Cliffs, NJ: Prentice Hall, 1993. 2.2.2

[45] A. V. Oppenheim and R. W. Schafer, *Discrete-time signal processing*. Upper Saddle River, NJ 07458: Prentice Hall international, Inc., 1999. 2.2, 2.2, 3.4, 3.4.1, 4.2, 4.3

[46] A. V. Oppenheim and A. S. Willsky, *Signals and systems*. Upper Saddle River, NJ 07458: Prentice Hall international, Inc., 1997. 2.2, 2.2, 3.4, 4.2, 4.3, A, A

[47] A. Papoulis and U. Pillai, *Probability, random variables and stochastic processes*. New York: McGraw-Hill Science/Engineering/Math, 2001. 2.2.2

[48] J. G. Proakis, *Digital signal processing*. Upper Saddle River, NJ 07458: Prentice Hall, Inc., 1996. 1, 2.2, 3.4.1, 4.2, 4.3, A

[49] ——, *Digital communications*. New York: McGraw-Hill Companies, 2000. 1.2, 2.2.2, 3.3

[50] F. H. Raab, P. Asbeck, S. Cripps, P. B. Kennington, Z. B. Popovic, N. Pothecary, J. F. Sevic, and N. O. Sokal, *RF and Microwave Power Amplifier and Transmitter Technologies -Part 1 to Part 5*. High Frequency Electronics, 2003. 1, 1.1, 1.2, 5.1, 5.2.3

[51] R. Raich and G. T. Zhou, "On the modeling of memory nonlinear effects of power amplifiers for communication applications," in *Digital Signal Processing Workshop and 2nd Signal Processing Education Workshop*, Oct. 2002, pp. 7–10. 1.1, 1.1, 2.1, 2.2, 2.4, 5.1

[52] W. J. Rugh, *Nonlinear system theory*. Baltimore: The Johns Hopkins University Press, 2002. 1.1, 2.1, 2.3, 2.3.1, 2.5.1, 5.1, 5.3, 5.3, 5.3, 5.4

[53] A. A. Saleh, "Frequency-independent and frequency dependent nonlinear models of TWT amplifiers," *IEEE Trans. Commun.*, vol. 29, pp. 1715–1720, Nov. 1981. 2.1, 2.2

[54] M. Schetzen, “Power-series equivalence of some functional series with applications,” *IEEE Trans. Circuits Syst.*, vol. 17, pp. 305–313, Aug. 1970. 1.1, 3.2

[55] ——, “Theory of pth-order inverses of nonlinear systems,” *IEEE Trans. Circuits Syst.*, vol. 23, pp. 285–291, May 1976. 5.2, 5.3

[56] ——, *The Volterra and Wiener theories of nonlinear systems*. Malabar, Florida: Krieger publishing company, 1980. 1.1, 1.1, 2.1, 2.3, 2.3.1, 2.3.2, 2.3.2, 2.3.2, 2.5.1, 3.2, 5.1, 5.2, 5.3, 5.4

[57] D. Schwingshackl, *Digital Enhancement and Multirate Processing Methods for Nonlinear Mixed Signal Systems*. Graz University of Technology, Graz, Austria: Doctoral Thesis, 2005. 4.1

[58] P. Singerl, “A new approach for efficient modeling of nonlinear passband systems for communication applications,” in *International Workshop on Nonlinear Circuits and Signal Processing*, Honolulu, USA, Mar. 2005, pp. 379–382. 1.3

[59] ——, “Digital predistorter based on frequency-domain Volterra kernel approximation,” pending patent application, Germany and United States, 22.05.2005. 1.3

[60] P. Singerl, A. Agrawal, A. Garg, Neelabh, G. Kubin, and H. Eul, “Complex baseband predistorters for nonlinear wideband RF power amplifiers,” in *Midwest Symposium on Circuits and Systems (MWSCAS)*, San Juan, USA, Aug. 2006. 1.3

[61] P. Singerl and H. Koeppl, “An efficient scheme for nonlinear modeling and predistortion in mixed signal systems,” pending patent application, Germany and United States,, 02.05.2006. 1.3

[62] ——, “A low-rate identification method for digital predistorters based on Volterra kernel interpolation,” in *Midwest Symposium on Circuits and Systems (MWSCAS)*, vol. 2, Cincinnati, USA, Aug. 2005, pp. 1533–1536. 1.3

[63] ——, “Volterra kernel interpolation for system modeling and predistortion purposes,” in *IEEE International Symposium on Signals, Circuits and Systems (ISSCS)*, vol. 1, Iasi, Romania, July 2005, pp. 251–254. 1.3

[64] ——, “Volterra kernel interpolation of nonlinear systems,” pending patent application, Germany and United States,, 22.04.2005. 1.3

[65] P. Singerl and G. Kubin, “Constructing memory-polynomial models from frequency-dependent AM/AM and AM/PM measurements,” pending patent application, Germany and United States, 19.04.2006. 1.3

[66] ——, “Chebyshev approximation of baseband Volterra series for wideband RF power amplifiers,” in *IEEE International Symposium on Circuits and Systems (ISCAS)*, vol. 3, Kobe, Japan, May 2005, pp. 2655–2658. 1.3

[67] ——, “Constructing memory-polynomial models from frequency-dependent AM/AM and AM/PM measurements,” in *IEEE International Symposium on Circuits and Systems (ISCAS)*, May 2007, submitted. 1.3

[68] ——, “Efficient approximation of baseband Volterra series for wideband RF power amplifierss,” pending patent application, Germany and United States,, 9.05.2006. 1.3

[69] J. Vuolevi and T. Rahkonen, *Distortion in RF power amplifiers*. Boston, London: Artech House, 2003. 1.1, 2.1, 2.2.3, 5.1, 6

[70] J. H. Vuolevi, T. Rahkonen, and J. P. A. Manninen, “Measurement technique for characterizing memory effects in RF power amplifiers,” *IEEE Trans. Microwave Theory Tech.*, vol. 49, pp. 1383–1389, Aug. 2001. 1.1, 2.1, 2.2.3, 5.1, 6

[71] H. Weinberger, A. Wiesbauer, M. Clara, C. Fleischhacker, T. Poetscher, and B. Seger, “A 1.8V 450mW vdsl 4-band analog front end IC in 0.18$\mu$m CMOS,” in *IEEE International Conference on Solid-State Circuits 2002 , San Francisco CA, USA*, vol. 1, Feb. 2002, pp. 326–471. 5.4.2

[72] E. W. Weisstein, *CRC concise encyclopedia of mathematics*. Chapman and Hall/CRC, 2003. 2.2, 3.2.1

[73] Y. Yong, J. Yi, J. Nam, B. Kim, and M. Park, “Measurement of two-tone transfer characteristic of high-power amplifiers,” *IEEE Trans. Microwave Theory Tech.*, vol. 49, pp. 568–571, Mar. 2001. 2.5.1

[74] G. Zhou and R. Raich, “Spectral analysis of polynomial nonlinearity with applications to RF power amplifiers,” *EURASIP Journal on Applied Signal Processing*, pp. 1831–1840, Dec. 2004. 2.1, 2.2.2

[75] A. Zhu, M. Wren, and T. Brazil, “An efficient Volterra-based behavioral model for wideband RF power amplifiers,” in *Microwave Symposium Digest, IEEE MTT-S international*, June 2003, pp. 787–790. 1.1, 2.1

[76] Y. M. Zhu, “Generalized sampling theorem,” *IEEE Trans. Circuits Syst.*, vol. 39, pp. 587–588, Aug. 1992. 4.1